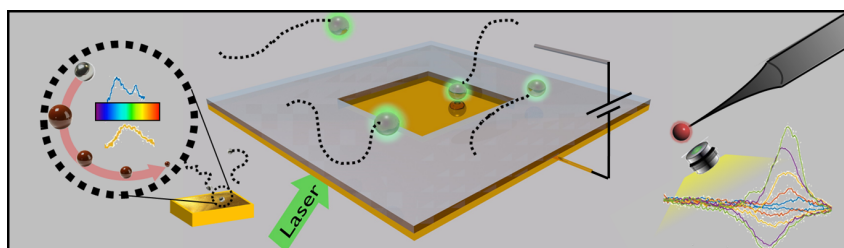# Opto-Electrochemical Methods for Imaging the Reactivity of Individual Nanoparticles

Vitor Brasiliense

A thesis presented for the degree of Doctor of Philosophy
Supervised by Fréderic Kanoufi and Gilles Tessier
Speciality: Electrochemistry

Thesis presented and publicly defended in Paris on the 11th of December 2017

President of the Jury	Pr. Isabelle Ledoux	ENS Paris Saclay
Reviewers	Pr. Julie Macpherson	University of Warwick
	Dr. Sébastien Bidault	Institut Langevin ESPCI
Examiners	Pr. Michel Orrit	Leiden University
	Pr. Marc Robert	Université Paris Diderot
Supervisor	Dr. Frédéric Kanoufi	Université Paris Diderot
Co-supervisor	Pr. Gilles Tessier	Université Paris Descartes

ITODYS - Interfaces, Traitments, Organisation et Dynamique des Systèmes
ED388 - Ecole Doctorale de Chimie Physique et Chimie Analytique de Paris Centre
Sorbonne Paris Cité

ii

Contents

Acknowledgements

I always struggle to write Acknowledgments. I wouldn't dare to say it is the hardest part of the thesis, but sure as hell it isn't the easiest. Just like an ensemble response is the collection of individual expressions, this thesis would not have been possible without countless interactions with the people around me over not only these last three years, but over my whole life. Although it would be impossible to mention everyone, I will start with the people that first encouraged me to study, my family: Mom, Lucas, you are amazing examples on how to be a great human being. It would not been possible to have come this far without you. I was extremely happy to see you at my defense - It was an important moment for me, and you are at least partially responsible for me being there as well. Muito Obrigado.

I'd also like to thank all my friends from the ESPCI, with whom not only have I learned how to speak French, but who were also my first interface with France when I first arrived in Paris, seven years ago. After all those travels, weekends, soirées with terrible music... Thomas Barrès, Oriane Tapparo, Gabriel Cournelle, Edouard Lees, François Bargain, Aurélien Duval, Mélanie Jacquet, Guillaume Chatté, Marc Gesnik, Sarah Christoph, un grand merci. Talking about my first years in France, I also would like to take the opportunity to thank Victor Hugo and Catarina Macedo da Silva (ou da Silva Macedo). Besides the friendship we shared over these six years, I would never be able to prepare the Feijoadas I served for my thesis reception without all those cooking evenings in each others houses!

I would also like to sincerely thank the wall color designer of Paris Diderot, that gave me matter to complain over these three years (*who thought fluorescent-green was a good idea!??*). Seriously speaking, I am grateful for all the dear friends I made in Paris VII (now all doctors - we are getting old!), Alexandra Tibaldi, Andrés Lombana, Jonathan Fouineau, Yong Ai, Célia Achaibou (*Félicitations pour ton mariage!*). All the good moments shared in and outside the lab, Bootlager's evenings, Asian Restaurants, "Rhum Arrangés", poorly organized camping trips made the PhD period more than fun and will not be forgotten!

Last, but not the least, I would like to thank my dear Lydia Merakeb, whom I only met at the end of my thesis, and that constitutes the biggest and happiest surprise of this year. Meeting you was *la cerise sur le gâteau* of a great year!

On the professional side, it was a very enriching experience to work between two research groups, between Electrochemistry and Optics. Such a complementarity of cultures, backgrounds and managing styles has been fundamental for the success of this work and for my personal growth. Not only I learned a lot of chemistry and optics, I was also able to understand two very different ways of making research.

Not less important, the working environment in both Paris Diderot and Descartes could not be more relaxed and stimulating! Starting from the drinking nights out, passing through all the very interesting discussions and positive atmosphere, and midday common lunches, it was super cool to be a PhD student here. Alice Dauphin, Lydiane Gantier, Léo Angele, Jane Stockmann (*livin' the dream!*), Jean Pinson, Jêrome Médard, Mihn Chau Nguyen, Jean-François Lemineur, merci beaucoup!

In particular I would like to thank two persons who were pivotal for the great atmosphere in both labs. Pascal Berto in Paris Descartes, for being a great person to work with, while teaching me so much about practical aspects of optics and lab organization (thanks for putting up with my *bordel* in the lab :P). Jean-Marc Noël, for the countless discussions about electrochemistry, SECM experiments, tennis matches and especially for the improvised apéros and ebriety stories (*Ablon, A-B-L-O-N*).

I would also like to thank Catherine Combellas, who first lured me into the Electrochemistry group of the ESPCI, and who constitutes the best example I am aware of on how to manage a research group. Not to mention advices on healthy nutrition and organization skills (which should be read "on how not to eat junk and keep my desk presentable").

Finally, I would like to thank my supervisors, from whom I learned so much not only about Science but about life in research.

Gilles Tessier, whose co-direction was pivotal for the success of my experiments. It was with great competence and optimism that you help me tackle from quotidian problems to big Science discussions. Thank you for the guidance!

Frédéric Kanoufi, from whom have I not only learned electrochemistry, but also the most fundamental aspects of what being a researcher is about. I feel I could not have been better guided over these three years. Not to mention being the nicest person to work with. A big, sincere, thank you!

<div align="right">Dr. Vitor Brasiliense</div>

Opto-Electrochemical Methods for Imaging the Reactivity of Individual Nanoparticles

Vitor Brasiliense

Abstract

A number of coupled optical and electrochemical single particle techniques are employed for investigating a variety of chemical systems at the level of individual objects. On the optical side, holography and visible spectroscopy are imbued with superlocalization principles pushing the applicability of these techniques down to sub-diffraction levels. Nanoelectrochemical techniques such as stochastic impacts and nanoelectrodes are used to complement this information, providing a much more complete characterization of the phenomena.

It is shown that this dual optical and electrochemical single particle characterization is actually crucial to understand complex nano chemical systems *in loco*. Starting from model reactions, such as Ag oxidation, the complexity of the studied phenomena and systems is progressively increased, as light is shed on transport phenomena, aggregation, as well as redox transformations and catalysis on complicated materials such as ill-defined transition metal (cobalt) oxides.

Keywords: Nanoparticles, Opto-Electrochemical Methods, Holography, Nanoelectrochemistry, Catalysis

Méthodes Opto-Electrochimiques pour Imager la Réactivité de Nanoparticules Individuelles

Vitor Brasiliense

Résumé

Dans ce travail, plusieurs méthodes opto-électrochimiques ont été développées et appliquées à l'étude de systèmes chimiques à l'échelle de l'objet individuel. Du coté optique, l'holographie et la spectroscopie visible ont été associées à la superlocalisation pour pousser l'applicabilité de ces techniques au-delà de la limité imposée par la diffraction. Des techniques nanoélectrochimiques, comme les impacts stochastiques et l'utilisation de nanoelectrodes, complètent cette étude en renseignant sur la réactivité et sur les étapes de transfert d'électrons. Ces études couplées caractérisent ainsi les phénomènes chimiques de façon bien plus complète.

Il est montré que cette caractérisation à la fois chimique et optique est en fait essentielle pour pouvoir comprendre le fonctionnement des systèmes nano chimiques *in loco*. En démarrant par des réactions modèle, comme l'oxydation de l'argent, la complexité des systèmes étudiés est progressivement augmentée, éclairant des phénomènes de transport, d'agrégation, ainsi que des transformation redox et de catalyse sur des matériaux complexes et mal définis tel que les oxydes de métaux de transition (cobalt).

Mots Clés: Nanoparticules, Méthodes Opto-électrochimiques, holographie, Nanoélectrochimie, catalyse

General Introduction: Coupling Electrochemistry and Optical Techniques

Anyone who has ever been to a *(decent)* rock concert should be familiar with the strange fact that a crowd seems to sing in perfect harmony. Although the vast majority of the concert attendees are not professional singers, the overall melody sounds perfectly in tune. If a recorder was to be placed under each persons mouth, a large number of, out of tune, distorted, slightly hysterical tracks would be heard. Yet when added up, all these voices seem to complement each other, forming an ensemble effect that is beyond any individual performance.

But... What if the information contained in those dissonant and mutually average was the actual key to discovering something new? What if we could select the best voices among the crowd? More than that, one must also come to the realization that there is more in a musician than a mere beautiful voice. Other things must be considered, how strong is his/her personality? How committed is (s)he to actually taking the time and trouble to getting there? And how, from a glance into a crowd could we possibly try to answer any of these questions, without actually getting to know each one of those persons individually.

I am of course no longer talking about people or concerts, but I find the analogy quite useful in describing the goal of my three years work, summarized in this thesis : To individually in situ address small objects reactivity. Instead of looking at the response of chemical entities through a highly convoluted ensemble signal, strategies are developed to give voice to every one of the single particles. This is really what my thesis is all about: describing chemical reactions at the scales of the individual entities involved. Over these pages, I want to tell chemical stories through the lips of the individual actors participating in it. And the actors we chose to focus on are nanoparticles.

But, again, just like people, the behavior of individual particles is hard to grasp through a single point of view. To meet someone only at work or only in leisure time gives us an incomplete understanding of that person's behavior. Likewise, by scaling down chemical reactions, we need to look at a phenomenon from more than one angle.

This can be quite a challenge since in the realms of the very small to simply see, hear or generally detect the consequences of individual particles behavior is difficult. It takes a great deal of sensitivity to listen to a single particle. For these reasons we looked up tools from the cutting edge fields of Plasmonics and Nanoscale Electrochemistry to help us. These two fast developing fields have been recently shown to be able to precisely address nano entities in situ. Moreover, they are remarkably complementary to each other, a point this thesis seeks to further reinforce. Just as plasmonics studies the interaction of small entities with photons in the visible range, nanoelectrochemistry tries to understand what happens when electrons are injected or withdrawn.

The text starts with a brief state-of-the-art review, on which the most relevant examples of interplay between Electrochemistry and Optics are summarized, and the latest efforts towards nanoscale characterizations of individual entities are described.

Chapter 2 starts by concept proving the complementarity of electrochemical and optical methods by studying a model system: silver nanoparticles oxidation. It is somehow iconic that the model system chosen was actually one of the first systems to be studied for its photochemistry, as silver photo-(electro)chemistry played a gigantic role on the development of photography [1]. In spite of a century-long research history, reaction details on the nanoscale are still unresolved. That is where top notch optical techniques come to aid. Super-localization holography and single particle visible spectrometry are used to reveal nanoparticle reactivity dynamics, or what happens when the particle is in the close vicinity of the electrode (a few nanometers apart).

However, as very well argued in the (now classical) P. W. Anderson's 1972 Science article *"More is Different"* [2], knowledge of a system's fundamental laws does not necessarily imply the ability to predict the way a system will behave at higher scale. Collective behavior is sometimes entirely unpredictable and the description of a system needs to be addressed with generalizations and laws proper to a given scale. This is the object of Chapter 3. Still using holography, together with analytical and numerical methods, we study aggregation, growth and transport properties of nanoparticles, putting forth phoretic phenomena such as diffusio- and thermophoresis.

Finally, Chapter 4 introduces a new strategy to study particles individually, using nanoelectrodes to (electro)synthesize them in situ. By attaching the particle to the electrode it becomes much easier to analyze situations where the particle grows, shrinks, or transforms. Moreover, a still particle can be cycled many times, allowing extensive electrochemical information to be derived. Further interplay between optics and electrochemistry is introduced, as optical monitoring is used not only to detect and size particles during the deposition, but also to deduce useful chemical information unavailable otherwise, in form of optical cyclic voltammograms.

Detailed technical discussion about the setups, calculation methods and fabrication protocols are separated from the main text and form an extra chapter A.

Chapter 1

Introduction: Coupling Electrochemistry and Optical Techniques

Chemistry, often called the central science, is a discipline of multiple scales. From the first chemical courses taught in college, chemistry is presented as a calm ocean seen from a distance. Small waves and fluctuations merge together in patterns impossible to discern, forming an harmonious and smooth pattern. Like tides, reactions happen in a regular, predictable way, perfectly described by well defined rate constants and concentrations. This macroscopic vision - familiar to everyday events and experiments - is in sharp contrast with the microscopic view of chemical systems, where violent collisions deform molecules to the point of ripping pieces apart and fusing others together. Chemical reactions on the microscale are generally the result of imperfect, chance-driven events.

The bridge between these two familiar but contrasted visions is still uncharted territory, little explored. The apparent calmness and regularity of macroscopic systems ensemble views stems from the fact that our observations are actually averages over many simultaneous events (seriously many... keeping in mind that 1 mole $= 10^{23}$). As we reduce the number of simultaneous events, the smooth curves leave place for fluctuations, and chemistry appears less and less tamed behind mean field notions such as rate constants and concentrations.

Over the past few years, advances in analytical techniques allowed a much deeper look into objects in the nano- to meso-scales. As we became able to observe chemical objects on a one-by-one basis, access to a much different world is granted, where events and entities have a much stronger personality. Stochastic effects and fluctuations such as Brownian motion, play an increasingly important role, drawing a world open to imperfection and individuality of behavior.

This chapter describes the different paths into this stormy reality - it briefly reviews the advances made over the past decades, which led towards different ways of achieving

the ultimate detection limit : single entities.

1.1   One vs Many: Individual and Collective Behavior in Nanosystems

The more we look carefully at materials in the nanoscale, the more we realize how profoundly and intrinsically heterogeneous they are at these dimensions. No two particles are alike, nor react in the same way. Moreover, it has been shown that even an individual nanoparticle often displays enormous spatial variability in reactivity [3, 4]. All these observations relate to the fact that in such small particles, surfaces atoms represent a large proportion of the total material. Defects such as grain boundaries, vacancies, surface orientation and roughness are hard to control and seem to have a strong impact on reactivity and catalytic properties [5]. *"God made the bulk, the surface was invented by the devil"*, as very well synthesized by quantum theory pioneer Wolfgang Pauli.

Substantial efforts have therefore been made to clarify the relation between a particle size/shape and activity, but this is a tough quest. Even the most monodisperse synthesis is almost never atomic precise, yielding differences in reactivity from one object to another.

For this reason, since the past few decades many analytical techniques have been developed to achieve ultimate spatial resolution: detection of individual objects, such as nanoparticles, molecules and atoms. This section briefly describes how the way towards individual objects studies was paved, and how different routes provide alternative insights into the objects reactivity. Special attention will be given, of course, to the main topics of this text, nanoscale electrochemistry and optics.

1.1.1   Seeing the very Small : Looking for Resolution

If seeing is believing, the refinement of microscopes over the 16th and 17th century concomitantly with the development of modern Science should be no coincidence. Indeed, the ability to address problems visually was of great importance on the early days of the scientific method[6].

To see very small objects is however a challenging task. Traditional optical microscopy is in general unfit for doing so, since it is fundamentally bound by diffraction, meaning that its resolution is limited by the wavelength of the light (typically 500 nm for visible light). One way around this limitation is to use lower wavelength, more energetic radiation. With this idea came the development of electron microscopy from the 1930's [7], which indeed lowered the resolution down to a few nanometers and eventually to atomic resolution. Until very recently however, the high energies involved, together with the nonexistence of a good method to prevent electron scattering, relegated electron microscopy methods to a exclusively ex-situ characterization technique status [8, 9].

It was however with the invention of the Scanning Tunneling Microscopy (STM) fifty years later that materials imaging achieved the unprecedented resolution of individual atoms [10]. Indeed, STM represents one of the first examples of direct interactions with matter at the nanoscale, and for that reason some consider STM invention as the founding stone of nanoscience [11]. Although initially limited to very restrictive conditions, requiring ultra high vacuum, complicated sample preparation, etc., STM and its many variants (AFM, SNOM, SECM...) quickly evolved and adapted to a wide array of experimental situations. Indeed, today local probe techniques are a standard analytical tool, of daily use for most scientists interested in nanoscale phenomena [11].

Altough impressive, great spatial resolution usually comes at the expense of time resolution (although examples of dynamical local probe studies exist [12, 13, 14]). While able to achieve the ultimate resolution, local probe methods had the inconvenience of being relatively slow, usually unable to properly resolve in time fast events such as chemical reactions. Moreover, the tip is an enormous object (relative to the entities herein studied), therefore it is always possible that it influences the system, changing its properties.

Besides, if a chemical system is to be understood, more chemical-specific information is required. Over the years that followed the invention and popularization of the STM, many other analytical tools were reported to resolve objects individually. To try to extensively describe them all would be a donquichottesque task. Instead we chose to concentrate on the ones more relevant to the subject of this thesis, electrochemistry and optics. Being potentially capable of high temporal resolution, electrochemistry and plasmonics reveal information of chemical nature, thus enabling further insight into a variety of chemical phenomena.

Seeing might be believing, but there is more in a chemical reaction than what meets the eyes.

1.1.2   Electrochemical Detection of Individual Objects

The importance of electrochemical tools for nanoscience is probably related to the relatively mature state of art of electrochemical (EC) instrumentation: to apply potentials accurately (within 2mV), and to measure small currents (down to fA) is nowadays possible with relatively simple equipment. Or perhaps it stems from the common interdisciplinarity of these two fields (EC and nanosciences), together with EC ability to modify surfaces and objects relatively easily. Whatever the reasons may be, it is clear that electrochemistry occupies a central position as a powerful analytical tool for nanoscale systems.

However, even the best available commercial potentiostats are only able to measure currents of a few fA, corresponding to a few ten thousands electrons per second. Some strategies had then to be developed in order to reliably analyze signals originating from single nano-objects and molecules.

Individual Molecules through Electrochemistry

The detection of individual molecules via electrochemical techniques can arise through a number of ways. Although most commonly associated with optical techniques, purely electrochemical techniques also have the potential to detect and analyse single molecules.

An electrochemical scanning probe technique, the scanning electrochemical microscope (SECM), for instance, can be used in individual nanoparticles studies, if nanoelectrodes are used to provide enough spatial resolution [15]. Going even further, the SECM has also been used to achieve electrochemical detection of individual molecules [16]. By bringing a slightly recessed nanoelectrode very close to a conductive surface, one can trap a single molecule in a very small confined space between the two electrodes. If then the substrate and electrode are polarized at opposite potentials with respect to the oxidation potential, the trapped molecule will be repeatedly oxidized and reduced, amplifying the signal and allowing single molecule detection. The concept is sketched in Fig.1.1 A. Although making use of a relatively complicated electrode geometry, this example illustrates well the idea of detection by signal amplification. A similar concept was recently addressed using recessed nanoelectrodes built by electrochemical etching of the tip [17].

The same principle of redox cycling amplification was then recently extended to more flexible geometries, using nanolithography techniques to create nanochannels and nanogaps in micro-to-nanofluidic devices [18, 19, 20], shown in Fig.1.1B. In this configuration, both the upper and lower electrodes are microelectrodes, therefore the current on both sides can be addressed. The symmetrical response observed when both electrodes are poised at potentials opposite with respect to the redox probe E^0 (shown in Fig.1.1C) is then an evidence of the back and forth movement of molecules, and should be proportional to the number of molecules between the electrodes. Discrete changes of the current magnitude are then a direct measure of the number of molecules inside the device.
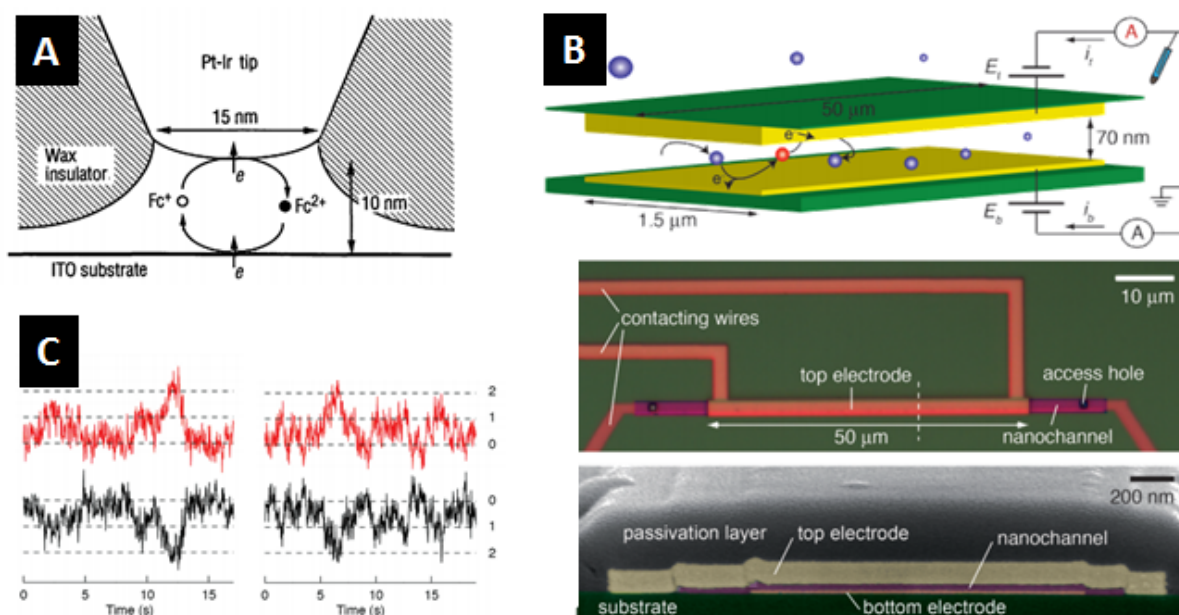
Figure 1.1: Concepts for the electrochemical detection of individual molecules. In A, a recessed electrode approaches an ITO electrode trapping a molecule in a volume of ≈ 1500 nm ^{3}. Application of a voltage between the electrodes makes the molecule repeatedly oxidize and reduce, generating a detectable current. [16] In (B), a recent revision of the concept, where nanolithography is used to create a nanochannel of width of a few μm and nanometric height, where the top and bottom walls are conductive surfaces. When the electrodes are poised appropriately, a molecule inside the channel repeatedly oxidizes and reduces, generating symmetric currents on the working and counter electrodes, as respectively shown in red and black (C)[18].

Individual nanoparticles using Electrochemistry

Signal amplification can also be achieved through catalysis, making creative use of the fact that one catalyst molecule generates many analytes, exchanging many electrons. This concept can be used to study nanoparticles individually. Suppose a certain redox reaction, say $O + e \rightarrow R$, that for a given potential will take place on a catalytic nanoparticle but not on the electrode. When the NP collides with the inactive electrode, it is polarized at the same potential as the electrode. The catalytic reaction will take place, but it will be limited to the NP surface, as the electrode is inactive. For all practical purposes, the NP will act as a nanoelectrode, with respect to this reaction. Since the reaction is catalytic, the current will be controlled by the reactant transport, rather than by the amount of catalytic material (See Fig.1.2 left). Ultimately the reactant on the particle surface will be completely consumed, and the current will be limited by diffusional transport of the analyte to the NP surface. In this ideal case, a current of magnitude $i_{ss} = 4\pi(ln2)n_0FDCr_0$ is to be expected [21], where F is the Faraday constant, D the diffusion coefficient, r_0 the NP radius and C the bulk reactant concentration. The success of the strategy depends on having a clean background current, i.e., an inactive electrode [22]. In order to avoid capacitive current, it is also desirable to shrink the electrode size down to the micro- or

nanometric dimensions.

Many current - time trace curves can then be obtained, depending on what happens to the particle after hitting the surface. For instance, if the particle stays at the surface and keeps its activity, a step-like response is expected. This situation is illustrated in Fig.1.2A, where each step corresponds to the arrival of one PtNP over the Au ultra micro electrode (UME).
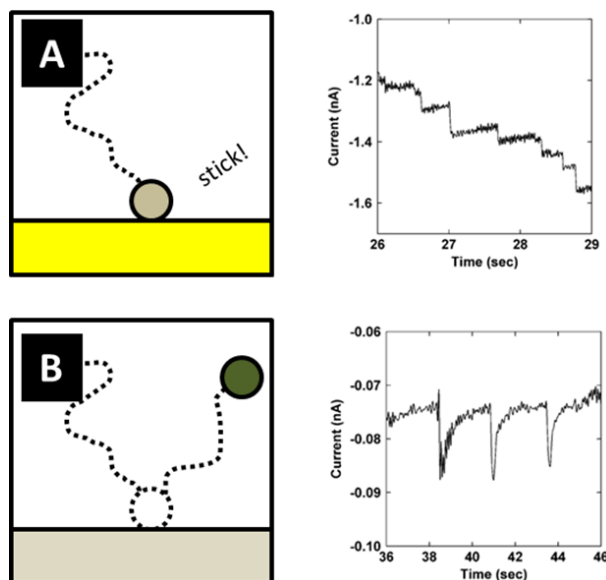
Figure 1.2: Typical expected single nanoparticle electrochemical responses in the case where the particles (A) stick to the electrode and remain active, and (B) eventually deadsorb and lose contact. Current-time traces adapted from [23].

It is also possible for the particle not to stick permanently to the surface, and only weakly adsorb on the electrode surface. In this case a *"blip"* response is expected. This is sketched in Fig.1.2 B, where each blip corresponds to the arrival of one IrOx NP catalyst (for the oxygen evolution reaction) over a Pt UME.

Blip responses are also observed in the case of deactivation upon collision with the electrode. This could happen for a number of reasons. For example, during catalysis, very reactive intermediates can be generated, which poison the particle surface, stopping the reaction. It could also happen as a result of the interaction of the particle with the electrode material. For instance, the latter was explored in the case of Hg UME to improve the reproductivity of the spikes [24, 25]. This is sketched in Fig.1.3.
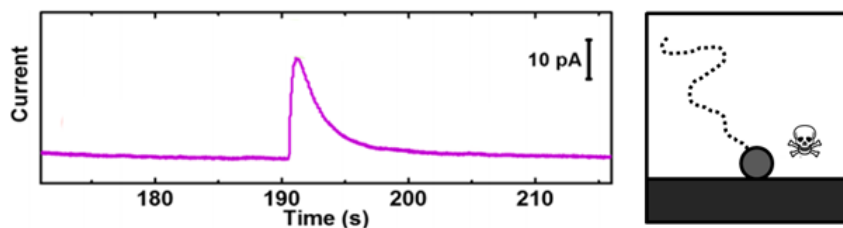
Figure 1.3: Deactivation through poisoning by amalgam formation, adapted from [24]

This strategy has proved itself quite useful to study a number of catalytic systems, including:

- hydrazine oxidation on Pt [26] in a variety of situations, such as aggregation [27, 28], electrode modification [29], poisoning [25], etc.

- proton reduction on Pt [21]

- oxygen evolution, hydrogen evolution and oxygen reduction on metal and metal oxide nanoparticles [30, 31, 32, 33, 34]

In particular, to address particles individually has helped reveal the profound heterogeneity taking place in these catalytic systems at the nanoscale [22].

Destructive Individual NP Impacts

Although catalytic reactions do provide large signal amplifications, enhancing the signal-to-noise ratio, modern instrumentation also allows study of NP direct reactivity, in the so called destructive impacts. The concept is similar to catalytic impacts: an inert electrode is poised at a potential where the particles are not stable. The collision of a NP with the electrode then triggers a redox reaction which transforms the particle and yields a measurable electrochemical peak. Since the particles hit the surface one at a time, this transient current contains individual NP information. Instead of reaction promoters, NPs take up the role of main analytes.

This opens up the way to studies of nanoparticles direct oxidation, reduction, dissolution and phase transformation, leading to an evolution of the way the technique was perceived by the electrochemical community. More than an asset for fundamental studies at individual particles, impact experiments became an useful chemical-selective characterization and diagnosis tool.

Reactivity from peak shape analysis: A lot of information about the particle reactivity can be gathered from impact experiments. Analysis of the peak can reveal much relevant information about the NP stability and reactivity. For example, from the duration of the peak, we can draw kinetic information: how high is the peak? How long does it last? Likewise, the potential at which the experiment is performed gives insight into the thermodynamics of the system : at which potential do we start to see peaks? Does the shape change with potential? [37]

NP intrinsic properties Intrinsic properties can be derived from a destructive electrochemical impact. For instance, if the particle reaction is total, its volume V can be obtained from the application of Faraday's law to the integration of the peak (exchanged charge, Q), using the particle density ρ and molar mass M (F is the Faraday constant and z is the number of exchanged electrons per reacted molecule):
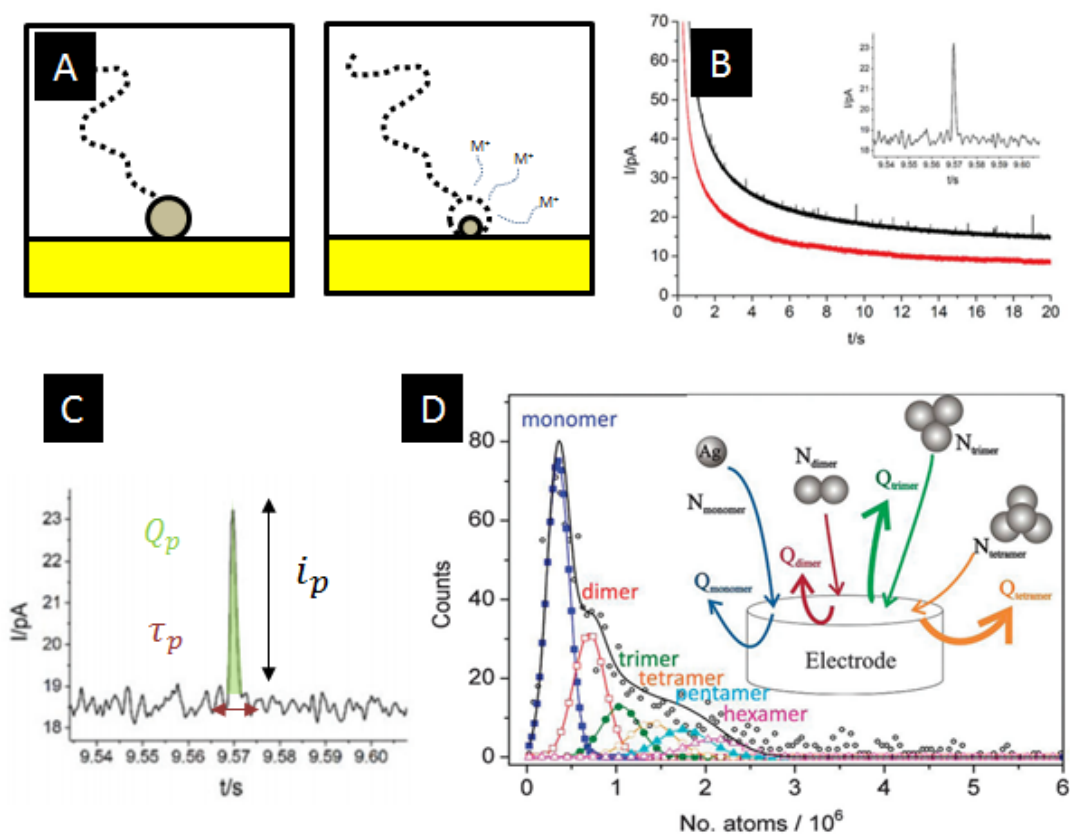
Figure 1.4: (A) Sketch of the Destructive Individual NP impacts detection strategy, where the particle is oxidized upon contact with the polarized electrode. (B) and (C) : The current time trace reveals oxidative spikes whose current magnitude, duration and overall charge help unveil mechanistic information about the nanoparticle reaction. In particular, the charges can be used to deduce the particle size, and therefore the agglomeration state of the NP solution can be addressed, shown in (D). Adapted from [35, 36]

$$V = \frac{QM}{zF\rho}$$

Using this idea, the particles size distribution can be obtained, and thus be used to address the aggregation state of a NP colloidal solution [38]. More than simply addressing the size distribution, core-shell geometries can be characterized [39, 40] by setting the potential to first react only the shell material, and later the rest of the particle.

The surface of the particles can also be quantified based on a similar strategy, by tagging the NP with a monolayer of redox reactive compounds, which will react exchanging electrons and leading to spikes whose charge is proportional to the particle surface[41, 42], accordingly to:

$$A = \frac{A_T N_A Q}{zF}$$

Where A_T is the area occupied by one redox active molecule, and N_A Avogadro's number. Based on that, more complete experiments can be designed, allowing determination of complex geometries, such as gold nanorods aspect ratios [42].

Concentration from Impact Frequency: By analyzing the frequency of impacts, it is possible to infer the NP concentration. If diffusion transport towards a disk UME of radius a is assumed, the frequency, f, relates to the NP concentration $[NP]$ and diffusion coefficient D_{NP} by [21, 43, 44] :

$$f = 4D_{NP}[NP]a$$

This expression was validated not only in lab conditions, but in a variety of media, such as seawater [45] and human sweat [46], highlighting the potential utility of the strategy for real field situations.

As far as stochastic impacts are concerned, nanoparticles are perfect prototypes to understand the role of stochasticity in nanosystems. This look at nanoparticles as *super molecules*, is a recent trend in chemistry and has more or less independently emerged in different fields of nanoscience [22]. This analogy is taken one step forward when plasmon resonances energies are considered, which is the theme of the next section (Sec.1.1.3).

Surface Changing Impacts

For completeness, it should be mentioned that individual nanoparticle impact detection can also be achieved by altering the area of the electrode. For example, the arrival of insulating polystyrene beads over an UME can be detected by reduction of the steady state current. The reaction of a redox mediator is kept in the diffusion limited regime, such that the current is proportional to the electrode area available for the reaction. Arrival
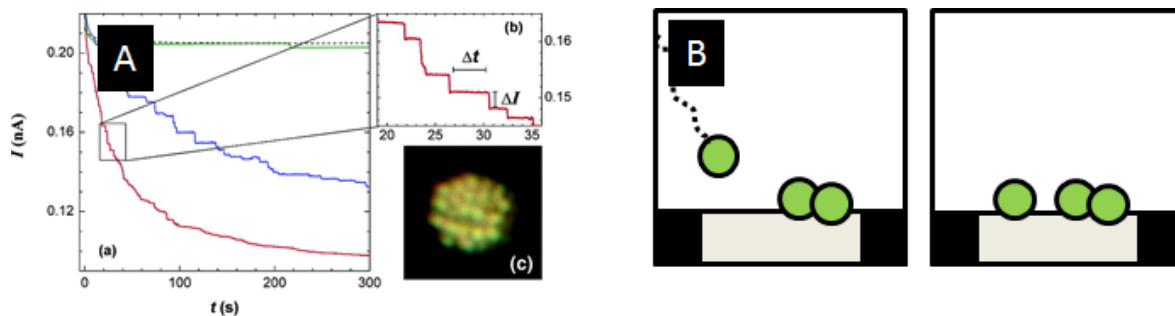
Figure 1.5: Arrival of insulating polystyrene beads blocks the electrode, leading to detectable stepwise current decrease (A) An ex-situ optical image taken after the end of the experiment is provided in the inset, showing the electrode covered by beads (Adapted from [48]). The situation is sketched in (B).

of entities that block the electrode therefore lead to a step-wise reduction of the current, the situation is sketched in Fig.1.5 [47]. These results were later confirmed by optical tracking of fluorescence tagged beads [48].

A similiar concept was recently employed for evaluation of the resistance of single carbon nanotubes (CNT). A potential difference is applied between two interdigitated comb-like microband electrodes. Since no redox reaction takes place, no meaningful current is recorded. The arrival of conducting nanowires however can short-circuit the electrodes, leading to a discrete enhancement of the current, corresponding to the conductance of one nanowire [49]. From the current/applied voltage relationship, the resistance of single NW can be evaluated.

Other Electrochemical ways of addressing individual entities

As a remainder, it should finally be added that other electrochemical strategies for studying single nanoparticles exist, which are not fully described here due to lack of space.

For example, White's group recently introduced a Coulter counter setup, allowing not only sizing and counting but also manipulating of individual nanoparticles [50, 51]. Nanoparticles can also be immobilized on nanoelectrodes, either by electrodeposition [52, 14], underpotential deposition [53], or by spearing them [54]. These *particle-on-a-stick* methods present the advantage of allowing prolonged electrochemical studies, but the data throughput is usually quite low, as only one particle is analyzed per experiment.

Scanning Electrochemical Microscope (SECM) probing can also be used to interrogate nanoobjects individually, either by positioning a nanoelectrode over the object surface and analyzing the reaction products[15], or by analyzing the change in the feedback response [55]. This approach can be taken even further if coupled to other techniques. For instance AFM-SECM force measurements can also be used to probe individual polymer molecules and protein immobilized on the electrode surface [56, 57].

Other forms of electrochemical microscopy, such as the scanning cell electrochemical microscopy (SECCM), can also be used to interrogate very small objects individually.
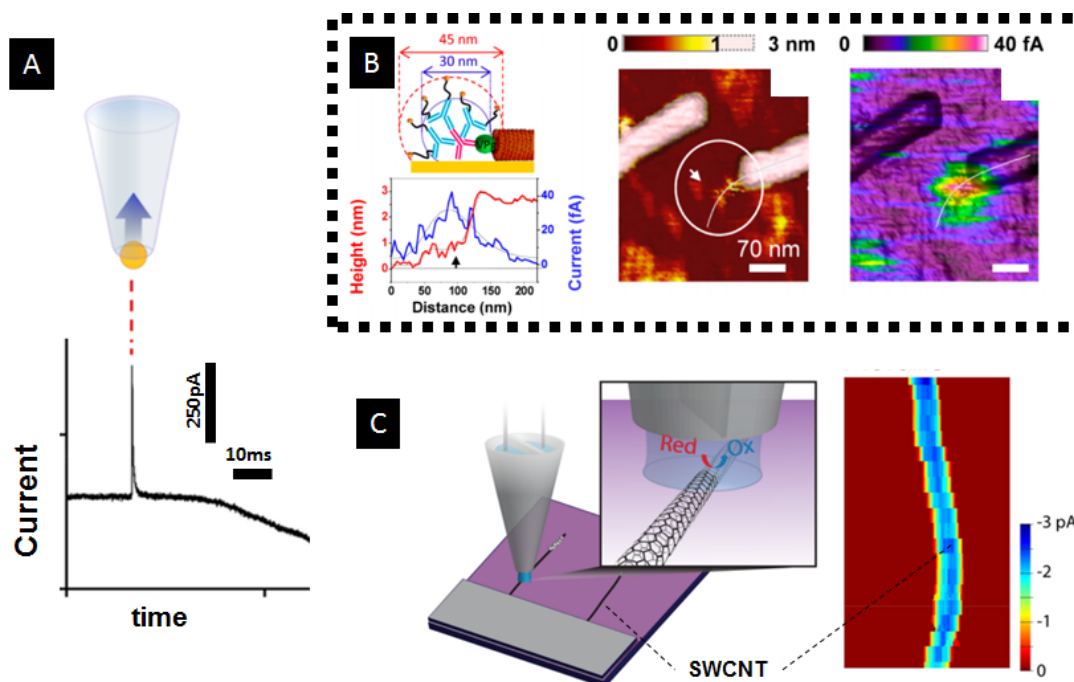
Figure 1.6: Electrochemical methods for studying individual objects (A) Nanopipettes as Coulter Counter: the passage of one particle modifies the conductivity of a nanopore leading to a peak, which can be used to size the nanoparticle (Adapted from [50]). (B) AFM-SECM coupled approach for studying the distribution of redox active groups over a single virus (Adapted from [56] (C) SECCM image of the reactivity of a Single Walled carbon nano wire (Adapted from [62]).

Through the use of nanopipettes, the reaction area is reduced to a few hundred squared nanometers, substantially lowering the background current and thus allowing detection of small signals. This setup was used to perform very precise impact experiments [58, 59, 60], as well as to image the reactivity of nanostructures such as carbon nanotubes [61, 62]. Some of these approaches are illustrated in Fig.1.6.

1.1.3 Nano-Optics and Plasmonics

The interaction of small structures with light, and its unusual properties have been empirically explored since ancient times. Iconic examples include the Lycurgus cup and churches stained-glass windows, both glasses containing nanoparticles, which make them have different colors according to the illumination incidence. More conscient uses of nanoparticles to change optical properties date back to Michael Faraday's pioneering experiments with Au colloidal solutions [63]. Rigorous explanations for the phenomena only begun to take form at the dawn of the 19th century, with seminal works by Gustav Mie [64], Wood [65], Rayleigh [66] and others.

Under certain conditions, the oscillation of the electromagnetic field on specific frequencies may trigger oscillations of free or weakly bound electrons (typically those of the conductive band on solids). In a surface, this may activate collective oscillations resonance, generating a propagating interfacial wave known as Surface Plasmon Polariton Resonance (SPPR). If the conductive surface is small compared to the resonance wavelength - which is the case for nano-sized structures illuminated with visible light, for example - localized surface plasmon resonance (LSPR) modes may be activated. Localized plasmons are highly dependent on the local dielectric environment of the particle, as well as on the size and shape of the nanostructure of interest. This allows fine modulation of the plasmon band energy, shape and intensity, which makes them specially fit for ultra-sensitive sensors design [67].

Although research on plasmonics was undertaken over the whole 20th century, recent years have witnessed an exponential increase of interest for the field [68], owing to a much more profound understanding of how LSPR modes can be tailored and how LSPR modes of different structures interact with each other.

In great measure, this knowledge was only possible from the development of optical techniques capable of studying nanostructures individually. Precise observation of LSPR shifts and interactions is rarely possible when analyzing NPs ensembles, due to severe broadening of the peaks, blurring the interesting phenomena. Experimental proof of these was only made possible by establishing a structure-LSPR relationship on a particle-by-particle basis.

Other factors crucial for the emergence of the field were : the increase of computational power, in order to perform meaningful simulations; abundant availability of numerical methods (since plasmonics can be well described from Maxwell equations); and the development of lithographic techniques and chemical strategies to synthesize nanoparticles of varied shapes [69]. Besides, the discovery of powerful surface enhanced spectroscopic methods, fully based on plasmonic effects, was key to motivate an increase of research in the field [70].

Plasmonic nanostructures have a natural ability to act as nano antennas. In doing so they create hotspots that can be used to increase the local intensity of the electromagnetic

field, enhancing spectroscopic signals by orders of magnitude, to the point of allowing single molecules detection [71, 72, 73].

The idea of considering nanoparticles as plasmonic atoms mentioned in Sec.1.1.2 is again found among the plasmonics community, as many analogies exist between atoms and nanoparticles. For instance, the electronic wavefunction of an electron and the electric potential around a metallic nanoparticle vary under similar scaling laws [68]. Moreover, the LSPR energies hybridize in a way analogous to molecular orbitals, allowing analytical prediction of the LSPR energies of complex structures from decomposition in simpler substructures and symmetry considerations [74, 75].

Hotspots can also be used as local sources of heat, and therefore as a tool to finely control temperature at the nanoscale [76]. Modulation of the photo induced thermal response allows design of sensing techniques descending down to the limits of very small single nanoparticles ($r \approx 1nm$) and single molecules [77, 78].

Moreover, the signal enhancement around plasmonic structures can also be coupled to scanning probe techniques to assess nano- to molecular scale information about chemical systems. This is the principle, for example, of Tip Enhanced Raman Spectroscopy (TERS), which exploit the plasmonic enhancement around an STM/AFM tip and the chemistry specificity of Raman signal to study (electro)chemical systems with molecular resolution [79, 80, 81].

Hot electrons emerging from LSPR are also potentially useful for chemistry, as they are capable of triggering chemical reactions, either by photochemical effects, direct reduction [82, 83], or by local temperature enhancement [84].

1.1.4 Fluorescence

Finally no overview of optical single entity detection methods would be complete without mentioning fluorescence. Fluorescence of single molecules, and specially on cryogenic conditions were among the first single molecules experiments ever performed [85, 86, 87].

I'll be brief, as the literature on fluorescence methods is too vast to be completely covered here, spanning over many fields such as biophysics studies of diffusion processes, fundamental physics, biochemistry, etc.

Fluorophores allowed the visualization of a myriad of chemical physical processes, especially in biological contexts. Starting from early fluoroscent molecules experiments in cold conditions [85], and particularly intensified since the discovery of green fluorescence protein (GFP), to use individual entities with fluorescent tags is today a common practice in biochemistry and biophysics [88]. With relatively little equipment involved, fluorescence techniques allowed qualitative imaging of intracellular processes, as well as extraction of quantitative data from the tags movement.

Fluorescence was also at the heart of the development of super-localization and super-resolution techniques, which will be the theme in the next section.
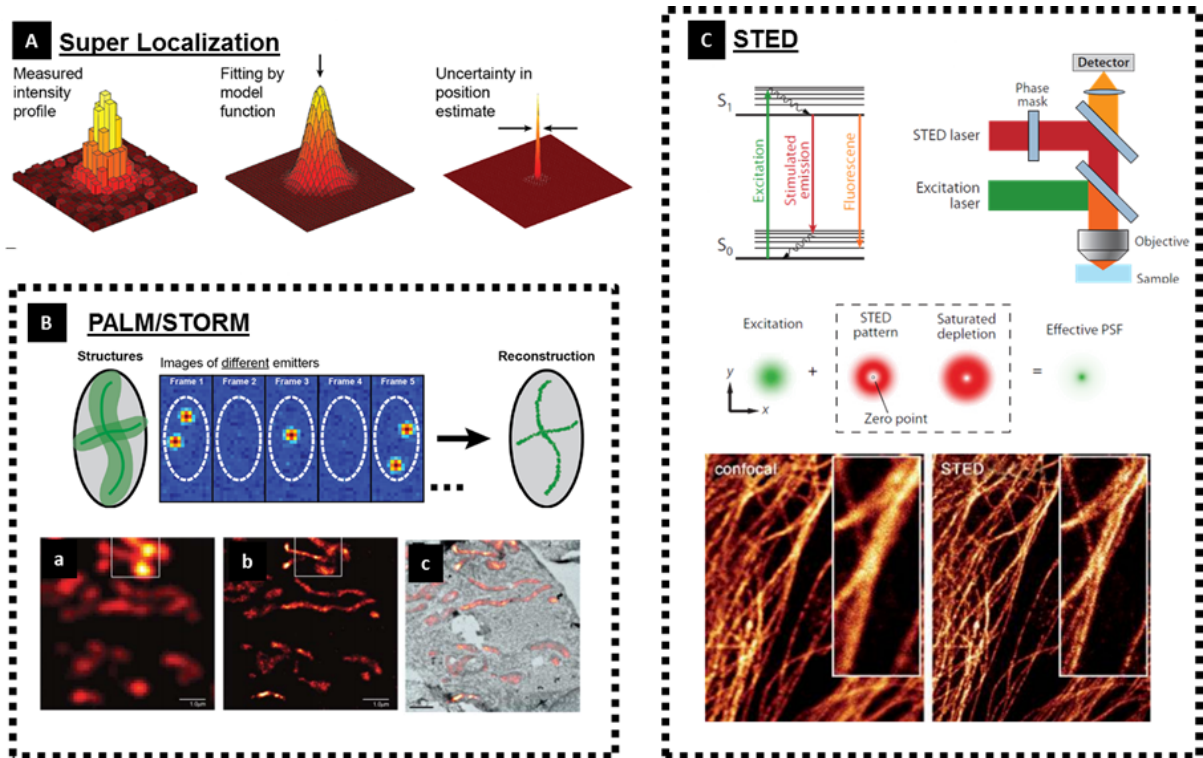
Figure 1.7: Super resolution Principles. (A) Superlocalization Concept, a common step for most superresolution techniques, the PSF is fit by a model function, enhancing the precision on the position estimate. (B) Palm/STORM principles; Stochastic activation of separated emitters that are superlocalized and put together, forming a superresolved image. The inset compares a regular image (a), a PALM image (b) and TEM image of the same structure, superimposed over the PALM image. (C) Principles of STED microscopy, an excitation beam is superimposed to a donut shaped beam that stimulates emission. Only the molecules on the center of the donut emit light by fluorescence. The inset compares the resolution of STED and confocal microscopy. Adapted from [90, 91, 92]

1.1.5   Return to Microscopy : Super-localization and Super-resolution

The ability to individually address single entities was also a key ingredient in pushing the limits of optical imaging further. As in all far-field optical methods, resolution limitations are imposed by diffraction of light. Diffraction and propagation act as a low-pass filter, limiting the resolution to a fraction of the wavelength - typically $0.6\lambda/NA$ (NA is the numeric aperture) for incoherent light or twice as much for coherent.

Superresolution microscopy techniques however have recently extended the applicability of optical techniques down to the nanoscale. Their importance was recognized with the award of the 2014 Chemistry Nobel Prize to super resolution techniques pioneers, Stephan Hell, Eric Betzig and William E. Moerner [89]. Building on these initial seminal works, techniques for stretching visible wavelength optics have been extended and multiplied.

A common ingredient to most superresolution schemes is to identify and localize individual light sources (emitters or scatterers) with great precision. This is done by fitting the point spread function (PSF) by analytical functions, typically Gaussian or Airy func-

tion profiles and later by using the characteristics of these functions (the Gaussian mean, for example) to evaluate the PSF center, which is a very good estimator of the emitter's position [89, 91, 93, 94]. The details then differ from technique to technique, a few examples are shown in Fig.1.7.

For example, Photo-activated localization (PALM) and Stochastic Optical Reconstruction (STORM) microscopies, consist in using fluorescent activation of emitters with low intensity excitation beams and/or particular fluorophore interactions to only activate a few molecules at a time, superlocalize them and by accumulating all the superlocalization events paint a pointillist super-resolved image [95, 94].

In another strategy, Stimulated Emission Depletion (STED) microscopy, one takes advantage of the ability to activate and deactivate the excited state of a molecule with photons of different frequencies. Structured light beams are then used to excite molecules on a diffraction-limited spot, and deactivate the excited state around it, using a donut shaped beam. If the relative intensity of both beams is regulated, it is possible to reduce the actual excitation spot to the size of one molecule. The pattern is then scanned throughout the image and superlocalization of individual emitters yields a superresolved image. [96, 93]

Not only for Biological Samples Superresolution techniques have found many of their most exciting applications in biological systems, but these systems and methodologies can just as likely be used for studying surface reactions, for example [98]. Strategies using superresolution principles have been developed for intraparticle identification of catalytic reactive sites for reactions involving fluorophores [98]. A few more examples of superlocalization using coherent light to study nanoparticles chemistry will be shown throughout this thesis.

Going Beyond Fluorescence While developed for (and making extensive use of) fluorescence, superresolution principles can just as likely be used with non-fluorescent probes. In this thesis, for instance, we make extensive use of the light scattered by nanoparticles to superlocalize them. Besides imaging, the coherent light scattered by metallic nanoparticles can be used to image optical fields with resolution as good as a few nanometers [99]. This is shown in Fig.1.8 where detection events based on AuNP scattering were used to image evanescent and propagating EM fields.

Mapping Chemical Reactivity in nano Catalysts Superlocalization methods were recently used to map the active sites of many catalysts. If the catalyzed reaction produces fluorescent products, the reaction of one molecule can be detected and superlocalized. The accumulation of many catalysis events leads to the mapping of the active sites on the catalyst surface. This method was used to map intraparticle distribution of catalytic activty
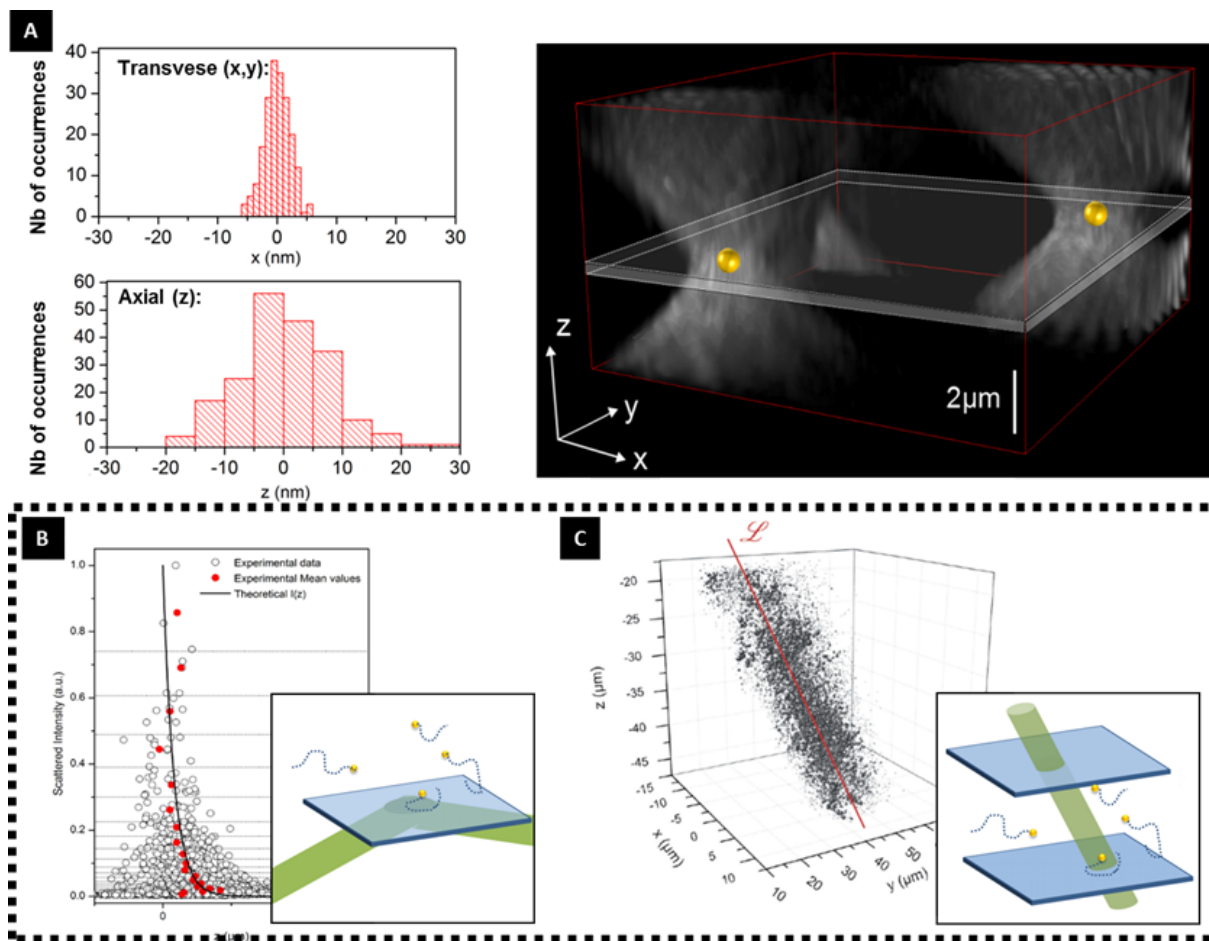
Figure 1.8: Superlocalization procedure applied to AuNP of 30 nm, imaged using an holographic setup. (A) A lower limit for the precision of the localization is determined by evaluating the position of two immobile AuNP. A precision of $3 \times 3 \times 10$ nm^3 is achieved. Some Examples of applications of nanoparticles superlocalization are shown. The concept is used to image the evanescent EM field resultant of total reflection of the laser at the air-glass surface(B) and a propagative EM wave (laser) (C). Adapted From [99].

on many nanostructures, such as PtNP [100, 101], Au nanoplates[102] and Nanorods [103], etc.

Superlocalization and superresolution methods are therefore an extremely useful tool to analyze nanoscale phenomena optically, and their usefulness also spans over many different fields.

1.2   Electrochemical Imaging and optical (electro)chemistry

Before proceeding to show how these single entity techniques overlap and can be relevant to the context of exploring electrochemical systems, it is worth mentioning already existing bridges between electrochemistry and optics. An exhaustive description of all efforts to couple electrochemistry with optical methods would be just as unbearable as it would be impossible to make. Indeed, most bulk and surface chemistry spectroscopical methods

make use of the interaction of molecules with light. Therefore, any experiment where Raman, IR, XPS, etc. were used to characterize a surface modified by electrochemistry constitute, in a way, an example of opto-electrochemical method. Even more explicitly coupled experiments and setups appear at a pace impossible to keep up [104].

Moreover *electrochemical modification - optical diagnosis* is not a one way street, as light can also be used to modify surface chemistry, and EC can just as likely be used as an analytical technique to detect these modifications. Lithography, silver-based photography, and surface modification by polymers or surface photochemical reactions are a few examples [105, 106].

Electrochemistry can just as likely be used to make reactivity-specific images, using a small electrode positioned close to a surface. This is the principle behind the scanning electrochemical microscope(SECM), mentioned in Sec.1.1.2. The SECM can also be used to locally modify surfaces [107], and to generate objects with special optical properties[108].

Likewise, spectroelectrochemistry has been extensively used to yield catalytic information about catalyst, and macro methods remain very relevant to this date [109].

All these methods, however rich in information, probe ensembles of objects. In the wake of single entity methods, and as stressed in the previous sections, there is a richness in responses that can only be appreciated when individual objects are probed one by one. The next section deals with the new step on optical-electrochemical methods development: the efforts to take these coupled strategies to their analytical limits, applying optical and electrochemical coupled methods to study single objects.

1.3 Taking Opto-Electrochemical Methods one Step Further: Individual Objects

As seen over Sec.1.1.1, single entity nanoscale studies are intrinsically stochastic and therefore permeated with noise, which generates modest signal to noise ratios. Taken together, these two characteristics make single entity studies prone to artifacts, which calls for coupled alternative characterization methods. Given the concomitant emergence from single entity studies from both plasmonics and single entity electrochemistry, it was more or less natural to try to couple these two fields. Efforts in this direction soon followed, with the appearance of quite a few studies in the recent literature. This section revises the most relevant ones. For a matter of organization, and to emphasize the synergy between electrochemistry and optics, I shall organize them in three subgroups, (i) studies where optical measurements are used to replace electrochemical measurements (ii) studies where electrochemistry is a key ingredient to generate the effects necessary to study individual objects and (iii) study of fields so intrinsically multidisciplinary that both measurements are equally important.

1.3.1   Using optics to replace electrochemical detection

Prolonged studies of individual nanoparticles are often rendered difficult by the problem of detecting tiny single NP electrochemistry signals. Moreover, individual *particle-on-a-stick* and near field studies suffer from low data throughput. This is a serious problem, given the intrinsic stochastic and noisy nature of single particle-molecule studies, often requiring lots of data to derive properties distributions.

In this context, far-field optical methods emerged as a viable alternative for simultaneously acquiring data over hundreds of nanoparticles, providing statistically sound data ensembles.

Spectral Monitoring of (Electro)Chemical Reactions   The position and intensity of the LSPR band are extremely sensitive to a particle's surface chemistry and electron density [110, 111]. This makes the LSPR a potentially great measure of these properties, allowing in situ fast tracking of chemical reactions.

In an example from Mulvaney's group, AuNPs were used to catalyze and monitor ascorbic acid oxidation. As the reaction proceeds, the AuNP acts as an electron buffer, receiving the electrons resulting from the redox reaction. This leads to an increase of electron density, which generates a measurable shift on the LSPR band position. Monitoring of the particles spectra thus allows to measure electron injection rates as low as 4600 electrons per second, corresponding to a current of $\approx 0.5 fA$ [112]. This sensitivity is competitive vis-a-vis the best commercially available EC potentiostats.

Long's group also used changes of plasmonic nanoparticles to monitor electrochemical reactions. For example, they showed that the scattering spectrum of copper nanoparticles can be used to follow surface chemistry and size variations. The electrodeposition and oxidation of plasmonic copper nanoparticles were monitored in this way[113, 114]. These are shown in Fig.1.9.

Exploring Plasmonic properties to design detectors   The LSPR spectral shift is not the only way to derive chemical information out of optical data. Plasmonic structures can be designed, for example, to detect a few absorbing molecules adsorbed on their surface based on quenching of the plasmonic band. The idea is to use NPs whose resonance overlaps with the analyte's absorption spectra, therefore the plasmonic resonance energy transfer (PRET) will quench the plasmonic scattering spectrum [115, 116]. This leads to a decrease of the NP scattered spectrum intensity. On the limit of low concentration with narrow absorption spectra, absorption peaks superposed to the spectrum can be seen, potentially decreasing the detection limit down to single molecule limit [115].

The sensitivity of propagating plasmons to near-field perturbations has also been successfully used to design detectors with great sensitivity - sometimes called SPP-sensing strategy. This concept was pioneered by Tao's group to build sensors capable of sizing
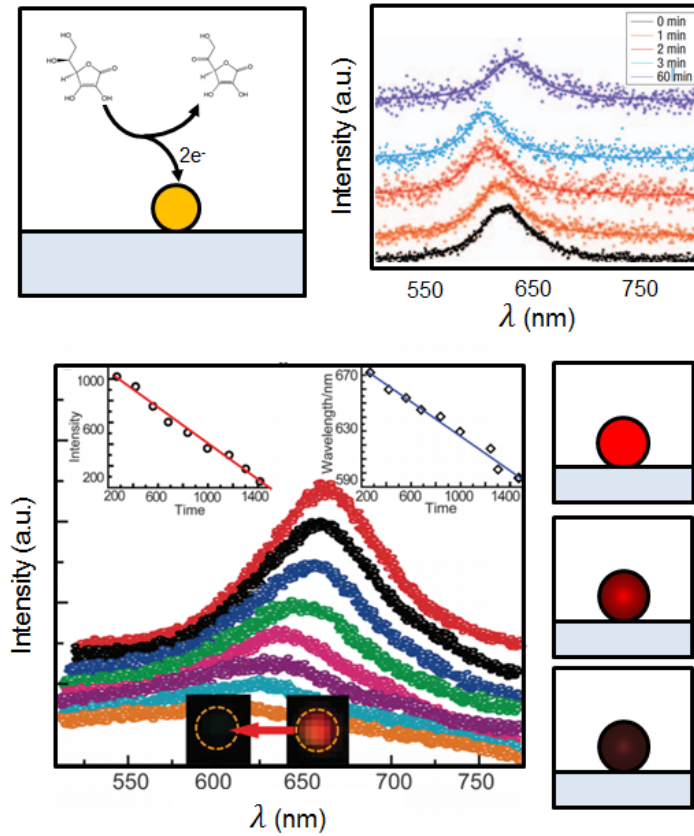
Figure 1.9: Monitoring chemical reactions through the spectra of nanoparticles. (up) Mulvaney's experiments, where the oxidation of ascorbic acid, catalyzed by the AuNP alters the electronic density of the particles, leading to a blue shift. After longtime ($\approx$ 60 min) relaxation processes bring the electronic density back to its equilibrium value (Adapted from [112]). (down) monitoring of CuNP oxidation through the spectral intensity and maximum wavelength (Adapted from [113]).
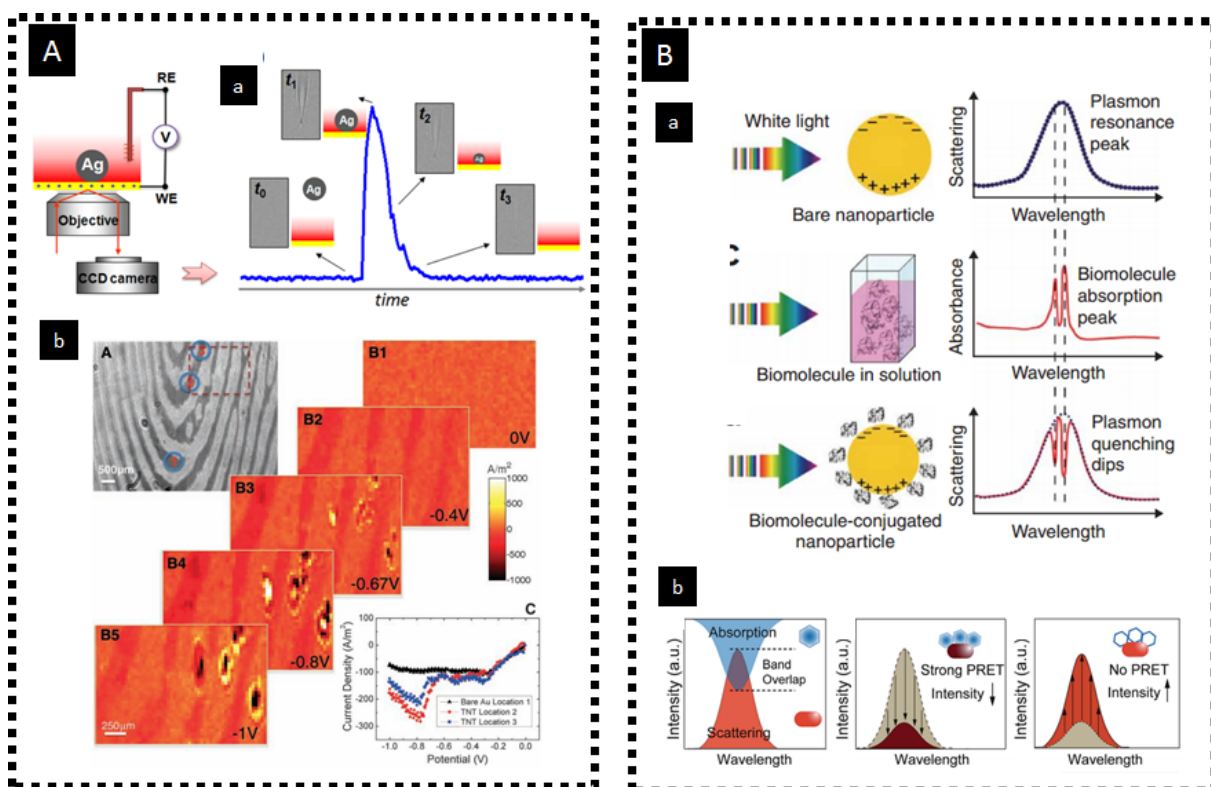
Figure 1.10: Examples of utilisation of plasmonic properties to image electrochemical processes. In (A) the scattering of surface plasmons imaging is used to detect (a) the arrival and electrooxidation of silver nanoparticles on an electrode surface [117] and (b) reduction of TNT particulates near a fingerprint [118] . (B) Plamonic resonance energy transfer used for detection of individual nanoparticles (in some cases single molecules), either through localized quenching of LSPR by molecules with (a) narrow absorption spectrum[115] or (b) large absorption bands [116], leading to localized quenched LSPR spectrum or to a decrease of the overall intensity.

and imaging single nanoparticles one by one[117, 118, 119].

In these experiments, a thin gold film is used both as electrode material and as a plasmonic substrate to support plasmon-polariton propagation. SPPR is very sensitive to its local dielectric environment, such as inhomogeneities in the optical index, either caused by the presence of small entities in the vicinity of the film or by concentration gradients in the near field (due to a chemical reaction, for example). These heterogeneities are enough to scatter the propagating plasmon, generating propagating electro-magnetic (EM) waves detectable in the far-field.

Besides individual nanoparticles of size down to 35 nm, the method is sensitive enough to allow detection of very small particulates (in the $\approx f$g range) of molecules, such as tri-nitro-toluene (TNT) [118]. A similar (but simpler) version of the method later came with the works of Pan and Hill, who used dark field optical detection to correlate particle size to intensity, thus being able to size the deposition of hundreds of AgNPs onto an electrode, as well as their dissolution. The detection limits of their setup was limited to particles of 46 nm diameter [120, 121].

Optical CVs Optically derived EC information can be made quite quantitative. For example, if the optical changes are reported against the potential, optical cyclic voltamograms (opCVs) can be recorded. Besides the aforementioned advantages of high throughput and sensitivity, these opCVs have the advantage of providing information *specific* to the reaction responsible for optical properties changes. All other EC parallel phenomena, such as double layer charging, parasitic reactions, catalysis get filtered out.

The charging and surface reactivity of gold nanoparticles and nanorods were addressed in this way recently. Changes in the spectrum maximum and overall scattered intensity revealed electroadsorption of different anions over the gold surface [122, 123], as well as oxidation reactions [124, 125].

Since the intensity change is proportional to a charging phenomena, its derivative can be assigned to a current. When plotted against the potential, one is able to derive opCV, corresponding specifically to the phenomena changing the optical properties. Besides gold, this strategy was also recently used to investigate lithium ions intercalation on cobalt-based $LiCoO_2$ nanoparticles[126]. These are illustrated in Fig.1.11. Finally, it is also worth mentioning that any optical property can be appropriated to build opCVs using this methodology. For example, a similar strategy was reported using fluorescence emission intensity [127].

At molecular scale, STM and AFM probes can be used to enhance the Raman scattering of molecules next to a surface to the point of single molecule detection. Tip enhanced Raman spectroscopy (TERS) setups can then be used to measure electrochemical reactions on a single molecule basis, and to build voltammograms from the accumulation of individual redox events [81].

In this section, many examples were shown on how single particle optical signal can be used as channel for chemical information. It was shown that in a few cases, single objects optical measurements can even replace electrochemical detection, allowing high throughput very sensitive monitoring of chemical processes.

By stopping in this section, one might have the impression that optical measurements are superior to electrochemical ones. This is an equivocated point-of-view that we shall try to dissuade in the next sections by showing that a real synergy exists between these two very different ways of observing objects at the nanoscale.

1.3.2 Electrochemically assisted optics

So far it has been shown how optics can be used as an analytical alternative to electronics in monitoring electrochemical measurements. However, this is not a one-way path: Electrochemistry can also be an asset in assisting optical studies. Indeed, electrochemical techniques can be extremely handy in creating objects for optical-oriented studies on plasmonics.

The most important example of this is perhaps the central role played by electrochem-
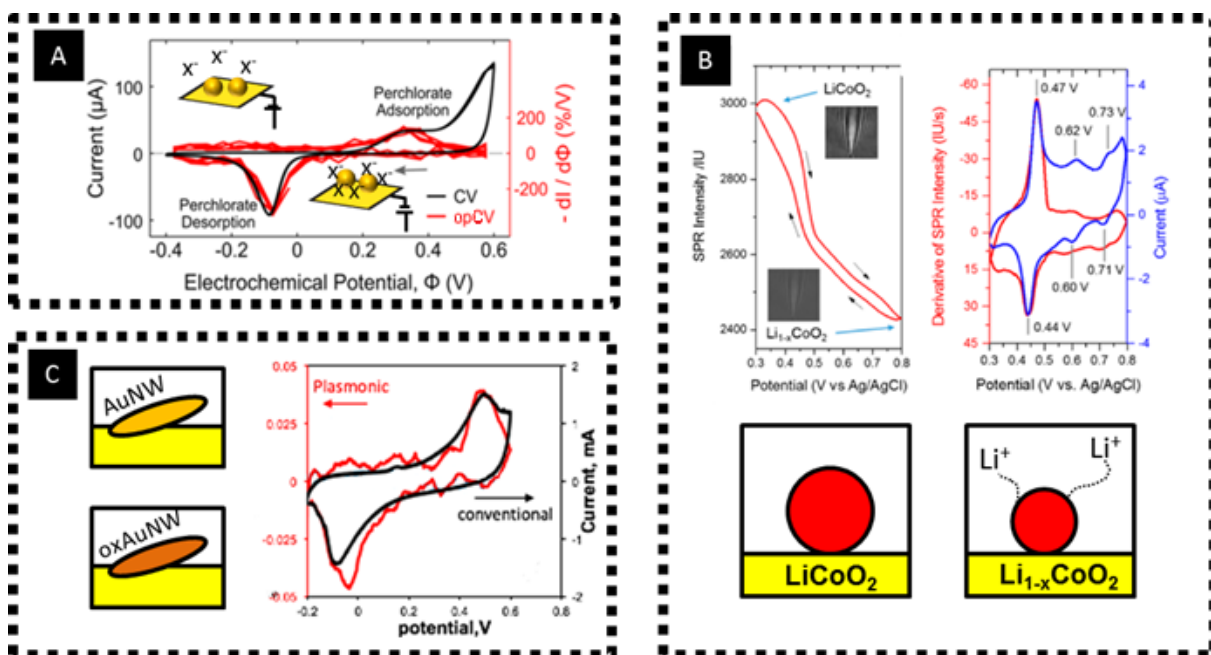
Figure 1.11: CV obtention through processing of optical scattered light. (A) Electroadsorption of anions onto AuNP surface, comparison of the single particle opCV and ensemble electrochemical trace (Adapted from [123]) (B) Lithium desintecalation and reintercalation reactions on $LiCoO_2$ particles (Adapted from [126])(C) Single Au Nanowires oxidation reaction (Adapted from [124])

istry in the discovery of surface-enhanced Raman effect (SERS). SERS was first observed and explained having pyridine on a silver electrode as a model system. In these pioneering experiments, it was the anodization of the electrode that triggered etching of the silver surface generating plasmonic structures responsible for the signal enhancement [128, 129]. Soon after, SERS studies enabled single molecules studies [130, 131], which attracted lots of attention to surface enhanced techniques[72], ultimately fostering the whole field and shaping plasmonics as we know it today. Taking into account the fast development that followed, one could say that in a way the whole success of the field of plasmonics actually owns a good deal of its hype to electrochemical experiments. Roughening of materials through electrochemistry is still today sometimes used to produce SERS active substrates[132]. Interestingly, with further developments in SERS materials and concepts, surface enhanced tools became quite an asset to study interfacial phenomena. Closing the positive feedback loop, SERS became an extremely useful concept to understand electrochemical phenomena, providing ultra-low product detection [133, 134], insight into double layer dynamics and adsorption phenomena [135, 136], etc. Electrochemical modulation through redox reactions can also be used as a key component to provide definitive proof of single molecule detection through SERS [137].

Good control of electrochemical depositing and polishing techniques can be crucial to obtain well defined plasmon supporting substrates. In a recent study, extremely precise measurements of light angular momentum were performed using electrochemically grown
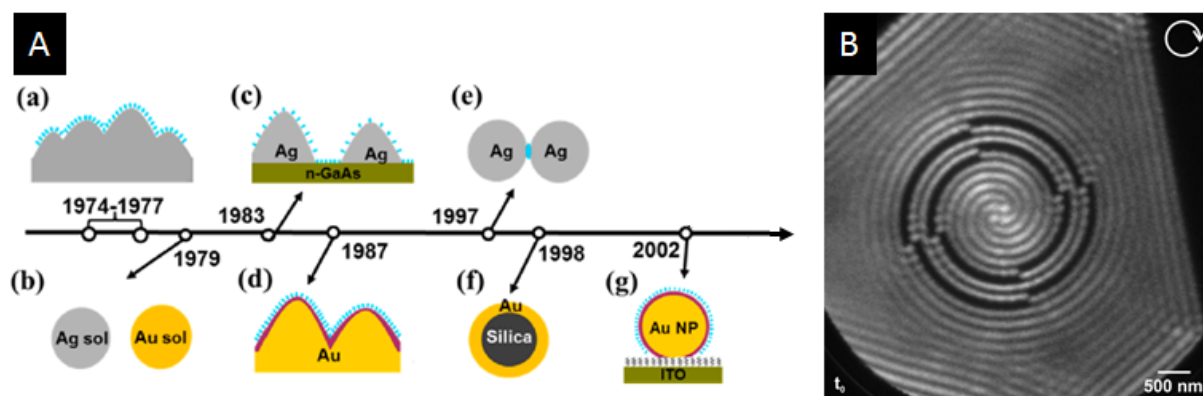
Figure 1.12: Examples where electrochemistry has played an essential role in generating or supporting optical-oriented studies. (A) Brief timeline of SERS important milestones. starting from its (a) first observations on Ag surfaces roughed by electrochemistry, then (b) on Ag and Au colloidal solutions, (c) nanoislands of Ag on conductive surfaces, (d) deposited transition metals on roughed Au surface, (e) Single Molecule SERS, (f) bio-functionallised Au Tags (Adapted from [140]), (g) under potential deposition and redox replacement transition metal on Au NP. (B) Rotating plasmons supported on atomic flat micrometric EC-manufactured Au-flakes [138]

atomic substrates, which were atomic flat over several micrometers [138, 139]. Such extraordinary homogeneity was key in obtaining the well-resolved plasmonic structures, as even the tiniest imperfection would scatter the plasmon, destroying the delicate patterns.

1.3.3 Electrochemically generated optical phenomena in single particles and photomodification of their properties

Finally, electrochemistry can also sometimes be used to generate optically active single molecules and or modulate their optical response properties. In an example from Orrit's group, single fluorophore activation was achieved by use of a redox mediator to activate immobilized methylene blue fluorescent probes on a single molecule basis[141]. Similarly, single molecules with high Raman cross-sections have also been generated electrochemically, and used in SERS[137] and TERS[80, 142] experiments.

The electrocatalysis of reactions generating fluorescent probes can also be used to enlighten the spatial distribution of active sites over catalytic nanoparticles, using super-localization methods [98]. Moreover, single molecule fluorescence methods also have the potential to enlighten mechanistic pathways [143] and identify intermediate species [103].

The electrochemical properties of semiconducting NPs can be modified by light, which can be probed at single particle scales. For example, NPs made of light-sensitive semi-conductor anastase TiO_2 material have been studied through the electrochemical impact technique. Depending on whether the particle had been irradiated with light, the direction of the steps can be reversed for a given potential, going from oxidative to reductive steps. What happens is that light can excite electrons to the conduction band and thus change the Fermi level energy. Depending on the electrode potential range with respect
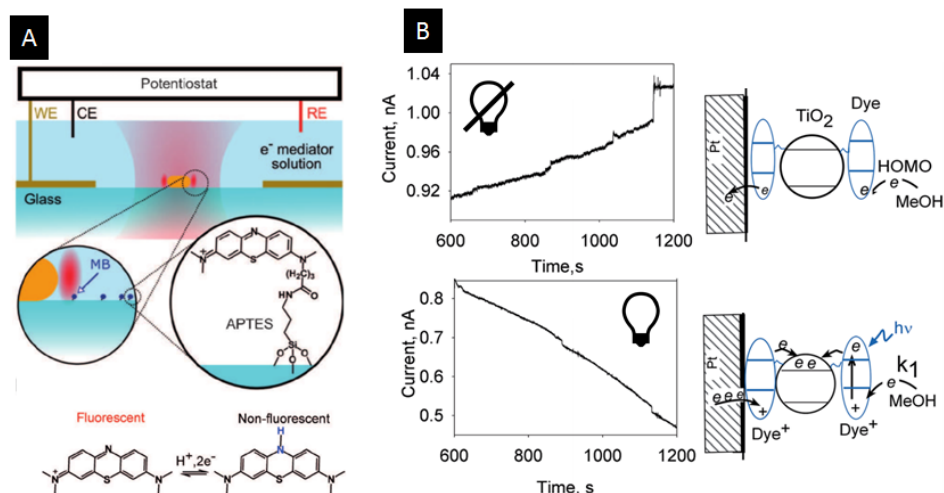
Figure 1.13: (A) Indirect electrochemical generation of a fluorescent molecule through a re-dox mediator, whose luminescence is exalted by the presence of a plasmonic nanorod [141] (B) Switching of electrochemical step impact behavior from anodic to cathodic by action of incident radiation (Adapted from [145])

to the new Fermi Level, electrons will flow on either one way or another [144, 145]. This is illustrated in Fig.1.13.

The emission of light in response to an electrochemical stimulus, electrogenerated chemiluminescence (ECL), has also been used to study molecules and nanostructures individually. For example, Bard's group used PtNPs to oxidize photoactive $Ru(bpy)_3^{2+}$ and a coreactant, triggering the ECL process, to detect NP collision with photodetectors. Potential dependent changes in the photoluminescence properties of silver nanowires have also been reported[146].

These examples highlight the complexity of optical-chemical small scale studies. On nano to molecular ranges, it is rare that the chemistry or physics of the analytes could be considered alone. Rarely the observation of small entities is with no chemical effects, and even more rarely can we modify a systems chemistry without provoking major alterations of their physical properties. These difficulties are however the price to pay for the detailed knowledge these studies provide. No pain, no gain.

1.4 What this thesis is all about.

Such is the context in which the work described in this thesis emerges. Although individual particles studies start to be more and more common, and a few examples of coupling optics and electrochemical methods to understand NP reactivity already exist, it is rare that an equal importance is given to both EC and optical measurements. In general, either EC or optics are used as a support and/or to generate the optical (EC respectively) response, as it was shown throughout this chapter.

If a simplified EC reaction $R \rightarrow O + e-$ is considered, one could *very heuristically* say that we have access to the electron flux via electrochemistry, while optical techniques reveal the rate of consumption/generation of R/O. In very simple cases, these two pieces of information may be redundant, but this is certainly not a general rule, and very often the actual mechanism is much more complicated.

The originality of this thesis work relies on not only using optics to derive electrochemical information, or to measure electron fluxes precisely. We are really interested in the complementarity of optical and electrochemical signals of individual objects, and in the information that can be extracted by comparing them. The next chapter will particularly stress out this point: starting with a very simple dissolution reaction, the complexity of the situation will be gradually increased, illustrating the emergence of the need for this coupled EC-optical single NP approach.

Chapter 2

Individual Silver Nanoparticles Electrochemistry. Part I: Electrochemical Reactivity and Complexing

The present chapter is heavily based on our publications in J. Am. Chem. Soc. [147], Acc. Chem. Res. [148] and Farad. Disc.[149]. The results herein presented are adapted from these publications.

The importance of the history of a scientific field is often neglected, in spite of its determinant role played in further developments [150]. In particular, the choice of first model systems is a crucial step in forging theory and ultimately define a system's characteristic generalizations and simplifications. In demonstrating a new concept, it is important to choose a model complicated enough to prove the utility of new ideas, but not *too* complicated to the point of obscuring its conclusions.

Take for instance the development of surface probe techniques. Before the invention of the STM, another very similar instrument already performed topographic measurements via tunneling current - the Topografiner [151, 11]. Although it operated by tunnel effect, and had all the elements common to scanning probe techniques, it failed to develop its full potential (at least partially) due to a bad choice of model systems. In contrast, Rohrer and Binning chose to apply the STM to image Silicon 7×7 surface, a strongly debated subject among surface scientists. This fortunate choice led to a much more efficient promotion of STM, as their image made the utility of the instrument crystal-clear. The image caused a big impact on the community, leading to further developments and adoption of surface scanning techniques by a wide audience [11]. While we do not compare the importance of our work to the discovery of the STM, careful care was taken to choose an interesting

model to explore.

In this chapter we describe our choice of model to explore the utility of our experimental concepts. We have studied the oxidation of silver nanoparticles as a guiding model, and to show what a combined optical- electrochemical approach could help unveil.

2.1   Not all that glitters is gold (or why silver?)

The importance and utility of silver has been recognized since Antiquity. Besides its aesthetically pleasant aspect, Ag has been recognized as a powerful antiseptic agent since old times: registers dating back to Herodotus describe the use of silver in containers to carry water and food, silver cutlery was used in Middle Ages, and silver solutions were routinely prescribed by doctors for a number of diseases until the twentieth century[152].

Although the exact mechanism still remains elusive, and is not likely to be unique, silver antibacterial action seems to be correlated to its ability to oxidize, progressively leaking Ag^+ ions into the environment [153, 154, 155]. The use of silver nanoparticles (Ag NPs) was then a natural step, for their high surface-to-bulk area would represent a way to efficiently monitor Ag^+ release rate. Moreover, Ag NPs can be more easily internalized, while surface functionalisation can target specific cellular population intake, which made Ag NPs very interesting candidates for targeted antibiotic delivery [156].

Indeed, market applications of Ag NPs are already numerous and growing, calling for further regulation for their use [154, 155]. In spite of extensive research , with numerous reviews over the last few years, the knowledge about Ag NPs reactivity does not seem to be enough to derive decisive and necessary regulation laws[152, 157].

Besides the pharmaceutical industry, plasmonic properties, specially the presence of a LSPR band, have sparked a lot of interest on nano silver research for sensors applications. The LSPR band of Ag can be tuned by size, allowing fine adjustment of the enhancement effect over almost the whole visible spectrum, as shown in Fig. 2.1. Besides, the dielectric constant of silver leads to much lower SP damping in the visible range as compared to most metals including gold. This has made it the metal of choice for LSP or SPP studies whenever its easy chemical transformation, and therefore poor stability under usual conditions, are not a problem.

Moreover, the plasmonic performance - for example the ability to generate SERS effect - is however extremely dependent on the surface state of the NP. Indeed it has been shown that the oxidation of just a few nanometers of Ag NP can lead to a decrease by orders of magnitude of the SERS enhancement factor [158]. All these applications could directly benefit from a more in depth detailed insight into the mechanism of silver oxidation.

Moreover, a considerable body of literature developed over the years, owing to the aforementioned applications. Due to this, there is a considerable amount of data on Ag NPs optical properties, allowing us to focus on the dynamics of the particles chemical
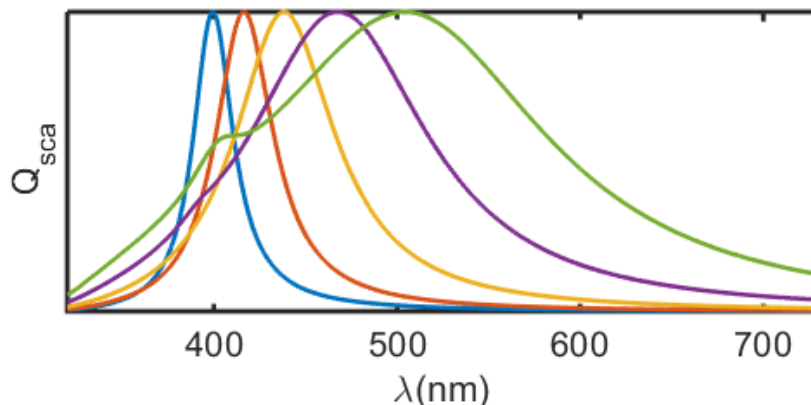
Figure 2.1: Normalized Spectra of Ag NPs with different sizes, $r_p = 5$ nm (blue), 20 nm (orange) 30 nm (yellow), 40 nm (purple) and 50 nm (green), calculated using Mie Theory. The peak position indicates the dependency of the LSPR with particle size. Optical indices were taken from [159].

reactions. Besides one of the core models for the plasmonics community, Ag NPs were also the main model for electrochemical destructive nanoimpact analysis (described in Sec.1.1.2, and revised in the next section), which also helped setting ideal operating conditions for the impact experiments.

Although thoroughly studied, lots of questions regarding reactivity were still open, since most studies focused on ensemble data or were incompletely characterized, with only in situ information about NP EC or optical information.

2.1.1 Silver NP reactivity through electrochemical impact experiments

Owing to all these many exciting special properties and following the trends towards the development of nanoscopic functional materials, a voluminous body of literature on Ag NP has been developed, covering synthesis methods [160, 161], surface chemistry [162, 163], toxicology [164, 165], etc.

The electrochemical properties of Ag NPs were first addressed through modified electrodes, with incidences for electrocatalysis and NP reactivity [36, 166, 167, 168]. These experiments however were only able to address ensemble properties. Following reports that EC properties could vary strongly with particle size and surface chemical state[169, 170], one quickly noticed that only limited insight was available if the particles were not analyzed individually. Interest was then shifted towards single NP techniques, specially after the introduction of electrochemical impact experiments [36] described in Sec.1.1.2. In these experiments, an electrode is polarized at a potential anodic with respect to the Ag/Ag^+ couple. An Ag NP impact therefore yields an electrochemical oxidation peak.

Oxidative spikes contain a lot of information about the electrochemical reaction. For

instance, the total charge that has been exchanged can be converted to the amount of oxidized material through Faraday's law. Moreover, the height and duration of the spike are indicative of the reaction kinetics, while the potential threshold at which spikes start to appear reveal the thermodynamics of the reaction [43, 36].

Using these strategies, Ag NP reactivity has been analyzed through nanoimpact experiments in a variety of media and conditions, such as sea water, physiological pH, presence of complexants, with different capping agents [171, 172], etc. Studies aiming at the characterization of nanoparticles structures from impact experiments also appeared, shedding light on core-shell structures[39, 40], helping understand alloying and de-alloying processes [173] and diagnosing the agglomeration state of a solution[38], all these at the level of individual NPs.

Deriving information on nanoparticles from impact experiments, however, remains an indirect way of studying them. Without a complementary in situ characterization process, it is rare to have unambiguous information about activity and size. For instance, suppose a silver particle interacts with an anodically polarized electrode and the oxidation-dissolution process starts from the contact area, breaking the electrical connexion between electrode and the nanoparticle. How would the corresponding spike look like? If partial oxidation takes place, the oxidative spike would be briefer, giving us the impression the particle is smaller than it actually is. Moreover, if the particle remains in the electrode vicinity, many smaller peaks would be recorded, overestimating the particle concentration. How would be the response of an aggregate? would each particle on the aggregate oxidize one by one, or would the full aggregate behave like a bigger particle? Are the particles in an aggregate electrically connected?

To answer all these questions, it is necessary to couple the aforementioned impact experiment with an alternative method to characterize particle's physical size and contact. This is where optical methods become relevant. The ability to see, linked to all the chemical capability provides a much more complete characterization of the process, removing most of the ambiguities.

2.2 Coupling 3D Microscopy to Electrochemical impact Experiments

> **⟹ Key Experiment Conception (#1):**
>
> - Observe single NP movement in 3D via holography
>
> - Wait until they reach a polarized electrode by diffusion
>
> - Analyse their reactivity through a combination of optical, electrochemical and spectroscopic monitoring

Optical methods are capable of imaging events such as impacts, situating them in space and allowing visual inspection of chemical reactions. In this section we describe the instrumental development we used in order to couple single-particle-sensitive 3D microscopy, holography, and electrochemical impact experiments. The principles of Holography most relevant to the present experiments are revised and the technique as a whole will be thoroughly discussed in Chapter A. Besides holography, single particle spectroscopy experiments are also performed to corroborate our conclusions.

As a first step, we will focus on a case where EC and optics are able to provide the same information, thus demonstrating the successful coupling between the two signals. Then, complexity is added by taking a look at a system where dissolution and electrochemical reaction do not necessarily happen simultaneously.

2.2.1 Holography

When suspended in a solution, NPs never stop moving. Random collisions with solvent molecules generate Brownian motion which keeps particles in a never ending movement. To be able to track their position and trajectories is therefore an essentially 3D problem, which calls for a three dimensional microscopy technique.

In spite of what Star Wars might say, an hologram is the processes of recording and reconstructing a wavefront scattered by an object. For particles smaller than the wavelength of the scattered light, this allows 3D reconstruction of volumes much bigger than the particle size, as sketched in Fig.2.2.

In short, a 532nm laser is used as both as signal and reference. The laser beam is split in two by a Beam Splitter (BS). The first part (called the *object beam*) is directed towards the sample at a high angle, in a total internal reflection (TIR) configuration. A prism is used to allow the light into a microfluidic cell. Since the incident light is rejected due to TIR, only the light scattered by the particle reaches the objective of the microscope, therefore forming a Dark Field detection scheme. The second part of the beam (called the *reference beam*), is sent to a second beam splitter to interfere with the Object beam, thus forming the interference pattern, which is numerically treated to yield the volume reconstruction. A more detailed description of the optical montage and data treatment can be found in Sec.A.1.

Besides being a 3D technique, holography presents other advantages. For instance, the scattering cross section of a NP scales as the particle volume. If the particle scatters an electromagnetic field E, most optical techniques are sensitive to $|E|^2$, therefore the detection intensity scales as the square of the particle volume. This dependency in r^6 quickly reaches the detection limitations when r is in the range of tens of nanometers or below. In off-axis holography, as explained in Chapter A, we detect the product of the EM field scattered by the particle ($\propto r^3$) and the reference beam (independent of r). Therefore the detection intensity scales as r^3, allowing the detection of smaller particles.

In our current configuration, shown in Figs A.4 and 2.2, and using a superlocalization procedure (described in Sec.A.2) we are able to detect immobile particles as small as 20 nm, with a localization precision as good as $3 \times 3 \times 10$ nm ^{3}. If the particles are moving, the precision results from a compromise between the localization accuracy, which improves with the number of collected photons and the exposure time, and the Brownian displacement, which increases the position uncertainty as the exposure time increases. This precision is typically around 60 nm in our experiments.

Sizing particle through MSD analysis

Three dimensional tracking of the particle represent an alternative way to determine particle size. If a particle random motion comes from collisions with smaller molecules, it should be sensitive to the particles size. In a heuristic mechanical explanation, if a solvent molecule collides with a particle, the total momentum should be conserved, therefore the bigger the particle, the slower it will move after the collision.

A succession of random shocks with the particle will then lead to an erratic movement known as Brownian motion, whose statistics have been throughly studied for at least a century [174, 175]. The position density function is expected to follow a Gaussian
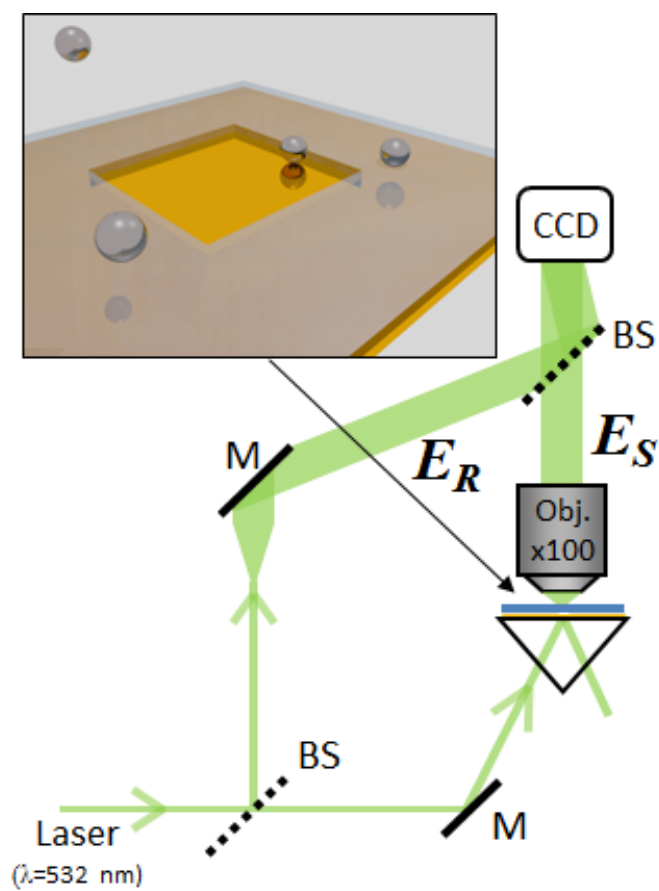
Figure 2.2: Principle of the holography setup used to monitor NPs in a microfluidic cell.
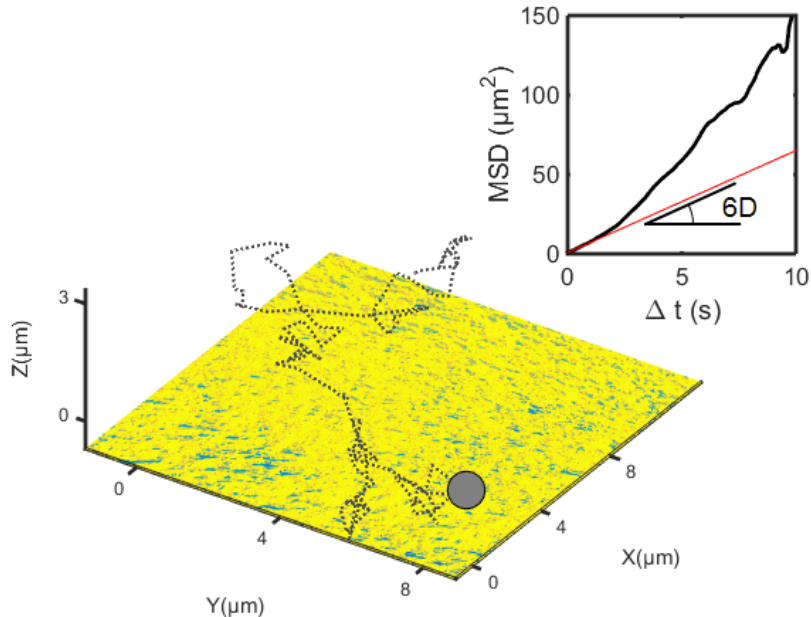
Figure 2.3: Experimental trajectory of a 50nm Ag NP diffusing near a gold electrode. The inset shows the MSD curve of the same trajectory and its linear fit, allowing estimation of the particle size from the slope of the linear curve.

distribution, whose width increases linearly with the elapsed time. Its 3D mean square displacement (MSD) is therefore proportional to $6D\Delta t$, where D is the particle's diffusion coefficient that might be connected to the particle hydrodynamic radius, r, through the Einstein-Stokes relation using the solution viscosity(η), Boltzmann constant (k_b) and the Temperature (T):

$$D = \frac{k_b T}{6\pi\eta r}$$

Through a linear fit of the MSD versus time curve we can then access particle size. The detailed procedure is presented and throughly explained in Sec.A.4, and illustrated in Fig.2.3. Recording the trajectory of a particle then represents an alternative (non electrochemical) way to evaluate the particle size.

2.2.2 Transparent electrodes in microfluidic cells

For performing holography in the transmission configuration used here, light needs to pass through the electrode, therefore the latter needs to be transparent. Almost any conductive material can be made transparent, provided that it is thin enough. Its electrical conductivity, however, also shrinks with thickness: Conductivity and transparency are usually conflicting demands for an electrode. In order to couple optics and electrochemistry, it was crucial to find an electrode material able to conduct current while keeping partial transparency (at least at the laser wavelength).

A few options satisfying these two requirements exist. Classical inorganic solutions include Indium-Tin-Oxide (ITO), fluorine doped tin oxide (FTO) and Zinc Oxide. These materials may seem like ideal candidates for general electrochemistry, but their deposition is not easy and surface homogeneity problems (leading to the presence of inactive regions) are fairly common, thus making their use complicated for impact experiments. Carbon based materials(such as carbon nanotubes[176], graphene [177]) and polymer based (for example, poly(3,4-ethylenedioxythiophene) [178]) materials are promising candidates, but their fabrication is not yet completely mastered, and their electrochemical properties not fully determined, therefore making their use not straightforward.

Thin metallic films, such as gold and platinum, can however be made transparent if they are thin enough. If these materials are to be used in our optical-electrochemical setup, a trade-off must be found. For Au thin films, if the film is kept thinner than the skin depth of the metal, typically 50 nm in the case of gold, it is fairly transparent, specially in the green region of the spectrum (around 532 nm), while still presenting fair conductivity. Moreover, gold films are easy to deposit, and electrode design and manufacture benefit from decades of development of lithographic techniques, granting great flexibility in electrode design.

The final electrode is shown in Fig.2.4. We took advantage of this easiness of manufacture to design gold patterns consisting in twelve independently addressable electrodes of $50 \times 50 \mu m^2$. This size was chosen since it is smaller than the size of the field of view of our microscope.

In this way we are able to visually monitor all the events taking place on the surface, while the small surface reduces the electrochemical background current, thus allowing the detection of low current spikes. The electrode fabrication protocol is fully described in Sec.A.6.

After the microfabrication process, the electrode is integrated into a microfluidic cell, using a paraffin film as a spacer that seals the sides of the chamber (thickness $\approx 100 \mu m$). Finally, capillary tubes are added as inlet and outlet, as shown in Fig.2.4.

2.2.3 Getting ready to observe impacts by holography and electrochemistry in fast dissolving conditions

The coupled electrochemical-optical response is then ready to be evaluated. We start by examining Ag NP oxidation under mass-transport limiting (thus fast kinetics) conditions. We selected electrolytes which are not able to form stable compounds with silver, or complex Ag^+, avoiding precipitation.

If no interaction with the electrolyte takes place, and the potential is set sufficiently higher than the oxidation potential the reaction is expected to happen at its fastest pace, limited only by Ag^+ ion solubility and diffusion away from the dissolving particle surface.
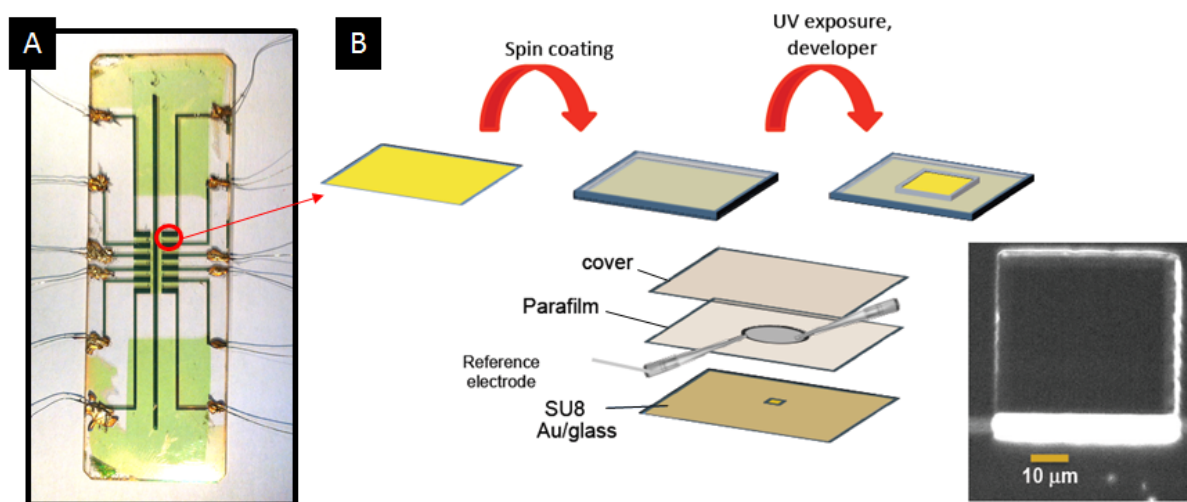
Figure 2.4: (A) Photo of the 12-electrode ensemble after the lithographic process. (B) Sketches of the microfluidic cell preparation.The inset shows a dark field image of the electrode surface - the square consists in exposed Au, while all the surroundings are recovered by a Si_2N_3 insulating layer.

In this case, the oxidation reaction should be limited by diffusion and the dissolution of the particle is expected concomitantly to the oxidation peak.

The experimental conditions need however to be set. Three parameters are involved : the NP concentration, as it regulates the frequency of collision events, the electrolyte concentration, essential for solution conductivity, and the applied potential.

NP concentration   For holographic measurements, the quantity of nanoparticles in the field of view needs to be controlled. However, if there are too many NPs in the solution, the light scattered by one NP is likely to interfere with the others (this is sometimes called the multiple-scattering regime) creating interference artifacts, which affect the holographic reconstruction process. Moreover, taken together, the light scattered by the ensemble of out-of-plane NPs generates a speckle background, lowering the dynamics of the measurement and therefore the signal to noise ratio. On the other hand, if the concentration is too low, measurements can be quite long, generating an intractable amount of data : a reconstructed 2 min hologram video sequence can easily contain as much as 100GB of data.

The concentration of NPs was set to 0.18 pM, corresponding to a regime where on average 5-6 particles are simultaneously present in the $50 \times 50 \times 20~\mu m^3$ monitored volume. This concentration in principle ensures an average of 5-10 impacts per minute while staying in the single optical scattering regime.

Electrolyte Concentration   Small particles are usually prone to aggregation in the presence of salts. For this reason, most commercial nanoparticles solutions usually contain

capping agents to stabilize the surface. Accordingly to DLVO theory of colloidal stability (named after Boris Derjaguin, Lev Landau, Evert Verwey and Theodoor Overbeek) [179, 180], addition of salt should trigger aggregation. Since electrochemistry measurements require dissolved charged species to ensure the solution conductivity, care must be taken to avoid aggregation.

Dynamic Light Scattering (DLS) measurements were performed to monitor the stability of the colloidal solution over time. Here, the Ag NP colloidal solution was diluted up to 0.18 pM in water containing salts at different concentrations. The Ag NPs were added at the last minute to avoid previous aggregation. Within 30 min - an upper limit for our experiments, no meaningful aggregation was observed until electrolyte concentrations of 100 mM. We therefore chose to limit the latter to 50mM, which is conductive enough to carry out electrochemical measurements.

Potential If Ag is used as quasi reference electrode, the formal potential for silver oxidation lays around 0V [171, 181]. To ensure diffusion limited reaction rates, we applied a strong overpotential of at least 500mV (typically 0.6 - 0.9V). Such choice was motivated by the fact that the NP properties could vary with respect to bulk Ag. For example, the presence of a thin oxide layer could influence the particle reactivity, slowing down the oxidation kinetics by orders or magnitude. Moreover, we used a silver wire as quasi reference electrode (AgQRE), therefore some variability could be expected in terms of the applied potential (up to 50mV). A strong overpotential ensures the oxidation to take place in the diffusion limited regime.

2.3 Correlated Impacts

With the microfluidic cell set, a freshly prepared solution of 0.18 pM Ag NP and 0.05M KNO_3 is injected into the cell under holographic monitoring. A number of particles moving under Brownian motion is seen in the vicinity of the electrode. During the experiment preparation time some particles also readily settle on the electrode surface.

The particle's random movement eventually leads some of them towards the polarized electrode. As demonstrated by Compton [182, 183, 45], and shown in Sec.2.1, every time a particle hits the polarized surface, it generates an oxidative spike corresponding to the reaction:

$$Ag_s \rightarrow Ag^+_{(aq)} + e^-$$
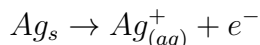
Since Ag^+ is a soluble species, the particle oxidation happens concomitantly to its dissolution. This process can be followed by optics, if the intensity of the scattered light on the electrode plane is registered over time. Light scattering objects, such as particles or surface defects, are seen as bright spots, with sizes corresponding to the diffraction
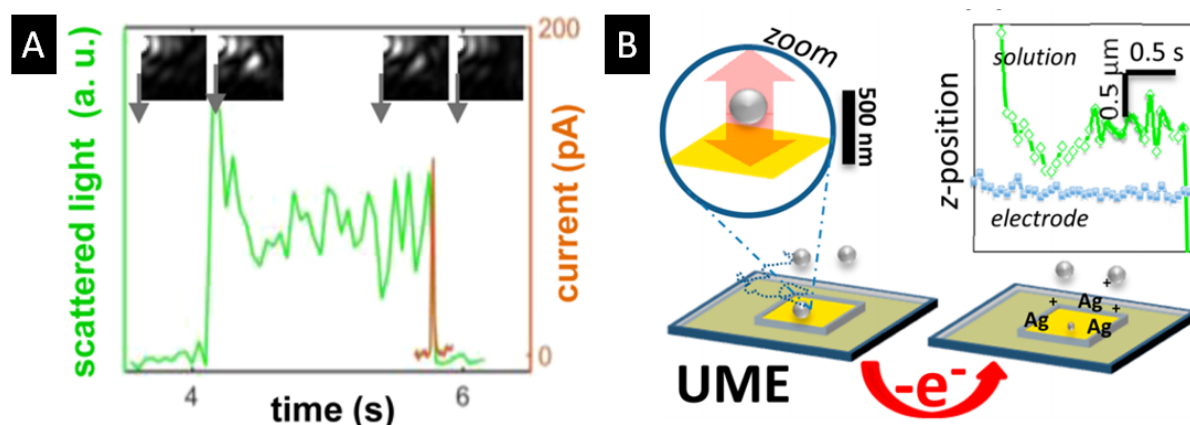
Figure 2.5: Simultaneous optical and electrochemical monitoring of the arrival of a particle. (A) The scattered intensity on the electrode plane is monitored over a region of interest of $2 \times 2\mu m^2$ (green) and compared to the electrochemical oxidative spike current (orange). The appearance of the current spike happens simultaneously to the particle dissolution, which corresponds to its optical disappearance. (B), the z-movement of the NP in the vicinity of the electrode is shown in detail with a $\approx 100nm$ precision using a superlocalization routine. For comparison, the z-movement of a surface defect is shown (blue trace).

spot ($\lambda/2 \approx 600$ nm wide).

This situation is shown in Fig.2.5. A diffusing particle lands on the electrode surface (near a surface defect). Some snapshots of the full movie are shown. They correspond to holographic reconstructions made in the electrode plane. Therefore, the arrival of the particle, at $t \approx 4$s, corresponds to an enhancement of the monitored scattered intensity (shown in green). After a residence time of ca. 1.8s, the particle oxidizes, as evidenced by the oxidative current peak (shown in orange). Simultaneously, the intensity drops back to background levels, evidencing that the particle was indeed dissolved.

To understand the existence of this residence time preceding the particle oxidation, one needs to take a closer look into the particle three dimensional movement. A 3D super localization procedure (Sec.A.2) was used to resolve the particle trajectory, revealing a stochastic movement in the vicinity of the electrode surface during the 1.8s residence time. This can be interpreted as the influence of a very thin layer of oxidized material, limiting the particle reactivity to a few active sites. The particle stochastic movement would then be a result of random collisions with inactive surfaces facets. Alternatively, the movement could result from stochastic interaction of the particle and the surface repulsing electrical double layers.

It is important to highlight that such a movement can only be analyzed thanks to the superlocalizaton process. Since the movement amplitude is much smaller than the 3D Point Spread Function (PSF, around 1μm), it would be impossible to detect using regular 3D microscopy techniques, such as confocal microscopy. Moreover, tracking validates the scenario of particle dissolution rather than simple desorption, which would have been observed with 3D imaging.
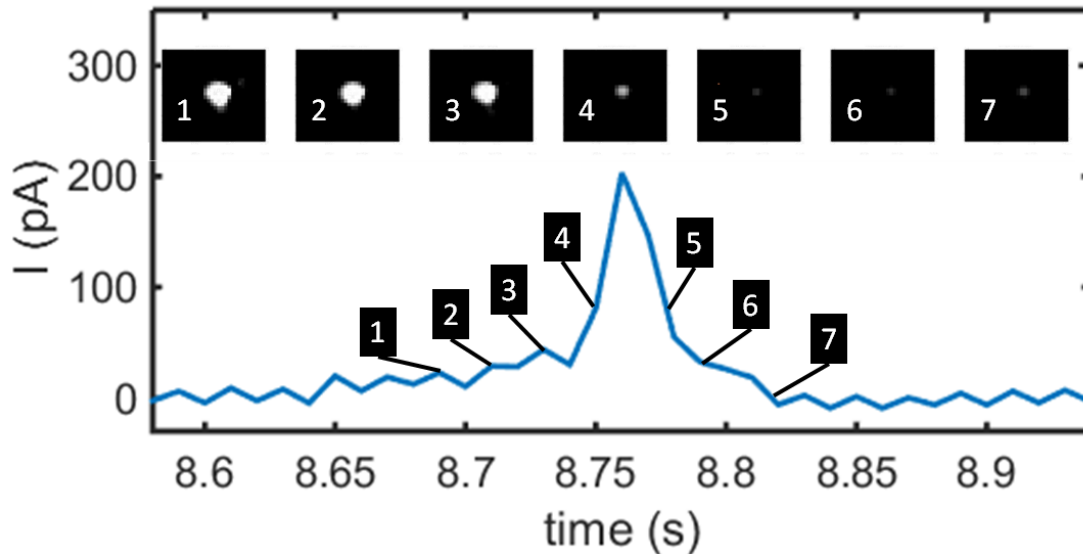
Figure 2.6: Dissolution of a particle sitting on the electrode concomitant to the electrochemical peak appearance, showing the simultaneity of both events. The image is an area of $2 \times 2.4 \mu m^2$ and the acquisition frequency is 20 Hz.

The same behavior is observed for particles already present on the electrode surface in the beginning of the experiments. After a random time, the particle finally dissolves, simultaneously with the occurrence of an oxidative spike. An example, evidencing the simultaneousness of the anodic spike and particle disappearance, is shown in Fig.2.6. As in the previous case, the adsorbed NP dissolves at the same time as the current peak appears, and no vertical desorption is observed.

One can take the comparison between electrochemical and optical traces one quantitative step further. Since every single molecule exchanges one single electron, the amount of charge contained in a peak (its integration) can be directly related to the amount of oxidized matter - and therefore its mass and volume - through Faraday's law. The particle radius can then be calculated by assuming a spherical shape, giving the (previsouly mentionned) expression:

$$Q = \frac{4\pi \rho F}{3M} r^3$$

As mentioned before, the intensity of the scattered light after the holographic reconstruction scales as the scattering cross section of the Ag NP, and therefore as the particle volume. Consequently, we can compare the EC charge with the total scattered light, as shown in Fig.2.7. Similar curves were drawn for each of the NPs oxidized (N=13), whichever the situation, pre-adsorbed or colliding NPs. In all cases, the integration of the EC peak charge coincides with the evolution of the particle volume ($\propto$ optical response).

The radius distribution obtained from the EC charge (r_{EC})can then be compared to bulk DLS measurements. Fig.2.8A shows the superposition of DLS-obtained size distributions and r_{EC}. Whenever it was possible to track arriving particles trajectories long
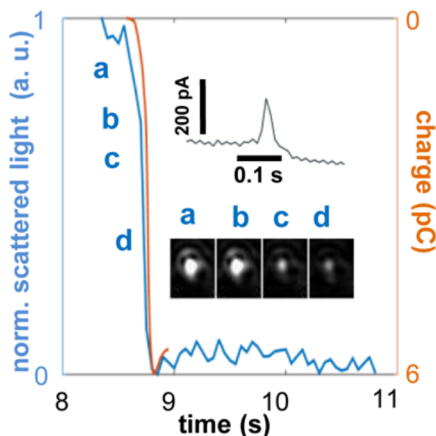
Figure 2.7: Oxidation of a pre-adsorbed particle. The total exchanged charge (orange) is compared to the inferred volume variation from scattered optical intensity (blue). In the inset, the oxidation peak and temporal evolution of $2 \times 2.7 \mu m^2$ reconstructed images of the plane of the UME (sampling rate: $\tau = 50$ms).

enough to perform MSD analysis, the measurements are corroborated by size estimations obtained through the MSD curve (r_H), in very good agreement. For example, in Fig.2.8B two typical examples of MSD analysis are shown, with $r_H = 48nm$ (while $r_{EC} = 55nm$) and $r_H = 47nm$ (while $r_{EC} = 51nm$).

2.4 Adding Complexity: precipitating agents

Up to this point, the same oxidation reaction was interrogated by optics and EC. The correlation of both signals was then taken as a validation that the experimental concept is working well. The signals however not always characterize the same thing: while optical scattering responds to the size and chemical nature of the particle (through its refractive index), electrochemistry measures exchanged electrons.

In the simple case of a reaction $Ag \rightarrow Ag^+ + e^-$, dissolution is fast and both phenomena happen at the same pace. What happens however if the product formation is decorrelated from the electron transfer step? How does the coupled approach manifest and to which extend can it provide us with new insight? Otherwise stated: How can the complementarity of optical and electrochemical signals be explored to address a much more complex chemical reaction? This is what will be explored in the present section.

In the present conditions, particle dissolution is controlled by diffusion of silver ions away from the surface. Since diffusional transport is proportional to the gradient of chemical species, one could imagine slowing down the dissolution process by limiting the Ag^+ concentration at the particle surface (and thus the overall gradient between the surface and the bulk solution, where $[Ag^+]_{bulk} \approx 0$).

It is a long known fact that the solubility of silver ions and its complexes can be limited in the presence of halides or pseudo-halides [184, 181]. If the overall silver solubility is
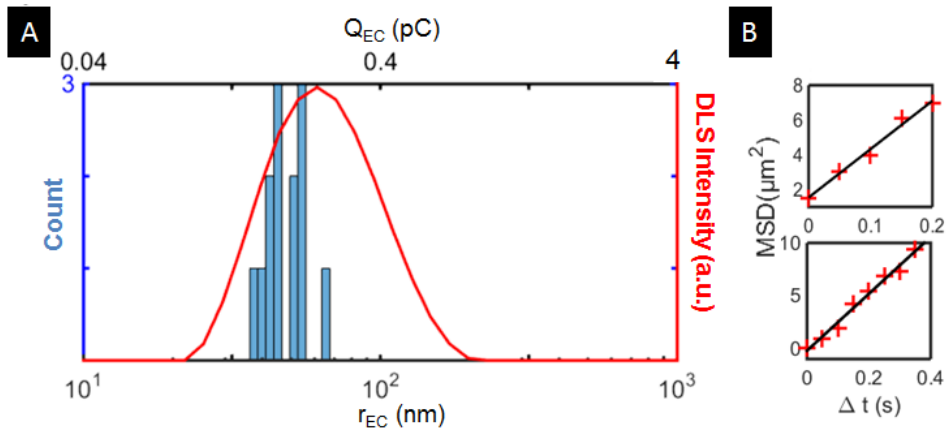
Figure 2.8: (A) Comparison of MSD size distribution and the radius obtained from integration of the electrochemical spikes. (B) Examples of MSD curves for size determination of arriving particles. On the top one, a diffusion coefficient of $4.5\mu m^2/s$ is obtained, corresponding to $r_H = 48$nm. Integration of the corresponding peak yields $r_{EC} = 55$nm. On the bottom one, $r_H = 47$nm and $r_{EC} = 51$nm.

dramatically reduced, the gradient becomes lower, and thus diffusional transport slows down. This is the strategy employed here, where thiocyanate SCN^- ions are added, slowing down the dissolution rate. Although the influence of $[SCN^-]$ on the dissolution rate is not surprising, one has no way to follow the electron exchange rate. We then propose to address the redox reaction rate using the electrochemical signal. Comparison of the electrochemical trace with the optically determined dissolution rates should then provide extra insight into the details of chemical oxidation/dissolution mechanism.

2.4.1 Monitoring Electrochemical Impacts in KSCN

In the presence of thiocyanate, a product of very limited solubility is expected to form. In a simplified representation, one can write:

$$Ag + SCN^- - e^- \rightarrow AgSCN_s \leftrightarrows AgSCN_{(aq)}$$

$$AgSCN_s + xSCN^- \leftrightarrows Ag(SCN_{x+1}^{x-})_{(aq)}$$
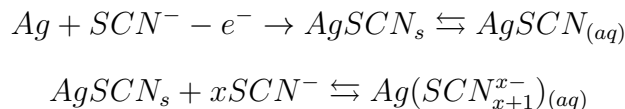
At higher $[SCN^-]$, soluble complexes with higher degrees of ligands are expected to form, thus enhancing the overall solubility and the dissolution rate. The dissolution rate can thus be tuned in the presence of these ions.

Unless expressed otherwise, all experimental conditions were kept the same as in the previous experiments (with KNO_3 as supporting electrolyte): high oxidation potential, such that the EC reactions are always diffusion limited and 0.18pM NP concentration, yielding no more than 5-6 particles in the field of view.

High (300mM) [SCN^-]   At high concentrations, under potentials high enough for the reaction to be diffusion limited (typically $0.7V$ vs AgQRE), EC nanoimpacts show that the electrodissolution process is equivalent to that observed in the absence of SCN^-, i.e. EC peaks of duration ca.0.1s are detected. It is then suggested that at this concentration the NP is dissolved as soon as the charge is injected. The electrochemical step becomes the rate limiting step and the electrodissolution is formally equivalent to the simplest case, $Ag \rightarrow Ag^+ + e^-$. These observations are in agreement with previous literature studies, with SPR monitoring of the electrode surface [117].

Low (50mM) [SCN^-]   At low SCN concentration, the dissolution is expected to be slow. Indeed, optical monitoring of the electrode surface during surface polarization reveals slow decrease of the scattered intensity profile - typically between 4-7 s. This represents an increase of two orders of magnitude with respect to the nitrate case. A few profiles are shown in Fig. 2.9. It is worth mentioning that the large dispersion in optical data is explained by the difficulty of sharply defining a dissolution time, as the intensity may decrease in a non-trivial way, with different slopes. These are likely to depend on the quantity of defects on the material, as well as the chemical environment and kind of electrical contact with the electrode. In order to extract a coherent characteristic time, only sharp decreasing steps (shown in Fig.2.9) were counted. As a result of the dissolution of a few (N=18) nanoparticles, a characteristic dissolution time, reported in Fig.2.10, is obtained.

As in the previous situation, the coupling of nanoimpacts with optical monitoring allows inspection of the charge injection process preceding this dissolution step. A typical example is shown in Fig.2.10, after some residence time during which the particle lies in the vicinity of the electrode, the particle is oxidized, yielding an electrochemical peak. Differently from the previous example, at high [SCN^-], the particle does not disappear immediately, instead it follows a variable incubation time of up to several seconds, after which the particle starts to slowly dissolve. This scenario was reproduced for N = 10 EC spikes, where oxidative spikes of up to 1s duration were followed by a time lag (up to $20s$) and noticeable dissolution within 4-7 s. These data were complemented with EC-only experiments with higher temporal resolution, over a Pt UME inside a Faraday cage, yielding impacts of same magnitude. EC impacts on Pt UMEs were also performed in 150 mM and 300 mM [SCN^-]. Although the characteristic duration of the charge injection varied between 0.2 and 1 s, it always remained much inferior to the dissolution time. The ensemble results are shown in Fig.2.10A, and in Fig.2.14 together with modeling results.

Possible explanations for the delay are manyfold: for instance the particle dissolution could be triggered by the presence of defects, which can be rare or stochastically present in nanosized materials.

The observed charge in all peaks was slightly above the nominal value for 50nm Ag
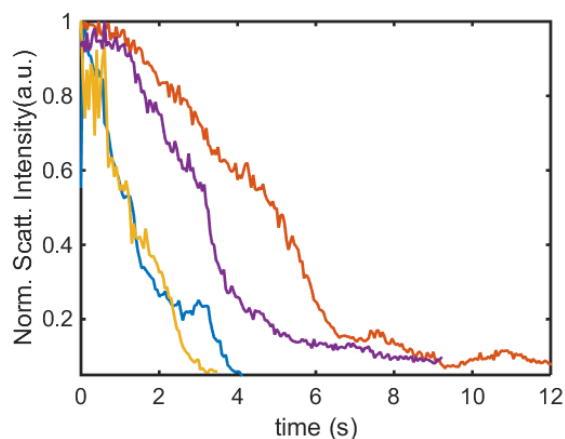
Figure 2.9: Optical intensity profiles of four individual dissolving NPs in the presence of 50mM KSCN.
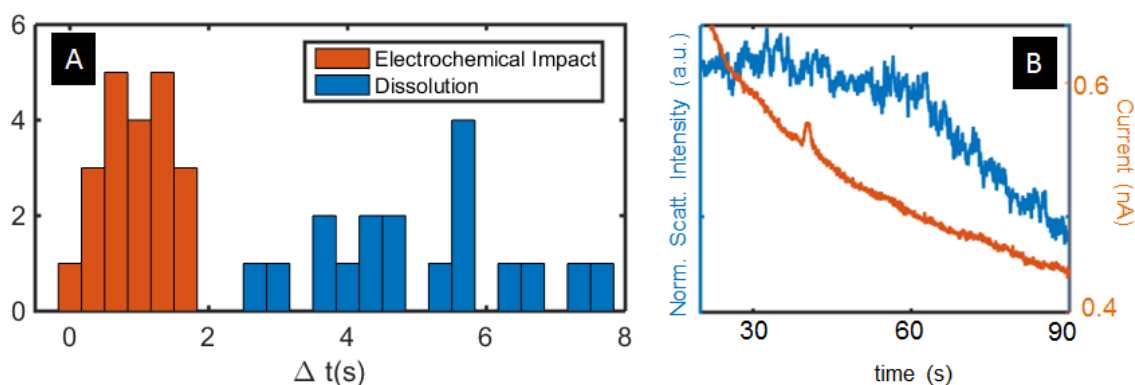
Figure 2.10: (A) Histogram of the characteristic individual times (peak durations) for EC impacts in 50 mM KSCN and optically determined dissolution rates. (B) Comparison of the charge injection peak and dissolution rate for a given nanoparticle.

NPs (typically 14 pC corresponding to a 70 nm particle) - this was in agreement with DLS size distributions after 20-30 min (typical total experiment time) and could reflect the beginning of the aggregation process.

In order to further validate these results, as well as to better understand the phenomena, we sought more information by extending our one-wavelength observations to the full visible spectrum.

2.4.2 Spectroscopic insight

The big disparity between the dissolution time and the electrochemical peak duration indeed suggests the presence of a reaction intermediate, according to the proposed mechanism.

For low $[SCN^-]$ (50mM), given the long characteristic times involved, a chemical characterization of the intermediate should be possible. Moreover, since the initial material
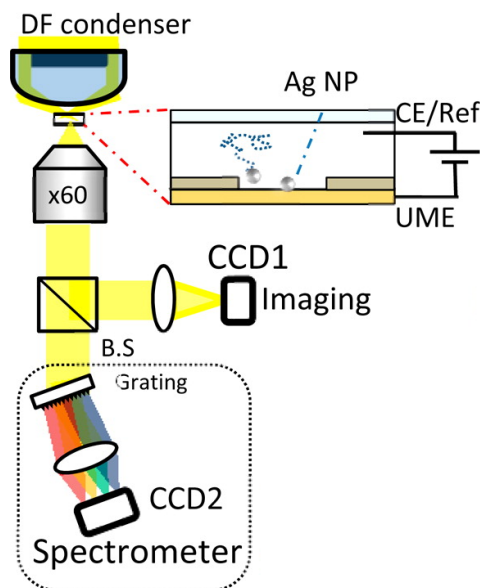
Figure 2.11: Single Particle spectra aquisition Setup

presents a characteristic plasmonic peak, a chemical reaction should lead to a dramatic change in the spectra. Therefore, we decided to probe the transformation using a single NP spectroscopic monitoring setup, shown in Fig.2.11, and thoroughly discussed in Sec. A.3.

In short, the particles were illuminated using a dark field condenser and a line-imaging spectrometer (Specime V8E) to image a linear region of the sample along one axis of the EM-CCD camera. The wavelengths ($\lambda = 450 - 700nm$) contained in each point of this line are then dispersed by a grating along the perpendicular direction of the camera. If a particle is sitting on the monitored line, its spectrum will be recorded. Given the light scattered by every particle, an exposition time of 1s was enough to obtain a decent signal to noise ratio, leading to a clear spectrum.

Individual Ag NPs on a Au electrode :   In order to characterize the spectrum of single Ag NPs over the Au film, a preliminary study was conducted. A large number of particles (N=56) is adsorbed onto a gold electrode, and their spectra are recorded. The average of all these spectra is shown in Fig.2.12.

The spectrum of single particles consists in two bands, reflecting the Ag NP in interaction with the Au electrode. The oscillating electrons on the Ag NP interact with free electrons of the conducting Au film, creating a *mirror-like* response, i.e. a system similar to a pair of particles separated by twice the particle-Au surface distance. The phenomenon can be understood qualitatively in the framework of hybridization models for the LSPR energies [75]. The oscillating eletrons in the Ag NP interact with the free electrons on the metallic Au electrode, inducing surface plasmons. The two electronic
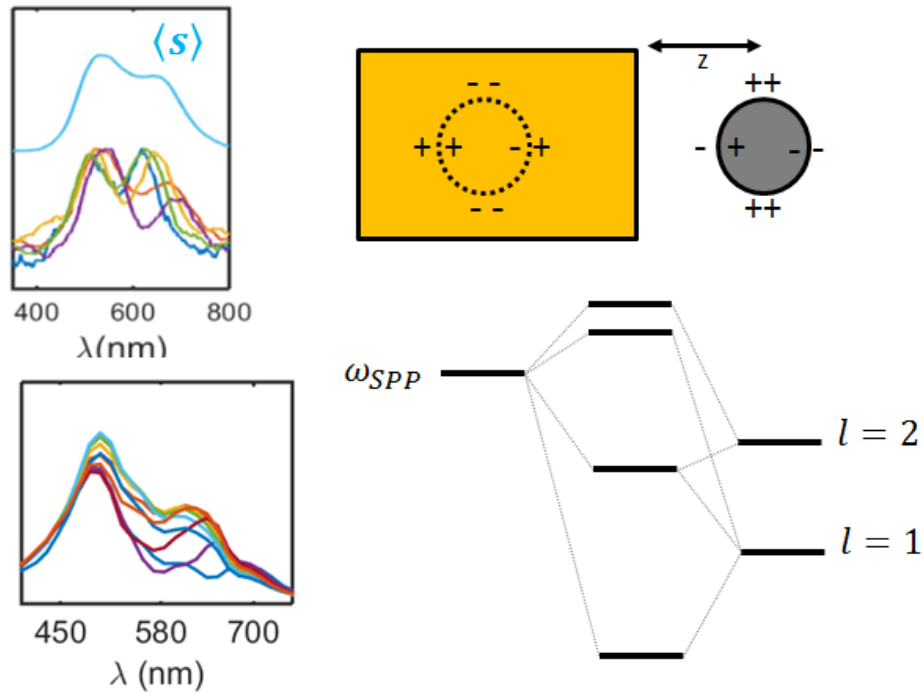
Figure 2.12: Averaged spectrum of N = 56 independent Ag NPs adsorbed over a Au film. Hybridization scheme for qualitative understanding of the interaction of plasmon oscillation. Two plasmon modes from the spheres hybridize and interact with the surface plasmon polarization mode of the surface, analogously to molecular orbitals energies. Adapted from [75]. Simulations using FDTD software of the Ag NP spectra in the vicinity of a Au electrode (different distances are shown), in good agreement with our experimental data

densities oscillations then interact, favoring two modes: in phase (lower energy LSPR) and out of phase (higher energy LSPR). The situation is analogous to the hybridization of molecular orbitals. A sketch is shown in Fig.2.12.

This interpretation is also corroborated by numerical simulations (using Finite Differences Time Domain, FDTD method, performed by our collaborator Robert Kuszelewicz), shown in Fig.2.12. The high energy band (around 500nm) is relatively stable but the lower energy band position depends on the distance between the particle and the electrode. Our observations are also in qualitative agreement with literature results using $Au-Ag@SiO_2$ heterodimers spectra [185].

These measurements therefore characterize the single Ag NP spectral response, and allow discrimination between aggregates and single particles based on their spectrum.

Individual Ag NP reactivity followed by spectroscopy : Since only a small fraction of the surface is imaged and dispersed by the spectrometer, to wait that a particle randomly lands on the inspected zone would not be feasible. Instead, we chose to wait until a large number of particles has arrived on the surface before polarizing the electrode. The arrival of NPs on the electrode surface is monitored visually and the slit position is optimized before the beginning of the experiment. Spectra are then recorded at frequency
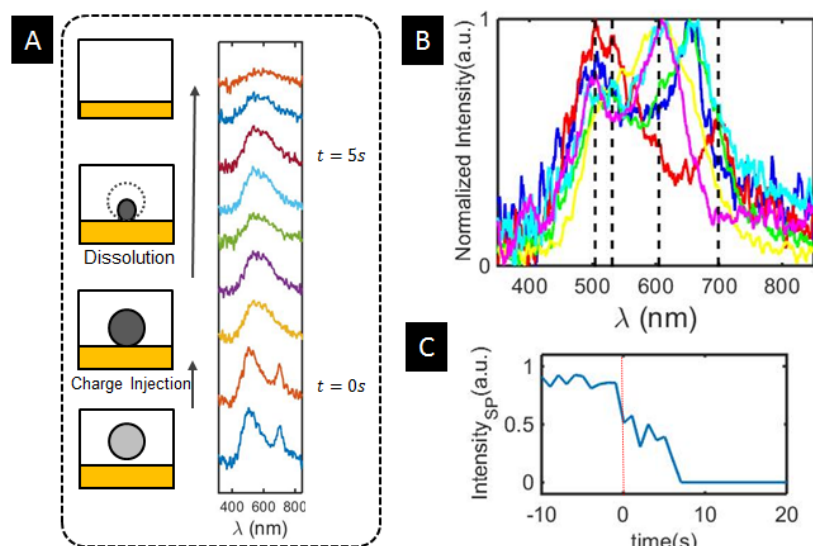
Figure 2.13: (A) Typical evolution of a single NP spectrum a function of time, at a sampling frequency of 1Hz, the electrode is polarized at t=0. (B) Spectra of different single Ag NPs over the Au electrodes. (C) Evolution of the total scattering intensity for a single NP during the experiment - the electrode is polarized at t=0, as indicated by the red line.

of 1 Hz, and the electrode is polarized a few seconds after the beginning of the video. The disadvantage of the methodology is that most particles react at the same time, at the beginning of the experiment (when the relaxation transient current is still present), thus blurring the EC signal. In the spectrometer experiments, EC was only used as a mean to trigger the electrodissolution reaction.

The evolution of a typical Ag NP spectrum is shown in Fig.2.13. The electrode is polarized at time $t = 0$, which is accompanied by a drastic change in the spectral shape, probably due to loss of the plasmonic coupling between the Ag NP and the gold film. This is interpreted as the formation of a thick non-plasmonic AgSCN material. Indeed, due to the non-metallic properties of AgSCN, the plasmonic coupling with the Au film is no longer expected, thus explaining the disappearance of the two peaks spectra.

By integrating the full spectra for each successive measurement, we recover the typical optical intensity response with time, as obtained in the holographic experiments. The observed timescales, lower than 1s for electron injection and $\approx 4-8s$ for total dissolution time, are in perfect agreement with the dissolution and electrochemical peaks observed in the previous holographic experiments.

These observations are compellingly supportive of our interpretation: when contact with the electrode is established, an electrochemical first step forms a low solubility intermediate, which is not fully soluble and dissolves with a longer characteristic time.

2.4.3   Quantitative Analysis of the dissolution rates

The oxidation reaction is expected to form an intermediate of very little solubility. If the kinetics of complex formation reactions is assumed to be fast, local equilibrium should be attained before diffusion has a chance to homogenize the solution. The particles dissolution will then be controlled by diffusion of soluble species away from the solid material.

This problem is very similar to the electrochemical dissolution (for example $M \rightarrow M^+$) of nanoparticles in the diffusion-limited regime [186]. In this simple case, the rate will be controlled by the diffusion of M^+ away from the electrode.

In our case, the problem is a slightly more complicated due to the presence of a complex chemical equilibrium controlling the concentration of M^+ at the electrode surface. Instead of considering the solubility of one species, one needs to take into consideration all soluble species. If diffusional properties of all soluble species are similar, one can simply consider the sum of them all as M^+. Writing generically a chemical symbol for the concentration of all soluble species at the surface as $[Ag_T^+](= [Ag^+] + [AgSCN_{aq}] + [Ag(SCN)_{2\,(aq)}^+] + [Ag(SCN)_{3\,(aq)}^{2+}] + Ag(SCN)_{4\,(aq)}^{3+})$, one has [186]:

$$\frac{dn_{Ag_T^+}}{dt} = -\frac{\rho}{M}\frac{dV_{NP}}{dt} = 4\pi D[Ag_T^+]r(t)ln2$$

Where ρ, M and V_{NP} are respectively the Ag NP density, molar mass and volume. Insoluble AgSCN is assumed to form only at the surface, in a way that its contribution for the silver physical properties is negligible. Writing V_{NP} as a function of the particle radius, r_0, gives:

$$r(t) = \sqrt{r_0^2 - \frac{2MD[Ag_T^+]ln2}{\rho}t}$$

The total dissolution time τ_d is then obtained when $r(t) = 0$:

$$\tau_d = \frac{r_0^2\rho[Ag_T^+]}{2MDln2}$$

In order to evaluate $[Ag_T^+]$, we need to consider the full range of chemical reactions taking place in the complex equilibrium at stake. These can be expressed as [184]:

$$Ag_{aq}^+ + SCN_{aq}^- \rightarrow AgSCN_s \qquad\qquad K_s = 10^{-12}M^2$$
$$Ag_{aq}^+ + SCN_{aq}^- \rightleftarrows AgSCN_{aq} \qquad\qquad K_1 = 10^{4.7}M^{-1}$$
$$AgSCN_{aq} + SCN_{aq}^- \rightleftarrows Ag(SCN)_{2\,(aq)}^+ \qquad\qquad K_2 = 10^{3.5}M^{-1}$$
$$Ag(SCN)_{2\,(aq)}^+ + SCN_{aq}^- \rightleftarrows Ag(SCN)_{3\,(aq)}^{2+} \qquad\qquad K_3 = 10^{1.2}M^{-1}$$
$$Ag(SCN)_{3\,(aq)}^{2+} + SCN_{aq}^- \rightleftarrows Ag(SCN)_{4\,(aq)}^{3+} \qquad\qquad K_4 = 10^{0.2}M^{-1}$$
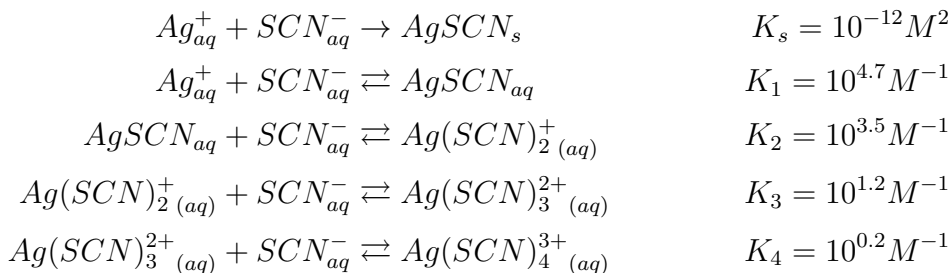
Using the definition of the solubility and complexation constants, we get:

$$[Ag_T^+] = \frac{K_s}{[SCN^-]} + K_sK_1 + K_sK_1K_2[SCN^-]+$$

$$K_sK_1K_2K_3[SCN^-]^2 + K_sK_1K_2K_3K_4[SCN^-]^3$$

This allow us to evaluate the dissolution time as a function of the thiocyanate concentration. Without any adjustable parameters, the resulting equation is in agreement with our observations, as shown in Fig.2.14. This is in precise agreement with the fact that the diffusion of soluble species away from the particle is the limiting step controlling the dissolution rate (and therefore the optical response) at low $[SCN]$. As $[SCN]$ is raised, the dissolution is accelerated and becomes comparable to the peak duration, at which point the oxidation probably becomes the rate determining step.
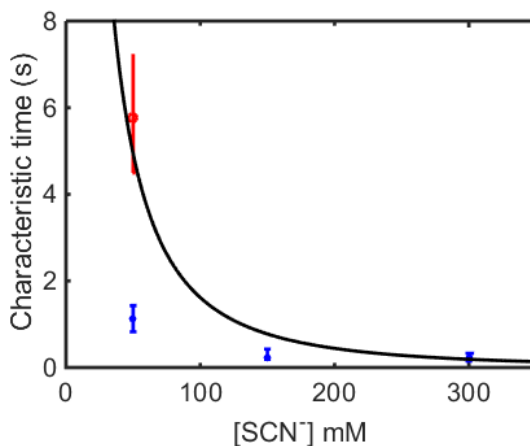
Figure 2.14: Dissolution time as a function of the thyocyanate concentration, $[SCN^-]$. The black solid line represents the calculated dissolution time as a function of $[SCN^-]$. Data in red are the optically evaluated dissolution rates, and the data in blue are the durations of the electrochemical impacts.

2.5   Conclusion

We have illustrated the coupling of electrochemical impact experiments with different optical techniques, using Ag NP electrodissolution reaction in a variety of media as an example. Besides validating the experimental coupling, we case-proved the utility of having access to both electrochemical and optical signals.

Under fast dissolution conditions - in the absence of precipitating anions - precipitation of Ag^+ is avoided and silver oxidation occurs at the same time as dissolution. In this simple case, both signals are completely equivalent and contain rigorously the same kind of information. This fact was put forth by comparing the two transient signals proportional to the variation of material - exchanged charge and scattering cross section - and noticing

the very good correlation between them. This allows us to conclude that both signals were indeed witnesses of the chemical reaction. Moreover, prolonged 3D tracking of the nanoparticles allowed MSD analysis, further characterizing the nanoparticles size and aggregation state. Moreover, superlocalization shed light on the dynamics of nanoparticle movement in the vicinity of the electrode, evidencing not expected residence times at the electrode surface.

Up to this point, however, the use of optics and electrochemistry was almost redundant - most information extracted from one technique could be retrieved from the other.

To highlight the full potential of the coupled approach we then increased the chemical complexity of the experiment by introducing ions that were able to form complexes and to limit the dissolution rate : SCN^-. In this case, we showed that the chemical and optical signals were complementary, as electrochemical impacts measured the total charge injected, and dissolution was monitored through the total scattered light.
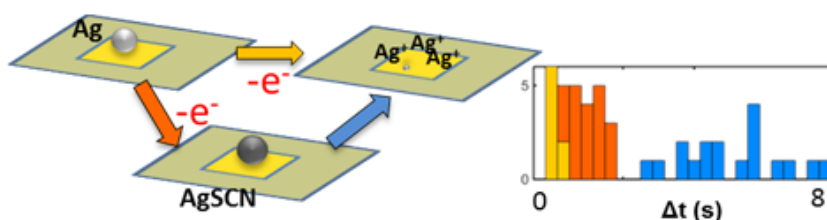
Figure 2.15: Sketch of the inspected reaction pathways and distribution of the duration of the probed events. In KNO_3, in yellow, Ag dissolution takes place directly, forming Ag^+. In the presence of 50mM KSCN, however, an intermediate AgSCN forms and uncouples the dissolution rate, monitored by optics (shown in blue), from the electron exchange step (in orange).

Spectroscopic experiments also allowed in situ determination of these phenomena - chemical transformation through a spectral transformation, dissolution from intensity decrease. This was done, however, at the expense of temporal resolution and could only be applied to slow reactions.

Finally, I would like to add that after the realization of our studies, many works quickly followed confirming most of our findings by the use of electronic systems with higher temporal resolution [187, 188, 189, 190]. This highlights the relevance of Ag NP oxidation as a flexible model system for electrochemical impacts experiments.

Even though Ag NP oxidation may be an overused example, the coupled use of nanoscale superresolution, plasmonic properties and nanoelectrochemistry allowed us to see better and further, identifying new phenomena.

Chapter 3

Individual Silver Nanoparticles Electrochemistry Part II: Transport and Aggregation

The present chapter includes data published in J. Am. Chem. Soc. [147], Nano Lett. [191], Farad. Disc.[149] and submitted to Chem. Sci. [192].

The previous chapter showed that the coupled electrochemistry optical monitoring of nanoparticles, can lead to a much less ambiguous characterization of chemical reactions in the nanoscale. The present chapter takes this strategy one step beyond, exploring the ability to resolve and track individual objects to evaluate and characterize more complex phenomena, such as particle transport, growth and aggregation.

We start by showing how the previously described setups can be used to directly observe NP aggregation. These measurements are then confirmed and complemented by probing the aggregate hydrodynamic size (by single particle tracking) and reactivity through evolution of its spectrum.

Then, the study is taken further ahead by introducing a new system, with smaller particles prone to stable agglomeration forming of supracrystals. This opens up the way to study directed movement of nanoparticle ensembles from individual particles trajectories. The physical origin of the phoretic movement can be multiple, and two experimental examples are provided: thermo- and diffusiophoresis.

The last part of the chapter is dedicated to an electrochemical way of synthesizing nanoparticles, and to how the ability of observing them together with Monte Carlo simulations and MSD analysis can be used to design strategies to characterize growth in situ and on a particle-by-particle basis.

Understanding the principles of particle transport is extremely important. To cite a few examples, it dictates parameters to be taken into account in sensors [193], helps predict

reactivity kinetics in the case of nanoparticles at low concentration, allows controlled electrode modification [183], and analytical quantification of NP concentration through impact frequency [21, 44, 194].

This chapter unveils the potential of optics to shed light on complex transport and reactivity situations, showing how to monitor events that electrochemistry can only probe indirectly.

3.1   Aggregation of Silver Particles : Two Particles
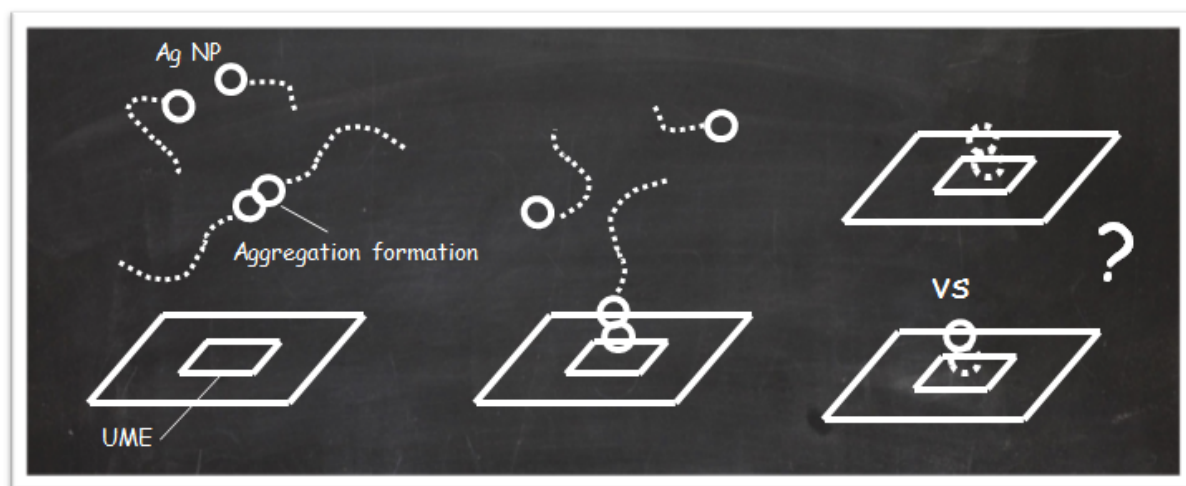
⟹ **Key Experiment Conception (#2):**

- Observe aggregate formation via holography and visible spectroscopy

- Monitor their reactivity when they impact a polarized electrode

- Observe wheter the whole aggregate oxidates at once or if the reaction happens stepwise

As mentioned in Ch.2, when in a solvent of high ionic strength (which is very often the case in electrochemical systems, due to the presence of the electrolyte), particles are prone to aggregation when they approach each other. According to DLVO theory [179, 180], this happens because the stronger the ionic force of the electrolyte is, the more it will screen out the effect of repulsive surface charges, favoring aggregation.

The reactivity of nanoparticles can be greatly impaired by the aggregation state of the colloidal solution. Moreover, since the impact technique is often used as an analytical tool to quantify particle concentration [38] and size nanoparticles, it is crucial to understand the role of aggregation on the transient current impact of a reactive nanoparticle[24, 28].

Using the ability to track particles movement in 3D, we were able not only to track events happening at the electrode surface, but also to monitor aggregation events taking

place in the solution. Further confirmation and reaction details can then be obtained by tracking the reactivity of the aggregate when it hits a polarized electrode.

3.1.1 Holographic follow up of an aggregation

While most in-situ techniques only allow indirect evidence of the aggregation of nanoparticles, holography allows direct monitoring of aggregation events. The setup described in Sec.2.1 was used to follow the Brownian motion of 50nm Ag NP in a NP suspension diluted down to 0.12pM (in number of particles) together with 50mM KNO_3. In the presence of salt, the repulsive double layer becomes thin, reducing its capacity to avoid particle aggregation. Interparticle collision therefore will very likely lead to the formation of aggregates. Although the collision of two particles is a rare event in a dilute NP solution, we were able to observe one such event directly, as shown in Fig.3.1A. Since even after the aggregation, the particles are small compared to the diffraction limit, they are seen by the CCD as a single bright (diffraction-limited) spot. While their size increase cannot be directly probed using the intensity of optical scattering, which is too sensitive to e.g. illumination inhomogeneities, it can still be probed via MSD analysis.

Indeed, tracking of the trajectory after the aggregation revealed a diffusion coefficient significantly smaller than that of a single 50nm Ag NP ($3.1\mu m^2/s$ vs $4.8\mu m^2/s$), which is consistent with an apparent hydrodynamic radius of 70nm. This radius strongly suggests that the tracked object is a NP dimer aggregate.

The particle is tracked until it hits the surface of a polarized gold UME ($E = 0.6V$ vs AgQRE). The optical intensity at the landing position is compared to the electrochemical response in Fig.3.1C. The EC impact indicates only partial oxidation of the aggregate, as the corresponding charge (obtained by integration of the electrochemical peak), indicates oxidation of a 50nm radius particle, i.e., a single Ag NP. This observation is further supported by the optical trace, that indicates that some material still remains over the electrode surface. The EC peak corresponds to a decrease of the optical intensity by a factor of ≈ 2.

These results point towards a stepwise reaction of aggregates in nitrate medium. In the next section we extend the observations to the presence of thiocyanate. In this medium, as shown in Ch.2, the reaction rate can be tuned, and thus slowed down, allowing spectroscopical monitoring of the reaction intermediates.

3.1.2 Spectroscopic evidence

This holographic monitoring of electrochemical impacts supports the idea that, at least in a nitrate medium, aggregates do not behave as bigger particles, but more like electrically isolated independent particles, mechanically held together but with a poor electronic connection.
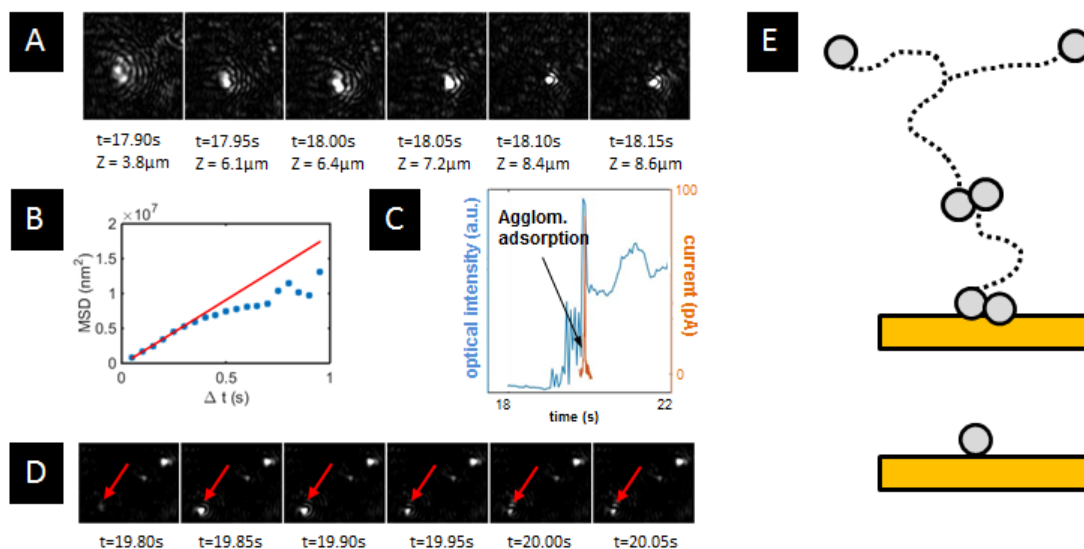
Figure 3.1: Direct observation of the formation of an agglomerate. (A) Timelapse showing the moment when two particles collide forming a single (diffraction limited) aggregate. Each image represents an area of $8.86 \times 9.84\mu$ m^2. (B) MSD analysis of the aggregate trajectory, revealing an apparent hydrodynamical radius of 70nm, compatible with an Ag NP dimer. (C) reactivity of the dimer upon collision with a polarized UME, showing both the optical response and the electrochemical spike resulting from the oxidation of one NP of the dimer. (D) Monitoring of the electrode surface showing arrival of the dimer and partial oxidation. Each image represents an area of $7.04 \times 6.88\mu m^2$. The complete sequence of events is sketched in (E).

This is shown to be true in other media as well. For example, in the presence of 50mM KSCN, a similar behavior was observed while monitoring the particle spectra. The experiment is similar to the one described in Sec.2.4.2: an Au microelectrode set up in a microfluidic cell is poised at a potential oxidant enough (0.6V vs AgQRE) to ensure fast Ag oxidation kinetics, so that the reaction rate is limited by mass transport. The intensity of the light scattered by particles on the electrode surface is monitored using a dark field condenser mounted over an inverted microscope equipped with a 60x objective (NA = 0.7) (See Fig.2.11).

While in Sec.2.4.2 the reactivity of single particles arriving at the electrode was monitored, we now monitor the arrival of aggregated nanoparticles. The aggregate size remains smaller than the diffraction limit, therefore we cannot distinguish the difference between agglomerates and single particles from the image alone. However, by recording the spectrum of a diffraction limited entity, agglomerates can be easily identified due to the following two reasons:

First, according to Mie theory, agglomerates are expected to scatter much more light than single particles. If the intensities of the scattered light of all the particles laying on the surface of the electrode are compared (see Fig. 3.2), we identify two different families, with a ratio slightly larger than 2 between their scattering intensities. These two populations are respectively attributed to single particles and dimers.
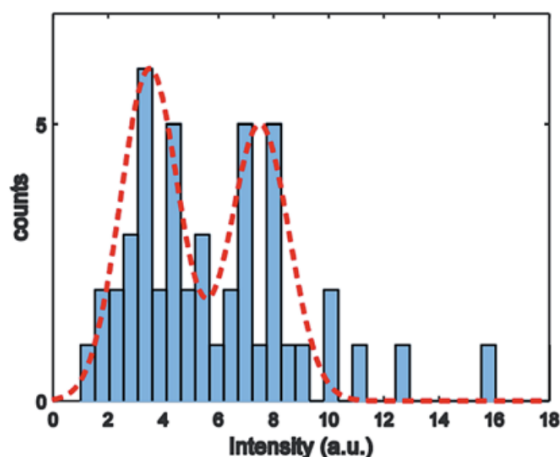
Figure 3.2: Scattered light intensity distribution for particles on the electrode surface. Based on Mie Theory and on the spectra shape, the first population, peaking at around 3 a.u., is assigned to single particles, while the second population, peaking at around 8 a.u., is assigned to agglomerates of single particles.

Second, the shape of agglomerate spectra is radically different from the spectra of a single particles. This can also be understood in terms of the plasmon hybridization diagrams such as the one shown in Fig.2.12: while for a single particle only the interaction of the particle with the electrode must be considered, the problem becomes much more complicated when extra particles are introduced. Indeed, with two particles, we must consider the interaction of the LSPRs of the two particles, convoluted with the interactions of each particle and the Au layer surface plasmon polariton (SPP). Given the spectral resolution of our equipment, these effects should manifest as a radical broadening of the LSPR peaks, which we indeed observe, as shown in Fig.3.3.

Again, just like in Sec.2.4.2, the spectrometer only monitors one small part of the electrode (one line). It is unlikely that the particle/aggregate would land on the monitored region over the course of the experiment. Instead, we wait until enough particles adsorb on the surface ($\approx$ 10min) before optimally positioning the spectrometer and poising the electrode.

One representative example is analyzed in Fig.3.3. Polarization of the electrode is accompanied ($E = 0.6$V vs AgQRE) by a drastic spectral change. As expected, at first the spectrum is very broad, convoluted, looking nothing like the ones shown in Fig.2.12. After polarization of the electrode, a drastic change of spectral shape is observed (characteristic time < 1s), followed by a gradual decrease in the scattered intensity, over 3-4s. At around 5s, the process repeats, with a violent spectral change, followed by slow intensity decrease. This behavior was reproduced by all the observed agglomerates (N=5). Finally, after the two oxidation events, the particle spectrum looks like the spectrum of a single particle. It is unclear why the single particle remains stable , but it is possible that the oxidation of the first particles leaves behind some residual material, possibly very insulating. This
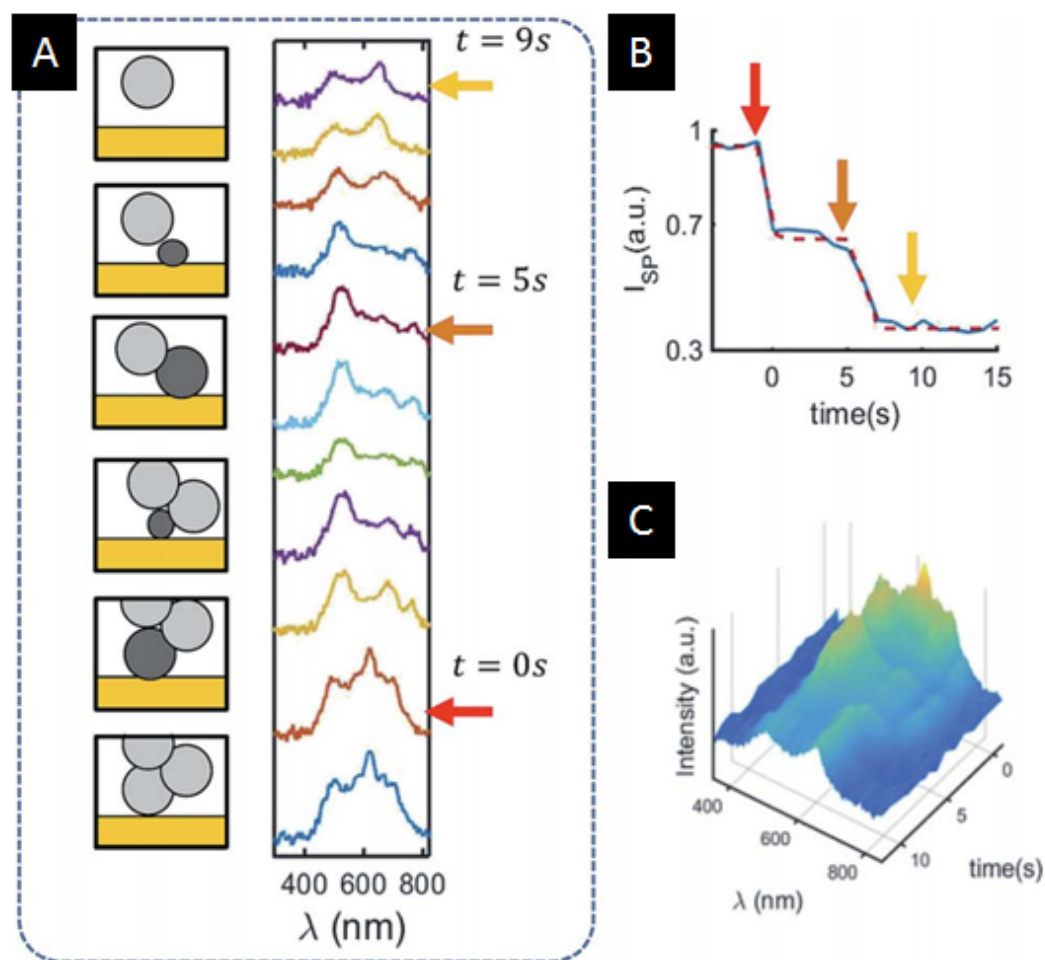
Figure 3.3: Spectroscopic monitoring of NP agglomerate. (A) Scheme illustrating a possible scenario explaining the spectra evolution shown ($f_{sampling} = 1Hz$), the red arrow (t=0) indicates electrode polarization. (B) Intensity profile, obtained by integrating the spectra, showing stepwise oxidation(t=0, then t=5s) of the agglomerate. (C) 3D profile illustrating the temporal evolution of the spectra.

locally passivates the electrode, changing the potential experienced by the single particle due to ohmic loss.

This is very indicative of an agglomerate that does not behave electrochemically as an unique entity. Instead, the oxidation of the agglomerate in the KSCN medium also takes place on a *one-particle-at-a-time* basis.

3.1.3 Conclusion: How does aggregation affect reactivity

In conclusion, we were able to show two examples of media (50mM KNO3 and KSCN) in which 50nm Ag NP aggregates do not behave electrochemically as bigger particles of equivalent volume. In these cases, the agglomeration state of the solution cannot be directly evaluated via impact experiments, as it does not seem to lead to a complete oxidation, and thus incomplete striping, probably due to poor electrical contact between

the nanoparticles.

These results are in apparent contradiction with some literature results, where the aggregation state of a colloidal silver NP solution was characterized through impact experiments (and shown in Fig.1.4D [36, 38]). The conclusions however are in fact compatible, as the detection of one peak vs multiple peaks is highly dependent on the temporal resolution of the measurements and particle size. Electrochemical distinction between single and multiple impacts depends on whether the time between two impacts is bigger or smaller than the temporal resolution of the electrochemical instrumentation [189, 190, 188, 187].

This idea is better illustrated with an example: Suppose that a particle dimer arrives at the electrode, and that each one reacts separately. Once the first particle has reacted, the second one is already in the vicinity of the electrode, and is likely to find its way towards the electrode much faster than a bulk particle. Based purely on diffusion, the characteristic time between impacts therefore varies as $\approx r_{NP}^2/D$. An increase on particle size of 5x (the difference between our experiments and the one from ref.[36, 38]), would then lead to a characteristic time 125x bigger, which is likely to become larger than the acquisition frequency, and thus detected as a single event. This diffusion only argument could explain the discrepancies observed. Noteworthy, with an acquisition rate fast enough, even single particles oxidation events can be decomposed into multiple peaks, as shown in many papers which followed the publication of our results [187, 189].

Therefore, caution must be taken when using impacts experiments as analytical tool to determine NP concentration from the impact frequency, and experiments should be designed carefully bearing in mind the aforementioned time scales.

3.2   Controlling the NP aggregation via its surface chemistry : Laser-assisted formation of Supracrystals
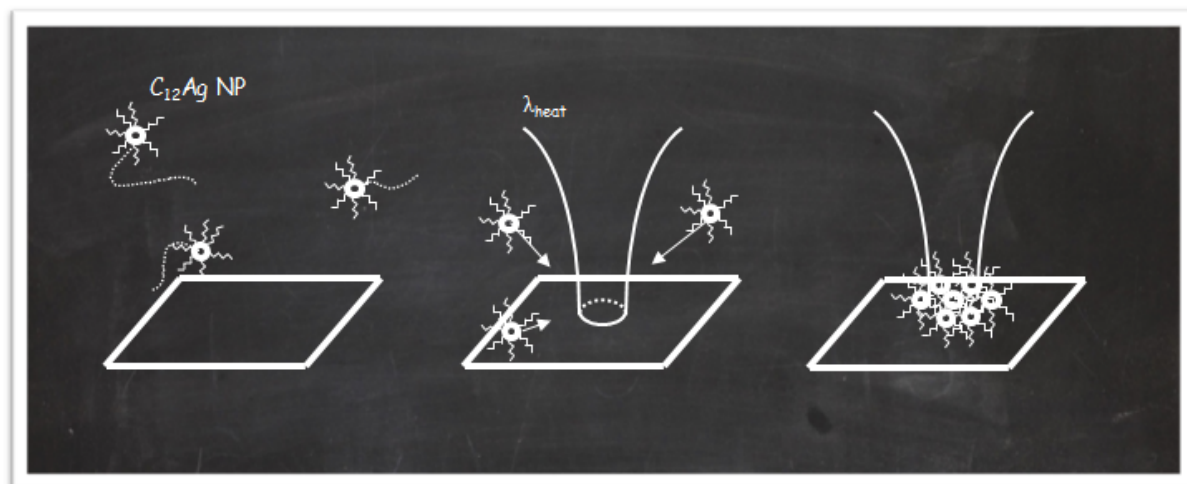
> ⟹ **Key Experiment Conception (#3):**
>
> - Observe nanoaggregates movement in 3D via holography
>
> - Generate a temperature gradient using a high power laser
>
> - Analyze the resulting migration and aggregation dynamics through the aggregates trajectories

As it was seen in the last section, aggregation can impact chemical reactivity in unexpected manners. This notion is taken further ahead in this section.

The surface of Ag NPs is modified with capping agents made of protective groups that trigger particular interactions leading to particle agglomeration in *a priori* chemically-controlled and organized way. Small nanoparticles have a tendency to aggregate due to attractive particle-particle Van Der Waals interactions[195]. In order to tailor particle interactions, a layer of thiol terminated C_{12} alkyl chains is added to the particle surface, which introduce repulsive steric interactions controlling aggregation. Chain-chain Van der Waals forces stabilize interactions once the aggregation is formed. The force balance is a compromise between these tunable attractive and repulsive forces, which can be controlled via particle size, material and chain length.

If particle size is very homogeneous, the agglomerates naturally organize in crystalline structures, called supracrystals [196]. As a consequence of the interaction of each particle's LSPR, aggregation might lead to strong increases of the local electric field, generating hotspots which can be very interesting for a number of analytical applications, such as surface enhanced sensing techniques [197, 198].

Since extensive levels of agglomeration are expected, it is unpractical to work with the (relatively big) $r = 50nm$ AgNPs, as the aggregation would lead to sedimentation of the
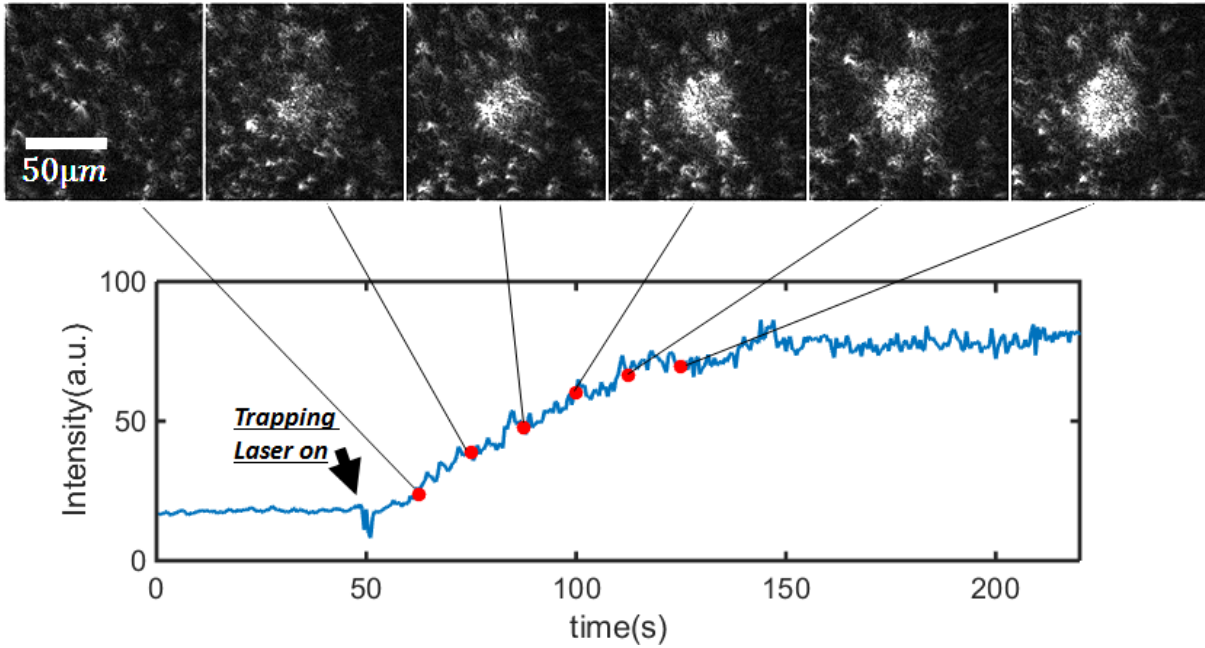
Figure 3.4: Laser assisted formation of an aggregate. Application of a laser can have a strong influence on the particles motion, driving them towards the laser beam spot and forming an aggregate of final size $\approx 50\mu m$. The trapping laser is turned on at $t = 50s$, as indicated by the arrow.

aggregates on the bottom of the cell. Instead, smaller particles ($r = 3nm$) with narrow size distribution ($< 8\%$) are used.

These changes drastically impact the dynamics and the scaling of the optical monitoring of the particle dynamics. Owing to their reduced size (smaller with respect to the particles used in Ch.2 by a factor $3/50 \approx 1/16$), these particles are much more susceptible to Brownian forces, moving $\sqrt{16}(= 4)$ times faster than the AgNP used in the previous section. Moreover, according to Mie's theory, they scatter $16^6 (\approx 1.6 \times 10^7)$ times less light, therefore precluding single NP direct detection in dynamical conditions. Instead, we can only detect agglomerates of particles after they aggregate, forming nanoaggregates, noted NAgg from now on. With the current limitations of our setup sensitivity, we are only able to observe the aggregates once they reach a critical size (of the order of 50nm). Assuming a CFC arrangement of the NPs in a supracrystal[195], this corresponds to an agglomerate of ≈ 1600 NPs.

Moreover the changes in surface chemistry and particle size also make the system susceptible to unexpected interactions. For instance, our first attempts to passively observe spontaneous aggregation formation using the holographic setup shown in Ch.2 revealed that the laser could have a definitive influence on the particles movement, generating a trapping effect: a micrometer large aggregate of smaller entities (NPs or NAggs) is formed upon laser excitation. The effect is illustrated in Fig.3.4. This section describes our efforts to observe, characterize and understand this trapping effect.

In order to study the particles movement, we need to trigger the effect in a controlled

way. For this a new holographic setup is introduced, using two lasers (one for observing the system and another to trigger the effect). The phoretic movement of the particles is then analyzed through a multiscale holographic approach. It is shown that by putting together ensemble and single-object analysis, we are able to characterize the phenomenon quite completely, thus enlightening the physico-chemical origins of the trapping.

3.2.1 Two lasers Setup

The two-laser setup is shown in Fig.3.5. It consists in two coexisting laser systems. The first one, a near infrared (NIR) low-power off-resonance laser ($\lambda_{obs} = 785nm$) was used to monitor the 3D motion of nano aggregates with a holographic configuration similar to the one described in Ch.2. The NIR laser beam is divided in two branches by a beam splitter, called the *object* and *reference* beams.

The sample is illuminated with the object beam through a prism in total Internal Reflection mode. This configuration allows rejection of the incident light, therefore collecting only the light scattered by the particles. This light is then sent to interfere with the reference beam, yielding an interference pattern that is recorded by a CCD camera. The hologram is then numerically reconstructed, forming a 3D image. Whenever large scale experiments were performed, we used a low magnification objective (x20, NA = 0.45), while for small scale experiments, a much more sensitive high magnification objective (x100, NA = 0.92) was employed.

The second beam, a high power laser (up to 2W) in the visible range ($\lambda_{trap} = 532nm$), is used to induce NAgg movement and trap the particles. This laser beam is oriented perpendicularly to the sample (normal incidence) by using a dichroic mirror, and is focused in the middle of the fluidic cell containing the nanoparticle solution (the sample) by the same objective used for observation. A telescope is used to control the size of the laser beam in the pupil of the objective, thus modulating the size of the laser spot on the focal plane (also called the waist) of the beam. Starting from a 2.5mm laser beam width, we decrease it by a factor 3.5. Taking into account the 10mm objective pupil, we thus have $d_{beam}/d_{pupil} = 14$, leading to a final beam waist of $w_h \approx 10\mu m$.

In spite of a large difference in laser power (with respect to the observation laser), the trapping laser does not impair our ability to observe the particles, since a long pass filter ($\lambda > 700nm$) is inserted before the CCD camera, to reject 532 nm light, as shown in Fig.3.5.

3.2.2 Nanoparticle building block synthesis

Monodisperse silver nanoparticles coated with dodecanethiol chains ($C_{12}AgNP$) were synthesized by our collaborators Pierre Aubertin and Lionel Chapus from Alexa Courty's group in Pierre and Marie Curie University (UPMC), following an improved version of
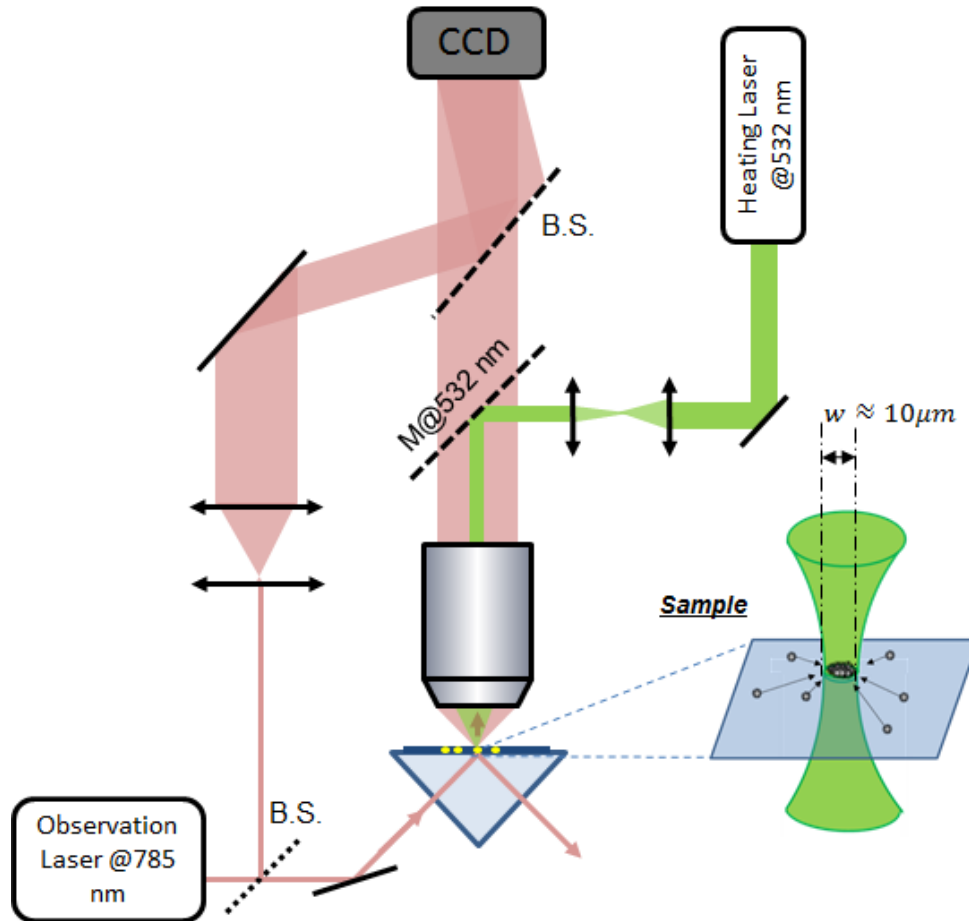
Figure 3.5: Two lasers setup used to independently observe and perturb the nanoparticles motion. The observation beam, at a wavelength near Infrared ($\lambda_{obs} = 785nm$) forms an holographic monitoring setup, while the excitation beam ($\lambda_{trap} = 532nm$) is focused on the sample and filtered from the CCD (M@532nm) thus creating a thermal gradient without saturating the camera or interfering with the observation beam. A telescope is used to control the excitation spot size and intensity. The inset shows the sample size, indicating the width of the heating beam ($\approx 10\mu m$)
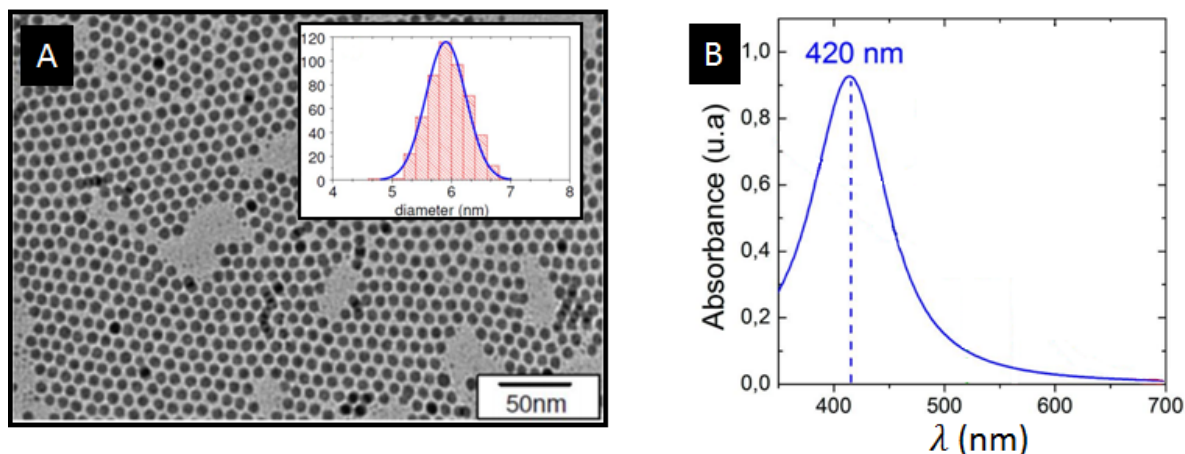
Figure 3.6: (A) TEM image of Dodecanethiol coated AgNp right after the synthesis procedure. Analysis of the TEM image yields the size distribution shown in the inset. The mean particle diameter is 5.9 nm with 8% polydispersity. (B) Vis Spectra of the $C_{12}AgNP$ dispersed in hexane (blue).Taken from Pierre Aubertin's PhD Thesis[202].

Stucky's procedure [199, 200]. This method yields spherical nanoparticles of diameters 4-7 nm with polydispersivity as low as $\leq 8\%$ [199, 200].

In short, the silver precursor, a $NO_3Ag(PPh_3)$ salt, is dissolved in ortho-dichlorobenzene (oDCB) in an inert atmosphere (N_2) and heated to 160^oC. An excess of dodecanethiol is then added under stirring, prior to the addition of tertbutylamine borane (TBAB), which will act as a reducing agent. After 60 min the reaction is stopped by cooling down the solution and the particles are precipitated by addition of ethanol [199]. A selective precipitation process [201] leads to a population of nanoparticles with a narrow size distribution (polydispersivity $\leq 8\%$), which are redispersed in hexane.This is characterized on dry samples by TEM images (shown in Fig.3.6A), and in solution by UV-Vis spectroscopy: according to Mie's Theory, 3nm radius AgNP should present a LSPR in the visible range, around 400nm.

The presence of thiols on the particle surface modify the spectrum by a decreasing its intensity and a redshifting the plasmon resonance position[201]. These effects are due to the combined effects of (i) a change of electronic density on the metal surface, and (ii) to a local change on the dielectric environment of the particles. The resulting UV-Vis spectrum is shown in Fig.3.6B.

3.2.3   Laser Assisted Supracrystal Formation

As mentioned in the beginning of the section, our first attempts to passively observe by holography the formation of the supracrystals were frustrated by the fact that the NAgg motion is dominated by the motion triggered by the laser. An experiment was then designed to analyze the laser triggered trapping effect in a more controlled way. In general terms, it consisted in passively observe the nanoparticles (using the low power NIR laser),

in the presence and absence of the excitation laser and later analyze their trajectories.

Sample Preparation

After the NPs are synthesized, they are dispersed and diluted in a mixture of 60:40 toluene-hexane, down to a concentration in nanoparticles of 0.44nM. This mixture of solvents is designed to be a compromise between limiting NP aggregation (toluene) and solubilization (hexane). If the solvent is too good (solvent-chain interaction $\gg$ chain-chain interaction), it solvates the C_{12} chains completely, making a stable colloidal solution which would difficultly lead to the formation of supracrystals. Indeed, UV-Vis spectrum of a colloidal solution of the Ag NPs in hexane shows a plasmon band at 420 nm, as expected for thiol-modified 5nm AgNPs [201]. On the other hand, if a very poor solvent is used, one can hardly disperse the particles in solution, as they easily aggregate and quickly precipitate. Prior Environmental TEM studies [195] have shown that in 60% toluene, supracrystals of radius of order 100-300 nm spontaneously form in solution. Since in this size range the NAgg can still be kept in suspension by Brownian forces, this composition range was picked on the experiments. Unless otherwise specified, the results herein shown are performed for 60% toluene, but the same range of phenomena takes place with 40% toluene, and (to a much lower extent) in pure toluene too.

Microfluidic cells similar to the ones previously described (See Fig.2.4) were produced using a layer of Teflon film ($\approx 500\mu m$ thick) as a spacer and Epoxy-based resin (TorrSeal) to seal the cell. These changes with respect to our previous cell concept were necessary since the hexane-toluene mixture is able to dissolve the parafilm spacer, causing leakage and subsequent evaporation. After assemblage, the cell is filled with the solution and ultrasonicated for $\approx$ 5 s, to disperse the NPs as well as possible without damaging them. Finally, the cell is placed in the two-laser holographic setup and the experiment is started.

Trapping Experiment

At first the trapping beam is off, and the system is passively observed using the low-power NIR laser ($\lambda_{obs} = 780nm$, $P = 90mW$). At this point, we only see a few NAggs moving randomly, describing a Brownian motion.

As the trapping laser is turned on, a radical change of behavior operates: the NP movement goes from Brownian to directional, towards the laser spot position. The movement of a few NAggs is tracked using ImarisTrack software, revealing quasi-linear trajectories (N = 66). A number of tracked trajectories in 3D is shown in Fig.3.7 and in 2D in Fig.3.8. The tracking analysis is limited to a region of interest, which excludes the area directly heated by the laser.

In Fig.3.8, the transition between regimes can be appreciated in detail. The average particles velocity is measured before and after the laser is turned on, as shown in the histogram included as inset of the figure. While the laser is off, the particles behave as
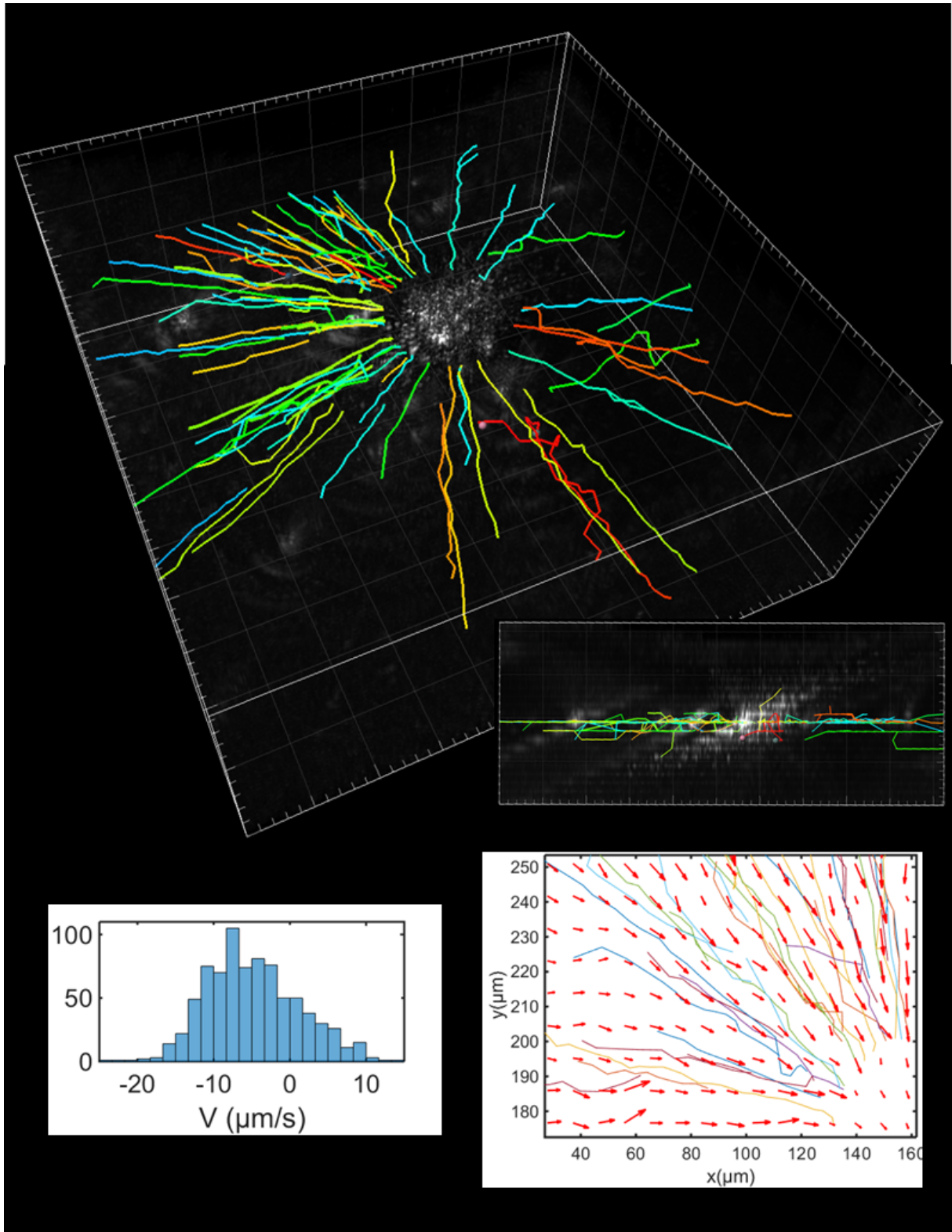
Figure 3.7: Tracking of the NAgg trajectories under a radial temperature gradient. The movement is mainly situated on the sample plane, as shown in the top inset, containing a side-view of the trajectories. The monitored volume is $250 \times 250 \times 2000 \mu m^3$. Tracking of the NAggs position allowed mapping of the drift velocity (shown in the inset on bottom right), and measuring its magnitude (bottom left).
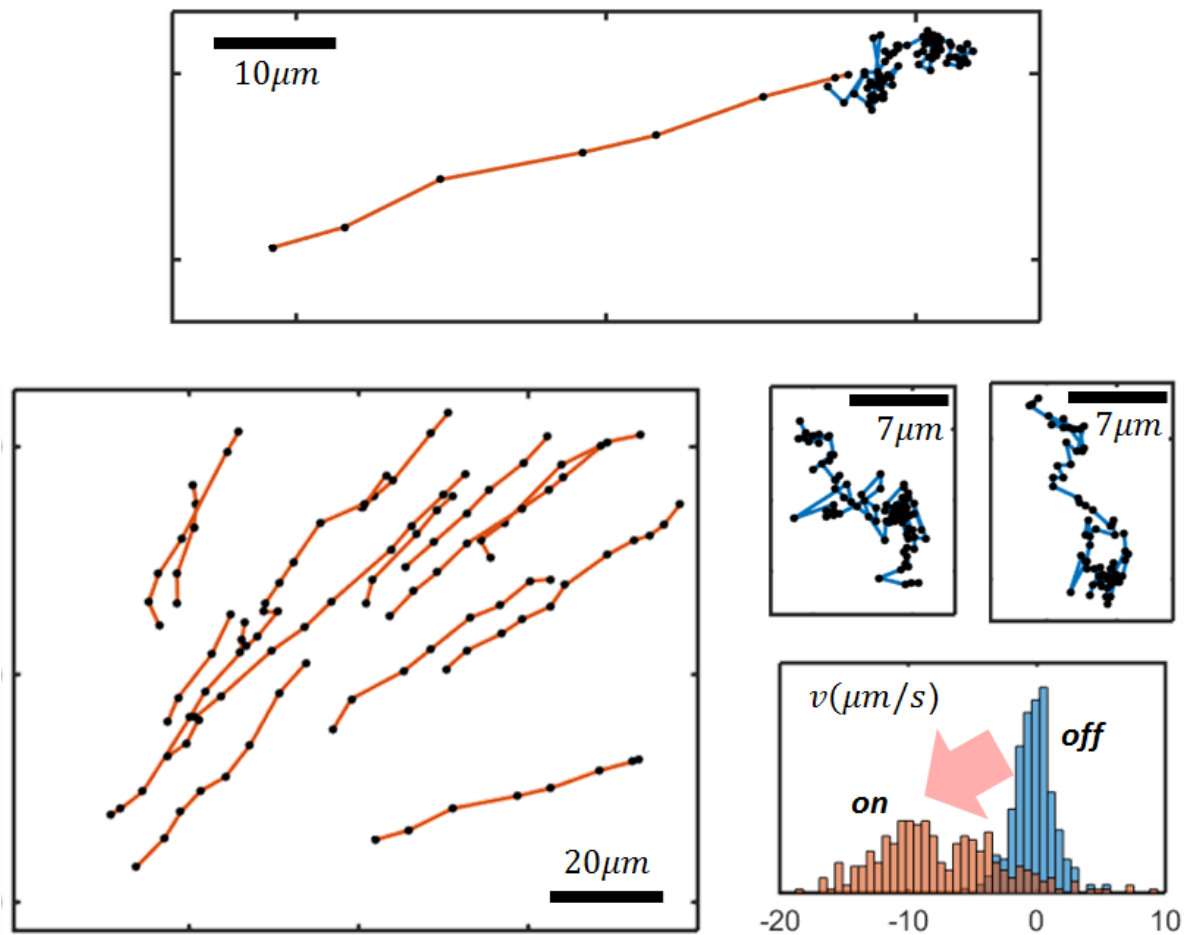
Figure 3.8: Transition from Brownian motion to Directional movement. The particles motion undergoes a violent change when the trapping laser is switched on. Before, they move by diffusion, describing a Brownian Motion (shown in blue), after, their movement becomes directional, with an average velocity of $10\mu m/s$ (orange).

Brownian walkers, with no preferred direction, and therefore $\langle v \rangle = 0$. Once the laser is turned on, the particles start to move towards the laser beam, with an average velocity $v \approx 10\mu m/s$. v is obtained by measuring the time derivative of the radial distance from the center of the trapping laser (hence the negative sign on the histograms).

In order to understand the physico-chemical origin of the trapping effect, it needs to be studied and characterized on different scales. For this reason, the analysis of these results will be then divided in two parts. First, the large scale dynamics of the phoretic phenomenon is analyzed using the aforementioned low magnification objective lens (x20, NA = 0.45). In particular this will be useful to measure the order of magnitude of the migration effect and estimate a velocity field profile. Unfortunately, not much can be said about the z movement of the particles, since the PSFs become distorted under this low magnification - one can only say that all the planes are monitored simultaneously.

Then, a high magnification objective (x100, NA = 0.92) is used to zoom in, allowing analysis at a smaller scale. These high magnification images will be used to provide a better estimate of the velocity drift, v, and determine particle size r_p on a *one-object-at-a-time* basis, therefore enlightening the influence of particle size on the drift velocity.

3.2.4   Large Scale dynamics: Characterizing the trapping forces

The first instants of the experiment, while excitation laser is still off and the particle still moves due to Brownian motion, allow estimation of the diffusion coefficient via MSD analysis. This procedure reveals a very broad and sparse distribution of the NAgg's apparent hydrodynamical radius, R_p, between 300 and 700nm.

We can use the measured values of the diffusion coefficient and drift velocity to characterize the motion transition quantitatively. The idea is to compare the time it would take for a particle to cross a given distance by diffusion ($\tau_D \approx L^2/D$) and the time it would take to cover the same distance ballistically $\tau_v = L/v$. This ratio is called the Peclet number (Pe) and characterizes *(for a given characteristic distance L)* how the movement of the NAgg is perceived.

$$Pe = \frac{\tau_D}{\tau_v} = \frac{Lv}{D}$$

Large Pe indicates that the particle will move almost deterministically, while small Pe indicates a diffusive movement. In the present experiment (Figs. 3.8 and 3.7), two characteristic length scales exist, and therefore two Peclet numbers can be defined.

The first one characterizes the magnitude of the trapping forces with respect to diffusion, considering the migration effects over distances of the order of half field of view. In this case, the large length scales involved ($L \approx 100\mu m$) and the measured average drift velocity ($10\mu m/s$, see Fig.3.7) reveal a dramatic change in the Peclet number, which goes from $Pe \approx 0$ to $Pe \approx 100 \times 10/0.5 = 1000$. This tells us that once the trapping laser is

on, stochastic effects can be safely neglected.

The second Peclet number (Pe_{DL}) is controlled by the spatial resolution of the experiment and measures the ability to notice diffusional effects during the experiment. For simplicity, the diffraction limit is taken as the spatial resolution of the experiment. This is really a best case scenario, as more often the spatial resolution is limited by the diffusion distances during the exposition time (for us, $\tau_{exp} = 10ms$, then $L_{DL} = \sqrt{D\tau_{exp}}$). If $L_{DL} = \lambda/2NA \approx 0.8\mu m$, we end up with $Pe_{DL} = v\lambda/(NA \times 2D) \approx 28$, which translates the fact that once the trapping laser is turned on, the particles enter a regime purely deterministic, i.e. stochastic effects cannot be measured.

The drift velocity is then measured over a large number of particles, revealing the order of magnitude of the excitation effect (See histogram in Fig.3.7).

Force Magnitude: For instance, v can be used to compute the force acting on the Naggs. Indeed, since Brownian forces can be neglected, we can directly apply Stokes law to evaluate the magnitude of the force needed to drag the NAggs at the measured velocity. Using the typical values of $r_0 = 300nm$ and $v = 10\mu m/s$:

$$F_{th} = 6\pi\eta_f r_0 v \approx 50 \ fN$$

We thus obtain an order of magnitude of the effect, which will be essential to determine the physical origin of the effect.

Force Direction: As far as the velocity direction is concerned, the particles seem to follow radial pathways, directed towards the trapping laser. This can be seen in the right inset of Fig.3.7, where all the velocity estimations were used to derive an average velocity field profile. Moreover, it seems that the velocity vectors are all contained on the xy plane, indicating that the movement is actually bi dimensional.

These large scale measurements provide an important global characterization of the migration phenomena. In contrast, the next section will use detailed high resolution observations to provide information on the process on a single NAgg basis.

3.2.5 Small Scale Dynamics: Measuring D and v NAgg by NAgg

By imaging the NAggs movement with higher magnification (Objective 100x, NA = 0.92) information on smaller characteristic scales can be assessed, and therefore become much more sensitive to diffusive effects. This can be seen by evaluating the Pe_{DL}. Since the sensitivity of the monitoring now allows detection of smaller NAgg ($\approx 100nm$ corresponding to $D = 5\mu m^2/s$), we now have $Pe_{DL} \approx 0.8$, which means that the diffusive effects are no longer negligible and may be measured.

We can thus hope to determine NAgg size via MSD analysis, therefore obtaining the size and velocity of each NAgg. Since the NAggs movement is a mixture between
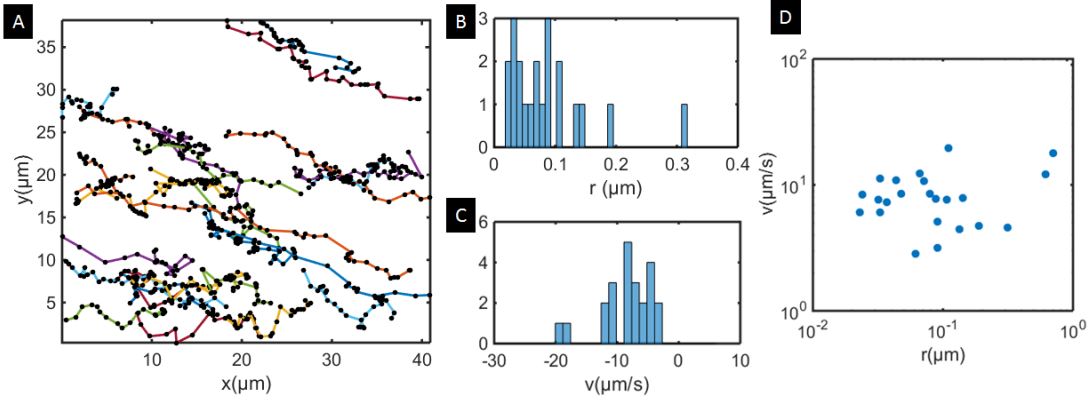
Figure 3.9: Small scale behavior images with x100 magnification. (A) Trajectories of small NAggs subjected to the laser-triggered directed movement. At this scale, diffusive effects are detectable during the particle trajectory, thus allowing single NAgg measurements of (B) the NAgg hydrodynamical radius, r, and (C) velocity v. (D) Comparison of r and v show no clear correlation.

diffusional and directional motion, the trajectories cannot be directly analyzed by MSD analysis as before (as in Ch.2). Instead, their movement needs to be seen as a random variable which can be decomposed in a deterministic and a stochastic component:

$$X(t) = B(t) + vt$$

The deterministic part vt, often called the drift, is assumed to be constant (or to vary very slowly on the timescale of the experiment). Since the stochastic part of the movement $(B(t))$ is a Brownian motion with zero mean, taking the average of consecutive frames allows access to the drift. By excluding the drift from the total movement, we measure $B(t)$, the Brownian part of $X(t)$. We can then estimate the particles size by applying MSD analysis on the drift-corrected movement. Similar results are obtained through a totally analogous procedure, consisting in fitting the MSD curve by a quadratic function of the form:

$$MSD = \langle X(t)X^*(t) \rangle = \langle B(t)B^*(t) \rangle + 2\langle B(t) \rangle vt + v^2 t^2$$
$$= 6Dt + v^2 t^2$$

The results of this analysis are shown in Fig.3.9. The lack of correlation between v and r indicated that the particle size does not seem to influence the velocity. Moreover, examination of the z component of the drift velocity ($v_z = 0.5 \pm 2.5 \mu m/s$) confirms our large-scale observations that the movement seems contained in the xy plane.
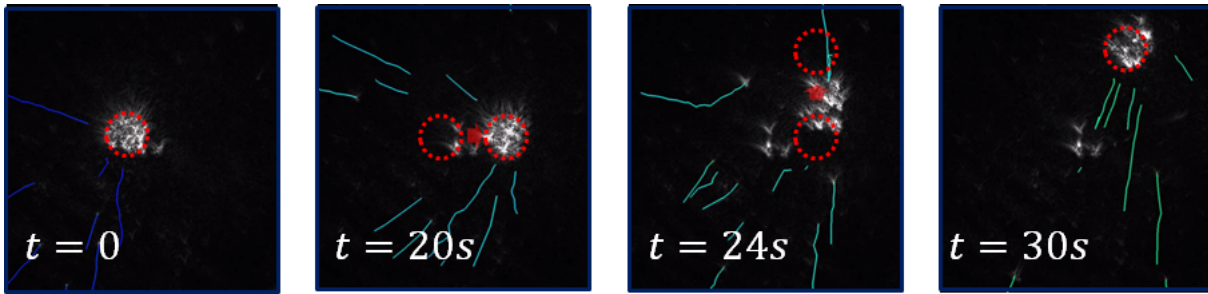
Figure 3.10: Manipulation of the agglomerate by reallocating the laser spot, and therefore by redesign of the temperature field. Starting from a formed aggregate at $t = 0$, the trapping laser position is changed at $t = 10$ and $20s$. The stable positions are shown in (A), (B) and (D), while (C) was included as an intermediate between pictures (B), and (D), where the aggregate is still moving. The trajectories of small NAggs not yet part of the aggregate are also shown to respond rapidly to a change in the laser position. Indeed, the trajectory tails represent the particle tracking over the past 10 frames (5s).

3.2.6 Manipulating the Crystal

The formed aggregate is not static and can be moved reliably, as shown in Fig.3.10. Indeed, if the laser position is changed over the course of the experiment, the full formed aggregate follows the laser to its new position. This is interesting because it allows dynamical manipulation of the plasmonic support.

Noteworthy, the particle migration profile was also strongly subjected to the position of the trapping laser, and showed quite a rapid response to changes in the temperature distribution profile. Indeed, if the heating laser was moved over the course of the experiment, the particle movement adapted almost immediately, as shown in Fig.3.10. Between the 2nd and the 3rd images, the laser is moved, and a particle initially moving towards the first position (visible on the top left, highlighted by the green dashed line), suddenly switches directions, and moves to the new position.

Having thoroughly characterized the NAgg's motion, we are now in position to discuss the phyical and chemical origins of the observed trapping phenomena.

3.2.7 Gravitational Forces (or why does the particles motion seems 2D?)

The 3D monitoring provided by holography shows large and small scale evidence that the particles motion is restricted to a plan ($v_z \approx 0$) and roughly independent of the exact z position where the laser is focalized. Moreover, even if some convection may be present (owing to the large cell height), the aggregate seems immune to its effects.

To explain why the aggregate seems to be confined to the glass slide vicinity, we perform a sedimentation analysis, aiming at determining at which size an agglomerate becomes prone to gravitational forces and sedimentation. As our instrumental setup only allows monitoring of relatively big NAggs ($> 30nm$), the diffusive component of the NAgg
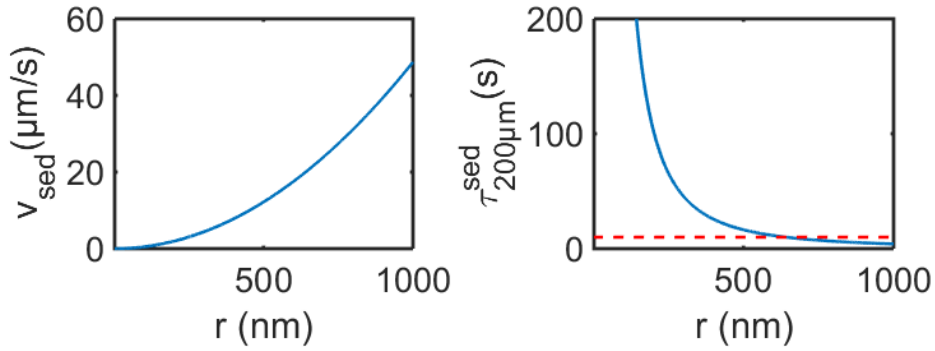
Figure 3.11: Sedimentation drift and characteristic times as a function of the aggregate size, as predicted from Stokes law. The dashed line, for reference, indicates 10s sedimentation time.

motion will be small over large time scales, and therefore the analysis can be limited to the high Peclet number case, the Stokes regime. Smaller particles are subjected to diffusion and advection and are likely carried away by convective flows.

For large particles, the sedimentation rate can be predicted from Stoke's law. Indeed, if Brownian forces can be neglected (high Peclet number), the gravitational force is balanced by the solution drag, which can be evaluated as a function of the particle radius (r), the solvent dynamic viscosity (η_f) and the drag velocity (v_{sed}):

$$F_d = 6\pi\eta_f r v_{sed}$$

Which leads to:

$$v_{sed} = \frac{(\rho_p - \rho_f) \; g \; r^2}{9\eta_f}$$

where ρ_f is the fluid density, g the acceleration of gravity, and ρ_p the NAgg density (taken as bulk Ag as a first order approximation). In our case, the solvent is a mixture of hexane and toluene, and its properties can be calculated assuming that the two solvents form an ideal mixture. This is indeed a good approximation since total solubility of hexane in toluene is observed. If the aggregate is formed at the focal point of the laser, say 200 μm away from the surface (a worst case scenario), the characteristic sedimentation time can easily be calculated, as shown in Fig.3.11

Manipulation of the crystals also shows that the interaction of the aggregate with the surface is not very strong. Indeed, if the laser is scanned laterally, the aggregate follows it, staying near the point of maximum intensity. Furthermore, if it encounters some defects (either fabrication imperfections or previously adsorbed NPs) on the glass surface, it only very weakly interacts with it (see Sec.3.2.6). This indicates that the aggregate is not chemisorbed, but only mildly physisorbed to the surface.

3.2.8 Optical forces and their role on the Trapping Mechanism

Optical forces are known to appear in the presence of a steep optical electro-magnetic (EM) gradient. Indeed, numerous works use optical gradients to trap and manipulate micro to nano object in a way similar to the one shown above. In fact, this is the principle behind optical tweezers [203, 204]. *Could optical forces then be reponsible for the trapping effect seen in our system?*

In this section we evaluate the magnitude of optical forces, showing that, although they may be involved in keeping the cohesion of the supracrystals once they are formed, they cannot explain the long-range forces observed.

We consider the trapping of particles smaller than the wavelength, on which the Rayleigh approximation is valid. The particles will be treated as a point-wise dipole. Although this is only the case for smaller particles (up to 300nm), we extend the limits of the methodology as an indicative of the magnitude of the forces involved. A finer calculation would include integration of the optical momentum flux, using the Maxwell stress tensor, but is beyond the point here. The interaction of the particle with the electro-magnetic field is evaluated from its polarizability, which can be calculated for a metallic nanoparticle of radius r as[204]:

$$\alpha = \frac{\alpha_0}{1 - \frac{ik^3\alpha_0}{6\pi\varepsilon}}$$

Where α_0 stands for the pointwise particle polarizability:

$$\alpha_0 = 4\pi\varepsilon_0 r^3 \frac{\varepsilon - 1}{\varepsilon - 2}$$

$k(= 2\pi/\lambda)$ is the wavenumber, ε is the relative permitivity of the medium, and ε_0 is the vaccuum dielectric permittivity. The (time averaged) force acting on a dipole is evaluated as [205]:

$$\langle F \rangle = \frac{1}{2} Re \left(\sum_{j=x,y,z} \alpha E_j \nabla E_j^* \right)$$

This force can be decomposed in contributions of the intensity gradient, a polarization gradient and a radiation pressure, but in our case only the intensity gradient force is of interest as it is directed towards the laser beam. It can be expressed as $\frac{1}{4} Re(\alpha)\nabla|E|^2$ and is shown for different particle sizes in Fig.3.12. In this calculation, it is assumed that a laser power of 16 mW is focalized on a diffraction-limited laser spot. The intensity gradient ($\nabla I = \frac{1}{2}\varepsilon_0 n_{Ag} c\nabla|E|^2$, with c being the speed of light on vacuum) is calculated as the difference between bulk field ($= 0$) and the average intensity density over the spot size. The calculation serves as a top limit for the forces acting on isolated particles.

In this calculation, we aim at evaluating a higher boundary for the optical forces acting
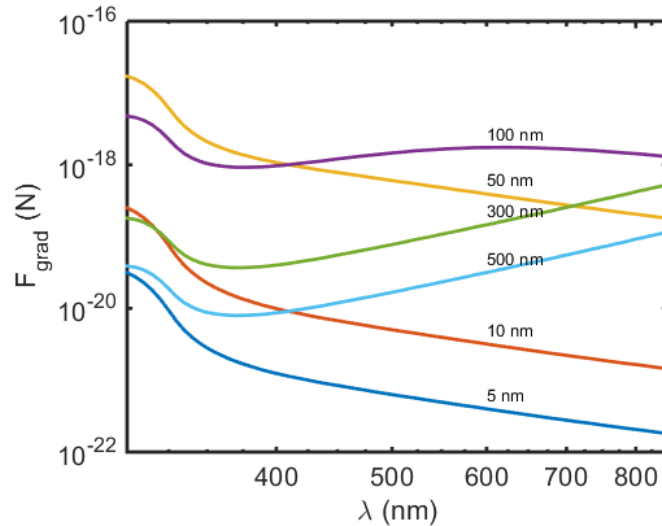
Figure 3.12: Calculated gradient force, based on silver properties, and assuming a perfectly focused laser beam for different particle sizes.

on a single particle. Optical forces are at least three orders of magnitude lower than the observed ones ($\approx 50 fN$). Together with the fact that the long-range optical gradients are much weaker than the ones assumed on the calculation, this constitutes a strong proof that optical forces are not the mechanism responsible by the phoretic movement. However, it cannot be ruled out that optical forces may enhance the cohesion of the formed supracrystal, as the hotspots resulting from the plasmonic interaction of the NPs could provide the extra intensity gradient. Indeed EM field enhancements of more than three orders of magnitude, concentrated over sub-wavelength regions are commonly reported in SERS substrates [80, 70].

3.2.9   Thermal Effects

So far, it was shown that the aggregates formation is mostly kept in the glass slide plane due to sedimentation effects, and that while optical forces might be responsible for keeping the aggregate together, they cannot explain the long-range forces acting on the particles.

   All the gathered evidence therefore points towards a mechanism of thermal origin. Indeed, small plasmonic nanoparticles are expected to absorb the electro-magnetic radiation, and heat as a consequence. The trapping laser would then serve as an energy source, heating the irradiated particles and consequently creating a temperature gradient. This could explain, for example, the long-range outreach of the effect and its fast response to the laser position. Indeed, if $L \approx 50 \mu m$ stands for the characteristic length of the source, the temperature gradient difference should extend to distances $\approx 5L \approx 250 \mu m$ (this is analogous to the depletion or diffusion zone around an UME in an electrochemical context). Moreover, the time required for heat to diffuse and establish a temperature gradient over $\approx 100 \mu m$ would be $\approx L^2 / \alpha_T^f (= 0.1s)$, where α_T^f is the thermal diffusivity

of the fluid. This is in agreement with our observations since the time lapse between two consecutive images would be sufficient for a thermal gradient to appear.

However, two thermal mechanisms can still explain the trapping effect: thermophoresis and free convection.

1. **Thermophoresis**, also called the Ludwig-Soret effect, is the movement of an analyte (particles, molecules) in response to a temperature difference. Thermophoresis in liquids is still a fervent debate in the literature, but it is more or less a consensus to describe the particles drift velocity as:

$$\vec{v_T} = -D_T \vec{\nabla} T$$

   where D_T is a proportionality constant with units homogeneous to $\mu m/sK$. D_T is sometimes called the thermal diffusion coefficient.

2. **Free Convection** (from now on, convection for short), is the advective movement of particles resulting from the motion of the fluid due to buoyancy forces created by a thermal gradient. Heat transfer from a hot source generates a difference of density of the fluid and thus fluid motion due to a force of order $\approx \Delta \rho_f g V$. g is the gravity acceleration, V is the characteristic volume of the affected zone, taken to be L^3 where L is the Aggregate size.

Different thermal profiles

In order to discriminate between the two mechanisms, we have designed an experiment in which an elliptical aggregate is formed. Further insight on the migration mechanism could be obtained if the phenomenon is analyzed in the presence of this less ordinary excitation. Thermophoretic movement is then expected to generate a drift velocity distribution following the temperature gradient, describing trajectories normal to iso-thermal lines. In a temperature field without radial symmetry, these paths should generate curved trajectories. Advective movement due to convection, on the other hand, should generate straight displacements in the xy plane, towards the hot spot.

This can be obtained, for example, by changing the excitation laser incidence angle from normal to an oblique angle, passing through a prism in a configuration similar to the object beam of the observation laser. Since the aggregate tends to form on the bottom of the sample, we get an elliptic excitation source, instead of cylindrical.

The tracked trajectories and measured velocity field are shown in Fig.3.13. Notice that the NAggs follow curved trajectories, apparently perpendicular to iso-temperature lines, as shown in Fig.3.13. This strongly supports the thermophoretic mechanism.

Thermal Analysis: The obtained velocity field suggests that particles follow the temperature gradient lines, in accordance with $\vec{v_T} = -D_T \vec{\nabla} T$.
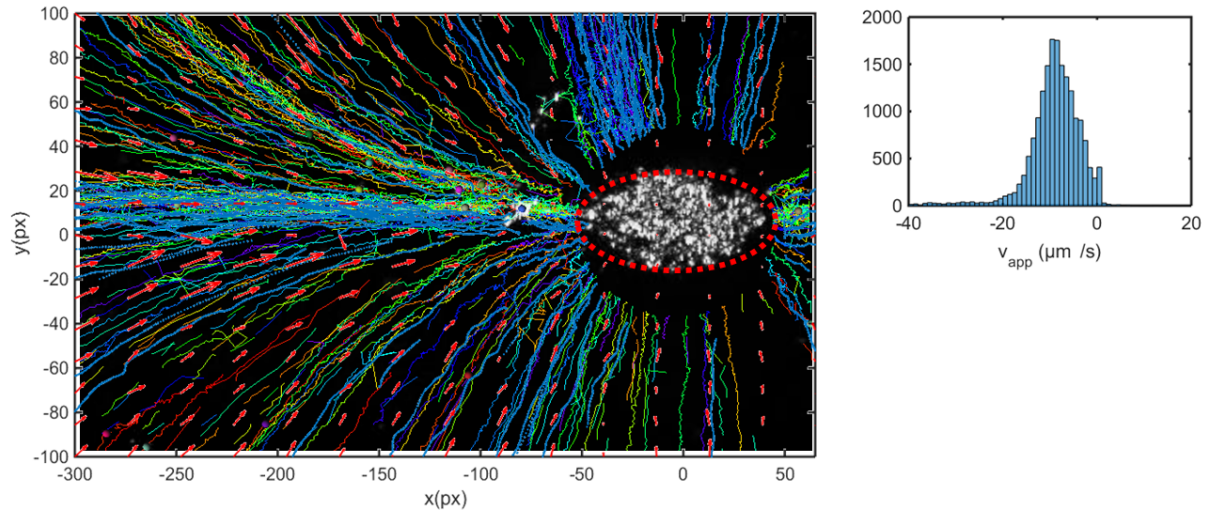
Figure 3.13: Particle Migration around an elliptical temperature field $f_s = 20$Hz.
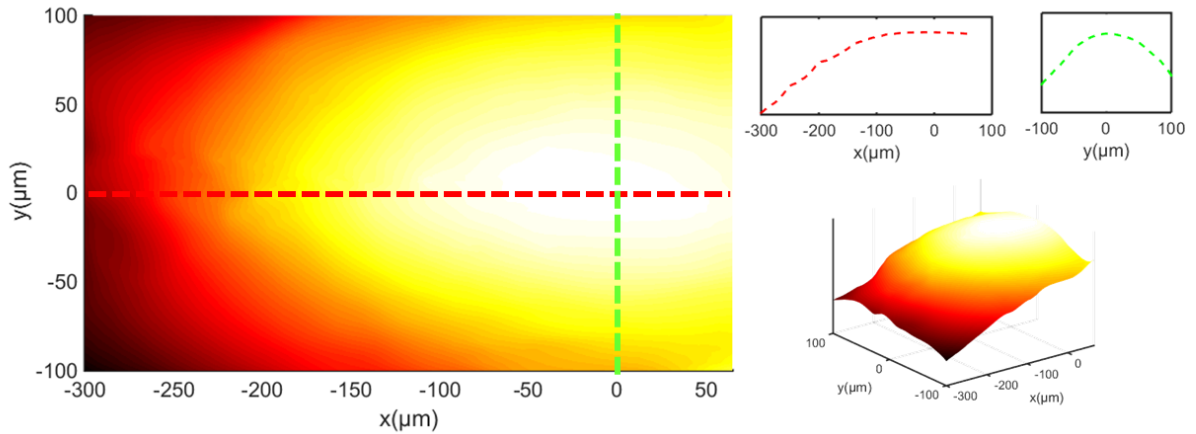
Figure 3.14: Integration of the velocity field around an elliptic field, revealing the shape of the temperature profile (in arbitrary units). The insets show two slices, as well as a 3D representation of the profile.

In this case, integration of v_t along the trajectories should be proportional to the temperature. By doing so, we may derive the form of the temperature profile. This is shown in Fig.3.14.

Convection: Orders of Magnitude

Owing to the thickness of our microfluidic cell (typically $\approx 500\mu m$, but experiments were successfully repeated with $100\mu m$ cells), convection cannot be ruled out *by design*. It is however unlikely that the observed movement is a result of convection, as it will be shown here.

In the first place, our holographic monitoring setup allows 3D imaging of the particles trajectories and no flux of particles in the z direction or outwards was detected. Moreover,

it would be hard to explain the curved trajectories of particles in the xy plane based purely on convection. Indeed, in the case of a convectional flux, the particles trajectories would go directly towards the zone where the densities differences are maximal,i.e. where z-component of the flux are maximal, giving rise to straight trajectories.

For very small particles however, direct observation is impossible and therefore advective movement still cannot be ruled out.

To help uncouple the effects of thermophoresis and convection, another experiment was conducted in the presence of a forced advection in the xy plane. Particles dissolved in toluene were used, as the NAggs size is usually limited in the presence of this solvent. Instead of sealing the microfluidic cell, a pressure gradient was created during solution injection.

When the light is enhanced, a small aggregate readily forms, while many small objects (probably saturated aggregates and/or impurities) keep being dragged by the advective flow in the xy direction. If aggregation was created by convection, the advective flow would be perturbed. The fact that little disturbance of the flow is observed favors a thermophoretic rather than convective mechanism.

Finally, it is also possible to rule out convection based on a dimensional analysis argument. Energy transport and the onset of fluid motion by natural convection are controlled by the Rayleigh number, Ra, a dimensionless number which describes the energy transfer from a heated object immersed in a cooler fluid. Ra is defined as:

$$Ra = \frac{g\beta_f \Delta T L^3 \rho_f}{\alpha_T^f \eta_f}$$

Where β_f is the fluid coefficient of thermal expansion, and L is the characteristic length scale of the thermal source, here taken as the aggregate size $\approx 50\mu m$. Evaluation of Ra for $\Delta T = 100K$ (again, a worst case scenario), then yields $Ra \approx 1$. This is insufficient for convective transport to be the dominant trapping mechanism, specially when one notice that the circulation around the aggregate would actually drag the particles away from the aggregate, instead of towards it [206].

Solvent Influence

Experiments were conducted in mixtures of hexane- toluene in different proportions. It is shown that the thermal responsivity of the material does not exist in pure hexane, as the particles remain dispersed in solution. Between 40-60% toluene, the supracrystals form readily when the heating laser is turned on, and present drift velocities between 5 and 10 μm/s, with little sensitivity on the particle size (at least to the limit of the sensitivity of the measurements) for a power of 200 mW. In the presence of pure toluene the particles show tendency to aggregate and many small aggregates are present from the beginning. The heating laser can still trigger some further aggregation, leading to steady saturation

of the phenomenon - likely due to particle depletion.

3.2.10   Mechanism Discussion

At this point, it seems clear that the particle movement cannot be generated by optical and plasmonic forces, or by convection, leaving thermophoresis as the most probable mechanism. As previously mentioned, thermophoresis in liquids, and specially in colloidal systems, is still a matter of debate in the literature.

In the simpler case of gases, no interparticle or fluid-particle interactions exist, therefore thermophoretic migration is a purely statistical phenomenon and it *always* presents a thermophobic behavior (following the direction hot $\rightarrow$ cold). Thermophoresis in liquid phases, in contrast, is subjected to a complex range of phenomena, including particle-particle interactions, solvent-particle interactions, concentration gradients, electric fields, etc. A richer array of phenomena can therefore be expected. For example, although in most cases the migration still occurs in the thermophobic direction, sometimes migration towards the hotter region (thermophilicity, also called negative thermophoresis) is also observed. For instance, for polymers in solution, bad-solvent conditions have been observed to generate negative thermophoresis [207, 208, 209].

Negative thermophoresis was also observed as a result of differential ionic migration, generating an electrical field, which could indirectly push the particles towards the colder regions [210, 211]. This mechanism is also unable to explain our results, as no salts are dissolved in the solvents - even if they were, the dielectric constant of the solvent is so weak that even soluble salts would hardly be dissociated.

For our system, all the evidences herein gathered - and especially the solvent dependency of the phenomenon - point towards a thermophoretic mechanism controlled by the interactions between solvents and the capping agent, the C_{12} chains, of the NPs.

In the literature, two possible chemical origins for thermophoresis have been proposed.

The first one is based on the dependency of Van der Waals interactions on the molecular density, which depends on temperature [212, 213, 214]. A gradient of temperature would then generate a gradient of forces on the solid-liquid interface, triggering flow and thus pushing the particle towards the cold side of the gradient. This mechanism can only account for positive thermophoresis, unless the density decreases with increasing temperature, which only happens in rare cases (such as water below $4^{o}C$).

The second one is based on entropy considerations [209, 215] and could account for the results of our experiments. The number characterizing thermophoretic movement, the Soret number $S_T = D_T/D$, is suggested to follow the following relation (D being the diffusion coefficient and D_T being the proportionality factor between the drift and the temperature gradient, i.e. $v_T = -D_T \nabla T$) :

$$S_T = -\frac{S}{k_B T}$$

Where S is the total entropy of the system. This explanation was shown to fit correctly the thermophoretic behavior of DNA chains, by considering the solvation and ionic shielding entropy[215]. Noteworthy, this expression however is in the heart of an interesting debate on whether or not thermophoresis can be described in terms of local equilibrium processes [214, 216].

In polymer solutions, bad solvent conditions have also been shown to lead to negative Soret numbers (and thus to thermophility). Comparison with in solution polymer chain systems is indeed relevant, as the volume occupied by alkyl chains is very expressive, comparatively to the volume of the metallic part (assuming the alkyl chains are well solvated, the C_{12} volume is between 1.9 and 2.8 times bigger than the metallic core volume).

Although the exact chemical origin remains elusive, it seems clear that it involves the C_{12}-solvent interactions. It is worth highlighting that most literature studies aiming at enlightening the thermophoresis mechanism in nanoparticle systems were performed via ensemble measurements, and thus on radically different conditions from ours, in terms of particle density and timescales [212, 217, 218].

Single entity experiments are still rather sparse. This kind of experiment is interesting because they allow access to phenomena at different scales, therefore requiring different experimental analyses, and allowing alternative insights into the mechanism [209]. For example, the specific relation between particle size and thermophoretic mobility is still under debate in the literature [219, 220, 221, 222]. Our simultaneous measurement of particle size and drift velocity suggest that, in our experiment conditions, particle size has no influence on D_T, in agreement with [219].

3.2.11 Conclusion: All-in-one Thermoresponsive plasmonic substrates

In this section, we showed how the protective functional groups can be used to promote reversible and controlled aggregation, thus making organized ensembles of nanoparticles, supracrystals. Moreover, due to their high absorption cross section induced by their plasmonic properties, the particles absorb light upon irradiation and heat up, creating a temperature gradient. The C_{12} chains also introduce new transport mechanisms, as the solvent-C_{12} interactions dependency with the temperature generates migration towards the irradiated regions (higher temperature), therefore being an example of negative thermophoresis. These three conjugated effects provoke the formation of an aggregate of micrometric size. Although the role of optical forces is negligible when the particles are dispersed, their aggregation and interaction of their LSPR generates hot spots, which are likely to enhance the local intensity gradient, contributing for the aggregation cohesion.

Such hotspots also have the potential to make the aggregate SERS active. This system then becomes interesting as it may represent a step forward in the integration of SERS

substrates into existing technologies, such as microfluidic chips. Indeed, as the substrate is ephemerally formed, and therefore the potentially SERS substrate can be generated on demand, i.e. avoiding clogging the microchannels.

Finally, it should be highlighted that the mechanistic analysis herein performed was only possible due to the tracking of individual entities. Although some details on the mechanism still remain a bit elusive,the ability of following aggregates individually granted us many clues about the mechanism, notably those necessary to rule out purely convective and all-optical mechanisms.

3.3 Another Phoretic Phenomena: Diffusiophoresis
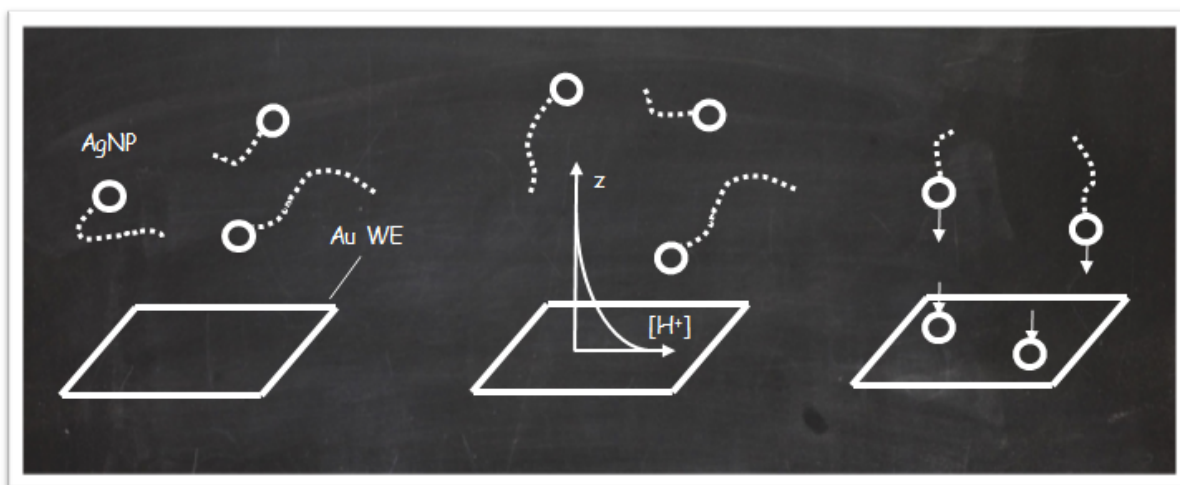
> $\implies$ **Key Experiment Conception (#4):**
>
> - Observe nanoparticles movement in 3D via holography
>
> - Generate a H^+ gradient through oxidation of the electrode
>
> - Observe the particle movement in response through MSD analysis and arrival frequency

Thermal gradients are not the only ones able to generate a force on particles and induce particle migration : for instance, a concentration of dissolved species is also capable of doing so. In this section, we show how single particle tracking and optical monitoring can allow a direct inspection of the frequency of particle arrival over an electrode. Enhancement on the arrival frequency, as well as particle tracking were used to reveal an unexpected migration mechanism, based on an electrogenerated proton concentration gradient.

3.3.1 Experiment Description

Electrochemical experiments often generate persisting concentration gradients. Under suitable migration conditions, these gradients can also generate an osmotic pression gradient, triggering nanoparticles migration, an osmo-phoretic mechanism called diffusiophoresis.

This can be seen by monitoring the arrival of 30 nm radius AgNP over gold electrodes. The setup used to monitor the NP movement in 3D is the same used in Sec.2.1, but a regular 50nm thick Au film was used as the electrode (large area, 7×7 mm^2).

Cyclic voltammetry is performed between 0 and 1V (vs Ag/AgCl), while the holographic setup presented in Ch.2 is used to monitor the particles position in 3D.
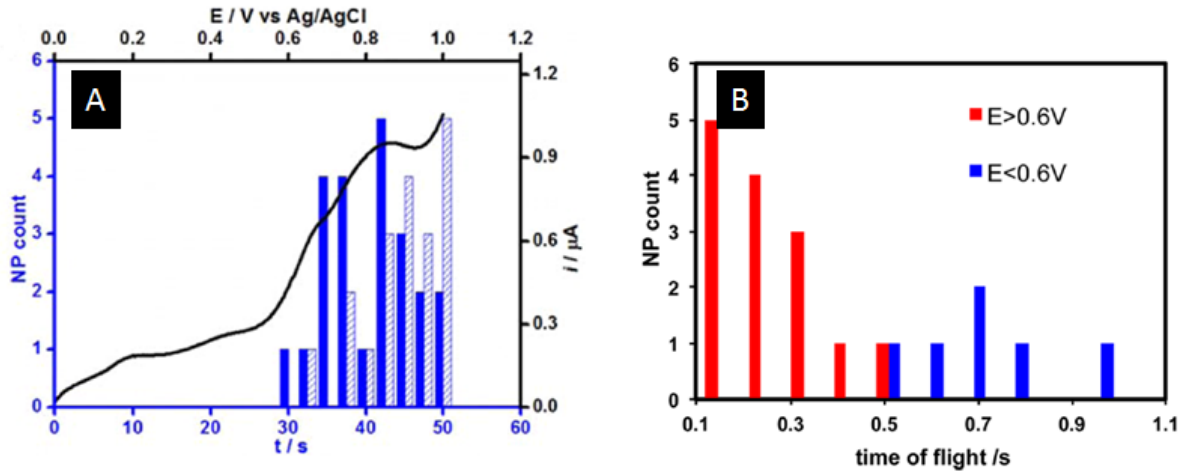
Figure 3.15: (A) Number of events of NPs adsorption onto (blue) or disappearance from (light blue) the electrode surface during a CV (forward scan shown as black line). (B) Distribution of time-of-flight of NPs in the depth of field of the optical observation during the CV. Here, the time-of-flight is defined as the time before the NP exits the depth of field (for E < 0.6 V) or adsorbs onto the electrode (for E > 0.6 V).

Starting from a potential of 0V (vs Ag/AgCl), the potential is slowly raised to 1V (scan rate = 10mV/s). As the potential is increased beyond 0.6V, the anodic current starts to increase, which is attributed to mild oxidation of the gold electrode, accordingly to:

$$2Au + 3H_2O \rightarrow Au_2O_3 + 6e^- + 6H^+$$
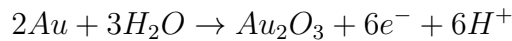
This creates a non uniform H^+ concentration profile. The concentration difference induces osmotic pressure differences, which is expected to generate NP drift (v_{diff}) of magnitude [223] :

$$v_{NP} = m_{NP}\frac{\partial ln[H^+]}{\partial z}$$

where m_{NP} is the particle mobility. By holography, one can detect particles once they enter a monitored volume (of about $50 \times 50 \times 10\mu m^2$). The time between the moment when a NP enters the volume and the moment it touches the electrode should depend sensibly on the existence of a drift, increasing by a factor equal to the Peclet Number ($=vL/D$), where the characteristic distance, L, corresponds to the monitored distance in the direction of the drift (z). This can be seen as a significant reduction of the time of flight, defined as the time the NP spends on the detection volume before it reaches either the electrode or the end of the monitored zone. This is shown in Fig.3.15B.

MSD Evidence for the existence of a drift The existence of the diffusiophoretic drift can be put forth by MSD analysis of the particle movement, as detailed in Sec.

A.4.1 of Ch.A, and mentioned in the previous section. A drift represents a deterministic component in the particle stochastic movement. The slope of the MSD curve is therefore increased by a factor $(vt)^2$. In the presence of migration, direct analysis of the MSD without correction leads to an overestimation of the diffusion coefficient, and therefore underestimation of the particle size.

Indeed, analysis of MSD curves in the presence and absence of concentration profile reveals a strong difference in apparent size. The smaller particle size observed is therefore an artifact associated to the fact that the particles movement is not purely Brownian, but in fact biased by the presence of a drift.

These observations are also corroborated by automatic tracking Nanosight microscopy measurements, as seen in Fig. 3.16A. Nanosight is a commercial microscope which allows tracking of single NPs in a plane (2D). Finally, finite-element COMSOL simulations were used to confirm the observed drift magnitude and activation potential, as shown in Fig.3.16B and C.

3.3.2   Conclusion: SPT in migration

In this small section we were able to study the migration of nanoparticles in response to a diffusion gradient, using a combination of electrochemical activation and individual particle tracking. Again the ability to track 3D movement of single NPs was essential to observe and quantify the migration mechanism. The analysis of MSD curves, in particular, was key in studying the phenomena. In the next section, these curves are considered with even more care, and used to quantify NP growth process.
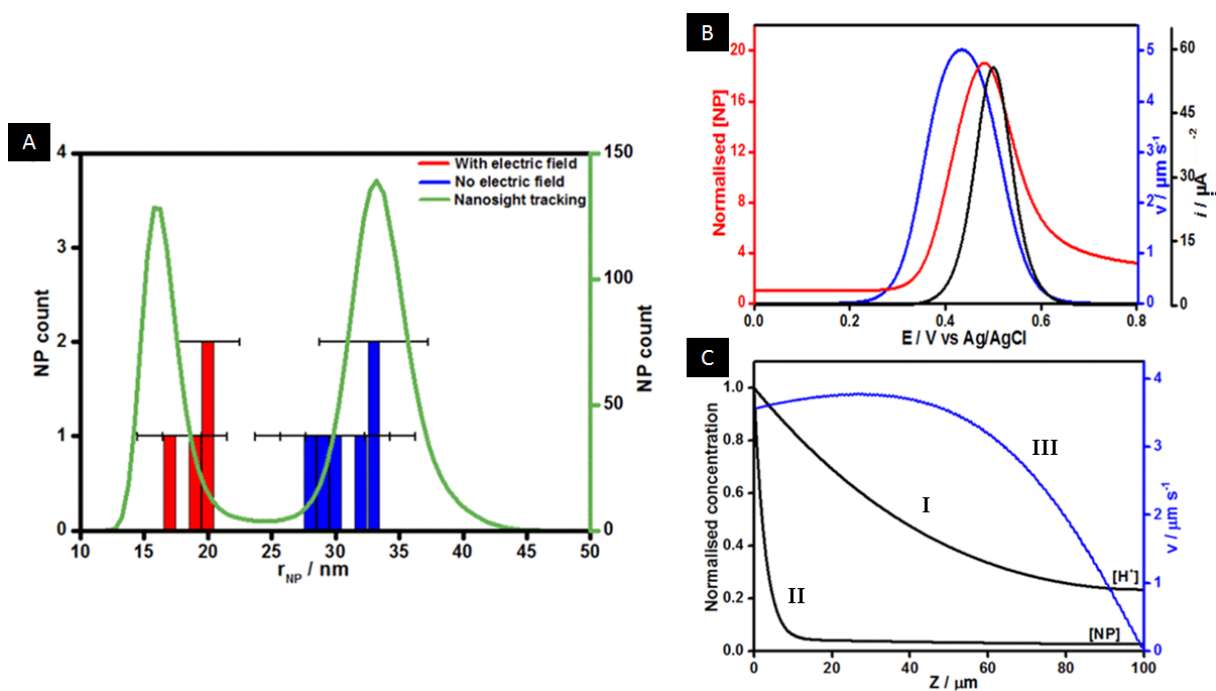
Figure 3.16: Evidences for osmotic drift. (A) Estimated *apparent* size distribution of Ag NPs tracked in the absence (blue) and in the presence (red) of electrochemical activation. Overlaid size distribution from NanoSight microscope performed at farther distance from the electrode (green) of 30 nm Ag NP solution while sweeping the electrode potential between 0.3 to 0.6 V. The smaller apparent size is artificial and reflects the presence of a bias (unaccounted for in the MSD analysis). (B) Simulated evolution profile of local NP concentration at an electrode generating diffusiophoresis for 30 nm radius NPs at the electrode surface with the electrode potential (red), with the theoretical CV (black) and the simulated fluid velocity profile in the channel due to diffusiophoresis (blue). (C) Simulated concentration profile along the normal to the electrode (electrode at z = 0) at the electrochemical peak potential of (I) electrogenerated H^+ due to Au oxidation (black), (II) subsequent NP concentration profile due to electrogenerated H^+ (black), and (III) velocity profile of Ag NPs in solution (blue).

3.4 Monitoring Particle Growth through Single particle Tracking
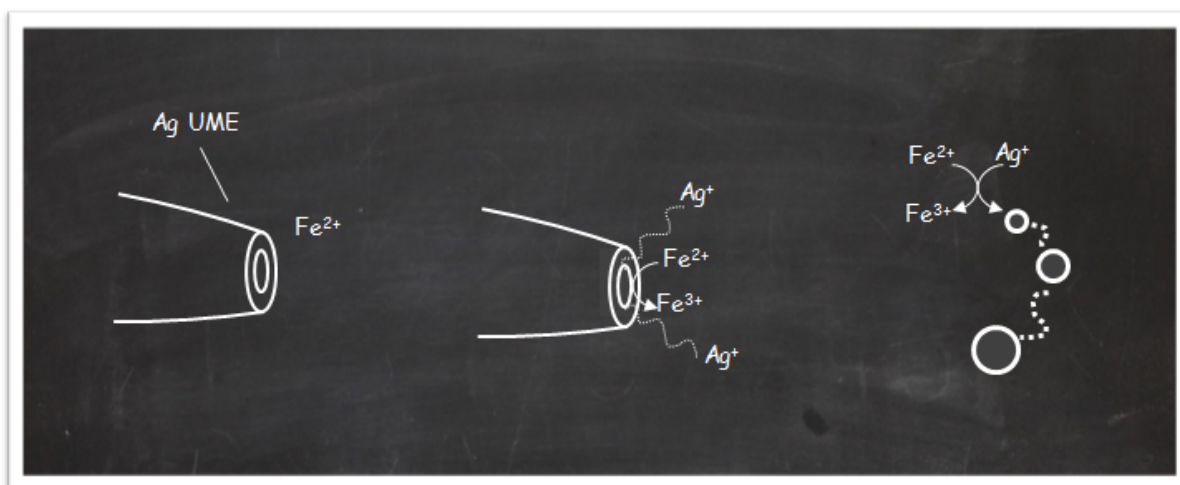
> ⟹ **Key Experiment Conception (#5):**
>
> - Electrochemically trigger NP synthesis in solution
>
> - Track the NPs motion
>
> - Analyze their size and growth through a combination of optical monitoring and MSD analysis

In the past two sections, MSD analysis was used to identify and quantify particle drift, putting forth migration mechanisms. In this section we take the strategy one step forward. NPs are synthesized using Ag UMEs as a sacrificial source of metallic ions, in the presence of a reducer. The appearance and growth of the nanoparticles is monitored optically in situ by using a dark field condenser. Single particle tracking and MSD analysis are then used to analyze growth and assess kinetic parameters.

3.4.1 Electrosynthesis Principle

The principle of the electrosynthesis strategy is to locally generate Ag^+ ions in a Fe^{2+} solution, thus provoking the following reaction:

$$Ag^+ + Fe^{2+} \rightarrow Ag^0 + Fe^{3+}$$
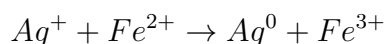
The reaction is possible since $E^0_{Fe^{2+}/Fe^{3+}}(= 0.77\text{V vs NHE}) < E^0_{Ag^+/Ag^0}(= 0.80\text{V vs NHE})$, therefore the chemical reaction is thermodynamically favored. To generate the Ag^+ ions, a metallic Ag electrode is polarized at a potential sufficiently positive to allow the electrodissolution of Ag: $Ag \rightarrow Ag^+ + e^-$. Since the Fe^{2+}/Fe^{3+} potential is less positive, the electrode region is locally depleted in Fe^{2+} ions, avoiding direct reduction of Ag^+ too close
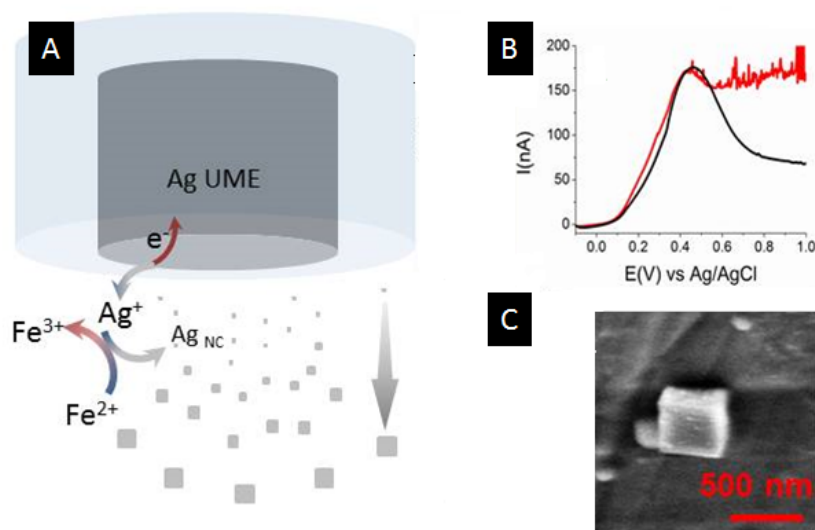
Figure 3.17: (A) AgNP Electrosynthesis Principle. (B) LSV recorded at the AgUME in the presence (red) and absence (black) of 50mM Fe^{2+}. (C) SEM image of a resulting cubic AgNP.

to the electrode surface. The principle is sketched in Fig.3.17A. A typical linear sweep voltammogram (LSV) is shown in Fig.3.17B, recorded at the AgUME in the presence and absence of 50mM Fe^{2+}.

Without Fe^{2+},we only see an oxidation peak at 0.5V (vs. Ag/AgCl) corresponding to the $Ag \rightarrow Ag^+$ oxidation. At high potentials, the surface probably becomes passivated by formation of oxides Ag_2O, which explains why we record a peak and not a diffusion-limited plateau, as expected for an UME.

If Fe^{2+} is present, a noisy plateau-like feature appears after the peak, suggesting that the oxidation of Fe^{2+} is kinetically hindered. Optical Dark Field (DF) monitoring of the electrode apex and the surrounding solution reveals that at this potential a large number of nanoparticles start to nucleate and grow from solution. It is shown then that the reduction of Ag^+ ions therefore happens in solution, at a certain distance from the electrode ($10 - 20\mu$m), controlled by the potential and the bulk concentration of Fe^{2+} ions. Besides the potential and $[Fe^{2+}]$, the CV scan rate (or pulse length, if a fixed potential is applied) can be used to modulate the size and number of NPs. For example, in the presence of 1mM Fe^{2+} and 50mM KPF_6 (as supporting electrolyte), particles of $r \approx 100nm$ are generated.

Tracking of the NP trajectories allows in-situ estimation of their sizes, through MSD analysis. Extensive particle tracking is performed in order to get good quality statistics. This process was aided by ImarisTrack module of the Imaris software. The results were then visually inspected and manually filtered. The resulting 255 tracked trajectories are shown in Fig.3.19B. The trajectory lengths ranged from 50 to 325 time steps (number of steps distribution can be seen in Fig.3.19C).

The result of the tracking of a large number of particles (N=255) is shown in the
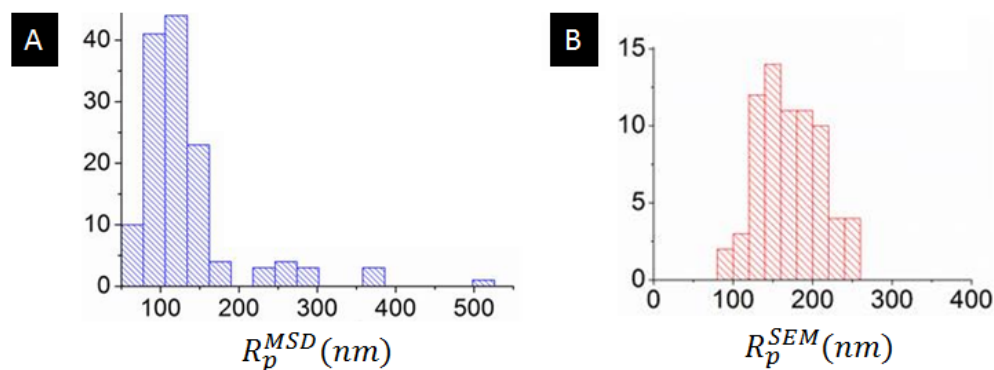
Figure 3.18: Size distribution after posing the AgUME for 10s at E = 0.7V in the presence of 1mM Fe^{2+} and 50mM KPF_6, determined by (A) MSD analysis of 255 trajectories and (B) Ex-situ size determination by SEM. The difference in size suggests particle growth.

histogram in Fig.3.18. Since the particles eventually diffuse and adsorb to the electrode surface, it is also possible to size them by imaging the electrodes ex-situ with SEM (an example is given in Fig.3.17). If the MSD- and SEM-determined size histograms are compared, we notice that the particles look bigger by SEM imaging, as shown in Fig.3.18. While classical MSD analysis probes the average particle size, the (ex-situ) SEM measures NP size at the end of experiment, therefore this difference could indicate particle growth. Moreover, the particles seem to change color during the experiment, going from blue to orange. This also corroborates the idea of particle growth, since Mie's Theory predicts that the LSPR band of plasmonic NP redshifts when particle size increases (See Fig.2.1).

The MSD analysis can however be further refined to increase its time resolution: by dividing the total trajectories in smaller segments, one can analyze the time evolution of the particle size, as it will be seen in the following section.

3.4.2 Extracting r(t) from MSD curves

The MSD analysis of a trajectory reflects the average diffusion coefficient during the trajectory. Indeed, since (for a single trajectory) MSD analysis averages displacements taken over all times, we end up with an information averaged on time. In simpler cases, where the properties do not vary with time the averaged value simply reduces to its constant value. Therefore, long enough trajectories can be divided in smaller segments, which can be analyzed separately via MSD. This procedure allows estimating the average diffusion coefficient on each segment and therefore to observe variations of the diffusion coefficient with time, from which the particle growth dynamics can be inferred[224]. The procedure principle is sketched in Fig.3.20.
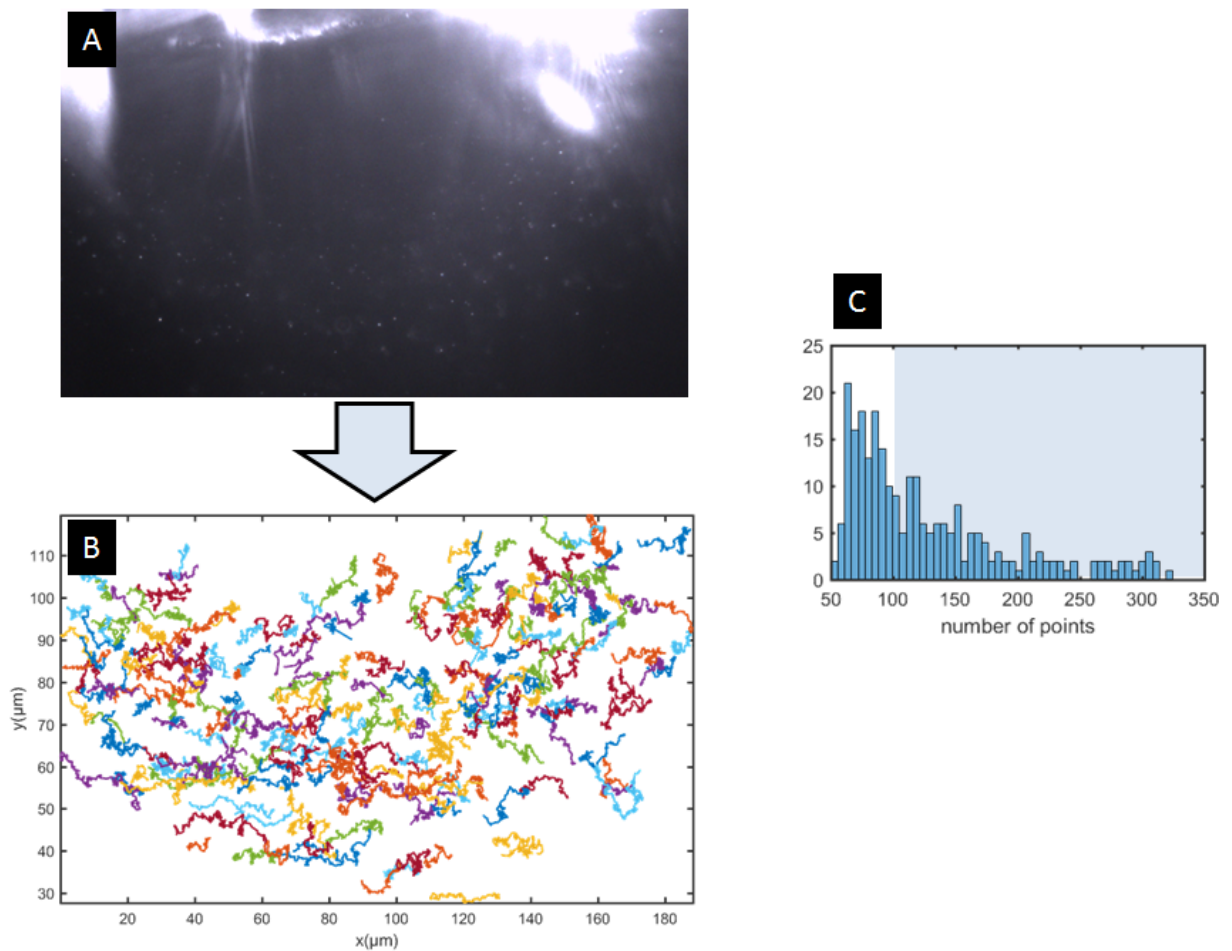
Figure 3.19: (A) Dark Field imaging of the electrode and its surroundings (B) Superposition of all the trajectories obtained using the ImarisTrack software. The spatial scales of figures (A) and (B) are the same. In (C) the length of the trajectories is represented on a histogram. Only particles tracked for longer than 100 time steps (highlighted in light blue) were considered for the MSD treatment.
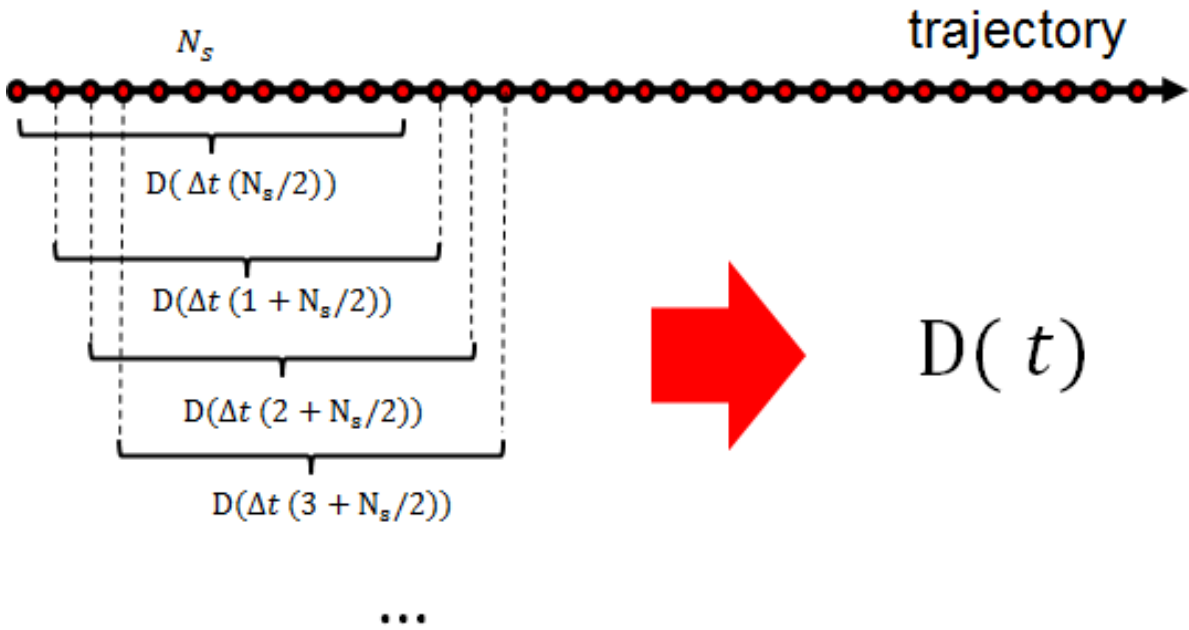
Figure 3.20: Illustration of the segmentation procedure used to estimate instantaneous diffusion coefficient variation with time. The trajectory of N time steps is segmented in $N - N_s$ subtrajectories of N_s time-steps. Each subtrajectory is analyzed separately, allowing an instantaneous (on a $N_s \Delta t$ timescale) estimation of $D(t)$. The proceedure grants access to $D(t)$, and therefore to $r(t)$ through Einstein-Stokes relation.

3.4.3   Growth Model

Owing to the particles small size, mass transport happens at a very fast pace. Steady state conditions should be established within milliseconds ($\approx r_0^2/D$, with D being the diffusion coefficient for the limiting species, Ag^+ or Fe^{2+}). Therefore, the reduction reaction is likely to take place under transport limited growth conditions (TLG). Since the particle growth takes place at a timescale much slower that the diffusion steady state time(a few seconds for growth versus $\approx 100\mu s$ for diffusion), the two phenomena uncouple and can be analyzed independently. The equations describing the growth rate under diffusion-limited conditions become entirely analogous to the steady state current at a spherical UME:

$$\frac{dV(t)}{dt} = \kappa r(t) \therefore 4\pi r^2 \frac{dr}{dt} = \kappa r$$

where all the physical parameters have been grouped in a single constant $\kappa = 4\pi c^b D V_m$, with $V_m = M/\rho$ the molar volume of the deposited material, c^b the bulk concentration of the mass-transfer limited species allowing the material deposition, and D its diffusion coefficient. The constant κ has the units of a diffusion coefficient ($\mu m^2/s$).

The solution of this differential equation yields:

$$r(t) = r_0 \sqrt{1 + \frac{\kappa t}{2\pi r_0^2}}$$

According to Einstein-Stokes relation, the instantaneous diffusion coefficient $D(t)$ of the NP is inversely proportional to its instantaneous radius r(t), therefore $D(t)$ can be obtained from the values of r_0 and D_0 of the NP size and diffusion coefficient at the start of the trajectory (t=0), if the constant κ can be estimated:

$$D(t) = \frac{D_0}{\sqrt{1 + \frac{\kappa t}{2\pi r_0^2}}}$$

Therefore, taking this model as an ansatz, the whole particle growth dynamics can be determined from the the particle size and the parameter κ. The particle size can *a priori* be estimated by the MSD analysis of the first segment, therefore leaving a single free parameter. κ is then determined by D(t).

3.4.4   Monte Carlo Simulations

The segmenting procedure analyzes relatively short trajectories through MSD analysis. This process is intrinsically stochastic, therefore fluctuations are expected. In order to evaluate the precision of the growth kinetics estimation, extensive Monte-Carlo simulations were performed and compared to the actual size evolution curve.

The detailed simulation algorithm is described in Sec.A.5, but in short, time is dis-

cretized in steps of length Δt. At time $t = 0$, the particle starts its trajectory at the origin, (0,0,0), and its position is updated by an amount Δr at every time step. According to Brownian motion statistics [174], the increments length follows a Gaussian distribution with mean zero and variance $2dD(t)\Delta t$, (d is the dimensionality of the experiment, for 2D images d=2), in a random direction θ (uniformly distributed over the unity sphere). The diffusion coefficient is recalculated at every time step according to the mass transport model and Stokes-Einstein relationship:

$$r(t_{i+1}) = r(t_i) + \frac{\kappa \Delta t}{4\pi r(t_i)}$$

3.4.5   Results

Through extensive testing of the procedure on Monte Carlo simulated trajectories, it was determined that at least 40 points were needed to perform a meaningful instant estimation of the particle size via MSD analysis.

Among the 255 tracked trajectories, only those which were long enough (more than 100 time steps) were considered for growth analysis. Among the analyzed trajectories, the ones showing significant growth, i.e., ratio between the radius at the beginning (r_0) and at the end (r_f) larger than 1.5 were used in the fitting procedure. As one can see, many particles show little or no growth, but at least 30 particles showed significant size increase, for which the growth parameter, κ, was estimated. The results are shown in Fig. 3.21A. The selection of the trajectories for kinetic analysis does not induce a bias, but filters the distribution - all unanalyzed curves correspond to the $\kappa \approx 0$ situation. Visual inspection of the histogram seems to indicate an exponential distribution of κ, possibly suggesting Poisson statistics.

The precision of the measurement can be evaluated through Monte Carlo studies, as shown in Fig.3.22. First, we can use the estimated parameters as input for simulated curves. The MSD curves of simulated and experimental trajectories can then be compared, revealing very good agreement (Fig.3.22A).

Moreover, we can estimate the error on the determination of κ, by repeating the procedure on a large number of trajectories simulated with the same parameters, as shown in Fig.3.22B. The error on the estimation of κ can be obtained by fitting the 1st and 3rd quartiles of the distribution, yielding $\kappa/\kappa_0 \in [0.5, 2]$, κ_0 being the value of κ used in the simulations (therefore $\kappa/\kappa_0 = 1$ corresponds to a perfectly precise measurement).

We are thus able to estimate growth on a particle-by-particle basis with a relatively good precision. These measurements reveal a profound heterogeneity in behavior, with some particles size changing steadily, sometimes overcoming saturation, and some particles not growing at all.

A number of reasons can be behind this surprising result: the heterogeneity of behavior can be due to a spatial variability of the concentration gradients, since the particles are
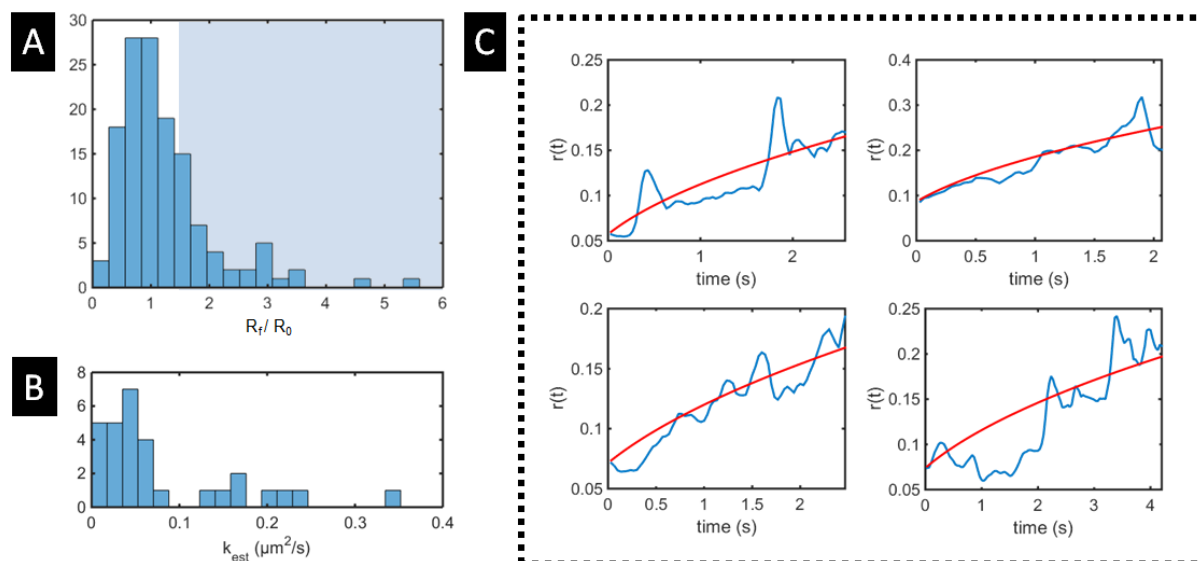
Figure 3.21: (A)Distribution of the ratio between the radius at the beginning of the trajectories (r_0) and the end (r_f). (B) For particles whose ratio was superior to 1.5 (N=30), estimation of the growth rate parameter. (C) Typical examples of a single NP instantaneous radius evolution with time (blue), experimental (red) theoretical. Starting from the top left, and in the clockwise direction: $D_0 = 4.2\mu\mathrm{m}^2/s, \kappa = 0.06\mu\mathrm{m}^2/s$; $D_0 = 2.8\mu\mathrm{m}^2/s, \kappa = 0.17\mu\mathrm{m}^2/s$; $D_0 = 3.3\mu\mathrm{m}^2/s, \kappa = 0.05\mu\mathrm{m}^2/s$; $D_0 = 3.4\mu\mathrm{m}^2/s, \kappa = 0.06\mu\mathrm{m}^2/s$

moving in a non homogeneous concentration field, and therefore the experienced bulk concentrations of reactants vary. This process is also altered by the number of particles present. It could also be due to an intrinsic stochasticity driving the beginning of the growth process - the nucleation step - thus making every particle experience growth at different paces, due to the non linearity of the square root law.

Whatever the reasons may be, our results highlight the importance of treating each particle individually, as the diversity of behavior would lead to over-damping of the measurements upon averaging, thus generating unrealistic conclusions.

3.5   Conclusion

A wide variety of chemical systems were studied in this chapter. They are all related to the use of single NP motion tracking for the understanding of chemical phenomena at NPs.

Starting from the follow up of aggregation through a combination of holography, spectroscopy and electrochemistry, it was shown that instant events (such as aggregation) are important, and can have a profound impact on NP reactivity. We then went on to show that single particle tracking can also help elucidate and unveil transport mechanisms, such as thermo- and diffusiophoresis. We then ended the chapter by showing that in solution, nucleation and growth of nanoparticles can be a very heterogeneous process, thus showing
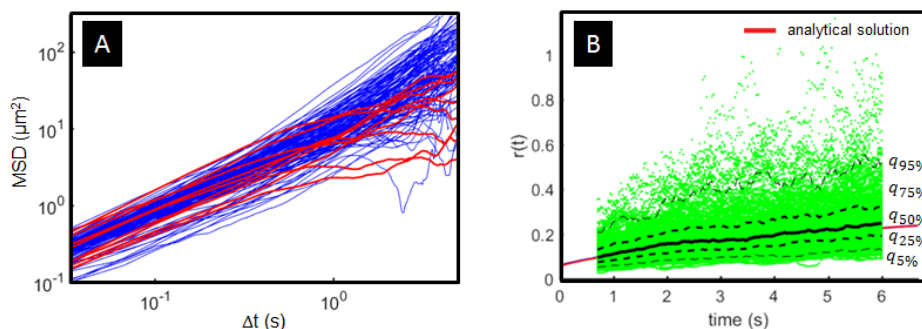
Figure 3.22: (A) MSD analysis of individual NP trajectories: (blue) experimental, (red) Monte Carlo simulation of growing NPs (D between 3 and $5\mu m^2/s$, κ between 0.05 and 0.2 $\mu m^2/s$). (B) Results of the application of the procedure to Monte Carlo simulations, for precision estimation. After repetition of the procedure over a large number of trajectories (N=300), the estimation distribution is compared to the analytical solution, used to generate the simulations. The 5, 25, 50, 75, and 95 % quantiles are represented, showing that the method is not biased.

the necessity of looking at these problems from a single particle perspective.

Indeed, to be able to track single objects was the guideline linking all the studies herein presented. These examples show how, at the nanoscale, transport and reactivity can be better described as stochastic processes rather than as mean field approximations. It becomes therefore essential to develop tools and strategies to study them as such, treating each entity (nanoparticle, nanoaggregate) individually. While it is true that continuum models and mean-field experiments are much more robust, and provide ways to measure ensemble behaviors, a stochastic description is much more adapted to, and therefore succeeds in, providing a much more detailed knowledge about these phenomena.

Chapter 4

Nanoelectrodes and Single Particle Electrochemistry

The present chapter is largely based on results previously published in Angew. Chem. Int. Ed. [225] and submitted to Anal. Chem. [226]. The results herein presented are adapted from these publications.

Up to this point, we have explored ways of studying nanoparticles individually either by separating them on time (one electrochemical impact at a time), or in space - using optics to spatially localize them. In this chapter we introduce another strategy to deal with particles individually : to synthesize them one by one.

Nanoelectrodes are used to electrochemically convert metal cations into small particles at the electrode tip. This method has the advantage of generating stable particles, that allow prolonged electrochemical studies. Unlike the previously described impact experiments, where only the transient current was detected, the particle can now be cycled reversibly over a wide potential window, permitting a much more complete electrochemical analysis. These studies have the potential to elucidate deposition processes, reversibility, quantify catalytic performance, evaluate long term stability, etc.

Electrochemical information, however interesting, is often ambiguous. If a complex situation with many chemical phenomena taking place simultaneously is to be solved, complementary characterization methods are needed. In this chapter it is shown that optical methods can help fill this gap.

Using a homemade dark field setup, superlocalization principles are applied to continuously size the particle with great precision, thus quantifying electro-deposition. Moreover, the visible spectrum is also recorded, revealing chemical transformations through changes in the scattered light intensity and spectrum shape. With this coupled approach, more complex chemical scenarios can be handled, such as simultaneous electro-catalysis and -deposition.

The concept is explored and built around the use of catalytic-relevant cobalt-oxide nanoparticles. Besides being good catalysts for a number of reactions, transition metal oxides, and cobalt in particular, are known to undergo numerous electronic transitions, frequently resulting in spectroscopic features in the visible range [227]. This makes them ideal candidates to unveil the potentials of the coupling.

The chapter opens with a discussion of the optical strategies and how optical imaging and superlocalization strategies can be applied to quantify particle deposition and growth. Next, we introduce how the optical index can also shed light on particle reaction and how all these concepts can be concatenated in a much more complex chemical environment, with the particle changing size, reacting and electro-catalyzing reactions at the same time.

4.1   Transition Metal Oxides for Water Splitting

Finding efficient and cheap catalysts for Oxygen and Water redox reactions has been among some of electrocatalysis research holy grails for a few decades. Indeed, to be able to operate water splitting reactions (oxygen and hydrogen evolution reactions, OER and HER respectively), as well as oxygen reduction reaction (ORR) under low overpotential conditions are the most fundamental bottlenecks keeping us from designing economic relevant fuel cells and fully integrated solar water splitting devices [228, 229].

Currently, most water splitting devices operate regardless of the cost of the catalysts, as the only materials with an economically competitive performance are noble and rare metals, such as Pt, Ru, Ir, some of their oxides and various alloys of noble metals[230, 231, 232]. Due to their high cost and scarcity, there is an enormous interest in replacing them by cheaper elements. Being available in large quantities naturally, first row transition metals are among the most promising candidates [231].

Cobalt Oxides and OER research share a common history dating back from more than 60 years [228]. However, cobalt-oxide based materials have regained the spotlights over the past few years, since the discovery of self-healing catalysts capable of long term efficient OER catalysis, at mild pH conditions [233, 234, 235, 236, 237].

Macro studies of catalytic films can already present a dose of complication, and their analysis is already seldom unambiguous. Reasons for that are that the chemical rates and selectivity may depend on particle size [238]. Since the electrodeposited material films are often not homogeneous on the micro to nano scale, spatial variability in reactivity is expected, introducing complicated interactions between different parts of the film. Indeed, when analyzed via SEM, electrodeposited cobalt oxide materials are shown to be composed of aggregated particle-like spheres, with characteristic size ranging from several nanometers up to a few micrometers [236, 237]. This is therefore the characteristic particle size length scale this chapter is aimed at.

Recent research on cheap alternative catalysts for OER has also presented a keen

interest in mixtures of metal oxides and hydroxides materials, such as layered double hydroxides (LDH) [239]. This path is also explored in the end of the chapter, once the usefulness of our coupled methodology to tackle the complexity of *one-material-only* systems has been proved.

4.2   Carbon nanoelectrodes preparation

The first step towards depositing single nanoparticles was to fabricate electrodes significantly smaller than the targeted particle size. Therefore, in order to study the properties of particles in the $50 - 500$ nm range, electrodes of $10 - 100$ nm radius were needed.

Carbon nanoelectrodes were fabricated using a high power CO_2-laser micropipette puller (P-2000 Sutter Instruments), according to a previously well established protocol [240, 241].

In short, the fabrication process consists in two steps. First, the quartz capillary is turned into a nanopipette. For that, the puller heats the middle of the capillary using laser pulses, while constantly testing the glass resistance . Once the capillary has soften, a high constant axial load is applied, stretching the hot capillary and forming the nanopipette. Next, the pipette is filled with butane gas (camping gas), and heated under argon flow using a flame torch. The gas is consequently pyrolysed and conductive carbon deposits on the glass walls. At the tip, a compact layer of conductive carbon deposits, seals the capillary and forms the nanoelectrode. This procedure is further detailed in Sec.A.7.

The nanopipettes geometry is analyzed by SEM imaging, while the tip chemistry nature and geometry/reactivity are characterized by Raman spectroscopy and steady state electrochemistry, respectively. Typical results are shown in Fig.4.1. The SEM image shows a well defined conical shape with a small tip, of $\approx 100nm$. Steady state current of the electrode in 1mM FeMeOH reveals a mass-transfer limited sigmoidal CV with a plateau, from which the nanoelectrode radius (r_{NE}) can be approximately extracted using the steady state current expression for a disk UME, $i_{SS} = 4nFDCr_{NE}$, with C the redox mediator concentration, F the Faraday constant, and n the number of electrons exchanged per redox molecule (while it is true that this expression can be improved to account for the small Rg value [242], we take it as a first order approximation). The Raman spectrum gives information about the chemical form of the pyrolyzed carbon. Three feature are observable: (i) a peak centered at $1576cm^{-1}$, known as the G band; (ii) a peak at about $1360cm^{-1}$, called the D band and (iii) a broad feature in the $2500 - 2800cm^{-1}$ region, known in the literature as the 2D or G' band. The G bands are characteristic of sp^2 carbon and are attributed to inter stack vibrations. The D band is usually attributed to defects, while the broad 2D band is an indicative of amorphous material. [243].
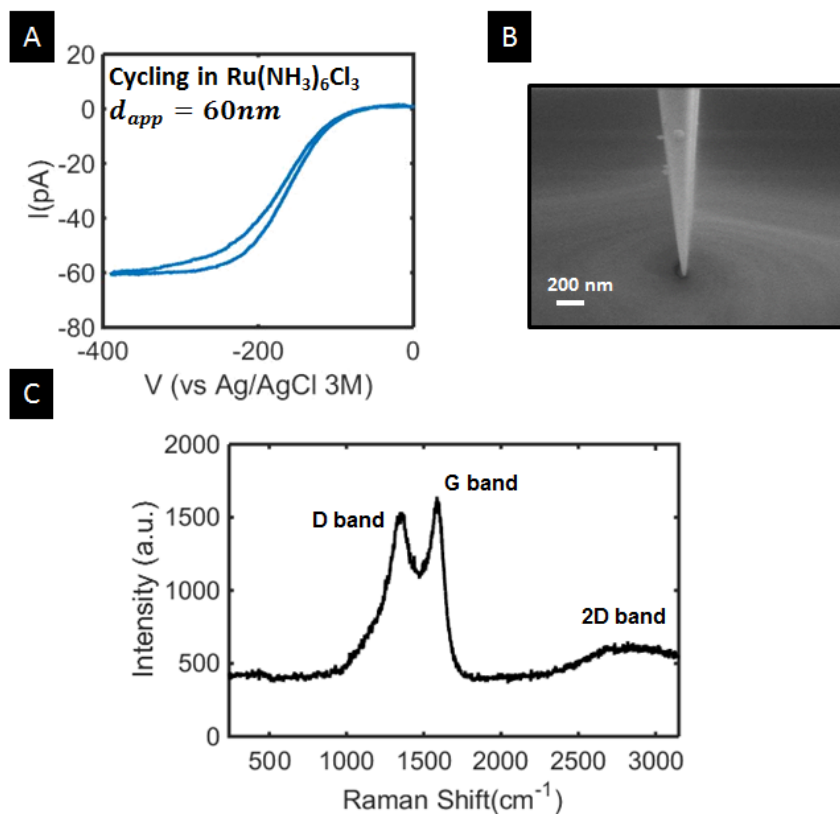
Figure 4.1: Nanoelectrode Characterization through (A) cycling in the presence of $5mM Ru(NH_3)_6Cl_3$ and $0.1MKCl$,yielding $d_{app} = 60nm$ (B) SEM imaging, revealing a well controlled conical geometry and (C) Raman spectrum, showing the D $(1360cm^{-1})$ and G peaks$(1576cm^{-1})$, a relatevely high D/G intensity ratio, together with a very faint presence of 2D band (in the $2500 - 2800cm^-1$ region) is indicative of a highly disordered (amorphous) graphitic material[240].
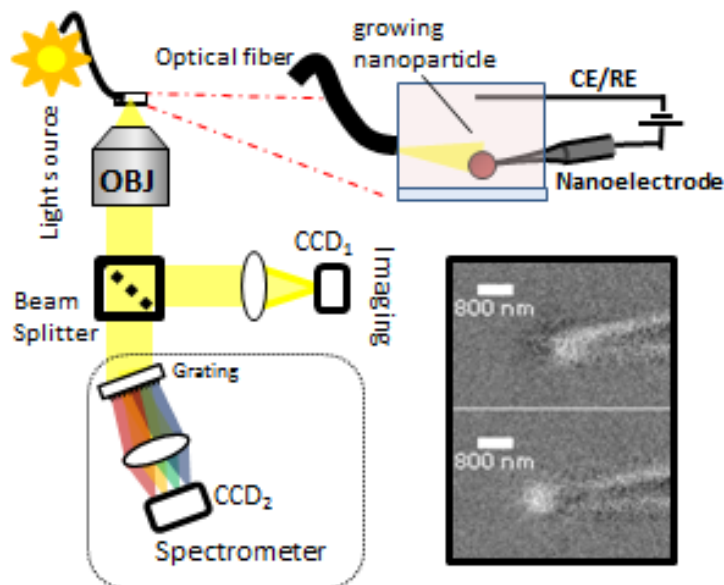
Figure 4.2: Dark Field Setup for nanoparticle monitoring over an electrode. The inset shows an example of cathodic particle growth: the application of a 5s -1V pulse leads to the appearance of a small particle (smaller than the point spread function). Both images have been substracted of an image taken just before the application of the pulse.

4.3 Monitoring Setup

The optical monitoring was achieved using an optical fiber to mimick dark field ilumination. This is sketched in Fig.4.2. The nanoelectrode is positioned in a drop cell, mounted on a thin glass slide on top of an inverted microscope, equipped with a long working distance objective (x60, NA = 0.7). With this configuration, focusing of the electrode is possible even if it is located far (> 0.5mm) from the glass slide. A multimode optical fiber (core diameter 1 mm, NA 0.2) coupled to a high intensity xenon arc lamp is then manually placed as close as possible to the electrode. It is oriented perpendicularly to the objective axis, minimizing direct incident light collection and therefore increasing contrast, mimicking a dark field illumination.

When spectroscopic information was needed, the detection path was slightly modified. Instead of sending the recorded image directly to an EM-CCD camera (Andor), the light is passed through a beam splitter (B.S.), which splits into two paths of equal intensity. One half is used to directly image the nanoelectrode using CCD1 (Fig.4.2), while the other half is passed through a line-imaging spectrometer (Specim Imspector V10E) allowing to record the spectrum using an EM-CCD Camera (CCD2 on Fig.4.2).

4.4 Single NP Electrosynthesis and Electrochemistry
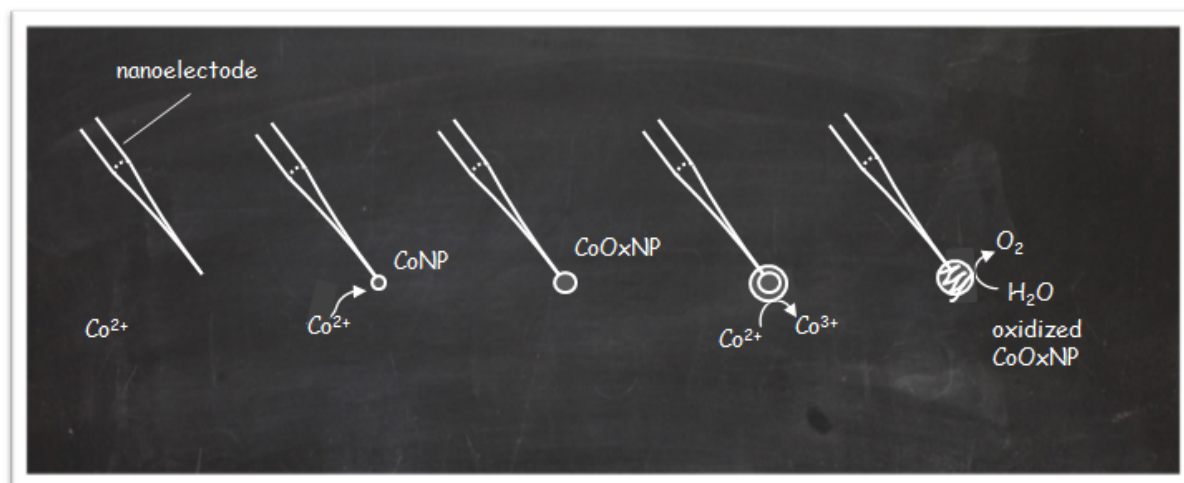
⟹ **Key Experiment Conception (#6):**

- Synthesize NP by electrochemical reduction of Co^{2+}

- Observe NP growth and oxidation through optical monitoring and superlocalization principles

- Analyze optical response variations with potential

- Investigate OER and ORR catalysis through a combination of the optical and electrochemical responses

In this chapter, the growth of Cobalt oxide NP (CoOx NP) from nanoelectrodes cycled in the presence of Co^{2+} is studied. This medium was chosen for two main reasons: (i) to avoid stability problems of the cobalt NP in the very alkaline and acidic local media (which may happen as a result of prolonged OER and HER); (ii) to grow particles continuously, thus evaluating the particle size influence on the observed chemical phenomena and (iii) to further stress the point that our coupled approach allows a much more insightful view of a complex chemical system, with numerous reactions happening at once.

Since the particles radius is expected to change during the experiments it is essential to be able to monitor their size continuously. For this reason, this section starts with an overview of the available optical strategies for measuring their size with maximal accuracy.

It will also be shown that optical data contain information about the nanoparticle chemical nature, which can be translated into electrochemical information. This is very interesting because it allows evaluating *particle specific* chemical transformations. In other words, it provides a way to separate faradaic current due to particle transformations, from everything else (catalytic current, capacitive current).

After stating these principles, we illustrate them by analyzing a complex example, on which a particle is continuously reduced and oxidized, progressively overgoing growth, redox reactions and catalyzing many reactions such as ORR and OER.

4.5 Particle Deposition routes

Individual particles are grown on the nanoelectrode apex from a 4 mM $CoCl_2$ solution, with 50 mM KCl as supporting electrolyte. In a two-electrode configuration, a silver wire is used both as a quasi reference electrode and counter electrode. Two routes for particle deposition are explored: particles are grown either using cathodic or anodic polarization.

In the cathodic route, in principle more intuitive, Co^{2+} is reduced to metallic Cobalt by application of a negative potential ($<$-0.9V vs AgQRE). This is done either by cyclic voltammetry (CV), or by applying pulses (chronoamperometry, CA). The latter is illustrated in the inset of Fig.4.2, where application of a -1V (vs AgQRE) pulse leads to the appearance of a diffraction-limited Co NP.

In any case, the integration of the reductive current over time leads to the cathodic charge, which can be used to evaluate the amount of Cobalt deposited using Faraday's law. The quantity of matter can easily be converted in an electrochemically estimated particle radius (r_{EC}). Thermodynamically, the most stable solid species at OCP (typically between -0.2 and 0 V vs AgQRE) is Co(II), therefore the molar volume (V_m) of $Co(OH)_2$ was used in the determination of r_{EC}. This observation is also in agreement with XPS spectra performed in thin films deposited under similar conditions, which revealed the absence of Co(0). r_{EC} is therefore calculated according to:

$$r_{EC} = \sqrt[3]{\frac{3QV_m^{Co(OH)_2}}{4\pi nF}}$$

In Fig.4.3, r_{EC} is compared to the radius obtained from ex-situ SEM images recorded right after the particle deposition process. A good aggreement is obtained, and deviations are attributed to the volume of the electrode and to imprecisions on the baseline estimation during integration of the cathodic current.

It is important to keep in mind that the actual deposition mechanism can be more complicated, as Cobalt and its oxides are able to catalyze oxygen reduction reaction (ORR), which allows further deposition routes, as further discussed in Sec. 4.8.1.

The second route is widely documented in the literature [233, 236, 234, 244] and involves the application of an anodic potential, generating the insoluble Co^{3+} species, which precipitates over the electrode, forming the catalyst. It is illustrated in Fig.4.4A-D. Unfortunately, we were unable to grow individual particles reproducibly from pristine electrodes in this way, possibly due to interference of OER reaction. This method of deposition was therefore only used to grow previously nucleated CoOx particles.

The details of the deposition mechanism are discussed in Section 4.8.2.
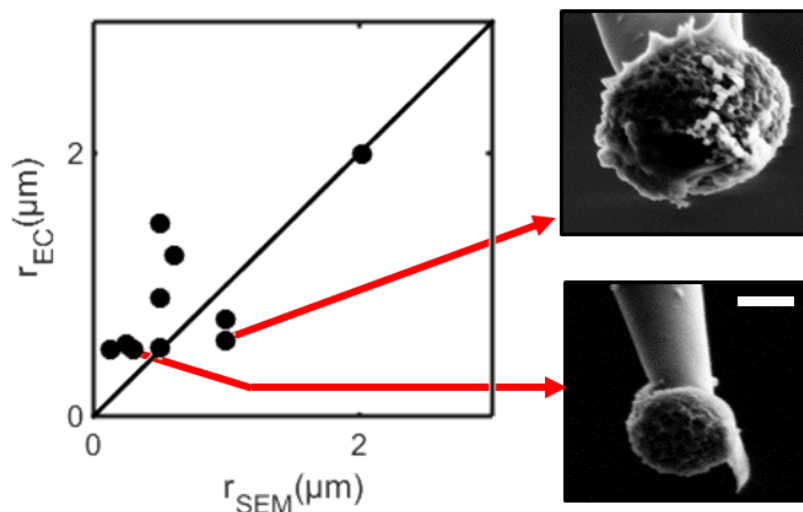
Figure 4.3: Comparison between small particles size obtained from the integration of the cathodic charge and from SEM images (two examples are provided). In accordance to XPS data and thermodynamics, the ex-situ particles are composed of $Co(OH)_2$. The scale bar for SEM images (shown in the bottom SEM image) is 360 nm.
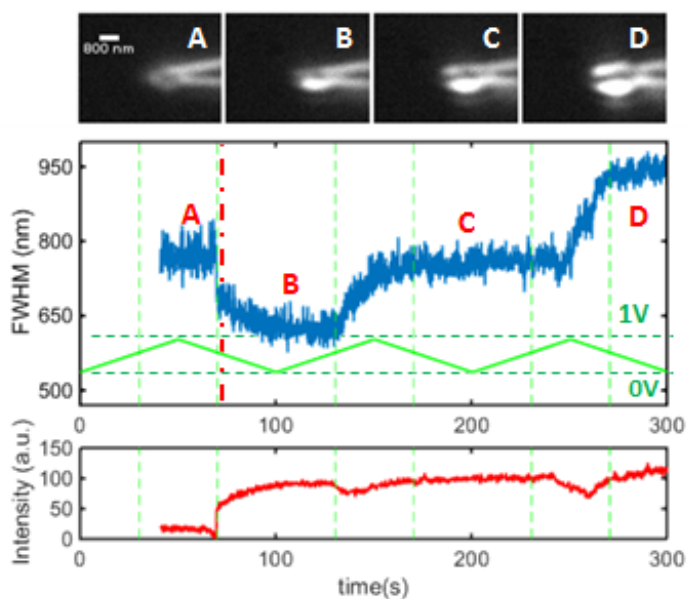
Figure 4.4: Co oxide particle growth during Co^{2+} oxidation. A stable Co nucleus pre-formed by reduction is further grown during oxidative cycles in a solution of 4 mM Co^{2+}, 50 mM KCl (vertical green dashed guidelines in the middle picture correspond to $E = 0.6V$, the red line indicates the time when the particle becomes comparable to the diffraction limit ≈ 650 nm, and thus spatially resolvable). The particle diameter is evaluated by fitting the image profile of the particle by a Gaussian curve (Blue trace on the middle figure, see Sec.4.6.1 and Fig.4.6 for further details). The full width at half maximum is an estimator of the particle diameter, $2R_p$. Each potential cycle corresponds to a variation in particle radius of roughly 50 nm. The red trace on the bottom figure shows the maximum, of the gaussian fit and corresponds to the maximum of the intensity profile. The increase in intensity corresponds to the moment where the particle signal dominates the total signal.
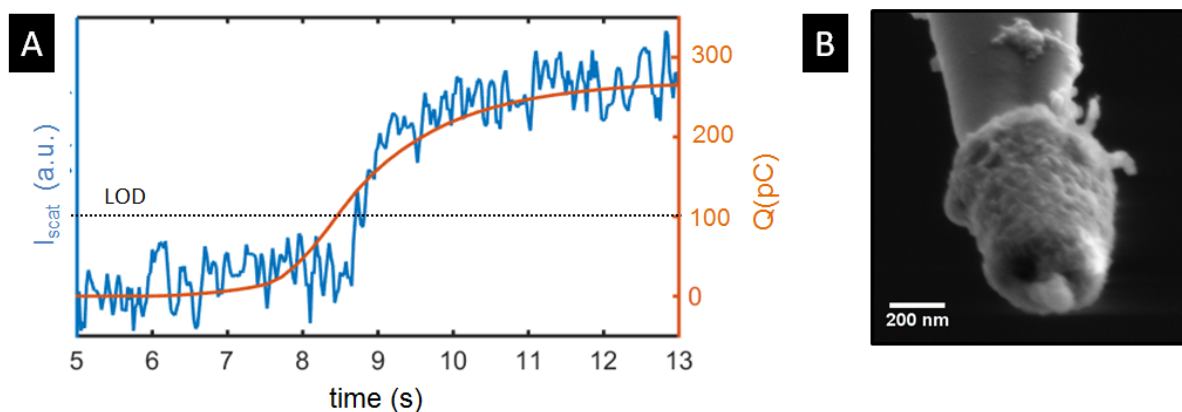
Figure 4.5: (A) Reductive deposition of a NP with a radius of ca. 200 nm during a CV (E between 0 and -1V vs Ag/AgCl) performed at 100 mV/s (B) SEM picture of the same particle, taken right after the deposition.

4.6 Particle Optical Detection and Sizing

As mentioned in the previous chapters, the Achilles' heel of optical techniques is its resolution, which is limited by light diffraction. According to the Rayleigh criteria, the resolution is limited to the point spread function (PSF) width :

$$1.22 \frac{\lambda}{NA} \approx 850 nm$$

This means that the actual image recorded is convoluted by an Airy function of this width, yielding an image where two objects that are too close ($d < 850$nm) cannot be resolved. Any attempt to quantify object size through imaging much below this limit is, at best, unfruitful. This section discusses strategies to overcome this limitation. Since the PSF introduces a characteristic length-scale of the problem, different strategies are used depending on the particle size to PSF ratio.

Regime 1: Small particles ($d/PSF \ll 1$) It does not mean that smaller particles cannot be detected, as it was done in Chapters 2 and 3. Indeed, if the intensity on the apex of the nanoelectrode curve is monitored during the deposition process, we see an increase of the scattered light which correlates to the increase of the cathodic current, as shown in Fig.4.5.

Regime 2: Particles size comparable to the PSF ($d/PSF \gtrsim 1$) Once the particles have sizes bigger than the diffraction limit, superlocalization principles can be used to characterize size *variations* with great precision.

For instance, as the particle size becomes slightly bigger than the PSF, an increase in particle size leads to an increase of the final diffracted pattern. One can understand this intuitively by thinking about the diffraction and imaging as a convolution operation by a

gaussian function representing the PSF.

We can thus evaluate particle size variations by taking a profile passing through the center of the particle and fitting it by a Gaussian function. The enhancement on the width of the resulting profile is an indication of the particle size. Therefore variations of the width are measurements of the size increase. A few fits of the profiles are shown in Fig.4.6A, and an application of this strategy was already shown, in Fig.4.4. One should notice that as the particle becomes bigger, the edges start to be resolved, decreasing the fit quality. The full width at half maximum (FWHM), however, is shown to be robust (error $< 10\%$) with respect to these effects.

Regime 3: Particle size bigger than the PSF ($d/PSF \geqslant 2$):   In the dark field illumination used, essentially only the edges of the particle scatter light. Once the particle is sufficiently big so that the two edges can be resolved, we can apply superlocalization procedures to estimate the edges position very precisely. Indeed, since each edge is convoluted by the PSF, it can be fitted by a gaussian whose mean is centered at the position of the edge of the object. Therefore finding the edge position corresponds to finding the gaussian mean (or equivalently, its maximum position). The diameter of the particle can then be easily infered by taking the distance between the two edges.

The procedure is illustrated in Fig.4.6A.The numerous errors at short times are due to the fact that the two edges are too close, failing to yield two well defined maxima used for the fitting procedure. This justifies, by the way, the existence of *Regime 2*. Likewise, if the overall intensity of the light scattered by the particle drops, (due to a change in the surface chemistry of the particle, for example), the quality of the fits is reduced, and the technique loses its accuracy.

4.6.1   Using Spectroscopic information for particle sizing

Another way to get around the resolution imposed by the diffraction limit is to record the full scattering spectrum of the particle. Although not traditionally seen as plasmonic materials, Co oxides exhibit moderate LSPR. This is shown in Fig.4.7, where the spectra of $Co(OH)_2$ NP of different sizes were simulated using Mie's Theory. In particular, one can notice the red-shift (Fig.4.7 top) that accompanies particle growth, characteristic of LSPR bands. A careful inspection of the spectrum reveals the presence of a few peaks, which red-shift when R_p increases.

The proposed strategy is then to follow the plasmon redshift and use this to quantify particle growth.

To make particles grow, we have applied 10s pulses of 1V, thus promoting growth by oxidation. This is shown in Fig.4.8A. The spectra (shown in Fig.4.8B) are recorded during the *rest* periods, when 0V is applied and the particle is back to its Co(II) state. In particular, it is possible to notice the presence of a peak on the spectra, which redshifts
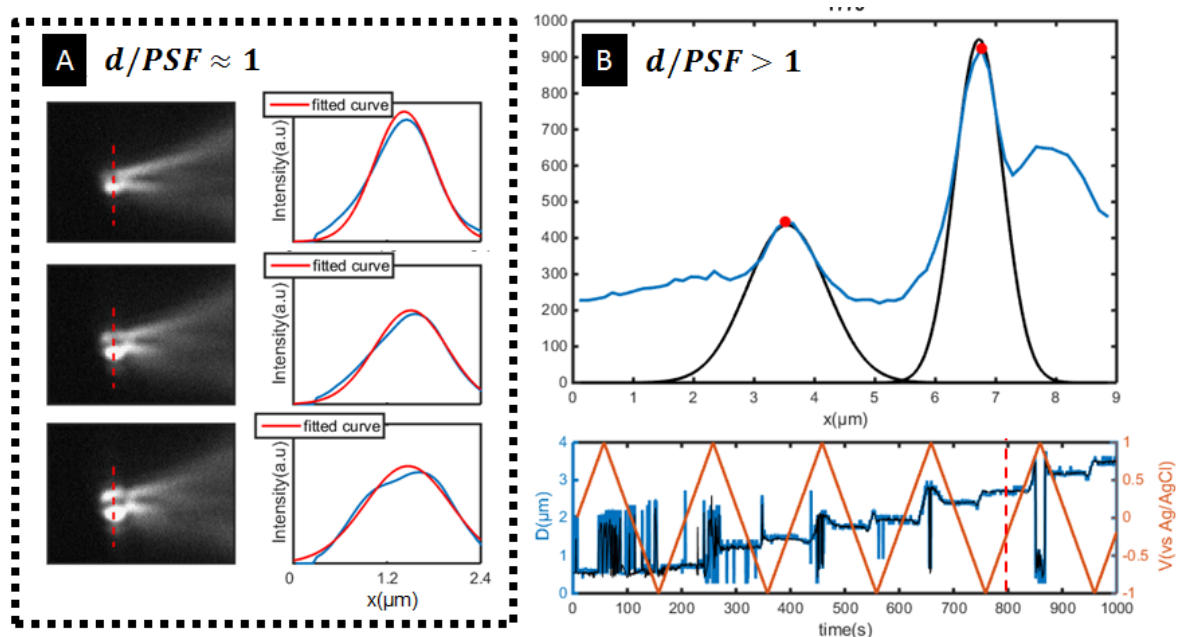
Figure 4.6: (A) Gaussian fit of the particle profile (for $d/PSF \approx 1$), showing the robustness of FWHM as an estimator of particle growth. (B) Localization procedure when $d/PSF \geqslant 2$ (Regime 3) Top: particle profile, with the position of two edges of the object from localization of their respective PSF maximum, and in black the gaussian fit of the edges profiles. Bottom: variation of the size with frame number during 5 repetitive cycles. The graph compares the particle size as determined by the maximum of the profiles (blue), and by superlocalizing them, using the black fits shown above. The profile shown on top is taken at the time designated by the red dotted line.
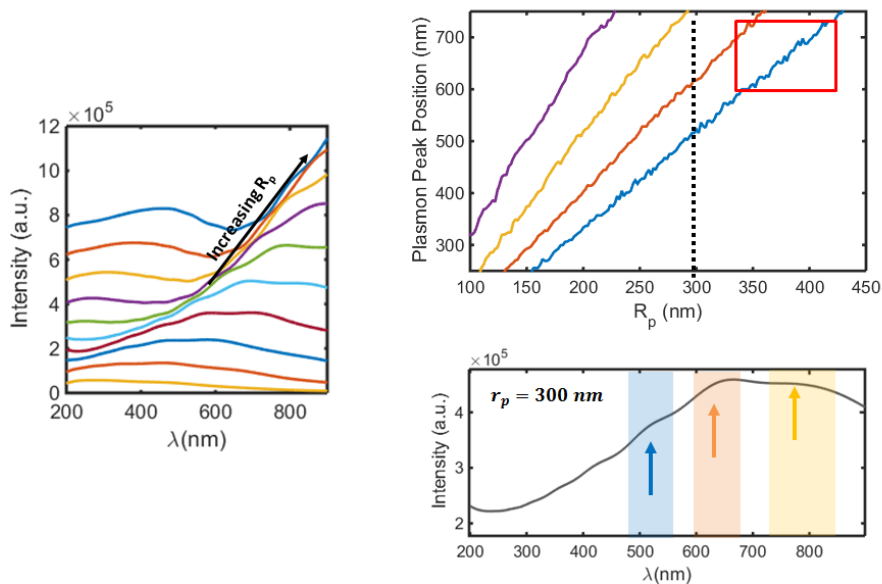
Figure 4.7: Simulations of CoOx NP near visible spectra using Mie Theory. (Left) Selected Mie Theory predicted spectra (from r = 100 to 460 with 40nm intervals). In particular the redshift that accompanies particle growth is readily seen, as well as a number of LSPR bands. (top) Simulated position of selected plasmon bands, as a function of particle size (R_p). The last LSPR band (in blue) was used to estimate the particle size (the inset shows the zone represented in Fig.4.8c), as it is the only one reliably detected on the spectra (Fig.4.8b). (down) Spectrum of a 300 nm radius particle (designated by the traced line on the upper figure), the highlighted regions correspond to the LSPR bands represented above.

upon repetitive particle growth (or potential cycling). The spectra redshifts are then compared to the ones expected from simulations (black line in Fig.4.8C), thus showing that it follows the expected trend quantitatively. Based on this strategy, an average radius increase of 8 ± 2 nm per cycle is detected.

It is important to highlight that, as presented, the technique can only assess particle size variations. In order to perform absolute measurements, a proper calibration of the LSPR- particle relationship would be needed. This isn't an easy task, since the similitude of the spectra is only qualitative, some discrepancies between the recorded and simulated spectra are observed, very likely due to the presence of the electrode, which was not taken into account. Moreover, the particle is assumed to be perfectly spherical, while SEM images taken at the end of the experiment reveal a oval shape. The final simulated particle size ($R_p = 405$nm) therefore only agrees with the observed SEM image within one order of magnitude (from SEM, $R_p = 705$nm). This difference is likely due to (i) the fact that the material is not perfectly compact, leading to a lower charge carrier density, and (ii) the presence of the electrode, creating a dielectric void in the center of the particle that was not taken into account in the model. Both these effects are expected to blue shift the spectrum, explaining the observed smaller apparent size.
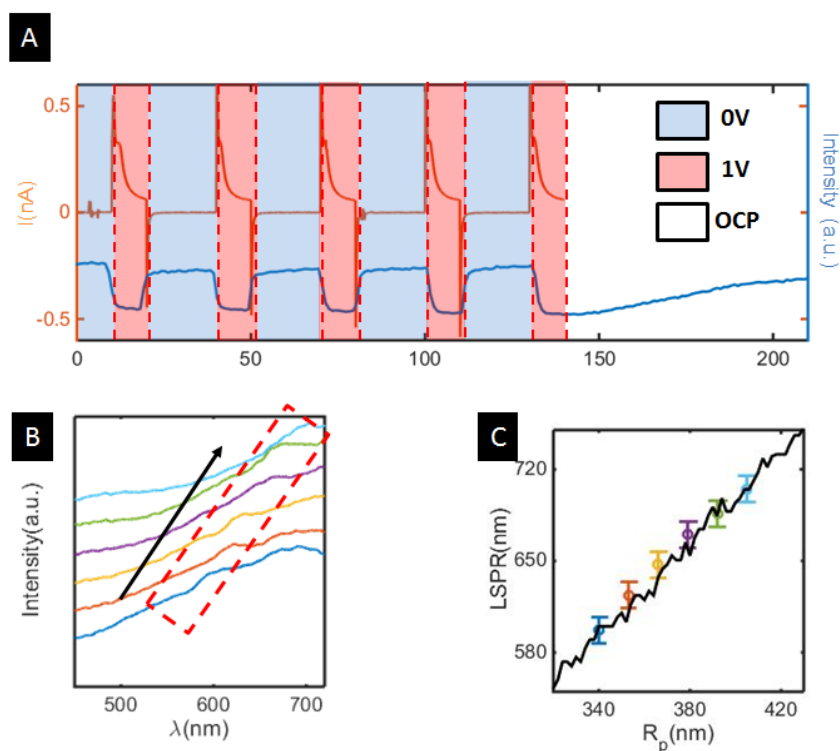
Figure 4.8: Spectroscopic strategy to size nanoparticles through quantification of the red-shift associated to growth. (A) Anodic growth of Co-oxide particle performed by alternative potential steps (1V electrodepostion, 0V) ended by relaxation at OCP. The spectra (B) presented were successively recorded when the NP is polarized at 0V (close to OCP), an thus consisted in Co(II) material, very likely $Co(OH)_2$. The particle scattered intensity (blue) and the resulting electrochemical current (orange) are shown. (B) The spectra (shifted in the y direction for clarity) reveal redshift, indicating particle growth. (C) Comparison of experimental peak positions (hollow circles) with Mie's theory (solid line, see Fig.4.7) allows estimating a 14 nm diameter growth per pulse.

4.7 Translating optical signal into electrochemical information

By looking at the optical monitoring of particles, shown in Fig.4.4 and Fig.4.8A, one might have noticed strong variation on the scattered intensity (I_{scat}) correlated to the appearance of electrochemical current. This suggests that these two processes are linked, either by causality or sharing common origin. In this section we show that this similitude indeed reveals that (electro)chemical information can be obtained directly from measuring the particles ability to scatter light.

4.7.1 Principle

In order to understand the decrease on I_{scat}, lets imagine how it would be changed by a general transformation, say $A \rightarrow B$. Assuming the two materials have different scattering cross sections (σ_{scat}^A and σ_{scat}^B), and that the optical response of a material varies linearly with its composition, this is a strong assumption, which actually neglects total volume variation on the NP due to the transformation and which takes only leading terms into account. Nevertheless, this model will still be used for the sake of simplicity. Deviations from this naive law are expected to be small, usually beyond our monitoring precision - specially for small particles.

Let I_0 be the intensity of the incident light. Before the transformation, the total scattered intensity is $I = \sigma_{scat}^A I_0$. Once the transformation starts to operate, we end up with a mixed material, with volumetric fraction $x_B = V_B/V_0$. The optical response of the material therefore becomes $I' = [(1-x_B)\sigma_{scat}^A + x_B\sigma_{scat}^B]I_0$. Therefore, the decrease on the scattered light can be expressed as $\Delta I = (\sigma_{scat}^B - \sigma_{scat}^A)(V_B/V_0)I_0$. The intensity variation is therefore proportional to the volume fraction of the product on the particle.

In the case of an electrochemical transformation, the volume of transformed material is proportional to the exchanged charge, Q_B, therefore the former expression can be used to link intensity variation and the exchanged charge: $\Delta I = kQ_B$, where $k = (\sigma_{scat}^B - \sigma_{scat}^A)(V_m^B/nF)(I_0/V_0)$ is a proportionality constant. If this expression is derived with respect to time, we are able to connect a variation on the optical intensity to a faradaic current which is *specific* to particle transformation processes:

$$i_{EC} = \frac{dQ_B}{dt} = -k \overbrace{\frac{dI_{opt}}{dt}}^{i_{op}}$$

Since an increase in material density leads to an increase of the scattered light, the minus sign was included so that the sign of the optical current (i_{opt}) agrees with the electrochemical conventions (oxidation current positive, reduction current negative).

4.7.2 Application for the $Co(II) \rightarrow Co(III)$ Transformation

The above strategy will be illustrated in the case of a $Co(OH)_2$ particle overcoming $Co(II) \rightarrow Co(III)$ transformation in aqueous medium. The particle is likely to form $CoOOH$, as suggested by the high ionic conductance of Cobalt oxide materials [245].

The particle is grown by alternatively cycling the nanoelectrode between -1 and 1V (vs AgQRE). The full situation will be further detailed in the next sections, for now we shall just focus on the zone around the $Co(II) \rightarrow Co(III)$ transformation. As in the CA's of Fig.4.8A, the $Co(OH)_2$ oxidation takes place around $0.65V$ vs AgQRE, giving origin to an anodic peak, and is associated to a decrease on the scattered intensity. The derivative (with respect to time) of the intensity, is then plotted against the potential for particles of many sizes (actually the same particle at different growth stages). The characteristic shape of a CV unveils a quasi-reversible, slightly asymmetric voltammogram. This optical voltammogram (opCV) is shown in Fig.4.9. If the anodic optical current peak is integrated, and compared to the integration of the actual EC current (i_{EC}) peaks, we may obtain a calibration curve that allows us to derive the proportionality constant k. This would then, *in principle*, allow to quantitatively transform the optical information into EC data.

This example illustrates well the potential of the optical signal to bear electrochemical information. It also points out the advantages of using optical signal to derive electrochemical information, as the original EC signals (shown in Fig.4.9C, for example) would be difficult to analyze, owing to the presence of other faradaic processes (for example, a catalytic current).

Having described the main techniques to be used to detect and quantify particle deposition, we shall, over the next sections show how they insert in a much more complex broader chemical context. In the presence of electrocatalytic and chemical reactions, we show how optics can help deconvolute Cobalt deposition in the presence of redox reactions.

4.8 Cathodic and Anodic Electrodeposition and catalysis

By applying the aforementioned strategies, it is possible to analyze reactions and transformations from three points of view: (i) exchanged electrons (from the EC trace), (ii) particle size (from superlocalization strategies described before) and (iii) particle-specific chemical signature, and the corresponding current-specific redox current (from the ability of the particle to scatter light). Together, these information characterize the particle nature and its transformations much more completely, with the potential to elucidate much more complex situations.

In this section, we apply our coupled approach to study the electrochemical trans-
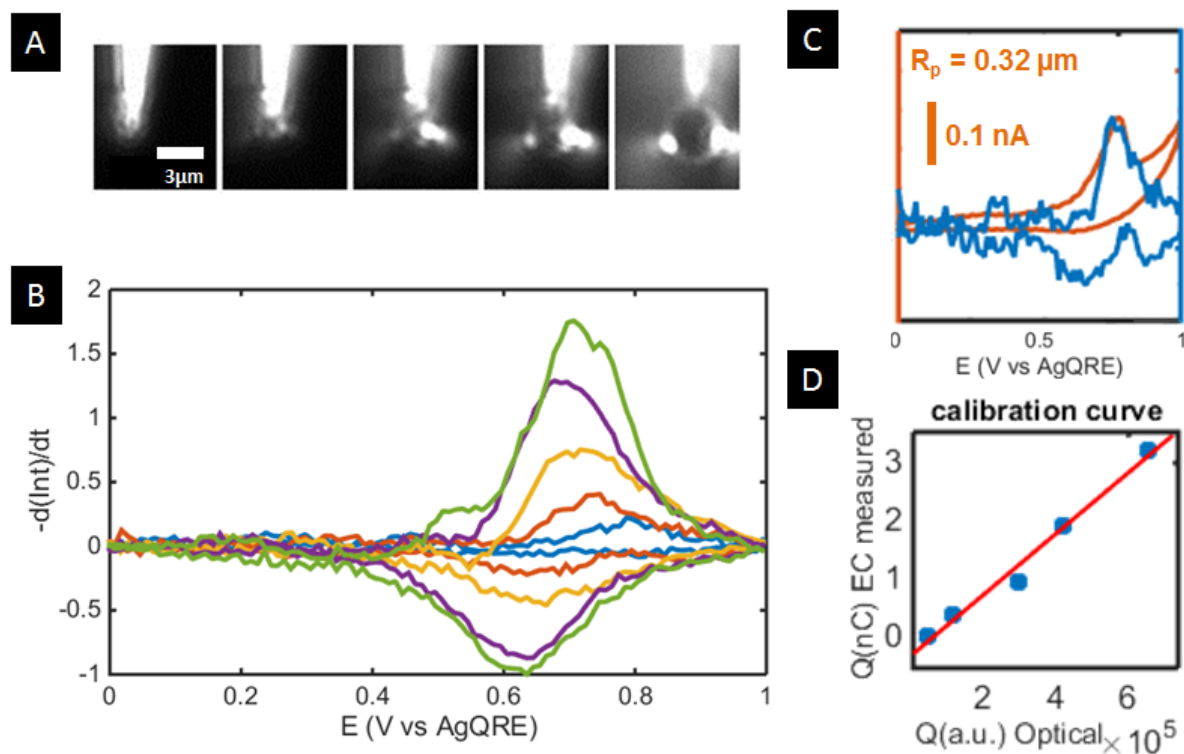
Figure 4.9: (A) Particle growth seen by dark field microscopy. (B) Extraction of electrochemical information from the optical signal, as the time derivative of the total optical intensity $-dI_{opt}/dt$ is plotted against the potential E, forming an optical CV (opCV). Each color correspond to the CV around the $Co(II) \rightarrow Co(III)$ transformation at different particle sizes: $R_p = 320$nm (blue), 650nm (orange), 900nm (yellow), 1230nm (purple) and 1600nm (green). (C) Comparison between the optical(i_{op}, in blue) and electrochemical (in orange) traces, showing that the change in optical index is indeed correlated to the appearance of a redox current peak. (D) Comparison between the charge obtained by integration of the electrochemical current and the optical current, showing a linear relation, which allows estimation of the proportionality constant k.
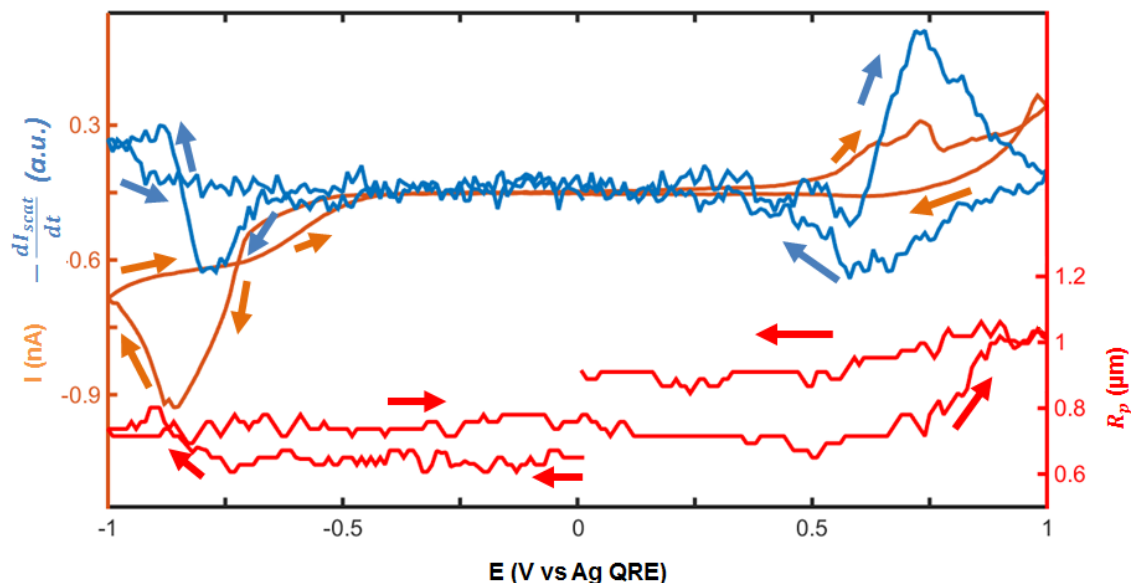
Figure 4.10: Simultaneous Monitoring of particle growth, optical response and electrochemistry during one full cycle, superposing the particle size (red), electrochemical trace (orange) and the particle-specific optically infered current (blue).

formations taking place at the apex of a carbon nanoelectrode in the presence of 4mM Co^{2+} and 50mM KCl. Starting from a pristine carbon nanoelectrode, the potential is cycled from -1V to 1V, resulting in the deposition of a particle (on the first cycle) and its subsequent growth.

The above described strategies to continuously size particle, together with the particle optical signature (through the derivative of the total scattered light, from now on called the "*optical current*", i_{opt}) and the direct electrochemical current are jointly used to analyze a complex chemical situation. In the presence of Co^{2+} ions, the electrode is cycled between anodic and cathodic potentials (typically, -1 and 1V vs AgQRE). A wide array of reaction simultaneously takes place, including electrodeposition, particle redox reactions and electrocatalysis of different redox reactions.

A typical experiment consists in starting from a diffraction-limited Co(0) particle electrodeposited on the nanoelectrode. The particle is first poised at 0 V, then cycled between 0 and 1 V and then repeatedly cycled between 1 and -1 V in the presence of 4 mM Co^{2+}. Each oxidative or reductive successive polarization cycle yields further growth of the particle at the most oxidizing and reducing potentials. One full cycle is shown in Fig.4.10.

One can see that many processes are happening simultaneously (particle growth, transformation, catalysis), which justifies our coupled approach. This typical cycle will be divided in an anodic and a cathodic part, and will be thoroughly analyzed, before turning our attention to size effects and scaling laws.
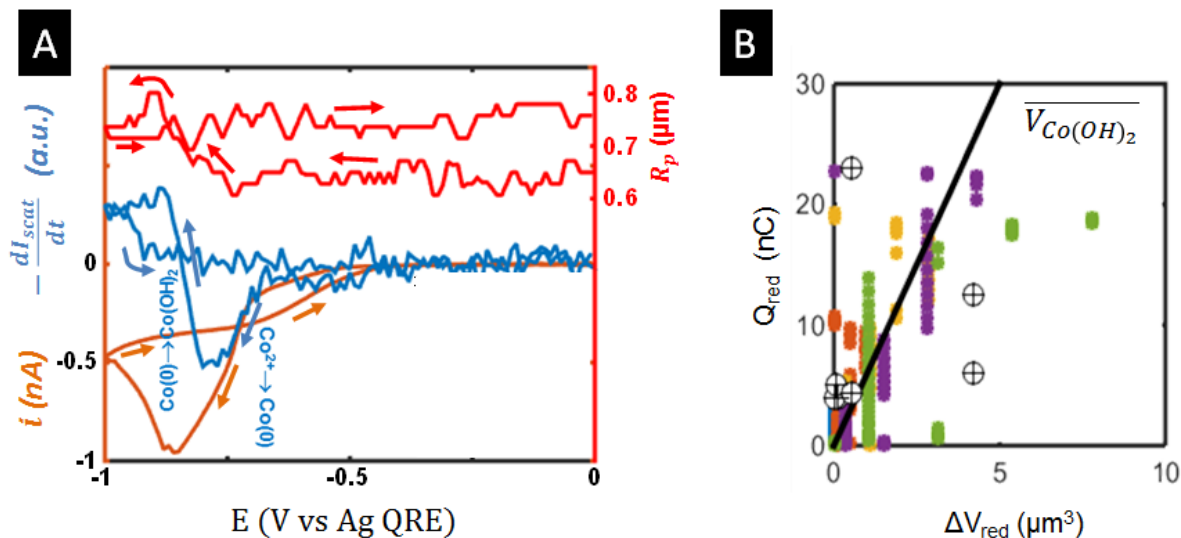
Figure 4.11: Opto-electrochemistry of an individual Co-based particle during reductive growth on a carbon nanoelectrode. (A) The cathodic current (orange) is compared to particle size (R_p, in red) and to the derivative of the scattered intensity, $i_{op}(= -dI_{scat}/dt)$. (B) Instantaneous charge and volume variations recorded during 4 potential cycles during the forward cathodic polarization from $-0.7 \rightarrow -1$ V. The black line corresponds to the expected trends according to Faraday's law with a molecular volume of $30 cm^3/mol$, consistent with the deposition of $Co(OH)_2$.

4.8.1   Cathodic Phenomena

The cathodic part of cycle is shown in Fig.4.11. The solution contains $CoCl_2$ 4mM and 50mM KCl, with the (uncontrolled) pH laying between 5 and 7. As the potential is lowered, nothing happens until the reduction potential for $Co^{2+} \rightarrow Co(0)$ is crossed ($\approx -0.65 V vs AgQRE$), when cathodic current starts to be detected, concomitantly with the appearance of a negative i_{opt}. Up to this point, all the electrochemical events take place at the nanoparticle, as all the exchanged electrons are detected both on the optical and EC currents. All the evidence then points towards direct reduction of Co^{2+} in $Co(0)$, reaction **1** in 4.12.

The particle size also increases accordingly, also in agreement to the Pourbaix diagram[246], $Co(0)$ is stable at this potential-pH range.

Quickly, however, the two traces become different. Since i_{opt} is sensitive to transformations of the particle while i_{EC} measures all electron exchanges with the electrode, this indicates that side reactions start to become important. This is indeed expected, since $Co(0)$ and its oxides are known as electrocatalysts of many reactions, such as oxygen reduction (ORR) and hydrogen evolution (HER) reactions, according to:

$$O_2 + 2H_2O + 4e^- \rightarrow 4HO^-$$

$$2H_2O + 2e^- \rightarrow H_2 + 2HO^-$$
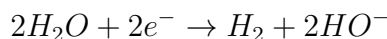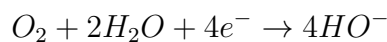
The sign of i_{opt} is also of interest, as it flips from cathodic to anodic, indicating that the
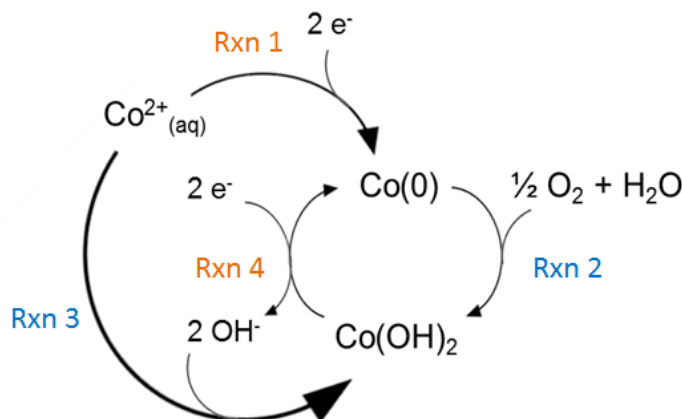
Figure 4.12: Suggested mechanism for the engaged cathodic phenomena.

particle scatters more light at first, and then its intensity decreases slightly. This suggests that the particle is oxidized. Since monitoring of the particle size do not reveal any size reduction, dissolution processes $(Co(0) \rightarrow Co^{2+})$ is highly unlikely, therefore the current signal change is assigned to the transformation $Co(0) \rightarrow Co(OH)_2$ (reaction **2** in Fig.4.12). Indeed, as HER and ORR happen at the electrode, they release hydroxide anions (OH^-), locally increasing the pH. This triggers the precipitation of Co^{2+} , according to $Co^{2+} + 2OH^- \rightarrow Co(OH)_2$ (reaction **3** in Fig.4.12). Moreover, the ORR itself can couple to the mechanism thus becoming responsible for the conversion of $Co(0)$ to $Co(II)$ species. All these reactions happen simultaneously, and are summarized in Fig.4.12.

The idea that ORR can couple to the deposition process can be reinforced by looking at the faradaic efficiency of the electrodeposition process. It can be analyzed by comparing the total cathodic charge and the volume variation of Co material. This is shown in Fig.4.11B. The solid line represents 100% faradaic efficiency for the deposition of $Co(OH)_2$ material, as calculated with to Faraday's law, using $V_m^{Co(OH)_2} = 30 cm^3/mol$. This means that all the charge passing through the electrode was used to reduce Co^{2+}, forming $Co(OH)_2$. Since no meaningful oxidative i_{EC} is detected, purely chemical steps must be included in the overall electrodeposition mechanism. These observations are consistent with the proposed mechanism, since it provides a path through which Co^{2+} can be used to reduce oxygen, forming $Co(OH)_2$ through a 2-electron reduction reaction. This corresponds to a combination of reactions **2**, **3** and **4** in Fig.4.12).

The formation of this species (only directly observable on the i_{op} trace) is concomitant with a reduction of the overall cathodic current, suggesting that the oxidized species $Co(OH)_2$ are less active when compared to $Co(0)$.

When higher potentials are reached $(< -0.9V)$, the growth seems to saturate, as the particle ceases to grow and i_{opt} goes to zero. The return trace of i_{EC} therefore

contains only the catalytic current. This corresponds to a $2e^-$ reduction of oxygen without intervention of Co^{2+}species, through reactions **2** and **4** . Indeed, the return trace of the electrochemical current shows a plateau characteristic of diffusion-limited processes, probably of the oxygen species. Indeed, if the expected steady state current is calculated, with $D_{O_2} = 2.2 \times 10^{-5} cm^2/s$ and $[O_2] = [O_2]_{sat} = 0.25 mM$ [247], one gets, for a spherical electrode of radius $R_p = 0.75 \mu m$ and a $n = 4$-electron reduction:

$$i_{ss} = 4\pi n F D_{O_2} [O_2]_{sat} R_p = 2.6 nA$$

This value lays in the same order of magnitude of the observed currents, and seems to indicate incomplete reduction of O_2, with 1 or 2 electrons per oxygen molecule. Indeed, with $n = 1$, one would get a steady state current of $0.65 nA$, very close to the observed value of $\approx -0.4 nA$. Another possible factor would be that the particle is not homogeneously active, and only a fraction ($\approx 20\%$)of the surface is actually capable of catalyzing ORR.

Interestingly, when we go back to potentials close to the open circuit potential (OCP), the particle does not redissolve (at least at the scale of a few hours), in disagreement with prediction based on thermodynamics (Pourbaix diagram). It is then suggested that the redissolution of $Co(OH)_2$ is kinetically hindered, i.e.the resulting material is metastable.

4.8.2   Anodic Phenomena

The potential then continues to be raised, and the anodic portion of the voltammogram is reached (between 0 and 1V). This is shown in Fig.4.13.

Electrochemically, oxidative current starts to be detected at $E > 0.55V$. Pairing the electrochemical data with i_{opt} reveals that the electrochemical transformation of the Co^{2+} species is associated with a dramatical decrease of the particles ability to scatter light. When oxidized, the particle turns off. This feature seems to be associated with the oxidation of the $Co(II)$ into $Co(III)$, which is expected to have a much lower electronic density and therefore to scatter much less light. Besides, Co(III) species formed at this potential range have been reported to strongly absorb visible light (a property sometimes referred to as electrochromism), which would also increase the turning-off effect [248, 126].

This oxidative peak can sometimes be associated to a broad peak on the reverse optical and electrochemical traces. It is however hard to analyze the electrochemical return quantitatively only based on i_{EC}, owing to the presence of a irreversible catalytic wave that appears when the potential is taken beyond the $Co(II) \rightarrow Co(III)$ peaks and blurs the voltammogram. This current is assigned to the oxidation of H_2O, releasing O_2 (OER).

We turn our attention to the $Co(OH)_2$ oxidation peaks. Simultaneous i_{opt} and i_{EC} peaks suggest that the $Co(OH)_2$ particle is being oxidized. Many species could form during the $Co(OH)_2$ oxidation, for example $CoO(OH)$, $Co(OH)_3$, Co_3O_4 or (most likely)
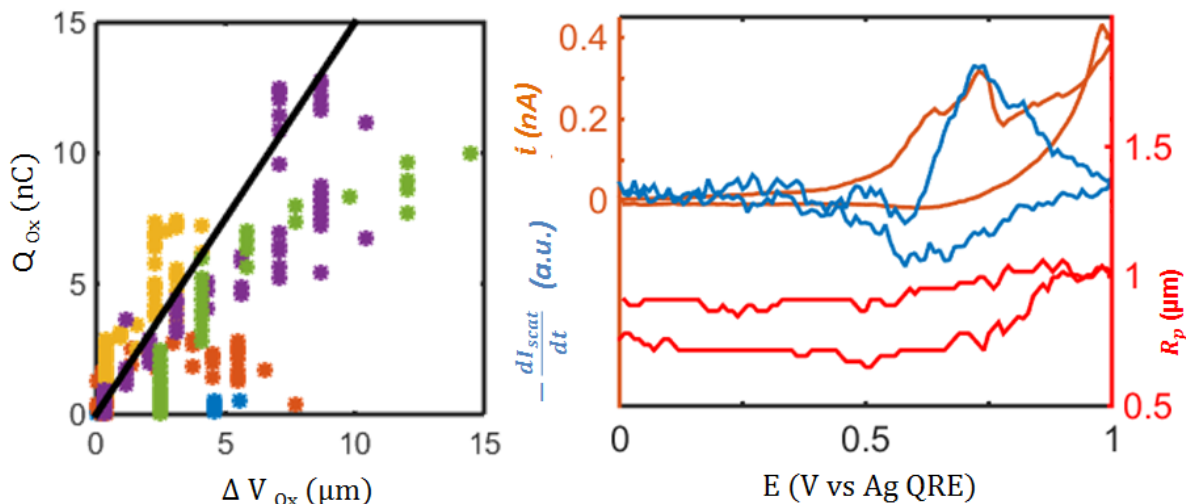
Figure 4.13: Opto-electrochemistry of an individual Co-based particle on a nanoelectrode poised at oxidative potentials. (A) The electrochemical current (orange) is compared to particle size (R_p, in red) and to the derivative of the scattered intensity, $i_{op}(= -dI_{scat}/dt)$. (B) Instantaneous charge and volume variations recorded during 4 potential cycles during the forward anodic polarization from $0.6 \rightarrow 1$ V. For reference, the black line corresponds to the expected trends according to Faraday's law with a molecular volume of 62 cm^3/mol, consistent with the volume occupied by each cobalt atom (typically a cube of 5Å width) in reported electrodeposited Co-oxide structures [235, 249].

a mixture between these species and $CoO/Co(OH)_2$. Owing to its smaller size, it is expected that H^+ presents higher mobility with respect to oxygen-containing species (such as OH^-, for example) in CoOx particles. Larger particle sizes are therefore likely to favor hydrogen richer species at sufficiently high reaction rates. This constitutes a mechanism through which R_p (particle size) can influence the properties of the particle. Moreover, the particle size increases at anodic potentials, suggesting that Co is simultaneously deposited from the solution (Co^{2+}). This could happen, for example, according to the following equation:

$$Co^{2+}_{(aq)} \xrightarrow{-e^-} Co^{3+} \xrightarrow{+2H_2O} CoOOH + 3H^+ \tag{4.1}$$
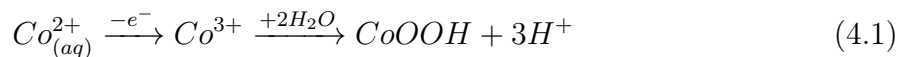
As in the cathodic part of the diagram, faradaic efficiency analysis reveals fair correlation between the total exchanged charge and the particle volume variation, as shown in Fig.4.13. The 100% faradaic efficiency is shown in black and corresponds to the Faraday's law using the molar volume of $V_{Ox}^m = 62cm^3/mol$, compatible with previously reported cobalt oxide material densities [249].

It is worth highlighting that eq.4.1 is probably a simplification of the chemical transformation that is actually taking place, as the final oxide material is probably a mixture of species, rather than a simple material. Indeed, assignment of these peaks is still under debate in the literature and explanations for the phenomena range from complex oxide

mixtures to semi-conductor materials [248, 249, 250].

A careful look at the electrochemical current peak reveals that the anodic process is a slightly ill-defined process, as the peak actually consists in a double peak. Moreover, the EC formal potential as well as the relative importances of these two peaks seem size dependent. At smaller sizes, the first peak is inexistent/less important, and becomes progressively bigger as the particle grows. Comparison between i_{EC}, i_{opt} and R_p in Fig.4.13 reveals that the particle starts to react prior to the onset of particle growth, suggesting that the first peak is due to a particle electrochemical transformation. The second peak appears concomitantly to an increase in R_p, thus revealing that this peak is more likely a precipitation process. The system also displays stochastic characteristics, suggesting that the full process is quite complicated, with numerous possible pathways for the reactions. This makes sense, as the complex nature of the cobalt material likely generates multiple pathways being sensitive to the local chemical conditions.

A more complete mechanism for the electrodeposition/OER is proposed in Fig.4.14, based only on Co(II) to Co(III) species conversion. This complicated (and speculative) diagram is included to illustrate how complexity and stochastic behavior can be easily introduced (and not necessarily to provide an accurate description of the engaged reactions).

Within this framework, since two $Co(III)$ species are present, two pathways for OER assisted electro deposition may exist. The first one makes intervene $Co(OH)_3$ species, using reactions **1** and **2-4a** while the second, based on $CoOOH$ uses reactions **1** and **2-4b**. In this context, stochasticity is not only possible but expected in the small particle regime level. Indeed, owing to their fast transport properties, small particles generate fast variations on the local pH near the surface. Most deposition and catalytic processes would release H^+, which are likely to quickly alter the local pH and thus the exact reaction pathway. The global reaction is consequently expected to depend very sensitively on transport properties (and therefore on the particle size). This sensitivity can therefore be at the origin of the stochasticity shown in Fig.4.13. Interestingly i_{op} also shows some variability. It is then speculated that the ratio between i_{ec} and i_{op} could contain useful information on the underlying mechanism. For the moment, however, no trends were observed. Other stochastic effects are discussed in Sec.4.9.

4.8.3 Limitations of the Optical approach

Until now, the discussion was limited to the implications of the $Co(II) \rightarrow Co(III)$ transformation, showing that Co(III) species engage on the oxidation of water mainly through a OER assisted electro-deposition. A survey of the latest literature on catalytic Co Oxides systems however reveal the existence of a second catalytic system, active at slightly more positive potentials (1.2-2V), related to the $Co(III) \rightarrow Co(IV)$ transformation. More importantly, this system has been shown to be more efficient than the one explored in the
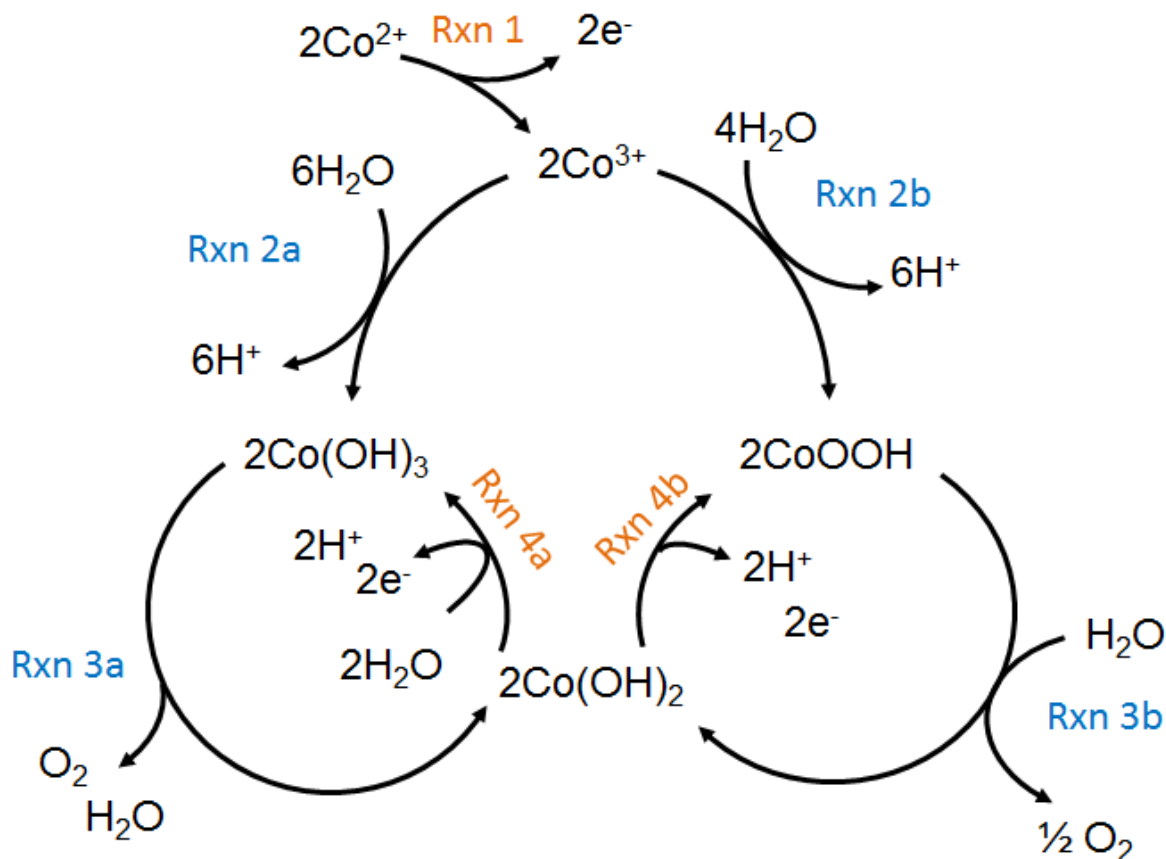
Figure 4.14: Proposed Mechanism for OER during Co deposition involving only Co species of low oxidation number (up to 3+).
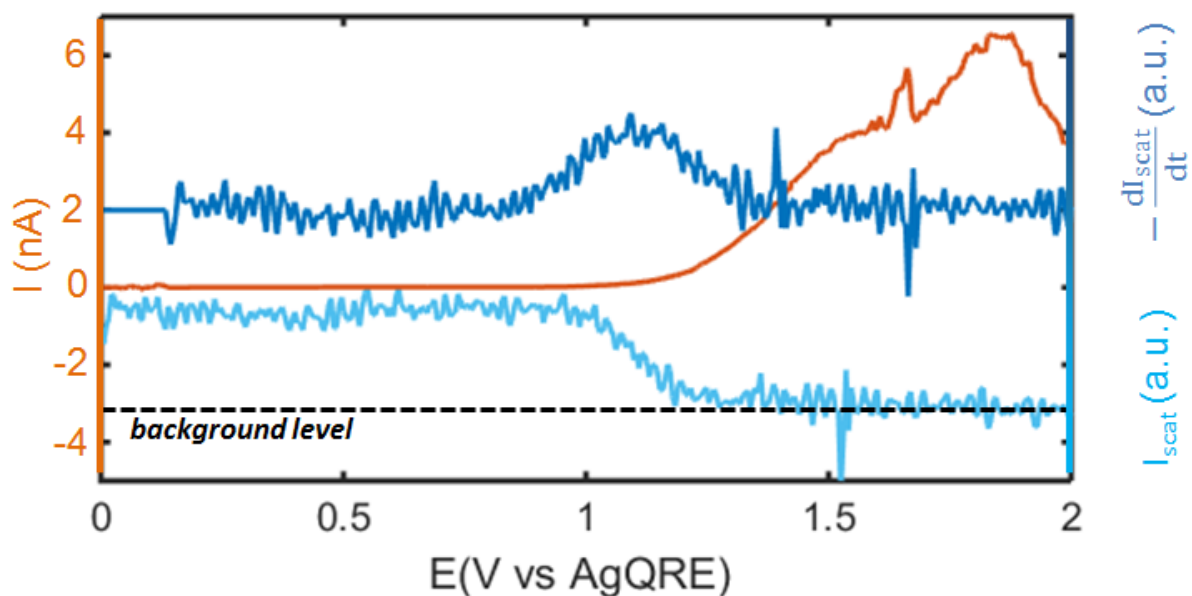
Figure 4.15: Optical monitoring of the OER at a single Co-oxide particle deposited onto a carbon nanoelectrode: the Co(II)→ Co(III) transition is located from the i_{op} trace. The electrochemical trace (orange) presents the OER catalysis (scan rate 10 mV/s, in the presence of 0.1M KCl electrolyte).
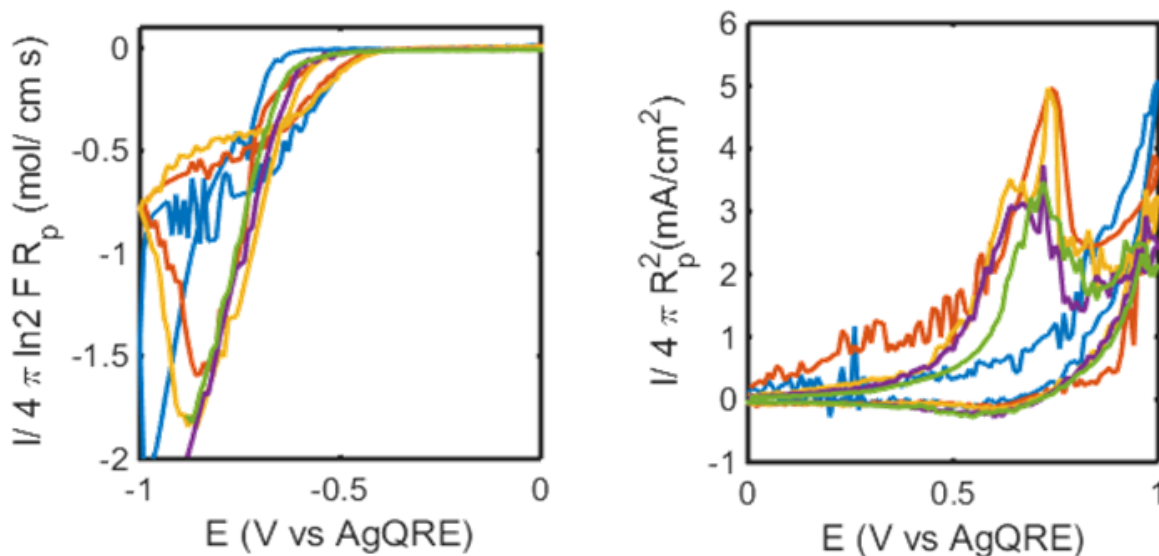
Figure 4.16: Comparison of the electrochemical trace of the particle between -1 and 1V in the presence of 4mM Co^{2+}. At each cycle, the particle grows, therefore this represent the same potential at different initial values of R_p. The anodic part of the voltammogram, shown in (A), can be normalized by R_p, thus suggesting diffusion-limited phenomena. In (B) the particles surface area $4\pi R_p^2$ is used to normalize the curves, thus indicating a kinetic limitation.

present section [249, 248, 251, 252]. One might therefore wonder why it has not yet been mentioned in the text.

This brings up one fundamental limitation of the strategy. As it was seen, the strategy behind recording variations of the scattering and representing it in a way directly comparable to an electrochemical current relies on the difference between the ability of each material to scatter light. Moreover, it was also shown that the scattering cross section of the Co species decreased with the oxidation degree of the oxide: $\sigma_{Co(0)} > \sigma_{Co(II)} > \sigma_{Co(III)}$. We reach therefore a dead end once the detection setup becomes unable to detect the particle.

That is what happens when Co(III) species are formed. The particle reaches the near total extinction levels, it *switches off* almost completely. Therefore, it becomes impossible for the camera to detect further transformations, such as the $Co(III) \rightarrow Co(IV)$. The situation is shown in Fig.4.15. One can easily see that the intensity reaches background noise levels, thus exhausting optical ability to transport chemical information, in the present setup configuration.

4.8.4 Scaling Laws and the influence of R_p

The ability of continuously determine the particle size is also interesting, as it enables the derivation of scaling laws that are quite useful on deciphering the molecular mechanism at stake. In the experiment herein discussed, described in Sec.4.8, the potential is alternated between -1V and 1V, and the particle overcomes many growth steps, such as the ones

described in Sec.4.8.2 and 4.8.1. Consequently, R_p increases after each cycle, and the voltammogram evolves accordingly. We can then compare the electrochemical traces of each cycle, in order to understand *how the particle size impacts the reactivity.*

For example, in Sec.4.8.1, we have evoked a catalytic mechanism based on diffusion limitation. In that case, the limiting current was shown to be proportional to R_p, as the steady state current is expected to follow $i_{ss} = 4\pi D_{O_2}[O_2]R_p$. This analysis is repeated for many particles, and indeed normalization by R_p make the traces of all particles superpose, thus confirming the interpretation given before, i.e., that the reaction is really diffusion-limited. This is shown in Fig.4.16A.

A similar procedure can be employed to analyze the $Co(II) \to Co(III)$ reaction peaks. In this case, however, the reaction does not seem limited by mass transport of species in solution, as the curves cannot be normalized by R_p. Instead, the curves superpose quite well when the particle surface, $4\pi R_p^2$, is used as the normalization factor. This can be seen in Fig.4.16B, and indicates that the reaction rate is limited by the kinetics of the reactions taking place at the solid-liquid interface.

These two contrasting examples once again indicate the number of different simultaneous phenomena taking place. The ability to image and detect size variations allows us to gather information, which would be extremely hard to obtain for a single particle based on electrochemical trace only. Scan rate analysis (cycling over many different scan rates) could be performed too, but (in the present case) this would necessarily involve averaging over different NPs, as the electrodeposition process is irreversible. This would scatter even more the results, as the nucleation step is highly dependent on the particle size, scan rate and changes the final morphology of the particle. Inter-particle comparison would therefore demand extensive statistics, ultimately broadening the information and hiding the phenomena. In short, to be able to size the particle allows us to derive extra chemical information in a quick and practical way, allowing us to derive complete results from a single particle. This is extremely helpful when trying to understand the underlying phenomena and mechanisms.

4.9 More on stochasticty: Morphology and Catalytical Activity

As mentioned in Sec.4.8.2, the voltammograms often show stochastic features, such as the peak position, the presence of a re-reduction peak on the CV return, etc... This was attributed to the sensitivity of the reaction system to local chemical conditions, together with a complex reaction mechanism. In this section we take the discussion a bit further, identifying trends and another possible source of stochasticity, attributed to particle morphology.
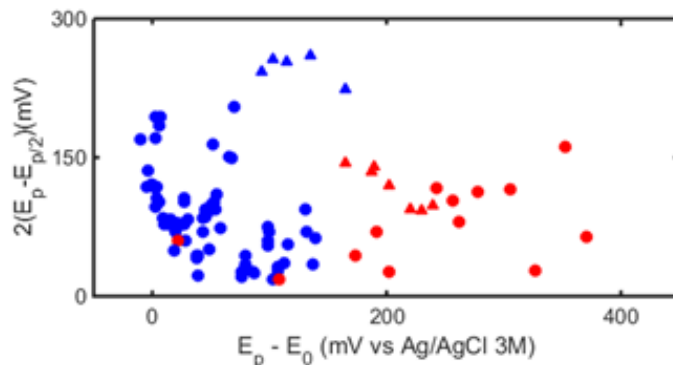
Figure 4.17: Scatter plot showing how the oxidation potential correlates to peak width (no correlation) and to the appearance of redox peaks for the return reaction (blue indicates the presence of a reduction peak, red indicates the absence). This seems to indicate that particles formed at higher potential tend to be more inert, i.e. the reductive wave shows slower kinetics. The plot gathers data of particles at two pH values : neutral (triangles, obtained from the optical response), and alkaline (circles, pH13).

Stochastic Peak Shapes   As discussed in the main text, the redox potential of the $Co(II)/Co(III)$ couple can display stochastic characteristics in micro-nanoparticles. For example, by gathering the analysis of the $Co(II) \rightarrow Co(III)$ peak from large number of CVs (optical and electrochemical), one notices that the shape of the peak is widely scattered. This is shown in Fig.4.17 where the position (with respect to the thermodynamic reaction potential E_0) and width of the peaks (distance between the peak potential E_p and the peak at half maximum $E_{p/2}$) are compared. We also notice that the return peak $(Co(III) \rightarrow Co(II)$, during the return trace is sometimes undetectable, indicating the slow kinetics of the inverse reaction.

Even though the data are scattered, some trends are visible:

(i) Particles that react at low overpotential values (lowest values of $E_p - E_0$) are often associated to broader peaks (highest values of $2(E_p - E_{p/2})$) suggesting successive transformations. In these cases, the return peak is generally present.

(ii) When the oxidation occurs at high overpotential, the peak tends to sharpen. For even larger overpotentials $(E_p - E_0 > 0.15V)$, the electrochemical or optical CV becomes irreversible, the reverse cathodic peak becomes undetectable, at the timescale of a few seconds (scan rate = 10mV/s). Similar behavior is detected optically. Optical monitoring shows that the process is reversible (the optical signal is recovered at longer time or lower potentials) confirming slow kinetics phase transformation processes with slow kinetics.

(iii) Besides unbuffered solutions (pH = 5-7), the aforementioned behaviors are also present when the pH is made more alkaline (pH=13) or when the particle is formed or placed in a phosphate buffer (pH=7.2), suggesting that the Cobalt oxidative electrodeposition remains a complicated mechanism in either case.

Morphology Evolution: Besides sensitivity to local chemical conditions (as suggested in Sec.4.8.2), this stochasticity could also be generated by evolution of the particle morphology. As the deposition process occurs concomitantly with side-reactions, the particles geometry may be poorly controlled. Especially, if particles are deposited under very *far-from-equilibrium conditions* such as potential pulses, fractal-like geometries with dendritic growth or multi-lobe growth are observed. In such cases, optical monitoring of the particle is a very useful asset to analyze the influence of the overall geometry on the electrochemistry.

Fig.4.18 shows the reconstitution of the opCV of a particle that was deposited cathodically at a fixed potential ($E = -1V$ vs AgQRE for 20s). As it can be seen in the inset, the particle morphology evolves over time, tending to a more spherical shape upon oxidative potential polarization. While electrochemical smoothening of the particle is monitored, the oxidation potential of the Co material, estimated from the opCV is decreased while no clear change in the direct electrochemical signature is detected, indicating that limitations due to poor conductivity may play a role in the observed E_0 variations.

The analysis of this stochastic behavior suggests that the position and width of the oxidation waves are correlated with the reversibility of both electrochemical and optical CVs. No clear correlation between particle size and redox potential was observed. It likely reveals the charge transfer resistance in such inhomogeneous shaped particles, which can be described as disorderly packed nanoparticulates of cobaltate crystallites.

4.10 Co-Ni oxide nanoparticles : Towards single particle composite materials studies?

We end the chapter with an opening towards the study of more complicated systems, such as Co-Ni particles. Indeed once the cobalt particles are deposited, one can change the solution and repeat the deposition procedure with other transition metals such as nickel, for example. This may raise all sorts of interesting questions such as: *How will the electrochemical response look like? Can the Nickel system act separately from the Cobalt or will they merge in a single alloy-like particle? Are there conditions on which the core-shell structure remain stable, or will the two metals necessarily mix?*

Although the experiments still remain insufficient to provide a definitive answer to any of these questions, I chose to briefly discuss a few of the preliminary results as this shows the potential of the technique to address more complex (and catalytically relevant) systems.

So far it was shown that nickel oxide can be deposited on a cobalt oxide particle by following the same procedure that led to the deposition of the $Co(OH)_2$ particle on the carbon nanoelectrode: the $Co(OH)_2$ particle is immersed in a 4mM $NiCl_2$ solution containing 50mM of KCl, and poised at cathodic potential (typically between -0.9 and
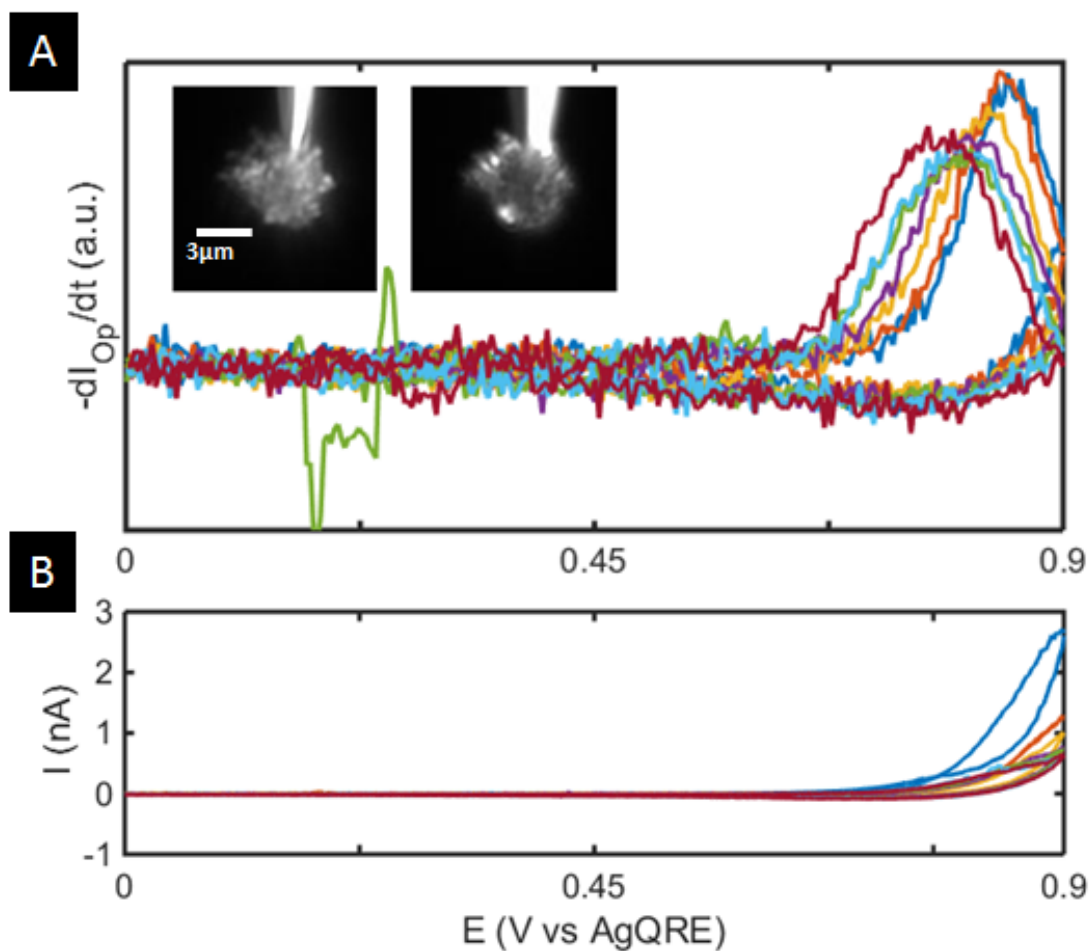
Figure 4.18: Change of particle morphology during successive cycles. Electrochemical of a particle deposited under far for equilibrium conditions (-1V for 20s). The particle is cycled successive times between 0 and 0.9 V (vs AgQRE), leading to smoothening of the particle initial fractal shape during the subsequent 7 cycles.
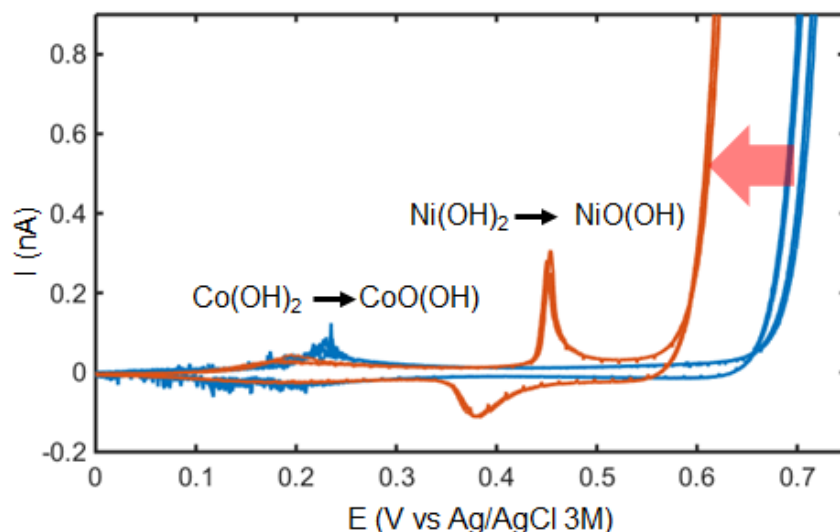
Figure 4.19: Cycling in KOH (pH 13) of a $Co(OH)_2$ particle before(blue) and after(orange) deposition of a $Ni(OH)_2$ layer. The CV shows that the addition of Nickel Oxide leads to a double system, where $Co(OH)_2$ is oxidized first (at around 0.2V), and then the $Ni(II)/Ni(III)$ system appears (at around 0.45V). The presence of Nickel leads to a substantial lowering of the overpotential for OER, of $\approx 100mV$ (indicated by the red arrow).

-1V), either by applying a potential pulse (CA) or by performing a CV. The resulting particle is then cycled in a highly alkaline solution (KOH pH 13), to quantify its ability to catalyze OER, the voltammogram is shown in Fig.4.19.

Two reversible systems can be identified when a layer of nickel oxide is present: the previously observed $Co(II)/$ $Co(III)$ couple, which appears at around 0.2 V at this pH (blue trace in Fig.4.19) remains almost unchanged, while a new redox couple, assigned to $Ni(OH)_2 \rightarrow NiOOH$ appears at around 0.45V [52].

Some influence of the nickel on the $Co(II)/Co(III)$ couple oxidation potential was observed, leading to believe that some alloying mechanism could also be present. Moreover, the presence of a layer of nickel oxide has the effect of canceling the optical extinction observed during the $Co(II) \rightarrow Co(III)$ transition, which can open up the way to the quantification of Ni deposition through optical techniques.

These first exciting results are very interesting as they open up the way for a coupled study of not only Co/Ni particles but a wide range of composite materials with cobalt (or any other optically active material) in their composition.

4.11 Conclusion

This chapter dealt with the analysis of single nanoparticle systems using a combination of electrochemistry with nanoelectrodes and optical monitoring of the particle through a straightforward, relatively easy to implement, dark-field configuration. Cobalt electro-

chemistry was used as an example, since its many possible oxidation states allowed us to demonstrate how the extra information provided by optics could help us deal with complexity.

Although (visible) optical techniques traditionally suffer from poor resolution owing to diffraction, superlocalization principles were used to push the applicability of optical techniques down to the 40nm range. This was shown to be quite an asset in the analysis of electro-deposition and catalytic molecular mechanisms.

The first information given by optics was particle size, R_p. This enabled monitoring of particle growth, thus allowing distinction between electro-deposition steps and purely catalytic regimes. Secondly, the change in the scattered intensity reflects a change in the particle chemistry, which can be used indirectly measure the transformation rates. This information is relative to the particle (electro)chemistry alone and therefore allows separation between redox transformations and catalytic mechanisms.

Using these monitoring tools, we analyzed the interchanges between Cobalt electro-deposition, redox bulk reactions and catalysis *in operando conditions*. For example, it was shown that Co cathodic deposition is capable of coupling to ORR, yielding a $2e^-$ reduction of oxygen forming $Co(OH)_2$.

A remarkable feature of the herein presented experiments was the presence of moderate stochasticity. Especially at the anodic part of the voltammogram, it is speculated that a complex reaction network could be at the heart of the sensitivity to the chemical environment, and thus to the observed stochasticity.

In any case, the phenomena observed in this chapter illustrates well the utility of having single particle optical and electrochemical signals to understand reactions taking place in a complex chemical context.

General Conclusion

We live in the wake of what is sometimes called the *nanoera*, with words like *nanoparticles*, and *nanometers* ubiquitous and irreversibly making their way towards our everyday lives.

With ambitions to understand the phenomena at the nano- and molecular scale continuously growing, it becomes absolutely necessary to develop tools able to interact and probe the world at these scales. This thesis started by revisiting many of the inventive strategies through which this very difficult task can be carried out. Since the first interactions with the nanoworld through scanning probe techniques and electronic microscopy, many new ways of looking at single nano-objects have been developed, spanning a variety of techniques and fields, electrochemistry and optics being two examples.

Nowadays, however, the challenge lays beyond simply *seeing* objects individually. In order to get a better glimpse into nanoscale phenomena, one needs to see them in action, *in situ* and *in operando*. Moreover, experiments at these scales are quite different from regular chemical experiments. Instead of averaging billions events or particles, we are now probing individual objects, and thus we can appreciate how stochastic chemistry looks at small scales. As seen in countless studies and papers (and in particular throughout the pages of this thesis), every nanoevent is, in a way, unique and needs to be observed and properly characterized on the spot. Since this can hardly be done by repetition and averaging, one needs new pairs of eyes looking at the same thing. In other words, coupled and *in operando* single objects studies are required.

Two scientific fields were identified as able to provide coupled and sensitive information simultaneously and accurately: electrochemistry and optics. Since these two disciplines study the effects of the interaction of electrons or photons with matter, they are able to provide different and complementary information, which is necessary to unambiguously study individual objects in the nanoscale.

In Chapter 2, this complementarity is attested by studying *at first* a simple model. The chapter is opened by a holographic-electrochemical study of the oxidation pf Ag NPs when they hit (collide with) an electrode. The goal of this first step was to show that in very simple chemical reactions, where the electron transfer step happens concomitantly to the dissolution of the particle, optical and electrochemical signals yield the same information. Indeed, that is what was observed: by comparing the injected charge during an oxidative impact with the particle volume variation (as measured through optical intensity), it was

concluded that both signals were perfectly correlated.

This correlation does not, however, mean that it is redundant to record both signals: they were merely concomitant since this was an example *engineered* to be simple, far from the general case in real chemical situations. So we set out to complexify the situation and stress out this point: by adding precipitating agent (thiocyanate), the rate of dissolution of the particle becomes controlled by the concentration of the precipitating agent and the intermediates stability. Therefore, in the presence of thiocyanate, the electron transfer time scale becomes dissociated from the dissolution time, and we are able to measure both the oxidation time (from EC signal) and the dissolution step (from the optical response).

Chapter 3, dealt with other ways through which complexity can arise. Aggregation, for instance, is expected to modify both the diffusing behavior and chemical reactivity of a nanoparticle, and it was the first theme of the chapter. Two cases of aggregation-related complexity are put forth : first, natural random aggregation and then controlled aggregation, where particles engineered to aggregate, forming organized ensembles (called supracrystals), were studied.

In the first case, we were able to directly monitor one aggregation event by holography, and to study the reactivity of aggregates both from electrochemical and optical points of view as they hit a polarized electrode. Mean square displacement was used to size the aggreate, then stochastic electrochemical impact revealed that the oxidation happens one particle after the other, and not as a whole. This was further confirmed in the case where a precipitating agent was present, since the low dissolution times allowed us to get a visible spectrum of the reaction intermediate.

In the second case, particles functionalized with C_{12} chains were studied. More than a way to control the aggregation by tailoring the molecular interactions, the C_{12} chains introduce an extra complication: as light is cast on the system, the particles migrate towards the laser spot. By tracking individual supracrystals, it was possible to characterize their motion completely, therefore gathering insight into the migration mechanism, which was actually temperature related: the laser heats the NPs due to their absorption cross-section, generating thermal gradients and thus the motion. Migration towards hotter regions thus triggers the formation of a light-controlled aggregate, in a mechanism called *thermophoresis.*

Regarding migration, this chapter also includes another single particle tracking study, in which it is shown that NP diffusion behavior can also be influenced by concentration inhomogeneities. An electrochemically generated pH gradient was used to make particles move directionally towards the electrode, an osmotic migration called *diffusiophoresis.*

In the same chapter, the utility of single particle tracking to study particles whose dimensions evolve with time was illustrated. After introducing an electrochemical strategy to synthesize NPs, we were able to track their motion and analyze the average size increase through a kinetic model. The growth process was shown to be heterogeneous, thus further

reinforcing the need of monitoring objects one-by-one.

Finally, chapter 4 showcases the generality of opto-electrochemical methods. The application of coupled optical and nano-electrochemical techniques is not limited to classical plasmonic materials such as Ag and Au, but can also be used for studying oxides and .

Pyrolized carbon nanoelectrodes were used to grow single Cobalt oxide nanoparticles, a known catalyst for a number of tricky reactions such as oxygen evolution and reduction reactions. Since in this case the particle is still, it was possible to perform a much more profound electrochemical study of the same particle. At the same time, the apex of the nanoelectrode (where the particle is) was monitored by dark field microscopy, thus allowing the study of chemical transformations of the particle, which impact its optical index, shape and size. It thus becomes possible to separate redox reactions affecting the particle chemistry from the other electrochemical processes, such as capacitive charging, catalytic current, etc. This allowed a much more profound analysis of the reaction mechanism and direct observation of particle state.

Moreover, using superlocalization principles, size changes as small as $40nm$ were monitored, allowing the quantification of (electro)deposition processes with great precision. This precision is achieved in a relatively easy to implement experiment, contrasting with other methods for quantifying material deposition such as quartz crystal microbalance. This also illustrates the utility of superlocalization strategies to study bigger (on the nano- to micro- range) structures very precisely.

This knowledge was then applied to shed light on complex situations where electrodeposition, precipitation, electrocatalysis and redox reactions are all happening at the same time. For instance, when the CoOx particle is brought to cathodic potentials, we show that Co electrodeposition quickly diversifies, and triggers chemical transformations. Soon the catalytic capabilities of the material become appreciable: oxygen reduction starts to occur, which eventually couples to the electrodeposition process.

Using relatively simple instrumentation it was possible to study complex phenomena in a chemically-relevant material, showing the potential of opto-electrochemical methods as an analytical asset for studying a variety of chemical processes.

In conclusion, numerous examples of single object studies were provided throughout the pages of this thesis. By analyzing nanosystems object-by-object it was possible to extract much richer information, and therefore to take the analysis much further.

On the one hand, nanoelectrochemical techniques such as stochatic impacts and nanoparticle growth, are shown to be extremely useful for their ability to reliably deliver information about nanoparticles reactivity, probing their reaction kinetics and thermodynamics. Single particle optical methods, on the other hand, are able to deliver trajectories, cross-sections, optical indexes, and thus grant many physical insights such as particles size, shape, growth, etc.

Taken together, these two big families of methods provide a relatively easy to im-

plement, non-invasive way of analyzing nanosystems. Their complementarity makes the characterization of chemical events much more complete, characterizing much more complex phenomena *in operando*. To be able to observe such specific chemical events as they happen brings us much closer to understanding them, potentially leading to a much better comprehension of the reactivity of nanoparticles, catalysts and general analytes in a real chemical environment.

During the three years of my PhD, I couldn't help noticing how much of a vivid and exciting challenge it is to perform chemistry at the scale of individual nanobjects. These systems challenge mean-field descriptions and can seldom be analyzed through the strategies and methods used for bigger, macro scale systems. If we are to succeed in understanding stochastic nano systems, experimental methods and strategies to dynamically probe and interact with matter at this level are desperately needed. The work contained in this thesis therefore showed that electrochemistry and optics are able to deliver these tools in a reliable and straightforward way.

Nevertheless, it is in the very nature of research itself that work never ends: answers always tend to bring up new questions. Having demonstrated the utility of single particle opto-electrochemical methods, the questions we may now think about addressing are endless: How much can we learn about core-shell nanostructures? What information can MSD curve provide about self-propelled particles? Can time resolution be increased by using more viscous solvents, such as an ionic liquid? Can hot-electrons (or hot-holes) be used to promote reactions? Being at the frontier between chemistry and physics, it is also anticipated that the setups presented here are also particularly adapted to study photochemical mechanisms. What would be the optical response of a semi-conducting particle? Can magnetic nanoparticles be studied, and remotely manipulated?

Improvements are always possible and are currently being pursued in our groups (improvement of spatial and time resolutions, integration of single particle Raman spectroscopy, etc). However, the developed tools and strategies herein presented are now working, running and ready to be applied to investigate other, more challenging, chemical reactions and materials.

Extra Chapter A

Experimental Methods

In order to ensure the readability of the manuscript, we choose to separate a detailed description of the experimental setup and technique from the results. This chapter deals with these experimental aspects.

Holography and its coupling with electrochemistry was the first step in our approach to the coupling between optical and electrochemical methods, and perhaps the most innovative (and challenging!) experiment performed. For this reason, this technique occupies a prominent position in the chapter. After a brief account on holography history and most significants developments, the experimental setup used in the experiments (Ch.2 and Ch.3) is discussed in detail. Particle superlocalization strategies and precision are also discussed in this context.

The section right after that deals with the instrumentation used for acquiring single nanoparticle spectra. Our experimental configuration is described and discussed. This is relevant for understanding the results presented on Ch. 2, Ch.3 and (briefly) on Ch4.

Next, the classical Mean Square displacement curve analysis allowing in situ particle sizing is explained, together with a light description of Brownian motion statistical properties and behavior. Single particle tracking is of interest for Ch.2 and Ch.3, where the statistical properties of the particles Brownian paths were used to derive mechanistic information on a variety of processes. The chapter ends with the detailed protocols used for designing micro- and nanoelectrodes.

A.1   Holography

"When we take a photograph, the image appears in the plane of the plate. But by Huygens' Principle the information which goes into the image must be there in every plane before the plate, also in the plane before the lens. How can it be there in that uniform whiteness? Why can we not extract it?" thought the Hungarian scientist Dennis Gabor while he was waiting for a tennis court to be free on Eastern 1947 [253]. From this epiphany point on, Gabor went on to create a technique whose developments would, in many ways, shape

Figure A.1: *"This is our most desperate hour. Help me, Obi-Wan Kenobi. You're my only hope."* Princess Leia Organa hologram, in Star Wars Episode IV : A new Hope, an iconic scene which illustrates the impact of holography on pop culture.

the way we think about optics today[253, 254, 255].

Gabor came across the idea of accessing 3D information encoded in a 2D plane while concept-proving a strategy to reconstruct complete wavefronts as part of his efforts to improve the performance of electronic microscopes[256]. His original approach to the impossibility of producing electron lenses without aberrations was to use no lenses at all, recording a distorted image that, although hard to grasp, had all the necessary information contained in the propagating wave. The original image would then be back-propagated using optical techniques, recovering the in-focus image.

He later realized that this technique had potential not only to yield nice images of the focal plane, but also to recover information about the sample contained outside the image plane. As it can be seen by the former quote, what Gabor realized was that *any plane* through which the light passed contained essentially the same information. Named Holography, from the greek "Write Everything", the technique consisted in combining the light scattered by an object with a reference source of light to create an interference pattern. The resulting fringes contained not only information about the amplitude of the wave (as most optical techniques usually do), but also about the phase of the light - in principle all the information needed to reconstruct the full wavefront.

Attracting attention from the scientific community since the very moment of its invention, holography never ceased to gather attention on itself. Although initially regarded as an academic curiosity, holograms were soon to prove their usefulness, especially after the popularization of coherent light sources (lasers). Shortly after its invention, holography crossed the walls of universities and made their way into art, science fiction and popular culture, as evidenced by countless references to it in movies and theater. The ability to see and produce three dimensional images has really stimulated society's collective imagination.

A.1.1 Principles and Earlier Versions

The full holographic procedure consists in two parts. At first, the interference pattern between a *reference beam* and light containing information about the sample (called the *object beam*) is recorded. The spatial information is encoded on a simple 2D image.

Later, this information is extracted in a reconstruction step and displayed. As the first holograms were recorded on a silver photographic film, they needed to be developed and later re-exposed to the reference wave to reveal the 3D image. In modern versions of the technique (such as the one described herein), all these steps are performed digitally, with CCD (Charge Coupled Devices) or CMOS (Complementary Metal Oxide Semiconductor) sensors replacing the photographic film and the decoding step being performed numerically, by back propagating the recorded wave.

Most recording media are sensitive to the intensity of the light they have been exposed to, and therefore to the square modulus of the field scattered by the object. For this reason, the information about the wave phase is usually unavailable in most optical imaging techniques. If * represents the conjugate of a complex number, we can write:

$$I_{rec} \propto |E|^2 = EE^*$$

If the incident wave consists in the superposition of two coherent waves (say, an object and a reference), the resulting wave is the addition of the field amplitudes, which can be written:

$$I_{rec} \propto |E_{obj} + E_{ref}|^2 = E_{obj}E_{obj}^* + E_{ref}E_{ref}^* + E_{obj}E_{ref}^* + E_{obj}^*E_{ref}$$
$$= |E_{obj}|^2 + |E_{ref}|^2 + E_{obj}E_{ref}^* + E_{obj}^*E_{ref}$$

The final hologram can therefore be decomposed in three distinct contributions: A component which is merely the sum of the intensities of the object and reference beams taken separately, a term which contains the relative phase between reference and object waves (also called first diffraction order, for reasons that will soon become clear), and its conjugated image.

In Gabor's first versions of the setup, the object and reference beams were parallel to each other, and these three components were hard to separate, which was very detrimental to the quality of his images. Indeed, this configuration often shows doubled images (twin-image problem), contains a lot of optical noise (mostly from the first two terms) and was very prone to instrumental artifacts, such as dust on the lenses. These defects set back holography popularization for a few years. In fact, it almost led to a loss of interest in the technique, as it seemed unnecessarily complicated for a relatively poor performance. In all justice, one should recall that the first versions of the experiment were performed with sources of very limited coherence, as lasers were yet to be invented. This fact alone, was enough to severely limit the quality of the images that could be obtained [253].

The solution for the twin-image problem came a few years later, from the experiments of Emmett Leith and Juris Upatnieks in the Willow Run Laboratory in Michigan [254, 257, 258]. Leith and Upatnieks were developing optical strategies for signal processing of synthetic aperture radar for the US Army and realized that the Gabor's approach could be useful to record radar images. Just as Gabor when working between optics and electron physics, Leith and Upanieks had terminology problems, as radar physics and optics used different languages. A first step was then to formulate optical theory in terms of information theory - which was, by the way, extremely influential for optics [254, 255, 253]. To think about optics experiments in a signal-processing and information theory viewpoint led to the solution of the twin-image problem. By introducing an angle between the object and the reference beams, Leith and Upanieks were able to completely separate the two images. This can be easily understood by considering the signal as a superposition of plane waves. The inclination introduces a phase-term $e^{i\phi}$ between object and reference beams, leading to the following expression for the recorded intensity:

$$I_{rec} \propto |E_{obj} + E_{ref}e^{i\phi}|^2 = E_{obj}E_{obj}^* + E_{ref}E_{ref}^* + E_{obj}E_{ref}^*e^{-i\phi} + E_{obj}^*E_{ref}e^{i\phi}$$

$$= |E_{obj}|^2 + |E_{ref}|^2 + E_{obj}E_{ref}^*e^{-i\phi} + E_{obj}^*E_{ref}e^{i\phi}$$

If we now think about it on Fourier space (the frequency domain, also called k-space in this text), we realize that multiplying by a phase term corresponds to a shift of the patterns on the Fourier space. This can be understood by considering that a multiplication by e^{-ia} in the real space amounts to a convolution by delta function $\delta(k-a)$ in the Fourier space.

Therefore when seen in the k-space, the phase containing terms (from now on called the +1 and -1 orders) are shifted in opposite directions (See Fig.A.7). The +1 and -1 orders become then spatially separated, allowing filtering of the unwanted orders, thus eliminating noise (continuous component) and the twin-image. The differences between the holograms of Gabor and of Leith-Upatnieks is illustrated in Fig.A.2.

This was a turning point for the development of Holography. Having solved this problem, Leith and Upatnieks produced very convincing holograms, not only of two dimensional semi-transparent objects, such as the ones treated until then, but also full images of real three dimensional objects (see Fig.A.3). From this point on, holography made the spotlights, gaining attention from both academic and general public. Ultimate recognition of the importance of the technique came soon later in 1971 with the award of the Physics Nobel Prize to Dennis Gabor *"for his invention and development of the holographic method"*.
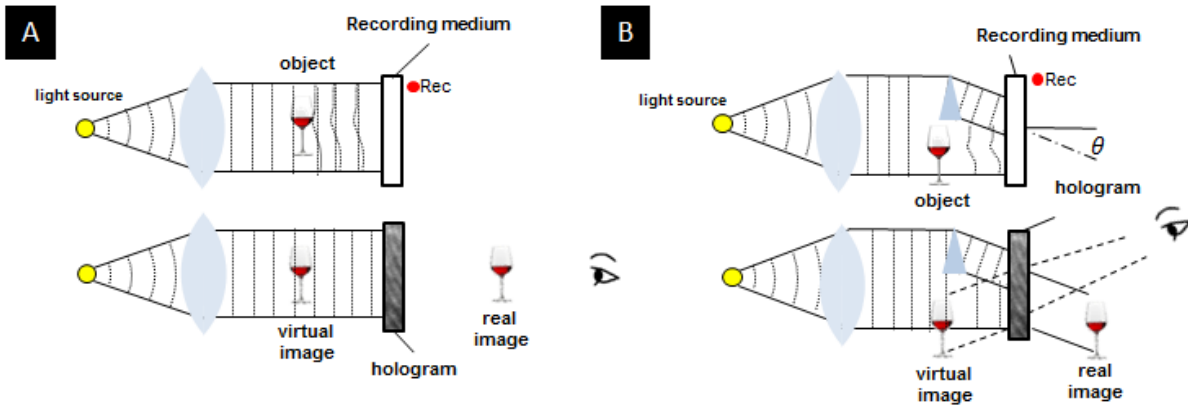
Figure A.2: Principles of Holography, comparison between (A) Gabor's inline and (B) Leith and Upatnieks off-axis setup. The recording steps are shown on the upper pictures while the reconstruction steps are on the bottom. In (A), a twin image is obtained, as the reference is parallel to the object beam and the images form on the same direction. When an angle θ is introduced between the reference and object, (B), the twin images are physically separated, thus solving the twin-image problem and yielding a much clearer reconstruction.

A.1.2 Further Developments and Digital Holography

From this point on, many innovations followed (See Fig.A.3), granting super fast hologram acquisition with pulsed lasers[259], holograms with the illusion of movement [260], with color [261], etc. An extensive survey would be rather pointless to this thesis (also probably impossible, as holography is still a steadily-growing field), as it would bore both the reader and myself. Instead, we shall concentrate on a few modifications of the original experiment in direct relation with our experimental setup.

In a broader context, holography also quickly found many new applications, such as non-destructive testing [262, 263], quality control [264], imaging in biological medium [265], vibration and deformation analysis [266] etc.

Of particular interest for this text was the shift from an analog support (such as the photographic plate) to a numerical medium. The idea of recording holograms digitally came out naturally with the development of computers. The first attempts of using computers to generate holograms date back to the late 1960's [267, 268], but they severely suffered from the poor computational tools available at the time. Digital holograms therefore only begun to become popular in the 1990's, when computer power was sufficiently available to allow rapid acquisition and numerical treatment for the reconstruction process[269, 263].

To treat holograms digitally has many advantages, such as the integrated recording and development procedure, the possibility of recording long time-lapses (videos), flexible data treatment, etc. Moreover, the low cost of the involved equipment makes numerical holography a much more economic choice. It has also been explored as creative 3D volumetric displays [270, 271]. Indeed, digital holography occupies quite a central place in many of very recent efforts towards augmented and virtual reality [272].
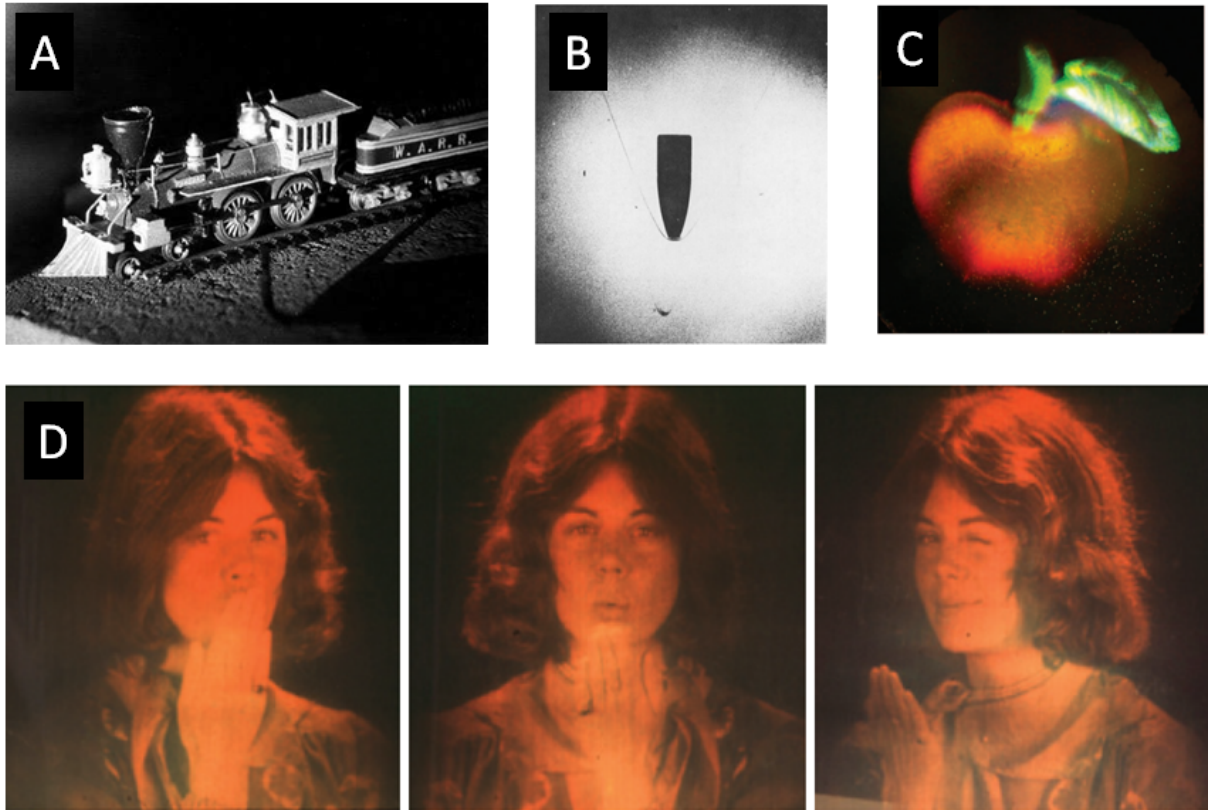
Figure A.3: Development of holography that shortly followed the original experiments. (A) 3D image of a toy-model of a train, from Leith and Upatnieks experiment [258, 253]. (B) pulsed-laser hologram of a bullet taken in plain flight [259]. (C) Hologram in colors [261]. (D) Famous holographic stereogram *Mini Kiss II*, as an example of an hologram with illusion of movement[260].
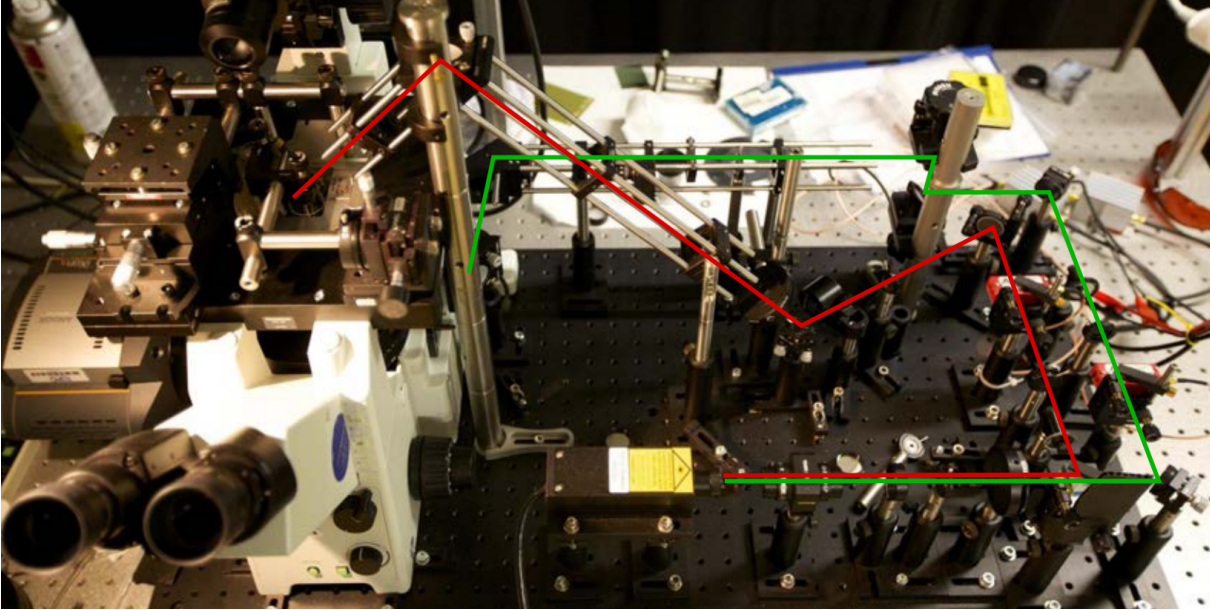
Figure A.4: Photograph of our dark field off axis holography setup used. The green light indicates the path of the reference beam, while the red one indicates the object beam

A.1.3 Optical Setup: Dark Field Digital Off-axis holographic microscopy

Having discussed the basics of holography, we are now in a position to focus on the setup actually used for the experiments. The whole setup is adapted to an inverted microscope Olympus IX71. A picture of the setup is shown in Fig.A.4, while a detailed description can be found in Fig.A.5.

A long coherence length single mode laser ($\lambda = 532$nm , $P = 80mW$) was used as light source. The excitation beam, which is split in two using a polarizing beam splitter (PBS). One part of this is used as the reference beam (E_{ref}), and the other as the object beam (E_{obj}). A half wave plate is placed just before the beam splitter in order to control the intensity power ratio $|E_{obj}|^2/|E_{ref}|^2$. Variable Optical Densities (OD) and half wave plates (HWP) are used to finely tune the power and polarization of each beam, allowing alignment of the polarizations of E_{ref} and E_{obj} and thus the maximization of the fringes contrast.

The object beam is conducted into the microfluidic cell (our sample) in a total internal reflexion (TIR) configuration using a glass prism, as shown in Fig.A.6. In this configuration, the light penetrates the cell at an incidence angle lower than the glass/water total reflection angle ($\approx asin(1.3/1.5) = 60.1^o$), but larger than that of the last glass/air interface ($\approx asin(1/1.5) = 41.8^o$). This ensures a dark field illumination and therefore maximization of the SNR.

Inside the cell, the laser beam interacts with the NPs, and the scattered light is collected by the microscope objective (typically a x100/0.9 NA, but x60/0.7 NA and
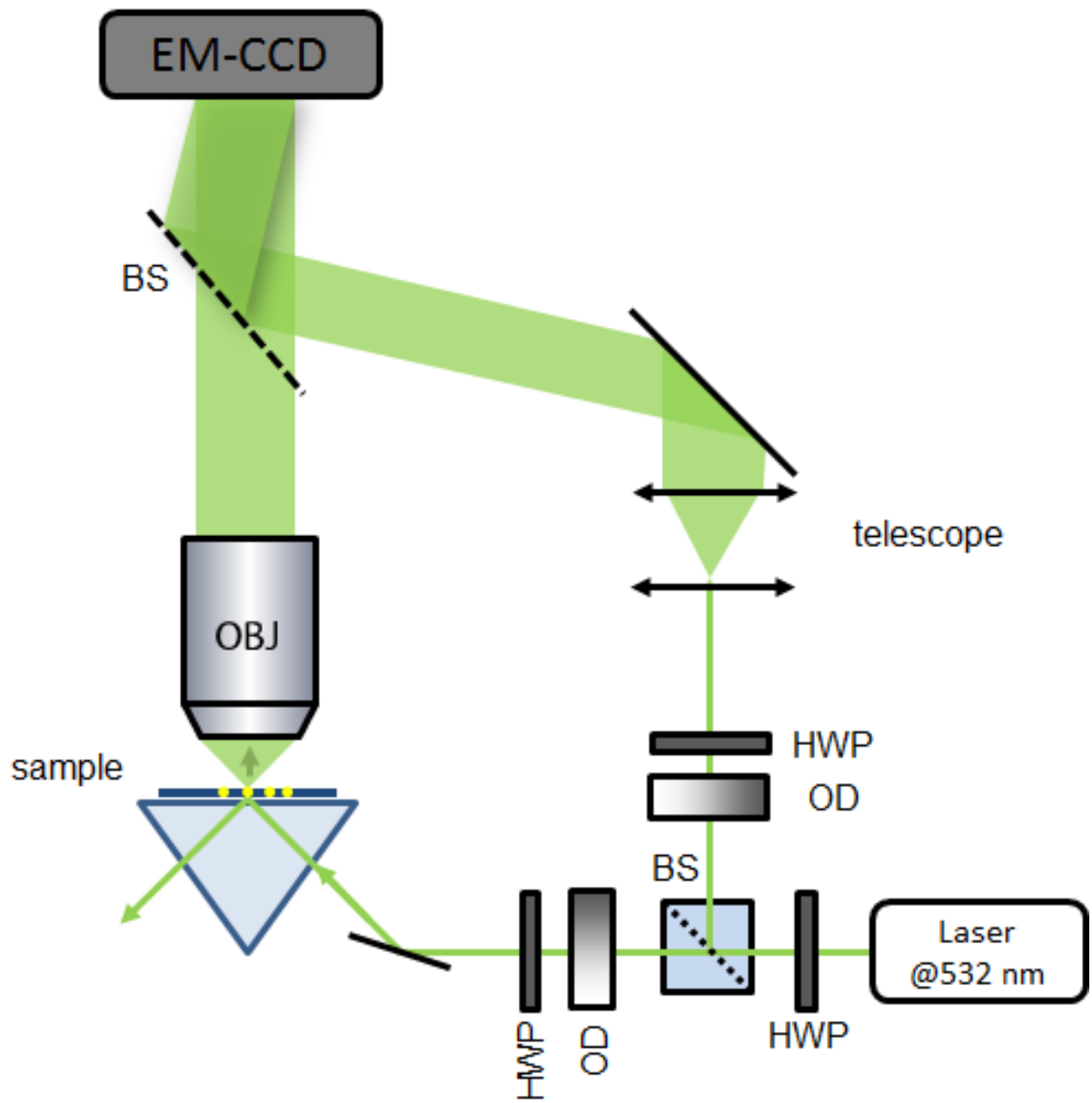
Figure A.5: Scheme of the optical setup used.
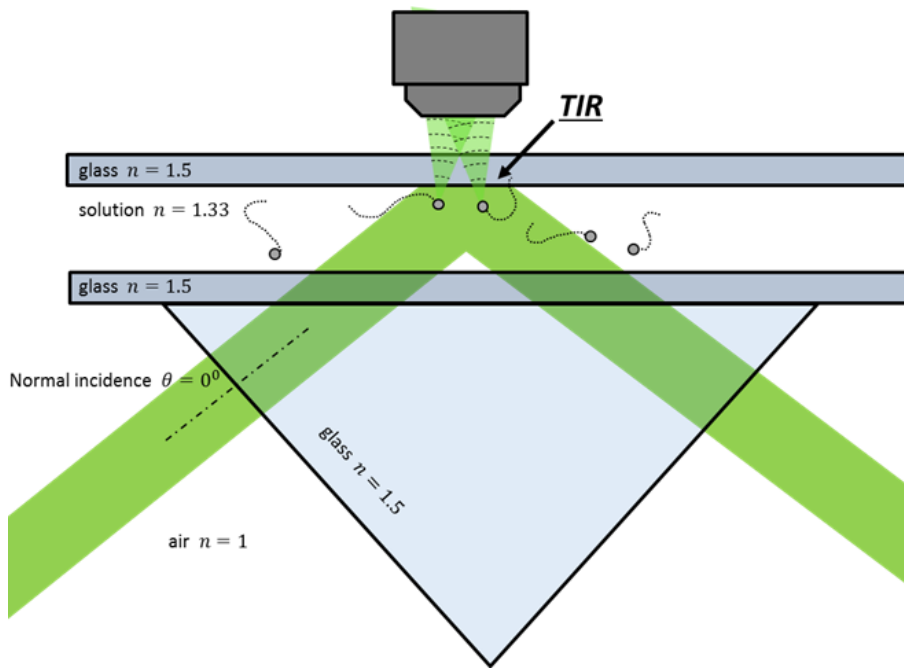
Figure A.6: Total Internal Reflection Configuration, creating a dark field configuration: the incident light is rejected and only the light scattered by the sample reaches the objective.

x20/0.45 NA were also used).

The reference beam is sent through a telescope in order to expand it (so that the full detector surface is covered), before passing through a mirror that regulates the off-axis angle.The beams are finally recombined using a semitransparent film and later sent to the EM-CCD camera.

The choice of the camera was also crucial as it would determine the maximal sensitivity and time scales. Unless stated otherwise a EM-CCD camera (Andor iXon3 885, cooled at 10^oC, up to 40 Hz acquisition rate for 512×512 images, with $8\mu m$ square pixels) was used for all holography experiments herein described.

A.1.4 From a hologram to a reconstructed volume: The holographic procedure

When the object beam is recombined with the reference, the hologram, i.e. an interference pattern like the one shown in Fig.A.7, is obtained. A careful inspection of the image, shown in the inset, reveals the presence of a few Ag nanoparticles. It is easy to notice that not only their presence alters the intensity of the pattern (more light is scattered), but they also modify the shape of the pattern, encoding the phase information that will later be used to determine the particle z-position (heuristically speaking).

The principle of the digital reconstruction procedure is first to obtain a clear measurement of the field in the z=0 plane, and then to numerically propagate it, generating images of the field on any desired z plane.

To describe the numeric reconstruction procedure we take off from the point where we left on Sec.A.1.1. The object field, E_{obj}, has passed through the microfluidic cell and interacted with the particles, therefore it contains the information about the sample. The beams are recombined with a beam splitter before reaching the CCD camera. The reference beam is inclined with respect to the object at an angle θ, forming an off-axis configuration, which allows the separation of the parasitic orders through a filtering procedure (which will be soon described). The field on the recording plane can then be described by:

$$= \underbrace{|E_{obj}(x,y,0)|^2 + |E_{ref}(x,y,0)|^2}_{\text{order 0}} + \underbrace{E_{obj}(x,y,0)E_{ref}(x,y,0)^*e^{-i\phi(x,y)}}_{\text{order -1}}$$
$$+ \underbrace{E_{obj}(x,y,0)^*E_{ref}(x,y,0)e^{i\phi(x,y)}}_{\text{order 1}} \quad \text{(A.1)}$$

The phase term $\phi(x,y)$ describes the effect of the inclination on the relative angle between the two beams. It is linear in both directions, and can thus be expressed as $\phi(x,y) = Ax + By$ in which A and B are coefficients fully determined by the angle θ.

The filtering and propagation operations are however easier to describe for plane waves, which is why the numerical treatment of the hologram starts with a dioptry correction.

Dioptry correction   In most holographic experiments, and particularly when using a relatively complex system such as a microscope, both the object and reference wave can be affected by phase curvature, either intentionally or due to imperfect focusing. Failure to observe this point can lead to major deformation of the reconstructed image and sensitive decrease on the precision [273]. Fortunately, this deviation from plane waves is spherical, and can easily be corrected numerically by using the following phase correction:

$$Diop_d(x,y) = exp(i\pi(x^2 + y^2)/\lambda d)$$

where d is a factor accounting for the effective curvature. Although it could be calculated, it is in practice easier to inspect the (spatial) spectral content of the signal to adjust it finely in the Fourier (wave vectors) space, as will be shown in the next section.

Besides being easy to deal with mathematically, it is preferable to work with plane waves, as the energy dispersion of a spherical wave could lead to unwanted aliasing effects.

Inspecting the image in the k-space   The image recorded on the CCD camera can be decomposed in its spatial frequencies by using a 2D Fourier transform, defined by:

$$\hat{E}(k_x, k_y, 0) = \iint_{-\infty}^{\infty} E(x,y,0)e^{-2\pi i(k_x x + k_y y)}dxdy$$

$\hat{E}(k_x, k_y, 0)$ is the image of the spatial frequency domain, also referred to as *k-space*

or *Fourier Space*.

In the k-space, the spatial frequencies can be easily visualized. Owing to the off-axis configuration, the different orders of the signal are multiplied by an extra $e^{i\phi(x,y)}$ term. A muliplicative term becomes a convolution product on the k-space (this is sometimes referred to as the *Convolution Theorem*). Since the Fourier transform (noted $\mathcal{F}(.)$) of a phase term is a Dirac Delta function, $\mathcal{F}(e^{iAx+iBy}) = \delta(k_x - A, k_y - B)$, the signal (Eq.A.1), then becomes:

$$
= \underbrace{\mathcal{F}\left(|E_{obj}(x,y,0)|^2 + |E_{ref}(x,y,0)|^2\right)}_{order0} + \underbrace{\mathcal{F}\left(E_{obj}(x,y,0)E_{ref}(x,y,0)^*\right) * \delta(k_x + A, k_y + B)}_{order-1}
$$
$$
+ \underbrace{\mathcal{F}\left(E_{obj}(x,y,0)^* E_{ref}(x,y,0)\right) * \delta(k_x - A, k_y - B)}_{order1}
$$
$$
\text{(A.2)}
$$

A convolution by a delta function corresponds to a shift, $f(x) * \delta(x - x_0) = f(x - x_0)$. It becomes therefore clear why the phase terms leads to a separation of the different orders in the k-space. This is also illustrated on Fig.A.7B.

At this point it is also easy to verify if the dioptry correction in the previous section was correctly performed, as the limits of the $+1$ order, which corresponds to the image of the back focal plane of the objective, should be sharp and not diffuse if the right correction factor d is chosen.

Real-time inspection of the k-space also allows the optimization of the angle between the object and reference planes, as it regulates the position of the $+1$ and -1 orders. The angle θ (and therefore the coefficients A and B) should then be regulated so that the orders occupy a maximum of spectral space without overlapping with each other [273, 274]. A correct separation in the Fourier space allows a correct filtering of the unwanted orders, as described in the following section.

Elimination of the parasitic orders With the orders well separated in the k-space, it is easy to design a filter to eliminate the unwanted -1 and 0 orders. In the real space, this corresponds to keeping only the modulated part of the signal, therefore eliminating most of the instrumental noise and the twin image.

After filtering, the selected order is brought to the center of the k-space. This physically correspond to a change in the frequency of the interference fringes, making the modulated parts of the signal become continuous, $(k_x, k_y) : (A, B) \mapsto (0, 0)$. This is shown in Fig.A.7C.

After these operations, we obtain a signal which corresponds to a clear full-information representation of the wavefront in the k-space. The image can be brought back to the real space by an inverse Fourier Transform:
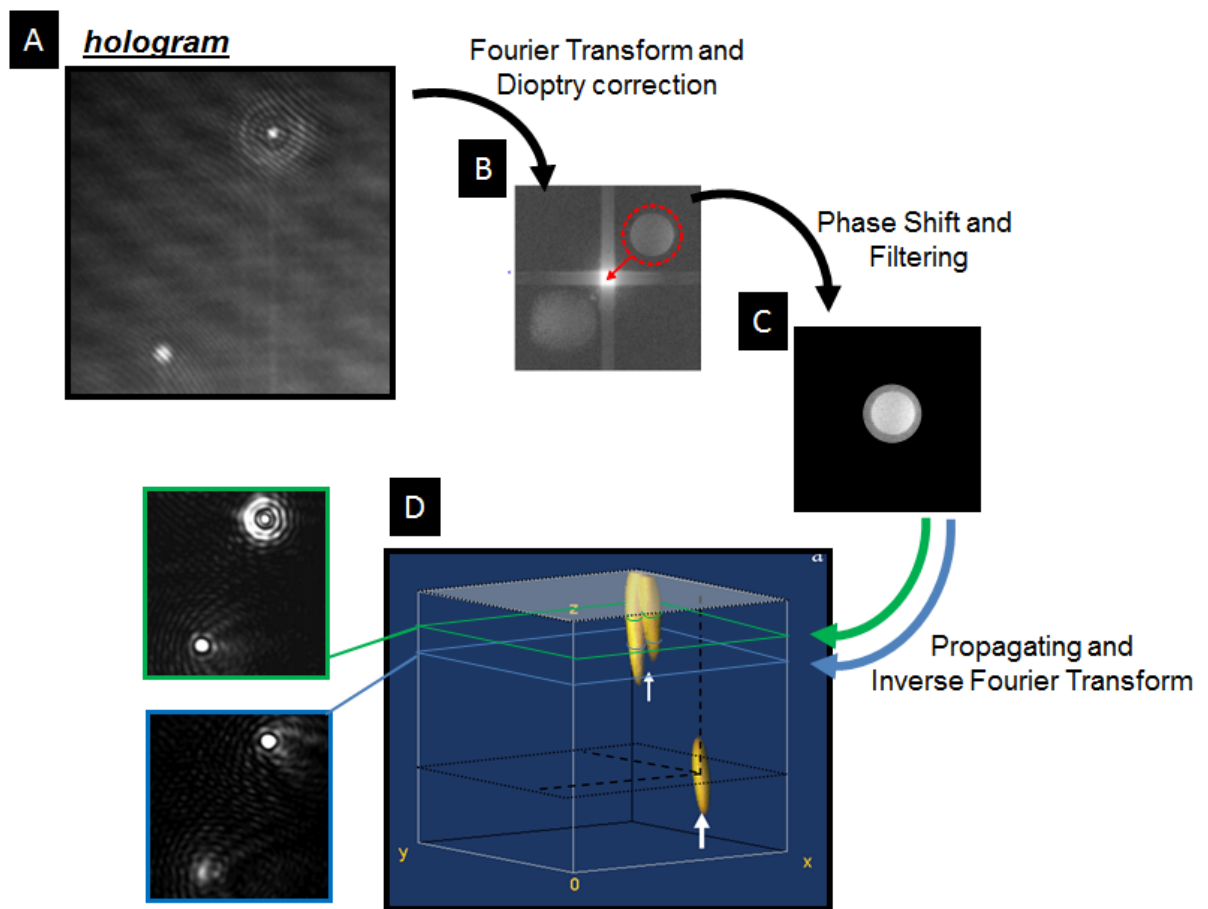
Figure A.7: Numerical reconstruction procedure: .

$$E(x, y, 0) = \iint_{-\infty}^{\infty} \hat{E}(k_x, k_y, 0) e^{2\pi i(k_x x + k_y y)} dk_x dk_y$$

The inverse transformation therefore yields a filtered image of the focal ($z = 0$) plane, $E(x, y, 0)$. The next section describes how to transform this into another arbitrary z plane using a propagation operator.

Propagation Factor We are now in the position to describe the transformation which allows to transform E(x,y,0) into E(x,y,z). For any given point in the $z = 0$ plane, we can consider how an infinitely brief impulsion would spread into any z plane. Owing to the linearity of the EM field propagation, we can then use the superposition principle to conclude that the distribution would be the sum of the contributions for all the points of the original E(x,y,0). In other words, if the impulsional response at a given plane is noted $G(x, y, z)$, we can write $E(x, y, z) = E(x, y, 0) * G_z(x, y)$. The impulsional response $G_z(x, y)$ is also called the *Green function*.

In the k-space, this convolution product becomes a simple multiplication by the Fourier Transform of $G(x, y)$, noted $\hat{G}_z(k_x, k_y)$:

$$\hat{G}_z(k_x, k_y) = e^{i\sqrt{k^2 - k_x^2 - k_y^2}z}$$

The wave vector $\vec{k} = (k_x, k_y, k_z)$ has a modulus $2\pi/\lambda$, with λ being the laser wavelength. This imposes a condition on the spatial frequencies k_x and k_y: $k_x^2 + k_y^2 \leq (2\pi/\lambda)^2$, which reflects the diffraction limit.

After the dioptry correction and the propagation matrix are applied, we can go back to the real space, recovering an image of the z plane(shown for two planes in Fig.A.7D). If this process is iterated over many evenly spaced planes, a full volume is obtained. Since for every plane, an independent calculation is done, this whole process is very prone to parallelization. For this reason a Graphical Processing Units (GPUs), which use hundreds of cores in parallel, are very adapted. Using the NVIDIA CUDA language, a procedure was designed to speed the reconstruction. An improvement by a factor of the order of 100 has been obtained by adapting a code initially proposed by F. Verpillat and M. Gross [275].

We then obtain a volume in which the intensity is calculated in each voxel of the volume (xyz), such as the one shown in Fig.A.7D.

Besides the propagation, the discretization of the hologram in the pixel matrix of the CCD camera also imposes a limit on the resolution of the hologram, acting as a low-pass filter. This imposes a cut-off frequency which depends on the pixel size L_{pix} and on the magnification M (Shannon-Nyguist Theorem). The cut-off frequency is of the order of $1/(ML_{pix})$. Since our goal in this thesis was always to image small isolated scatterers, however, these resolution limits can be partially overcome by application of

superlocalization techniques, which are discussed in the next section.

A.2   Superlocalization in the context of holography

A.2.1   Superlocalization Principle

The ideas behind superlocalization and superresolution methods were already outlined in Sec.1.1.5. They are based on the understanding that for isolated scatterers, the diffraction spot is centered in the emitter/scatterer position. The shape of the PSF can then be fit by theoretical expressions and the center of these function can be pointed with great precision, thus providing a much better estimation of the exact localization of the scatterer.

The improvement provided by the superlocalization is therefore essentially driven by the quality of the fit, i.e. the signal-to-noise ratio of the measurement, and mainly depends on the number of detected photons, $N_{photons}$. Actually, each photon can be understood as an independent estimation of the emitter position. At high enough photon counts, the precision should therefore scale as $\sqrt{N_{photons}}$ [276].

Usually, Gaussian functions are used to describe the PSF shape, but parabolas can just as likely be used, for the sake of simplicity. The number of pixels used in the fit is not the most critical parameter, as long as there are enough pixels to provide a decent estimation of the superlocalization (typically $> 3 \times 3$ pixels), and in the absence of parasitic features. Typically, it is desirable to limit the fitting region to the size of the diffraction spot.

In the holography experiments herein described, the four closest neighbours were considered for fiting the diffraction limited spots by either Gaussian Functions in the x,y directions, and the two closest in the z direction to fit the PSF by a parabola. These parameters and strategies were empirically determined and correspond to an extend of ≈ 300nm.

A.2.2   Localization Limits

Finally, we conclude this experimental section on holography by discussing the limits of the localization procedure. Two main sources of imprecision exist. First, the intrinsic error of the localization, which depends heavily on the signal to noise ratio, and second the error due to possible movements of the particle during the image acquisition time. The dominant source of incertitude depends on the exact experimental condition, as will be analyzed shortly.

The intrinsic error of the localization process can be identified by analyzing immobile particles. As the superlocalization process relies on fitting the PSF, the imprecision are highly dependent on having a clear signal. A good Signal-to-noise ratio (SNR) is therefore crucial for obtaining a good localization procedure. For immobile particles, and using heterodyne detection (with SNR ≈ 100), it is possible to superlocalize NP with

a precision as good as $3 \times 3 \times 10$ nm^3, as shown in Fig.1.8. This however is a best-case scenario degraded results are expected for moving particles and in the absence of heterodyne filtering [99]. In our experiments, we can evaluate the localization procedure precision by looking at a scattering point located at the electrode surface, which might be either a defect or a still particle. In this case, the localization precision is around $10 \times 10 \times 30$nm^3 [148, 277].

A particle moving in solution suffers from a more compelling source of uncertainty: the fact that its position is not fixed during the signal acquisition. Therefore the actual detection represents a mean position during the exposure time, which moves at average distance of $\sqrt{2D\tau_{exp}}$. For our setup conditions as described above we typically used $\tau_{exp} \approx$ 1ms, therefore for 50 nm particles ($D = 4.8\mu m^2/s$) this corresponds to an uncertainty of $\approx 100nm$ in all directions. As the particle approached a surface, the diffusion coefficient is hindered, improving the localization precision down to $50 \times 50 \times 50nm^3$.

In order to maximize the precision, there is necessarily a trade-off between exposing long enough so that a good SNR is obtained, but not too long, so that the particle movement does not blur the acquisition.

The difficulty of addressing much smaller particles resides in the fact that the two components of the error tend to increase: exposition error due to the fact that the particles move faster, and intrinsic error due to an overall smaller scattering cross section. For our actual experiments conditions, one can expect to address particles of at most 20 nm radius, at best.

It is interesting to highlight that increasing the laser power can considerably decrease the exposure time and increase scattering, thus reducing the imprecision. However, other parasitic effects appear with higher laser power, such as localized heating, that must be accounted for.

A.3   Plasmonics and Nanoparticles Spectroscopy

The theory that describes light scattering by small objects compared to the wavelength, the Mie Theory, was first developed more than one century ago [278]. Most of its developments stem from the central problem of light scattering by a homogeneous sphere, which was originally solved by Gustav Mie at the beginning of the century [64]. This analytical theory can accurately predict the spectrum of the light scattered by isolated objects in a solution but the spectra may deviate from Mie Theory predictions when the objects are near other particles, or next to a conducting surface.

Although Mie theory was eventually used for estimating particles spectra, a precise calculation of the spectra in the general case was instead performed by numerical simulations, using a variety of methods, such as FEM (using COMSOL, such as done in Sec.3.3), or finite differences (using FDTD, as in Sec.2.4.2).

A.3.1   Spectral Acquisition Setup

In the works presented in this thesis, two very similar setups were used to acquire the spectra of individual NPs, differing only in the way in which dark-field illumination was achieved.

In the first setup, used to monitor NP over a transparent electrode in Sec.2.4.2, an air dark-field condenser (Olympus U-DCD, NA = 0.8-0.92), was used to excite the nanoparticles with a high illumination angle. Attention must only be paid to the fact that the illumination angle should be superior to the collection angle of the objective, thus avoiding collection of the incident light.

In the second setup, used to monitor nanoelectrodes in Ch.4, a multimode optical fiber (core diameter 1 mm, NA = 0.2) coupled to a broadband xenon arc lamp of high intensity. The optical fiber is manually placed as close as possible to the nanoelectrode. It is oriented perpendicularly to the objective axis, minimizing direct incident light collection and therefore increasing contrast.

After being scattered by the sample, the light is collected by the microscope objective is split in two pathways using a beam splitter. One part is collected directly by a first camera (CCD1), giving a dark field image of the sample. The second branch is directed to a line-spectrometer (Specim Imspector V10E) operating in the visible range and then sent to a second camera, CCD2.

The image obtained with CCD2 directly shows the spectra of the different scattering objects present on the different pixels of a given line (the red line schematically drawn in the DF image) of the plane of the UME.

With this configuration, CCD1 images the reactivity on the whole field of view, while CCD2 monitors the spectroscopic changes associated to the reactivity of selected NPs present in a defined region (line) of the image.

The recorded signal is a mixture of the spectrum of the particle, background noise, and is spectrally inhomogeneous. For this reasons, it needs to be numerically treated, as described next.

A.3.2   Processing of the spectra

Once recorded, the spectra needs to be treated in order to reduce noise and to account for the spectral distribution of the illumination. For that reason, the spectrum of the background (a region where no particle is present, called $Bg(\lambda)$) is measured and subtracted from the raw spectrum ($RawSpect(\lambda)$). This operation is followed by normalization by the intensity of the illumination ($IL(\lambda)$), itself subtracted by the camera instrumental noise($Inst(\lambda)$), also called dark noise, which is measured by switching off the illumination and recording a spectrum. Otherwise stated:

$$NormSpect(\lambda) = \frac{RawSpect(\lambda) - Bg(\lambda)}{IL(\lambda) - Inst(\lambda)}$$

This ensures the recording of standardized spectra with minimal noise, and was applied to all spectra shown in this thesis.

A.4 MSD and size estimation from Brownian Motion

Small colloidal particles in suspension endure persistent collisions with solvent molecules, which propel them in random directions. The resulting stochastic movement is known as Brownian motion and has been extensively studied over the last century [174]. It is intimately related to diffusion processes, as it shall be seen.

Being a stochastic process, the resulting trajectories cannot be reliably described in a deterministic fashion. They can however be well characterized through their statistical properties, which provide useful information about the particles, such as size and anisotropy. Heuristically, the main idea is that the bigger a particle is (compared to small solvent molecules), the smaller the influence of the collisions will be. Therefore more collisions will be needed to move the particle a given distance, and, since the collision frequency is roughly constant, the amplitude of the fluctuations of the particle position will be smaller, i.e. it will move more 'slowly'.

In order to extract useful information out of this erratic movement, one has to state these intuitive ideas more precisely, in a quantitative way.

Mathematically, two assumptions are made: that the movement has no preferred direction (although this condition may be relieved by including a drift on the particle movement, as it will be seen), and that it has no memory - what is sometimes called the *Markovian property.* This last condition reflects the fact that the collision of a small entity with the particle happens quite fast and instantaneously transfers energy to the particle. This is fully justified in the context of our experiments, as the duration of the collision is indeed much smaller than all the other timescales considered.

Since there is no preferred direction, an axis can be arbitrarily defined and the projections of the movement along each of the axes will have zero mean, i.e., $\mathbb{E}[R_i] = 0$, $\mathbb{E}[X]$ being the expected value of a random variable X.

By considering that the movement has no memory, we can divide any timeline in arbitrarily small intervals, and see the total displacement of the particle as the sum of independent position increments. The *no memory* assumption assures us that the position increments over each of these subintervals are independent.

If the subintervals are made equal, the position increments constitute a set of independent identically distributed random variables. The central limit theorem can then be applied to the sum over all subintervals, and conclude that the displacement on each time interval will be normally distributed with zero mean (no preferred direction). As a

consequence, if more and more time intervals of a given length are considered, the wider the distribution will be.

We can then define a coefficient that will describe how fast the position probability distribution widens over time, i.e. how efficiently the solvent collisions are dispersing the particle.

Provided the system characteristics are not changing over time (a property called ergodicity), the displacement distributions over different time intervals will be the same, therefore the variance of the total displacement will increase linearly as a function of time. Since the mean of the movement is zero, this also holds true for the second moment of the distribution (the mean square displacement), meaning that $< x^2 > \propto \Delta t$. This coefficient, D, is called the diffusion coefficient and is defined as $D = \frac{<x^2>}{2\delta t}$. It is related to the particle size and the medium properties through the Einstein-Stokes relation:

$$D = \frac{k_b T}{6\pi\eta r}$$

By measuring the mean square displacement (MSD) for different time intervals, we can therefore estimate the effective (hydrodynamic) radius of the particle. In single particle experiments, this information is particularly useful, since it is a method to determine particle size on a particle-by-particle basis. It is also a way of determining if drift is present or if the particle is bound to a particular region of the system. Indeed, if the movement is purely diffusive, the probability density function (PDF) of the particle position is a centered Gaussian with $2Dt$ variance per dimension order d. Therefore the MSD is expected to vary linearly with time and the slope to be equal to $2dD$ (See Fig.A.8).

If the particle is bound to a certain region of space, the particle will not be able to move further away, therefore once the particle has a fair probability of having met one of these boundaries, the PDF of the particle displacement will start to change from a Gaussian to an uniform distribution. The final and initial position become perfectly uncorrelated as all information about the initial position is progressively lost. The MSD curve will saturate at this point, as shown in Fig.A.8.

On the other hand, in presence of a drift velocity (v), the particle displacement can be decomposed into a stochastic and a deterministic component. The displacement pdf will be a Gaussian with variance $2Dt$ and mean equal to vt (See Fig.A.8). The diffusion coefficient can still be extracted, but localization errors can make this a delicate operation in practice, as will be discussed in section A.4.1.

These simple examples show how the analysis of MSD curves is a fruitful strategy to study diffusion processes. Indeed, it has been widely used by the biophysics community to probe anomalous diffusion processes of not only small particles but also molecules, bacteria, viruses, fluorescent probes such as quantum dots, etc. More than determining its hydrodynamic radius, MSD analysis has the potential to provide information about the object anisotropy [279], chemotaxis [280], medium properties characterization, etc. Also,
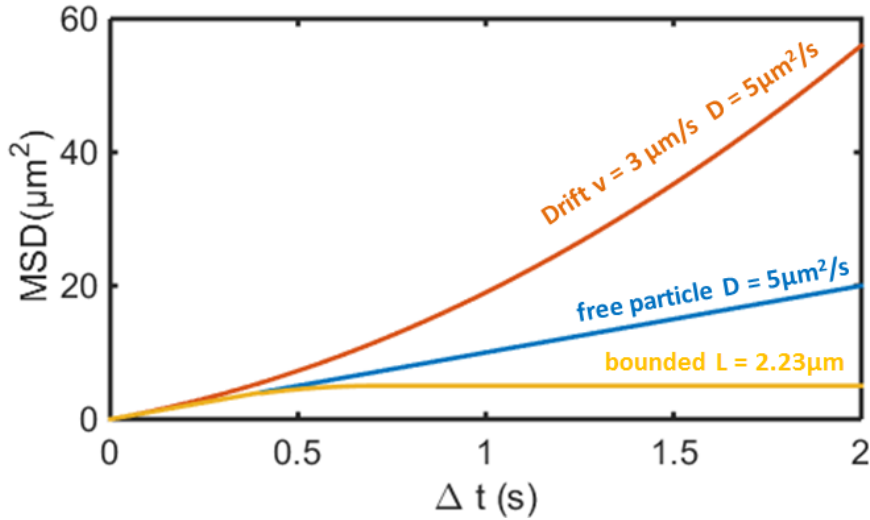
Figure A.8: Expected MSD curves (1D) in the cases of (blue) a freely diffusing particle ($D = 5\mu m^2/s$), (orange) diffusion in the presence of a drift velocity ($v = 3\mu m/s$) and (yellow) diffusion in a limited region of space (a box $\Omega = [-L, L]$, with $L = 2.23\mu m$).

being a single entity technique, MSD analysis also has the potential to reveal heterogeneity among a given population.

A.4.1 Time Average MSD and precision

One difficulty of the interpretation of MSD curves is that a large ensemble set is necessary in order to accurately estimate the mean square displacement. This triggers two major complications for MSD curve anaylsis. First, a practical complication, the analysis becomes extremely time consuming, as even modest error tolerance will require the tracking of a large number of particles. Secondly, and more importantly, to average measurements over different particles destroys the single-entity character of the measurements, hiding heterogeneities in the population.

One way of overcoming the second difficulty (but not the first), is to individually manipulate particles, thus repeating the same experiment again and again, always using the same particle. This has been achieved using optical tweezers, for example [281].A more convenient way, however, is to make use of the fact (or assumption) that the particle properties remain the same over times much longer than the measurement duration. In this case, statistical averages and time averages become indistinguishable, and we can achieve statistical soundness by merely tracking the same particle long enough. The idea is that the trajectory can be divided in many smaller trajectories, which can be averaged to obtain a time-averaged mean square displacement curve (TAMSD). In practice, if a trajectory consists in N positions, evaluated at discrete times $t = 1...N\Delta t$, the TAMSD is evaluated as:

$$TAMSD(i\Delta t) = \frac{1}{N-i} \sum_{k=1}^{N-i} \left(x((k+i)\Delta t) - x(k\Delta t)\right)^2$$

In this sense, the measurements performed in this work are essentially TAMSD, but we have chosen to label them as "MSD measurements" in the main text for simplicity. It can be shown through Monte Carlo Simulations that if the system is ergodic (meaning that statistical averages and time averages are equivalent) and perfectly homogeneous, these two approaches (small trajectories for many different particles or big trajectory of a single particle) are equivalent. In this case, the precision of the method depends on the number of points of the trajectory.

A.5   Monte Carlo simulation for Diffusion Models

Monte Carlo methods usually refer to simulations techniques using stochastic methods. They are particularly useful in describing the behavior of single diffusing particles, and were used to predict the average behavior of our systems and evaluate the precision of the MSD related procedures.

In general terms, the Monte Carlo procedure herein employed for simulating diffusion consisted in performing a *numerical experiment*: time is discretized in small time steps of length Δt and the displacement rules are stipulated in terms of probability distributions. For example, the displacement in one direction of a diffusing particle under Brownian motion during an interval Δt is described by a normal distribution with zero mean and variance $2D\Delta t$. Let $B_i^{\Delta t}$ be a random variable following this distribution. If the displacements $B_i^{\Delta t}$ are added, a random brownian motion trajectory forms. Otherwise stated , with $\mathcal{N}(\mu, \sigma^2)$ representing a normal distribution of mean μ and variance σ^2:

$$X(t = k\Delta t) = \sum_{1}^{k} B_i^{\Delta t}, \text{ with } B_i^{\Delta t} \sim \mathcal{N}(0, 2D\Delta t)$$

Higher Dimensions   if the movement is two- or three- dimensional, it can be constructed from the one-dimensional case either by (i) considering it as a combination of three orthogonal independent 1D Brownian motion or (ii) by sampling a random direction and decomposing a displacement of variance $6D\Delta t$ in three orthogonal components. The random direction was constructed from two uniformly distributed random variables, U and V, using the following operations: $\theta = 2\pi U, \phi = arccos(2V - 1)$. Then, $x = \cos\theta\sin\phi, y = \cos\theta\cos\phi$,and $z = \sin\theta$. This assures a homogeneous distribution on the unit sphere.

Deterministic Components   If the movement has a deterministic component (such as a drift velocity, as in Sec. 3.2), it can be added manually at each time step. For
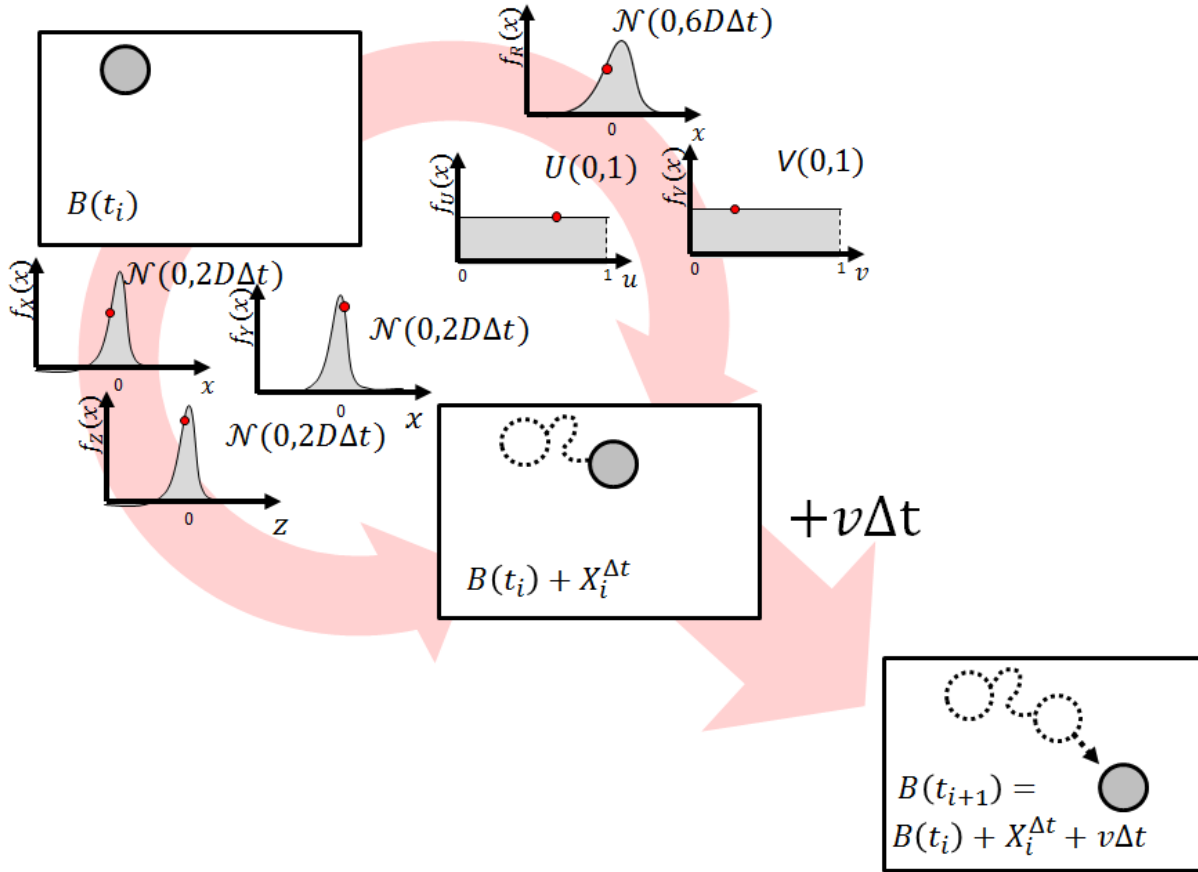
Figure A.9: Illustration of the Monte Carlo algorithm used for simulation of particle diffusion. the two sampling techniques are shown, as well as how to deal with the presence of deterministic components (such as a velocity drift).

example, in the case of a 3D BM with a drift v on x-direction, after each time step, $X(t)$ is incremented by an amount $v\Delta t$, in addition to the stochastic component.

The full algorithm is illustrated in A.9. This kind of simulation is quite useful when dealing with systems subjected to stochastic laws as they can reveal general laws (by making the trajectories very long or divided in arbitrarily small time steps Δt) or to directly simulate the outcomes of an experiment (by matching the simulation parameters and the experimental ones, for example: $\Delta t = 1/f_{sampling}$, with $f_{sampling}$ being the experimental sampling rate).

A.6 Lithography and Electrode Fabrication

All the transparent microelectrodes used in holography experiments were fabricated using lithography (See Sec. 2.2.2 and 2.2.3). In the present section, the details of the fabrication procedure are further developed.

Optical lithography is a widely applied, versatile technique for patterning surfaces

with micrometric precision. In a nutshell, it consists in using a combination of chemical etching, materials deposition, and usage of photosensitive resists that either become soluble (positive resists) or unsoluble (negative resists) upon exposure to light to design a layer-by-layer structure.

Wildly developed in order to meet the needs of the semi-conducting industry, lithography is nowadays a mature science. Its protocols are extremely reliable and performant, but require a very clean environments to be applied properly.

Throughout this thesis work, two different lithographic procedures were applied. The first one aiming at producing an array of twelve gold microelectrodes patterned with a Silicon Nitride insulating layer (Au/Si_3N_4) and the second one, simpler, intending to produce ITO or gold surfaces patterned with a polymer ($SU-8$) layer. All patterns were transfered from a custom-made lithographic mask, produced by Selba S.A. (4" bright field, chrome down).

A.6.1   Gold Microelectrode Array

The first lithographic process starts with the printing of a Au motif on a glass slide. After careful cleaning of the Au surface ($\approx$ 5 min cleaning in isopropanol and acetone, followed by exposure to O_2 plasma for 4 min and heating at 120^oC), the lithographic process starts with the spincoat deposition of a layer of a positive photosensitive resine (TI35-ES) corresponding to the negative of the intended Gold pattern. A 50 nm Gold layer is deposed by electron beam evaporation (Plassys MEB 505S). The resine is then removed by soaking it in acetone, thus leaving only the Au layer where there was no resine (a step known as lift-off). At the end of this step, we end up with an array of twelve electrodes printed over a glass slide, as shown in Fig.A.10. The next step is to isolate the whole electrode surface except a small window of $60 \times 60\mu m^2$, which is the only part of the surface that will get in contact with the solution.

In order to do so, the whole glass slide is covered with a layer of Si_3N_4 (the proportions are not really stoechiometric, but it will be referred to this way for simplicity), deposed by plasmon enhanced chemical vapor deposition (Corial D250). Next, a layer of positive resine is deposed (A1818), exposing only a $60 \times 60\mu m^2$ window on each electrode. The final step consisted in etching the Si_3N_4 layer by plasma etching (Sentech SI500). The resist layer protects the electrode surface, therefore the insulating layer is only etched over the $60 \times 60\mu m^2$ windows, thus defining the microelectrode.

The full procedure is illustrated in Fig.A.10. The detailed protocol is given below, at the end of this section.
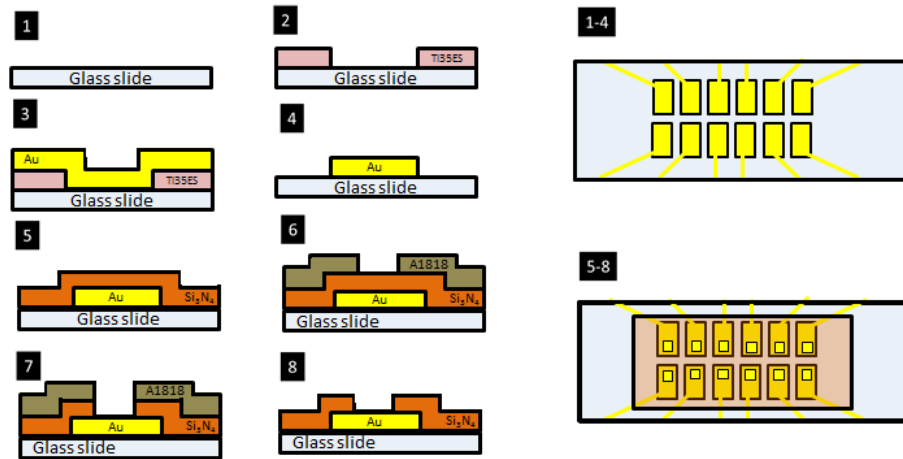
Figure A.10: Array of twelve independently addresable electrodes, obtained at the end of the lithographic printing process

A.6.2 ITO microelectrodes

Whenever ITO electrodes were used, the patterning procedure used for Au could not be employed, as the relatively high temperatures during PECVD caused the ITO electrode surface to drastically change. In this case, we opted for a direct patterning using SU-8 polymer.

Starting from an ITO (or sometimes Au) -coated glass slide, we rinse it carefully in acetone and isopropanol ($\approx$ 1min). Next, a negative resist is spin-coated and the slide is exposed to UV light for 20s. Due to a defect in the mask pattern, a second exposure might be needed in order to ensure a big enough insulating area (otherwise the microfluidic cell manufacture becomes quite challenging). The exposure is followed by heating at 95°C for 3 min 30s and by development in SU8-developer (1-Methoxy-2-propyl acetate) for 2 min 30s.

Protocol: Au/Si_3N_4 electrode

- Clean the glass slide

  - 5 min in Acetone followed by 5 min in Isopropanol
  - Dry on Nitrogen flow
  - 4 min Oxygen plasma (80% of max power(200W); generator frequency 40 KHz)
  - heat at 120°C for 4 min

- Resin spincoat

  - Spincoat TI-Prime (adhesion promoter) 500 rpm for 3s (for spreading) followed by 4000rpm for 30s

---

– Wait 1 min.

– spincoat Resin Ti-35ES.

– Heat at 100°C for 3 min.

• Exposure

  – set parameters to soft contact, exposure time 20s

  – WEC, adjust the height

  – move lever from contact to gap and align the mask

  – Expose for 20s ($\approx 200 mJ/cm^2$)

• Post treatment and Development

  – heat at 40°C for 10 min

  – heat at 130°C for 2 min

  – Exposure on flood mode (parameters : *flood exposure*)

  – Develop the pattern by immersing the glass slide on MIF326 or AZ326 (verify) for 45s. Carefully clean it with water and dry it using nitrogen flow.

• Thin Film Evaporation

  – clean by oxygen plasma for 5 min

  – evaporate Ti, deposit 2-5 nm at 0.05 nm/s

  – wait 5 min for the system to cool down

  – evaporate Au, deposit 45-50 nm at 0.05nm/s

• Lift off

  – put it in acetone for at least 5 min to remove the resist. use a seringe and ultrasound to help detach the resist. *NB : avoid direct air contact because if the acetone evaporates, gold residues might irreversibly attach to the surface - for a cleaner surface, use 2-3 acetones baths*

  – rinse in isopropanol

• Chemical Vapor Deposition

  – clean the chamber and insert electrodes (careful, it is hot!)

  – deposit 400 nm Si_3N_4

  – clean by oxygen plasma for 5 min

- Electrode Patterning and Etching

  - Spincoat Lithograpgy exposed goes away
  - use RIE to etch the unprotected parts of the electrode
  - clean the electrode in acetone until the remaining resin is completely gone

---

Protocol: ITO/Su-8 electrodes

- Clean the ITO surface

  - 5 min in Acetone followed by 5 min in isopropanol
  - dry under Nitrogen flow
  - 4 min Oxygen plasma (80% of max power(200W); generator frequency 40 KHz)
  - heat at 120^oC for 4 min

- Spin Coat the SU8-2010 resist over the ITO surface

  - spin coating 5000rpm 10s then 45000 rpm for 30s
  - Soft bake at 95^oC for 2min 30s

- Exposure

  - set parameters to hard contact, 14s exposure
  - WEC, adjust the height
  - Move lever from contact to gap and align the mask
  - Expose it (verify the parameters first)

- Post Treatment and Development

  - Hard Bake at 95^oC for 3min30s
  - Develop the pattern by immersing the ITO slide on SU8-Developer
  - Rinse it using isopropanol 10s, followed by water, isopropanol (again) and water
  - Dry under Nitrogen flow

A.7   Carbon Nanoelectrodes fabrication procedure

Carbon nanoelectrodes were fabricated according to a procedure established in literature [241, 52]. As already mentionned in Ch. 4, the electrode fabrication procedure consists in two steps. First, a laser puller is used to fabricate a nanopipette, which is later filled with butane gaz and heated, causing pyrolisis of the gaz and consequent deposition of conductive carbon on the quartz walls.

A.7.1   Pulling the capillaries

The capillary pulling steps are entirely performed by the laser puller (shown in Fig.A.11B). A focalized 20W CO_2 based laser beam (3.5mm diameter beam with 4mR divergence) is reflected by a scanning mirror which distributes the energy over 1-8 mm of the center of the capillary. The capillary is constantly held at a constant (low) axial load, and the creep velocity is monitored. Once it reaches an user-specified threshold value, the heating turns off and after a delay (also specified by the user) the axial load is enhanced to the value specified by the parameters (this step is also called the hard pull), leading to the formation of two nanopipettes, as shown in Fig.A.11A.

The whole process is controlled by five parameters, a graphic representation of their effects is given in Fig.A.11D:

- Heat (HEAT): this parameter controls the power of the laser used, and therefore the ultimate temperature reached at the capillary tip, all other parameters held equal.

- Filament (FIL): this controls the scanning pattern of the laser beam, which can vary between 1 and 8 mm. This therefore specifies the energy distribution profile.

- Velocity (VEL): as the glass softens, the creep velocity increases. This parameter represents the threshold value after each the hard pull will start.

- Force of the hard pull (PULL): this controls the force used during the hard pull.

- Delay (DEL): this parameter determines the time delay between the moment when the heat turns off and the pull starts.

After these steps, a nano pipette is obtained. For a given set of parameters, the pipette size is quite reproducible. The pipette charateristic however can vary with the pressure, humidity, and ambient temperature conditions,etc. This may require re-optimization of the parameters every few weeks. For reference, the latest parameters used were: **HEAT**=740 **FIL**=5 **VEL**=55 **DEL**=160 **PULL**=210
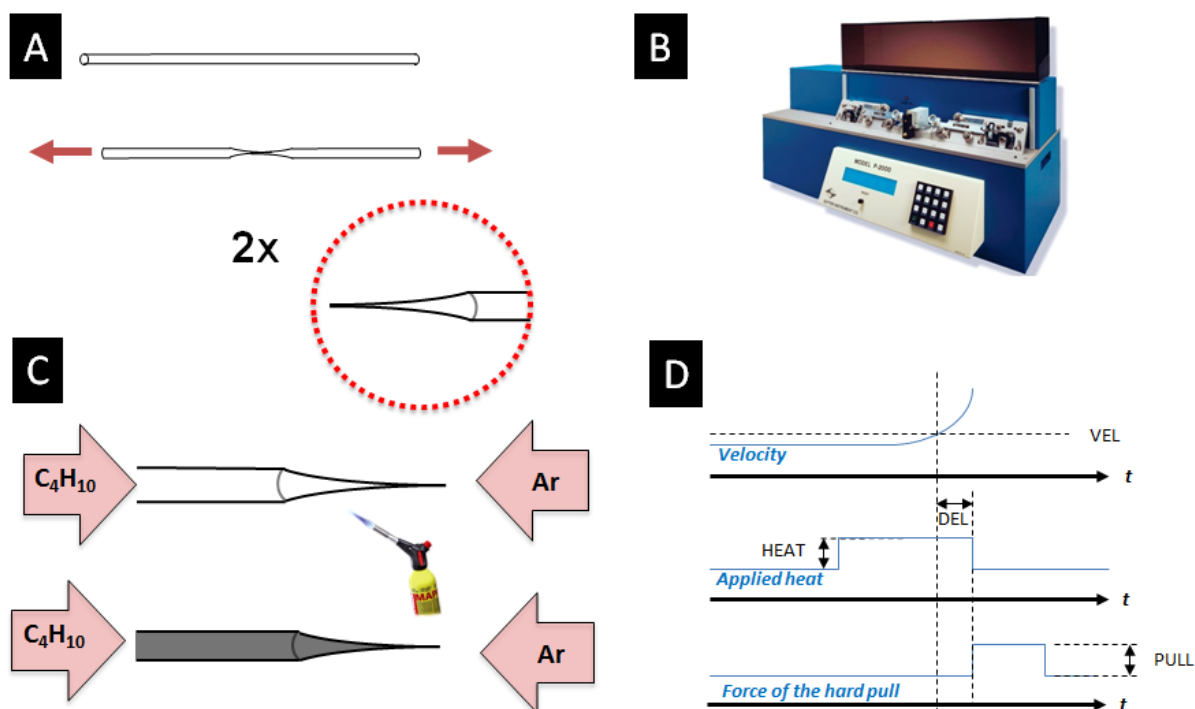
Figure A.11: Carbon Nanoelectrode fabrication procedure

A.7.2 Pyrolysis

Each nanopipette is then transformed into a nanoelectrode by filling it with butane gaz (camping gaz) and heating it with a butane burner (actually made for *crème brulée*). The electrode should be heated from the tip to the body and back in around 10-20 seconds, to ensure the deposition of a dense layer of pyrolyzed material on the apex.

This is the least controlled step on the nanoelectrode fabrication, and very likely the main source of variability on electrode size (especially between different operators).

A.7.3 Electrochemical characterization

Once pyrolysed, the nanoelectrodes are ready for use. However, it is still necessary to estimate their size, which can be done in first approximation by determining the steady-state current for the oxidation/reduction of some redox mediator. Typically, this was performed by cycling between -0.1 and 0.4 V (vs AgCl 0.1M) in 1mM Ferrocene methanol(FcMe) and measuring the steady state current plateau, I_{SS}. The electrode radius a can then be estimated with the following expression: $i_{SS} = 4FD[FcMe]a$, using $D \approx 10^{-5} cm^2/s$.

Although it is true that for very small electrode ($a \lesssim 10nm$) the continuum description used to derive this equation start to fail, it remains a good estimator of the order of magnitude of the electrode radius, thus serving well the goal of characterizing electrode size in a simple way.

Bibliography

[1] Raphael Meldola. *The Chemistry of Photography*. Elibron Classics, 1889. (p.2).

[2] P. W. Anderson. More is different. *Science*, 177(4047):393–396, 1972. (p.2).

[3] Rui Han, Ji Won Ha, Chaoxian Xiao, Yuchen Pei, Zhiyuan Qi, Bin Dong, Nicholas L. Bormann, Wenyu Huang, and Ning Fang. Geometry-assisted three-dimensional superlocalization imaging of single-molecule catalysis on modular multilayer nanocatalysts. *Angew. Chem. Int. Ed.*, 126(47):13079–13083, 2014. (p.4).

[4] Justin B. Sanbur, Tai-Yen Chen, Eric Choudhary, Guanqun Chen, Erin J. Nissen, Elayne M. Thomas, Nigmu Zou, and Peng Chen. Sub-particle reaction and photocurrent mapping to optimize catalyst-modified photoanodes. *Nature*, 530(7588):77–80, 2016. (p.4).

[5] Chung-Yeh Wu, William J. Wolf, Yehonatan Levartovsky, Hans A. Bechtel, Michael C. Martin, F. Dean Toste, and Elad Gross. High spatial resolution mapping of catalytic reactions on single particles. *Nature*, 541(7638):511–515, 2017. (p.4).

[6] Stefan W. Hell. Nobel lecture: Nanoscopy with freely propagating light. *Rev. Mod. Phys.*, 87:1169–1181, 2015. (p.4).

[7] A. Bogner, P.-H. Jouneau, G. Thollet, D. Basset, and C. Gauthier. A history of scanning electron microscopy developments: Towards wet-stem imaging. *Micron*, 38(4):390 – 401, 2007. (p.4).

[8] Joseph P. Patterson, Patricia Abellan, Michael S. Denny, Chiwoo Park, Nigel D. Browning, Seth M. Cohen, James E. Evans, and Nathan C. Gianneschi. Observing the growth of metal organic frameworks by in situ liquid cell transmission electron microscopy. *J. Am. Chem. Soc.*, 137(23):7322–7328, 2015. (p.4).

[9] Taro Uematsu, Masahiro Baba, Yoshifumi Oshima, Tetsuya Tsuda, Tsukasa Torimoto, and Susumu Kuwabata. Atomic resolution imaging of gold nanoparticle generation and growth in ionic liquids. *J. Am. Chem. Soc.*, 136(39):13789–13797, 2014. (p.4).

[10] G. Binnig, H. Rohrer, Ch. Gerber, and E. Weibel. 7x7 reconstruction on si(111) resolved in real space. *Phys. Rev. Lett.*, 50:120–123, Jan 1983. (p.5).

[11] Cyrus C.M. Mody. *Intrumental Community*. MIT Press, 2011. (pp.5, 5, 29, 29).

[12] K. Suto and O.M. Magnussen. In situ video-stm studies of sulfate dynamics on au(1 1 1). *J. Electroanal. Chem.*, 649(1–2):136 – 141, 2010. (p.5).

[13] Craig A Jeffrey, David A Harrington, and Sylvie Morin. In situ scanning tunneling microscopy of bismuth electrodeposition on au(1 1 1) surfaces. *Surf. Sci.*, 512(1–2):L367 – L372, 2002. (p.5).

[14] Jeyavel Velmurugan, Jean-Marc Noel, Wojciech Nogala, and Michael V. Mirkin. Nucleation

and growth of metal on nanoelectrodes. *Chem. Sci.*, 3:3307–3314, 2012. (pp.5, 12).

[15] Michael V. Mirkin, Tong Sun, Yun Yu, and Min Zhou. Electrochemistry at one nanoparticle. *Acc. Chem. Res.*, 49(10):2328–2335, 2016. (pp.6, 12).

[16] Fu-Ren F. Fan and Allen J. Bard. Electrochemical detection of single molecules. *Science*, 267(5199):871–874, 1995. (pp.6, 7).

[17] Je Hyun Bae, Yun Yu, and Michael V. Mirkin. Recessed nanoelectrodes for nanogap voltammetry. *ChemElectroChem*, 3(12):2043–2047, 2016. (p.6).

[18] Marcel A. G. Zevenbergen, Pradyumna S. Singh, Edgar D. Goluch, Bernhard L. Wolfrum, and Serge G. Lemay. Stochastic sensing of single molecules in a nanofluidic electrochemical device. *Nano Lett.*, 11(7):2881–2886, 2011. (pp.6, 7).

[19] Pradyumna S. Singh, Enno Katelhon, Klaus Mathwig, Bernhard Wolfrum, and Serge G. Lemay. Stochasticity in single-molecule nanoelectrochemistry: Origins, consequences, and solutions. *ACS Nano*, 6(11):9662–9671, 2012. (p.6).

[20] Qianjin Chen, Kim McKelvey, Martin A. Edwards, and Henry S. White. Redox cycling in nanogap electrochemical cells. the role of electrostatics in determining the cell response. *J. Phys. Chem. C*, 120(31):17251–17260, 2016. (p.6).

[21] Xiaoyin Xiao and Allen J. Bard. Observing single nanoparticle collisions at an ultramicroelectrode by electrocatalytic amplification. *J. Am. Chem. Soc.*, 129(31):9610–9612, 2007. (pp.7, 9, 11, 54).

[22] Allen J. Bard, Hongjun Zhou, and Seong Jung Kwon. Electrochemistry of single nanoparticles via electrocatalytic amplification. *Isr. J. Chem.*, 50(3):267–276, 2010. (pp.7, 9, 11).

[23] Seong Jung Kwon, Hongjun Zhou, Fu-Ren F. Fan, Vasily Vorobyev, Bo Zhang, and Allen J. Bard. Stochastic electrochemistry with electrocatalytic nanoparticles at inert ultramicroelectrodes-theory and experiments. *Phys. Chem. Chem. Phys.*, 13:5394–5402, 2011. (p.8).

[24] Donald A. Robinson, Aditya M. Kondajji, Alma D. Castañeda, Radhika Dasari, Richard M. Crooks, and Keith J. Stevenson. Addressing colloidal stability for unambiguous electroanalysis of single nanoparticle impacts. *The Journal of Physical Chemistry Letters*, 7(13): 2512–2517, 2016. (pp.8, 8, 54).

[25] Radhika Dasari, Kevin Tai, Donald A. Robinson, and Keith J. Stevenson. Electrochemical monitoring of single nanoparticle collisions at mercury-modified platinum ultramicroelectrodes. *ACS Nano*, 8(5):4539–4546, 2014. (pp.8, 9).

[26] Xiaoyin Xiao, Fu-Ren F. Fan, Jiping Zhou, and Allen J. Bard. Current transients in single nanoparticle collision events. *J. Am. Chem. Soc.*, 130(49):16669–16677, 2008. (p.9).

[27] Steven E. F. Kleijn, Beatriz Serrano-Bou, Alex I. Yanson, and Marc T. M. Koper. Influence of hydrazine-induced aggregation on the electrochemical detection of platinum nanoparticles. *Langmuir*, 29(6):2054–2064, 2013. (p.9).

[28] D. A. Robinson, J. Duay, A. M. Kondajji, and K. J. Stevenson. Mechanistic aspects of hydrazine-induced pt colloid instability and monitoring aggregation kinetics with nanoparticle impact electroanalysis. *Farad. Disc.*, 193:293–312, 2016. (pp.9, 54).

[29] Alma D. Castañeda, Timothy M. Alligrant, James A. Loussaert, and Richard M. Crooks. Electrocatalytic amplification of nanoparticle collisions at electrodes modified with poly-

electrolyte multilayer films. *Langmuir*, 31(2):876–885, 2015. (p.9).

[30] Jeffrey E. Dick and Allen J. Bard. Toward the digital electrochemical recognition of cobalt, iridium, nickel, and iron ion collisions by catalytic amplification. *J. Am. Chem. Soc.*, 138 (27):8446–8452, 2016. (p.9).

[31] Jeffrey E. Dick and Allen J. Bard. Recognizing single collisions of ptcl62+ at femtomolar concentrations on ultramicroelectrodes by nucleating electrocatalytic clusters. *J. Am. Chem. Soc.*, 137(43):13752–13755, 2015. (p.9).

[32] Seong Jung Kwon, Fu-Ren F. Fan, and Allen J. Bard. Observing iridium oxide (irox) single nanoparticle collisions at ultramicroelectrodes. *J. Am. Chem. Soc.*, 132(38):13165–13167, 2010. (p.9).

[33] Christopher C. M. Neumann, Eduardo Laborda, Kristina Tschulik, Kristopher R. Ward, and Richard G. Compton. Performance of silver nanoparticles in the catalysis of the oxygen reduction reaction in neutral media: Efficiency limitation due to hydrogen peroxide escape. *Nano Res.*, 6(7):511–524, 2013. (p.9).

[34] Ying Wang, Eduardo Laborda, Kristina Tschulik, Christine Damm, Angela Molina, and Richard G. Compton. Strong negative nanocatalysis: oxygen reduction and hydrogen evolution at very small (2 nm) gold nanoparticles. *Nanoscale*, 6:11024–11030, 2014. (p.9).

[35] Christopher Batchelor-McAuley, Joanna Ellison, Kristina Tschulik, Philip L. Hurst, Regine Boldt, and Richard G. Compton. In situ nanoparticle sizing with zeptomole sensitivity. *Analyst*, 140:5048–5054, 2015. (p.10).

[36] Kristina Tschulik, Christopher Batchelor-McAuley, Her-Shuang Toh, Emma J. E. Stuart, and Richard G. Compton. Electrochemical studies of silver nanoparticles: a guide for experimentalists and a perspective. *Phys. Chem. Chem. Phys.*, 16:616–623, 2014. (pp.10, 31, 31, 32, 59, 59).

[37] Loretta S. Y. Ly, Christopher Batchelor-McAuley, Kristina Tschulik, Enno Katelhon, and Richard G. Compton. A critical evaluation of the interpretation of electrocatalytic nanoimpacts. *J. Phys. Chem. C*, 118(31):17756–17763, 2014. (p.9).

[38] Joanna Ellison, Kristina Tschulik, Emma J. E. Stuart, Kerstin Jurkschat, Dario Omanović, Margitta Uhlemann, Alison Crossley, and Richard G. Compton. Get more out of your data: A new approach to agglomeration and aggregation studies using nanoparticle impact experiments. *ChemistryOpen*, 2(2):69–75, 2013. (pp.11, 32, 54, 59, 59).

[39] Kristina Tschulik, Kamonwad Ngamchuea, Christoph Ziegler, Max Gregor Beier, Christine Damm, Alexander Eychmueller, and Richard G. Compton. Core-shell nanoparticles: Characterizing multifunctional materials beyond imaging: Distinguishing and quantifying perfect and broken shells. *Adv. Funct. Mater.*, 25(32):5149–5158, 2015. (pp.11, 32).

[40] Lucy R. Holt, Blake J. Plowman, Neil P. Young, Kristina Tschulik, and Richard G. Compton. The electrochemical characterization of single core–shell nanoparticles. *Angew. Chem. Int. Ed.*, 55(1):397–400, 2016. (pp.11, 32).

[41] Yi-Ge Zhou, Neil V. Rees, and Richard G. Compton. The electrochemical detection of tagged nanoparticlesvia particle-electrode collisions: nanoelectroanalysis beyond immobilisation. *Chem. Commun.*, 48:2510–2512, 2012. (p.11).

[42] Blake J. Plowman, Neil P. Young, Christopher Batchelor-McAuley, and Richard G. Comp-

ton. Nanorod aspect ratios determined by the nano-impact technique. *Angew. Chem. Int. Ed.*, 55(24):7002–7005, 2016. (p.11, 11).

[43] Yi-Ge Zhou, Neil V. Rees, and Richard G. Compton. The electrochemical detection and characterization of silver nanoparticles in aqueous solution. *Angew. Chem. Int. Ed.*, 50 (18):4219–4221, 2011. (pp.11, 32).

[44] Emma J. E. Stuart, Yi-Ge Zhou, Neil V. Rees, and Richard G. Compton. Determining unknown concentrations of nanoparticles: the particle-impact electrochemistry of nickel and silver. *RSC Adv.*, 2:6879–6884, 2012. (pp.11, 54).

[45] E. J. E. Stuart, N. V. Rees, J. T. Cullen, and R. G. Compton. Direct electrochemical detection and sizing of silver nanoparticles in seawater media. *Nanoscale*, 5:174–177, 2013. (pp.11, 39).

[46] Her Shuang Toh, Christopher Batchelor-McAuley, Kristina Tschulik, and Richard G. Compton. Electrochemical detection of chloride levels in sweat using silver nanoparticles: a basis for the preliminary screening for cystic fibrosis. *Analyst*, 138:4292–4297, 2013. (p.11).

[47] Bernadette M. Quinn, Pieter G. van't Hof, and Serge G. Lemay. Time-resolved electrochemical detection of discrete adsorption events. *J. Am. Chem. Soc.*, 126(27):8360–8361, 2004. (p.12).

[48] Stephen E. Fosdick, Morgan J. Anderson, Elizabeth G. Nettleton, and Richard M. Crooks. Correlated electrochemical and optical tracking of discrete collision events. *J. Am. Chem. Soc.*, 135(16):5994–5997, 2013. (p.12, 12).

[49] Xiuting Li, Christopher Batchelor-McAuley, Lidong Shao, Stanislav V. Sokolov, Neil P. Young, and Richard G. Compton. Quantifying single-carbon nanotube-electrode contact via the nanoimpact method. *The Journal of Physical Chemistry Letters*, 8(2):507–511, 2017. (p.12).

[50] Martin A. Edwards, Sean R. German, Jeffrey E. Dick, Allen J. Bard, and Henry S. White. High-speed multipass coulter counter with ultrahigh resolution. *ACS Nano*, 9(12):12274–12282, 2015. (pp.12, 13).

[51] Kim McKelvey, Martin A. Edwards, and Henry S. White. Resistive pulse delivery of single nanoparticles to electrochemical interfaces. *J. Phys. Chem. Lett.*, 7(19):3920–3924, 2016. (p.12).

[52] Jan Clausmeyer, Justus Masa, Edgar Ventosa, Dennis Ohl, and Wolfgang Schuhmann. Nanoelectrodes reveal the electrochemistry of single nickelhydroxide nanoparticles. *Chem. Commun.*, 52:2408–2411, 2016. (pp.12, 123, 154).

[53] Yongxin Li, Jonathan T. Cox, and Bo Zhang. Electrochemical responses and electrocatalysis at single au nanoparticles. *J. Am. Chem. Soc.*, 132(9):3047–3054, 2010. (p.12).

[54] Yun Yu, Yang Gao, Keke Hu, Pierre-Yves Blanchard, Jean-Marc Noël, Thangavel Nareshkumar, Kanala L. Phani, Gary Friedman, Yury Gogotsi, and Michael V. Mirkin. Electrochemistry and electrocatalysis at single gold nanoparticles attached to carbon nanoelectrodes. *ChemElectroChem*, 2(1):58–63, 2015. (p.12).

[55] Jiyeon Kim, Hui Xiong, Mario Hofmann, Jing Kong, and Shigeru Amemiya. Scanning electrochemical microscopy of individual single-walled carbon nanotubes. *Anal. Chem.*, 82

(5):1605–1607, 2010. (p.12).

[56] Laurent Nault, Cécilia Taofifenua, Agnes Anne, Arnaud Chovin, Christophe Demaille, Jane Besong-Ndika, Daniela Cardinale, Noélle Carette, Thierry Michon, and Jocelyne Walter. Electrochemical atomic force microscopy imaging of redox-immunomarked proteins on native potyviruses: From subparticle to single-protein resolution. *ACS Nano*, 9(5):4911–4924, 2015. (pp.12, 13).

[57] Agnes Anne, Mohamed Ali Bahri, Arnaud Chovin, Christophe Demaille, and Cecilia Taofifenua. Probing the conformation and 2d-distribution of pyrene-terminated redox-labeled poly(ethylene glycol) chains end-adsorbed on hopg using cyclic voltammetry and atomic force electrochemical microscopy. *Phys. Chem. Chem. Phys.*, 16:4642–4652, 2014. (p.12).

[58] Stanley C.S. Lai, Petr V. Dudin, Julie V. Macpherson, and Patrick R. Unwin. Visualizing zeptomole (electro)catalysis at single nanoparticles within an ensemble. *J. Am. Chem. Soc.*, 133(28):10744–10747, 2011. (p.13).

[59] Minkyung Kang, David Perry, Yang-Rae Kim, Alex W. Colburn, Robert A. Lazenby, and Patrick R. Unwin. Time-resolved detection and analysis of single nanoparticle electrocatalytic impacts. *J. Am. Chem. Soc.*, 137(34):10902–10905, 2015. (p.13).

[60] Steven E. F. Kleijn, Stanley C. S. Lai, Thomas S. Miller, Alexei I. Yanson, Marc T. M. Koper, and Patrick R. Unwin. Landing and catalytic characterization of individual nanoparticles on electrode surfaces. *J. Am. Chem. Soc.*, 134(45):18558–18561, 2012. (p.13).

[61] Aleix G. Guell, Katherine E. Meadows, Petr V. Dudin, Neil Ebejer, Julie V. Macpherson, and Patrick R. Unwin. Mapping nanoscale electrochemistry of individual single-walled carbon nanotubes. *Nano Letters*, 14(1):220–224, 2014. (p.13).

[62] Petr V. Dudin, Michael E. Snowden, Julie V. Macpherson, and Patrick R. Unwin. Electrochemistry at nanoscale electrodes: Individual single-walled carbon nanotubes (swnts) and swnt-templated metal nanowires. *ACS Nano*, 5(12):10017–10025, 2011. (p.13, 13).

[63] Michael Faraday. The bakerian lecture: Experimental relations of gold (and other metals) to light. *Phil. Trans. Royal Soc. London*, 147:145–181, 1857. (p.14).

[64] Gustav Mie. Beiträge zur optik trüber medien, speziell kolloidaler metallösungen. *Annalen der Physik*, 330(3):377–445, 1908. (pp.14, 143).

[65] R W Wood. On a remarkable case of uneven distribution of light in a diffraction grating spectrum. *Phil. Trans. Royal Soc. London*, 18(1):269, 1902. (p.14).

[66] Lord Rayleigh. On the dynamical theory of gratings. *Phil. Trans. Royal Soc. A*, 79(532): 399–416, 1907. (p.14).

[67] Alexandre G. Brolo. Plasmonics for future biosensors. *Nat. Photon*, 6(11):709–713, 2012. (p.14).

[68] Sergey V. Gaponenko. *Introduction to Nanophotonics*. Cambridge University Press, 2010. (pp.14, 15).

[69] Naomi J. Halas. Plasmonics: An emerging field fostered by nano letters. *Nano Lett.*, 10 (10):3816–3822, 2010. (p.14).

[70] Katherine A. Willets and Richard P. Van Duyne. Localized surface plasmon resonance spectroscopy and sensing. *Annu. Rev. Phys. Chem.*, 58(1):267–297, 2007. (pp.14, 74).

[71] Eric C. Le Ru and Pablo G. Etchegoin. Single-molecule surface-enhanced raman spectroscopy. *Annu. Rev. Phys. Chem.*, 63(1):65–87, 2012. (p.15).

[72] Jon A. Dieringer, Robert B. Lettan, Karl A. Scheidt, and Richard P. Van Duyne. A frequency domain existence proof of single-molecule surface-enhanced raman spectroscopy. *J. Am. Chem. Soc.*, 129(51):16249–16256, 2007. (pp.15, 24).

[73] Peter Zijlstra, Pedro M. R. Paulo, and Michel Orrit. Optical detection of single non-absorbing molecules using the surface plasmon resonance of a gold nanorod. *Nature Nanotech.*, 7(6):379 – 382, 2012. (p.15).

[74] Hui Wang, Daniel W. Brandl, Peter Nordlander, and Naomi J. Halas. Plasmonic nanostructures: Artificial molecules. *Acc. Chem. Res.*, 40(1):53–62, 2007. (p.15).

[75] P. Nordlander and E. Prodan. Plasmon hybridization in nanoparticles near metallic surfaces. *Nano Lett.*, 4(11):2209–2213, 2004. (pp.15, 46, 47).

[76] Guillaume Baffou and Romain Quidant. Thermo-plasmonics: using metallic nanostructures as nano-sources of heat. *Laser and Photon. Rev.*, 7(2):171–187, 2013. (p.15).

[77] David Boyer, Philippe Tamarat, Abdelhamid Maali, Brahim Lounis, and Michel Orrit. Photothermal imaging of nanometer-sized metal particles among scatterers. *Science*, 297 (5584):1160–1163, 2002. (p.15).

[78] A. Gaiduk, M. Yorulmaz, P. V. Ruijgrok, and M. Orrit. Room-temperature detection of a single molecule's absorption by photothermal contrast. *Science*, 330(6002):353–356, 2010. (p.15).

[79] Zhi-Cong Zeng, Sheng-Chao Huang, De-Yin Wu, Ling-Yan Meng, Mao-Hua Li, Teng-Xiang Huang, Jin-Hui Zhong, Xiang Wang, Zhi-Lin Yang, and Bin Ren. Electrochemical tip-enhanced raman spectroscopy. *J. Am. Chem. Soc.*, 137(37):11928–11931, 2015. (p.15).

[80] Stephanie Zaleski, Andrew J. Wilson, Michael Mattei, Xu Chen, Guillaume Goubert, M. Fernanda Cardinal, Katherine A. Willets, and Richard P. Van Duyne. Investigating nanoscale electrochemistry with surface- and tip-enhanced raman spectroscopy. *Acc. Chem. Res.*, 49(9):2023–2030, 2016. (pp.15, 25, 74).

[81] Michael Mattei, Gyeongwon Kang, Guillaume Goubert, Dhabih V. Chulhai, George C. Schatz, Lasse Jensen, and Richard P. Van Duyne. Tip-enhanced raman voltammetry: Coverage dependence and quantitative modeling. *Nano Lett.*, 17(1):590–596, 2017. (pp.15, 23).

[82] Van-Quynh Nguyen, Yong Ai, Pascal Martin, and Jean-Christophe Lacroix. Plasmon-induced nanolocalized reduction of diazonium salts. *ACS Omega*, 2(5):1947–1955, 2017. (p.15).

[83] Yong Ai, Van Quynh Nguyen, Jalal Ghilane, Pierre-Camille Lacaze, and Jean-Christophe Lacroix. Plasmon-induced conductance switching of an electroactive conjugated polymer nanojunction. *ACS Appl. Mater. Interfaces*, 9(33):27817–27824, 2017. (p.15).

[84] Guillaume Baffou and Romain Quidant. Nanoplasmonics for chemistry. *Chem. Soc. Rev.*, 43:3898–3907, 2014. (p.15).

[85] M. Orrit and J. Bernard. Single pentacene molecules detected by fluorescence excitation in a p-terphenyl crystal. *Phys. Rev. Lett.*, 65:2716–2719, 1990. (p.15, 15).

[86] Michel Orrit. Single-molecule spectroscopy: The road ahead. *J. Chem. Phys.*, 117(24):

10938–10946, 2002. (p.15).

[87] S. Nie, D.T. Chiu, and R.N. Zare. Probing individual molecules with confocal fluorescence microscopy. *Science*, 266(5187):1018–1021, 1994. (p.15).

[88] Roger Y. Tsien. The green fluorescent protein. *Annu. Rev. Biochem.*, 67(1):509–544, 1998. (p.15).

[89] W. E. (William E.) Moerner. Nobel lecture: Single-molecule spectroscopy, imaging, and photocontrol: Foundations for super-resolution microscopy. *Rev. Mod. Phys.*, 87:1183–1212, Oct 2015. (pp.16, 17).

[90] Bo Huang, Mark Bates, and Xiaowei Zhuang. Super-resolution fluorescence microscopy. *Annu. Rev. Biochem.*, 78(1):993–1016, 2009. (p.16).

[91] Alex von Diezmann, Yoav Shechtman, and W. E. Moerner. Three-dimensional localization of single molecules for super-resolution imaging and single-particle tracking. *Chem. Rev.*, 117(11):7244–7275, 2017. (pp.16, 17).

[92] Tobias Müller, Christian Schumann, and Annette Kraegeloh. STED microscopy and its applications: New insights into cellular processes on the nanoscale. *ChemPhysChem*, 13 (8):1986–2000, 2012. (p.16).

[93] Stefan W. Hell. Far-field optical nanoscopy. *Science*, 316(5828):1153–1158, 2007. (p.17, 17).

[94] E. Betzig. Proposed method for molecular optical imaging. *Opt. Lett.*, 20(3):237–239, Feb 1995. (p.17, 17).

[95] Eric Betzig, George H. Patterson, Rachid Sougrat, O. Wolf Lindwasser, Scott Olenych, Juan S. Bonifacino, Michael W. Davidson, Jennifer Lippincott-Schwartz, and Harald F. Hess. Imaging intracellular fluorescent proteins at nanometer resolution. *Science*, 313 (5793):1642–1645, 2006. (p.17).

[96] Stefan W. Hell and Jan Wichmann. Breaking the diffraction resolution limit by stimulated emission: stimulated-emission-depletion fluorescence microscopy. *Opt. Lett.*, 19(11):780–782, Jun 1994. (p.17).

[97] Tao Chen, Bin Dong, Kuangcai Chen, Fei Zhao, Xiaodong Cheng, Changbei Ma, Seungah Lee, Peng Zhang, Seong Ho Kang, Ji Won Ha, Weilin Xu, and Ning Fang. Optical super-resolution imaging of surface reactions. *Chem. Rev.*, 0(0):null, 0.

[98] Tao Chen, Bin Dong, Kuangcai Chen, Fei Zhao, Xiaodong Cheng, Changbei Ma, Seungah Lee, Peng Zhang, Seong Ho Kang, Ji Won Ha, Weilin Xu, and Ning Fang. Optical super-resolution imaging of surface reactions. *Chem. Rev.*, 117(11):7510–7537, 2017. (pp.17, 17, 25).

[99] Ariadna Martinez-Marrades, Jean-François Rupprecht, Michel Gross, and Gilles Tessier. Stochastic 3d optical mapping by holographic localization of brownian scatterers. *Opt. Express*, 22(23):29191–29203, Nov 2014. (pp.17, 18, 143).

[100] Kyu Sung Han, Guokun Liu, Xiaochun Zhou, Rita E. Medina, and Peng Chen. How does a single pt nanocatalyst behave in two different reactions? a single-molecule study. *Nano Letters*, 12(3):1253–1259, 2012. (p.18).

[101] Xiaochun Zhou, Nesha May Andoy, Guokun Liu, Eric Choudhary, Kyu-Sung Han, Hen Shen, and Peng Chen. Quantitative super-resolution imaging uncovers reactivity patterns

on single nanocatalysts. *Nature Nanotech.*, 7:237–241, 2012. (p.18).

[102] Nesha May Andoy, Xiaochun Zhou, Eric Choudhary, Hao Shen, Guokun Liu, and Peng Chen. Single-molecule catalysis mapping quantifies site-specific activity and uncovers radial activity gradient on single 2d nanocrystals. *J. Am. Chem. Soc.*, 135(5):1845–1852, 2013. (p.18).

[103] Hao Shen, Xiaochun Zhou, Ningmu Zou, and Peng Chen. Single-molecule kinetics reveals a hidden surface reaction intermediate in single-nanoparticle catalysis. *J. Phys. Chem. C*, 118(46):26902–26911, 2014. (pp.18, 25).

[104] Wolfgang Kaim and Jan Fiedler. Spectroelectrochemistry: the best of two worlds. *Chem. Soc. Rev.*, 38:3373–3382, 2009. (p.19).

[105] Avni Berisha, Catherine Combellas, Géraldine Hallais, Frédéric Kanoufi, Jean Pinson, and Fetah I. Podvorica. Photochemical grafting and patterning of metallic surfaces by organic layers derived from acetonitrile. *Chem. Mater.*, 23(15):3449–3459, 2011. (p.19).

[106] Meriem Bouriga, Mohamed M. Chehimi, Catherine Combellas, Philippe Decorse, Frédéric Kanoufi, Alain Deronzier, and Jean Pinson. Sensitized photografting of diazonium salts by visible light. *Chem. Mater.*, 25(1):90–97, 2013. (p.19).

[107] Sandra Nunige, Renaud Cornut, Hassan Hazimeh, Fanny Hauquier, Christine Lefrou, Catherine Combellas, and Frédéric Kanoufi. Reactivity of surfaces determined by local electrochemical triggering: A bromo-terminated self-assembled monolayer. *Angew. Chem. Int. Ed.*, 51(21):5208–5212, 2012. (p.19).

[108] Roman G. Fedorov and Daniel Mandler. Local deposition of anisotropic nanoparticles using scanning electrochemical microscopy (secm). *Phys. Chem. Chem. Phys.*, 15:2725–2732, 2013. (p.19).

[109] Derek J. Wasylenko, Carlos Rodríguez, Michael L. Pegis, and James M. Mayer. Direct comparison of electrochemical and spectrochemical kinetics for catalytic oxygen reduction. *J. Am. Chem. Soc.*, 136(36):12544–12547, 2014. (p.19).

[110] Jorik van de Groep, Matthew T. Sheldon, Harry A. Atwater, and Albert Polman. Thermodynamic theory of the plasmoelectric effect. *Sci. Rep.*, 6:23283, 2016. (p.20).

[111] Matthew T. Sheldon, Jorik van de Groep, Ana M. Brown, Albert Polman, and Harry A. Atwater. Plasmoelectric potentials in metal nanostructures. *Science*, 346(6211):828–831, 2014. (p.20).

[112] Carolina Novo, Alison M. Funston, and Paul Mulvaney. Direct observation of chemical reactions on single gold nanocrystals using surface plasmon spectroscopy. *Nature Nanotech.*, 3(10):598–602, 2008. (pp.20, 21).

[113] Li-Xia Qin, Chao Jing, Yang Li, Da-Wei Li, and Yi-Tao Long. Real-time monitoring of the aging of single plasmonic copper nanoparticles. *Chem. Commun.*, 48:1511–1513, 2012. (pp.20, 21).

[114] Hao Zhou, Qing Liu, Frankie J. Rawson, Wei Ma, Da-Wei Li, Di Li, and Yi-Tao Long. Optical monitoring of faradaic reaction using single plasmon-resonant nanorods functionalized with graphene. *Chem. Commun.*, 51:3223–3226, 2015. (p.20).

[115] Gang Logan Liu, Yi-Tao Long, Yeonho Choi, Taewook Kang, and Luke P. Lee. Quantized plasmon quenching dips nanospectroscopy via plasmon resonance energy transfer. *Nat.*

Meth., 4:1015–1017, 2007. (pp.20, 20, 22).

[116] Chao Jing, Zhen Gu, Tao Xie, and Yi-Tao Long. Color-coded imaging of electrochromic process at single nanoparticle level. *Chem. Sci.*, 7:5347–5351, 2016. (pp.20, 22).

[117] Yimin Fang, Wei Wang, Xiang Wo, Yashuang Luo, Shaowei Yin, Yixian Wang, Xiaonan Shan, and Nongjian Tao. Plasmonic imaging of electrochemical oxidation of single nanoparticles. *J. Am. Chem. Soc.*, 136(36):12584–12587, 2014. (pp.22, 22, 44).

[118] Xiaonan Shan, Urmez Patel, Shaopeng Wang, Rodrigo Iglesias, and Nongjian Tao. Imaging local electrochemical current via surface plasmon resonance. *Science*, 327(5971):1363–1366, 2010. (p.22, 22, 22).

[119] Xiaonan Shan, Ismael Diez-Perez, Luojia Wang, Peter Wiktor, Ying Gu, Lihua Zhang, Wei Wang, Jin Lu, Shaopeng Wang, Qihuang Gong, Jinghong Li, and Nongjian Tao. Imaging the electrocatalytic activity of single nanoparticles. *Nature Nanotech.*, 7(10):668–672, 2012. (p.22).

[120] Caleb M. Hill and Shanlin Pan. A dark-field scattering spectroelectrochemical technique for tracking the electrodeposition of single silver nanoparticles. *J. Am. Chem. Soc.*, 135 (46):17250–17253, 2013. (p.22).

[121] Caleb M. Hill, Robert Bennett, Chen Zhou, Shane Street, Jie Zheng, and Shanlin Pan. Single ag nanoparticle spectroelectrochemistry via dark-field scattering and fluorescence microscopies. *J. Phys. Chem. C*, 119(12):6760–6768, 2015. (p.22).

[122] Benjamin S. Hoener, Chad P. Byers, Thomas S. Heiderscheit, Agampodi S. De Silva Indrasekara, Anneli Hoggard, Wei-Shun Chang, Stephan Link, and Christy F. Landes. Spectroelectrochemistry of halide anion adsorption and dissolution of single gold nanorods. *J. Phys. Chem. C*, 120(37):20604–20612, 2016. (p.23).

[123] Chad P. Byers, Benjamin S. Hoener, Wei-Shun Chang, Stephan Link, and Christy F. Landes. Single-particle plasmon voltammetry (sppv) for detecting anion adsorption. *Nano Lett.*, 16(4):2314–2321, 2016. (pp.23, 24).

[124] Yixian Wang, Xiaonan Shan, Hui Wang, Shaopeng Wang, and Nongjian Tao. Plasmonic imaging of surface electrochemical reactions of single gold nanowires. *J. Am. Chem. Soc.*, 139(4):1376–1379, 2017. (pp.23, 24).

[125] Chao Jing, Zhen Gu, and Yi-Tao Long. Imaging electrocatalytic processes on single gold nanorods. *Faraday Discuss.*, 193:371–385, 2016. (p.23).

[126] Dan Jiang, Yingyan Jiang, Zhimin Li, Tao Liu, Xiang Wo, Yimin Fang, Nongjian Tao, Wei Wang, and Hong-Yuan Chen. Optical imaging of phase transition and li-ion diffusion kinetics of single licoo2 nanoparticles during electrochemical cycling. *J. Am. Chem. Soc.*, 139(1):186–192, 2017. (pp.23, 24, 114).

[127] Chenghong Lei, Dehong Hu, and Eric J. Ackerman. Single-molecule fluorescence spectroelectrochemistry of cresyl violet. *Chem. Commun.*, pages 5490–5492, 2008. (p.23).

[128] M. Fleischmann, P.J. Hendra, and A.J. McQuillan. Raman spectra of pyridine adsorbed at a silver electrode. *Chem. Phys. Lett.*, 26(2):163 – 166, 1974. (p.24).

[129] David L. Jeanmaire and Richard P. Van Duyne. Surface raman spectroelectrochemistry. *Journal of Electroanalytical Chemistry and Interfacial Electrochemistry*, 84(1):1 – 20, 1977. (p.24).

[130] Shuming Nie and Steven R. Emory. Probing single molecules and single nanoparticles by surface-enhanced raman scattering. *Science*, 275(5303):1102–1106, 1997. (p.24).

[131] Katrin Kneipp, Yang Wang, Harald Kneipp, Lev T. Perelman, Irving Itzkan, Ramachandra R. Dasari, and Michael S. Feld. Single molecule detection using surface-enhanced raman scattering (SERS). *Phys. Rev. Lett.*, 78:1667–1670, 1997. (p.24).

[132] Wei Wang, Yi-Fan Huang, Dong-Yu Liu, Fang-Fang Wang, Zhong-Qun Tian, and Dongping Zhan. Electrochemically roughened gold microelectrode for surface-enhanced raman spectroscopy. *J. Electroanal. Chem.*, 779:126 – 130, 2016. (p.24).

[133] Chao-Yu Li, Jin-Chao Dong, Xi Jin, Shu Chen, Rajapandiyan Panneerselvam, Alexander V. Rudnev, Zhi-Lin Yang, Jian-Feng Li, Thomas Wandlowski, and Zhong-Qun Tian. In situ monitoring of electrooxidation processes at gold single crystal surfaces using shell-isolated nanoparticle-enhanced raman spectroscopy. *J. Am. Chem. Soc.*, 137(24):7648–7651, 2015. (p.24).

[134] Juan Wang, Jin-Chao Dong, Ji Yang, Yong Wang, Chen-Jie Zhang, Min-Min Xu, Bing-Wei Mao, Jian-Lin Yao, Jian-Feng Li, and Zhong-Qun Tian. In situ SERS and SHINERS study of electrochemical hydrogenation of p-ethynylaniline in nonaqueous solvents. *Electrochem. Commun.*, 78:16 – 20, 2017. (p.24).

[135] Jian-Feng Li, Yue-Jiao Zhang, Alexander V. Rudnev, Jason R. Anema, Song-Bo Li, Wen-Jing Hong, Panneerselvam Rajapandiyan, Jacek Lipkowski, Thomas Wandlowski, and Zhong-Qun Tian. Electrochemical shell-isolated nanoparticle-enhanced raman spectroscopy: Correlating structural information and adsorption processes of pyridine at the Au(hkl) single crystal/solution interface. *J. Am. Chem. Soc.*, 137(6):2400–2408, 2015. (p.24).

[136] Gema Cabello, Xue-Jiao Chen, Rajapandiyan Panneerselvam, and Zhong-Qun Tian. Potential dependent thiocyanate adsorption on gold electrodes: a comparison study between SERS and SHINERS. *J. Raman Spectrosc.*, 47(10):1207–1212, 2016. (p.24).

[137] Emiliano Cortes, Pablo G. Etchegoin, Eric C. Le Ru, Alejandro Fainstein, Maria E. Vela, and Roberto C. Salvarezza. Monitoring the electrochemistry of single molecules by surface-enhanced raman spectroscopy. *J. Am. Chem. Soc.*, 132(51):18034–18037, 2010. (pp.24, 25).

[138] G. Spektor, D. Kilbane, A. K. Mahro, B. Frank, S. Ristok, L. Gal, P. Kahl, D. Podbiel, S. Mathias, H. Giessen, F.-J. Meyer zu Heringdorf, M. Orenstein, and M. Aeschlimann. Revealing the subfemtosecond dynamics of orbital angular momentum in nanoplasmonic vortices. *Science*, 355(6330):1187–1191, 2017. (p.25, 25).

[139] Boya Radha, Mohammed Arif, Ranjan Datta, Tapas K. Kundu, and Giridhar U. Kulkarni. Movable au microplates as fluorescence enhancing substrates for live cells. *Nano Res.*, 3 (10):738–747, 2010. (p.25).

[140] Jian-Feng Li, Yue-Jiao Zhang, Song-Yuan Ding, Rajapandiyan Panneerselvam, and Zhong-Qun Tian. Core-shell nanoparticle-enhanced raman spectroscopy. *Chem. Rev.*, 117(7): 5002–5069, 2017. (p.25).

[141] Weichun Zhang, Martín Caldarola, Biswajit Pradhan, and Michel Orrit. Gold nanorod enhanced fluorescence enables single-molecule electrochemistry of methylene blue. *Angew. Chem. Int. Ed.*, 56(13):3566–3569, 2017. (pp.25, 26).

[142] T. Touzalin, A. L. Dauphin, S. Joiret, I. T. Lucas, and E. Maisonhaute. Tip enhanced raman spectroscopy imaging of opaque samples in organic liquid. *Phys. Chem. Chem. Phys.*, 18:15510–15513, 2016. (p.25).

[143] Justin B. Sambur and Peng Chen. Distinguishing direct and indirect photoelectrocatalytic oxidation mechanisms using quantitative single-molecule reaction imaging and photocurrent measurements. *J. Phys. Chem. C*, 120(37):20668–20676, 2016. (p.25).

[144] Ashantha Fernando, Suman Parajuli, and Mario A. Alpuche-Aviles. Observation of individual semiconducting nanoparticle collisions by stochastic photoelectrochemical currents. *J. Am. Chem. Soc.*, 135(30):10894–10897, 2013. (p.26).

[145] Krishna K. Barakoti, Suman Parajuli, Pushpa Chhetri, Ganesh R. Rana, Rezvan Kazemi, Ryan Malkiewich, and Mario A. Alpuche-Aviles. Stochastic electrochemistry and photoelectrochemistry of colloidal dye-sensitized anatase nanoparticles at a pt ultramicroelectrode. *Faraday Discuss.*, 193:313–325, 2016. (p.26, 26).

[146] Daniel A. Clayton, Diane M. Benoist, Yan Zhu, and Shanlin Pan. Photoluminescence and spectroelectrochemistry of single ag nanowires. *ACS Nano*, 4(4):2363–2373, 2010. (p.26).

[147] Vitor Brasiliense, Anisha N. Patel, Ariadna Martinez-Marrades, Jian Shi, Yong Chen, Catherine Combellas, Gilles Tessier, and Frédéric Kanoufi. Correlated electrochemical and optical detection reveals the chemical reactivity of individual silver nanoparticles. *J. Am. Chem. Soc.*, 138(10):3478–3483, 2016. (pp.29, 53).

[148] Vitor Brasiliense, Pascal Berto, Catherine Combellas, Gilles Tessier, and Frédéric Kanoufi. Electrochemistry of single nanodomains revealed by three-dimensional holographic microscopy. *Acc. Chem. Res.*, 49(9):2049–2057, 2016. (pp.29, 143).

[149] Vitor Brasiliense, Pascal Berto, Catherine Combellas, Robert Kuszelewicz, Gilles Tessier, and Frederic Kanoufi. Electrochemical transformation of individual nanoparticles revealed by coupling microscopy and spectroscopy. *Farad. Disc.*, 193:339–352, 2016. (pp.29, 53).

[150] Ilya Prigogine and Isabelle Stengers. *La Nouvelle Alliance*. Gallimartd, 1979. (p.29).

[151] Russell Young, John Ward, and Fredric Scire. The topografiner: An instrument for measuring surface microtopography. *Rev. Sci. Instrum.*, 43(7):999–1011, 1972. (p.29).

[152] Svitlana Chernousova and Matthias Epple. Silver as antibacterial agent: Ion, nanoparticle, and metal. *Angew. Chem. Int. Ed.*, 52(6):1636–1653, 2013. (p.30, 30).

[153] Siddhartha Shrivastava, Tanmay Bera, Arnab Roy, Gajendra Singh, P Ramachandrarao, and Debabrata Dash. Characterization of enhanced antibacterial effects of novel silver nanoparticles. *Nanotechnology*, 18(22):225103, 2007. (p.30).

[154] Sukumaran Prabhu and Eldho K. Poulose. Silver nanoparticles: mechanism of antimicrobial action, synthesis, medical applications, and toxicity effects. *Int. Nano Lett.*, 2(1):32, 2012. (p.30, 30).

[155] Georgios A. Sotiriou and Sotiris E. Pratsinis. Antibacterial activity of nanosilver ions and particles. *Environ. Sci. Technol.*, 44(14):5649–5654, 2010. (p.30, 30).

[156] Ping Li, Juan Li, Changzhu Wu, Qingsheng Wu, and Jian Li. Synergistic antibacterial effects of β-lactam antibiotic combined with silver nanoparticles. *Nanotechnology*, 16(9):1912, 2005. (p.30).

[157] Steffen F. Hansen and Anders Baun. When enough is enough. *Nature Nanotech.*, 7:409–411,

2012. (p.30).

[158] Yun Han, Robert Lupitskyy, Tseng-Ming Chou, Christopher M. Stafford, Henry Du, and Svetlana Sukhishvili. Effect of oxidation on surface-enhanced raman scattering activity of silver nanoparticles: A quantitative correlation. *Anal. Chem.*, 83(15):5873–5880, 2011. (p.30).

[159] P. B. Johnson and R. W. Christy. Optical constants of the noble metals. *Phys. Rev. B*, 6: 4370–4379, 1972. (p.31).

[160] Virender K. Sharma, Ria A. Yngard, and Yekaterina Lin. Silver nanoparticles: Green synthesis and their antimicrobial activities. *Adv. Colloid Interface Sci.*, 145(1–2):83 – 96, 2009. (p.31).

[161] Klas I. Udekwu (eds.) Emilio I. Alarcon, May Griffith. *Silver Nanoparticle Applications: In the Fabrication and Design of Medical and Biosensing Devices.* Engineering Materials. Springer International Publishing, 1 edition, 2015. (p.31).

[162] B. Buszewski, K. Rafilska, P. Pomastowski, J. Walczak, and A. Rogowska. Novel aspects of silver nanoparticles functionalization. *Colloids Surf., A*, 506:170 – 178, 2016. (p.31).

[163] Aishwarya Sooresh, Hyeogsun Kwon, Robert Taylor, Patricia Pietrantonio, Michelle Pine, and Christie M. Sayes. Surface functionalization of silver nanoparticles: Novel applications for insect vector control. *ACS Appl. Mater. Interfaces*, 3(10):3779–3787, 2011. (p.31).

[164] Karla Chaloupka, Yogeshkumar Malam, and Alexander M. Seifalian. Nanosilver as a new generation of nanoproduct in biomedical applications. *Trends in Biotechnol.*, 28(11):580–588, 2010. (p.31).

[165] Catalina Marambio-Jones and Eric M.V. Hoek. A review of the antibacterial effects of silver nanomaterials and potential implications for human health and the environment. *J. Nanopart. Res.*, 12(5):1531–1551, 2010. (p.31).

[166] Sarah E. Ward Jones, Fallyn W. Campbell, Ronan Baron, Lei Xiao, and Richard G. Compton. Particle size and surface coverage effects in the stripping voltammetry of silver nanoparticles: Theory and experiment. *J. Phys. Chem. C*, 112(46):17820–17827, 2008. (p.31).

[167] Ian Streeter, Ronan Baron, and Richard G. Compton. Voltammetry at nanoparticle and microparticle modified electrodes: Theory and experiment. *J. Phys. Chem. C*, 111(45): 17008–17014, 2007. (p.31).

[168] Fallyn W. Campbell, Stephen R. Belding, Ronan Baron, Lei Xiao, and Richard G. Compton. The hydrogen evolution reaction at a silver nanoparticle array and a silver macroelectrode compared: Changed electrode kinetics between the macro- and nanoscales. *J. Phys. Chem. C*, 113(33):14852–14857, 2009. (p.31).

[169] W. J. Plieth. Electrochemical properties of small clusters of metal atoms and their role in the surface enhanced raman scattering. *The Journal of Physical Chemistry*, 86(16): 3166–3170, 1982. (p.31).

[170] Her Shuang Toh, Christopher Batchelor-McAuley, Kristina Tschulik, Margitta Uhlemann, Alison Crossley, and Richard G. Compton. The anodic stripping voltammetry of nanoparticles: electrochemical evidence for the surface agglomeration of silver nanoparticles. *Nanoscale*, 5:4884–4893, 2013. (p.31).

[171] Her Shuang Toh, Kerstin Jurkschat, and Richard G. Compton. The influence of the capping agent on the oxidation of silver nanoparticles: Nano-impacts versus stripping voltammetry. *Chem. Eur. J.*, 21(7):2998–3004, 2015. (pp.32, 39).

[172] Eden E. L. Tanner, Kristina Tschulik, Romilly Tahany, Kerstin Jurkschat, Christopher Batchelor-McAuley, and Richard G. Compton. Nanoparticle capping agent dynamics and electron transfer: Polymer-gated oxidation of silver nanoparticles. *J. Phys. Chem. C*, 119(32):18808–18815, 2015. (p.32).

[173] En Ning Saw, Viktoria Grasmik, Christian Rurainsky, Matthias Epple, and Kristina Tschulik. Electrochemistry at single bimetallic nanoparticles - using nano impacts for sizing and compositional analysis of individual agau alloy nanoparticles. *Faraday Discuss.*, 193:327–338, 2016. (p.32).

[174] Ubbo F. Wiersema. *Brownian Motion Calculus*. John Wiley & Sons, 2010. (pp.34, 91, 145).

[175] Crispin Gardiner. *Stochastic Methods: A Handbook for the Natural and Social Sciences.* Springer, 2009. (p.34).

[176] Agnieszka Rutkowska, Tahani M. Bawazeer, Julie V. Macpherson, and Patrick R. Unwin. Visualisation of electrochemical processes at optically transparent carbon nanotube ultra-microelectrodes (ot-cnt-umes). *Phys. Chem. Chem. Phys.*, 13:5223–5226, 2011. (p.37).

[177] Edgar J. Lopez-Naranjo, Luis J. Gonzalez-Ortiz, Luís M. Apatiga, Eric M. Rivera-Muñoz, and Alejandro Manzano-Ramírez. Transparent electrodes: A review of the use of carbon-based nanomaterials. *J.Nanomater.*, 2016(4928365):12, 2016. (p.37).

[178] Luis Santos, Pascal Martin, Jalal Ghilane, Pierre-Camille Lacaze, Hyacinthe Randriama-hazaka, Luisa Maria Abrantes, and Jean-Christophe Lacroix. Electrosynthesis of well-organized nanoporous poly(3,4-ethylenedioxythiophene) by nanosphere lithography. *Electrochem. Commun.*, 12(7):872 – 875, 2010. (p.37).

[179] B. Derjaguin and L. Landau. Theory of the stability of strongly charged lyophobic sols and of the adhesion of strongly charged particles in solutions of electrolytes. *Progress in Surface Science*, 43(1):30 – 59, 1993. (pp.39, 54).

[180] E.J.W. Verwey, J.T.G. Overbeek, and K. van Nes. *Theory of the Stability of Lyophobic Colloids: The Interaction of Sol Particles Having an Electric Double Layer.* Elsevier Publishing Company, 1948. (pp.39, 54).

[181] W.M. Haynes. *CRC Handbook of Chemistry and Physics.* CRC, 97th edition, 2016. (pp.39, 42).

[182] Shaltiel Eloul, Enno Kätelhön, Christopher Batchelor-McAuley, Kristina Tschulik, and Richard G. Compton. Diffusional nanoimpacts: The stochastic limit. *J. Phys. Chem. C*, 119(25):14400–14410, 2015. (p.39).

[183] Chuhong Lin and Richard G. Compton. Size effects in nanoparticle catalysis at nanoparticle modified electrodes: The interplay of diffusion and chemical reactions. *J. Phys. Chem. C*, 121(5):2521–2528, 2017. (pp.39, 54).

[184] G.Charlot. *Les méthodes de la Chimie Analytique : Analyse Quantitative Minérale.* Masson et Cte, 5th edition, 1966. (pp.42, 49).

[185] Anna Lombardi, Marcin P. Grzelczak, Aurélien Crut, Paolo Maioli, Isabel Pastoriza-

Santos, Luis M. Liz-Marzán, Natalia Del Fatti, and Fabrice Vallee. Optical response of individual au-ag@sio2 heterodimers. *ACS Nano*, 7(3):2522–2531, 2013. (p.47).

[186] Ian Streeter, Ronan Baron, and Richard G. Compton. Voltammetry at nanoparticle and microparticle modified electrodes: Theory and experiment. *J. Phys. Chem. C*, 111(45): 17008–17014, 2007. (p.49, 49).

[187] Stephen M. Oja, Donald A. Robinson, Nicholas J. Vitti, Martin A. Edwards, Yuwen Liu, Henry S. White, and Bo Zhang. Observation of multipeak collision behavior during the electro-oxidation of single ag nanoparticles. *J. Am. Chem. Soc.*, 139(2):708–718, 2017. (pp.51, 59, 59).

[188] En Ning Saw, Markus Kratz, and Kristina Tschulik. Time-resolved impact electrochemistry for quantitative measurement of single-nanoparticle reaction kinetics. *Nano Res.*, Jul 2017. (pp.51, 59).

[189] Jon Ustarroz, Minkyung Kang, Erin Bullions, and Patrick R. Unwin. Impact and oxidation of single silver nanoparticles at electrode surfaces: one shot versus multiple events. *Chem. Sci.*, 8:1841–1853, 2017. (pp.51, 59, 59).

[190] Wei Ma, Hui Ma, Jian-Fu Chen, Yue-Yi Peng, Zhe-Yao Yang, Hai-Feng Wang, Yi-Lun Ying, He Tian, and Yi-Tao Long. Tracking motion trajectories of individual nanoparticles using time-resolved current traces. *Chem. Sci.*, 8:1854–1861, 2017. (pp.51, 59).

[191] Anisha N. Patel, Ariadna Martinez-Marrades, Vitor Brasiliense, Dmitry Koshelev, Mondher Besbes, Robert Kuszelewicz, Catherine Combellas, Gilles Tessier, and Frédéric Kanoufi. Deciphering the elementary steps of transport-reaction processes at individual Ag nanoparticles by 3D superlocalization microscopy. *Nano Lett.*, 15(10):6454–6463, 2015. (p.53).

[192] Jean-Marc Noel, Vitor Brasiliense, Kevin Wonner, Veronique Rouchon, Catherine Combellas, Kristina Tschulik, and Frédéric Kanoufi. Local electrosynthesis and in situ characterization of uncapped colloidal silver nanocubes and gold nanoflowers. *submitted to Chem. Sci.*, 2017. (p.53).

[193] Todd M. Squires, Robert J. Messinger, and Scott R. Manalis. Making it stick: convection, reaction and diffusion in surface-based biosensors. *Nat. Biotechnol.*, 26(4):417–426, 2008. (p.53).

[194] Kristina Tschulik, Robert G Palgrave, Christopher Batchelor-McAuley, and Richard G Compton. Sticky electrodes for the detection of silver nanoparticles. *Nanotechnology*, 24 (29):295502, 2013. (p.54).

[195] Karima Ouhenia-Ouadahi, Amandine Andrieux-Ledier, Johannes Richardi, Pierre-Antoine Albouy, Patricia Beaunier, Peter Sutter, Eli Sutter, and Alexa Courty. Tuning the growth mode of 3D silver nanocrystal superlattices by triphenylphosphine. *Chem. Mater.*, 28(12): 4380–4389, 2016. (pp.60, 61, 65).

[196] Alexa Courty, Johannes Richardi, Pierre-Antoine Albouy, and Marie-Paule Pileni. How to control the crystalline structure of supracrystals of 5-nm silver nanocrystals. *Chem. Mater.*, 23(18):4186–4192, 2011. (p.60).

[197] Lionel Chapus, Pierre Aubertin, Suzanne Joiret, Ivan T. Lucas, Emmanuel Maisonhaute, and Alexa Courty. Tunable SERS platforms from small nanoparticles 3d superlattices: comparison between gold, silver and copper. *ChemPhysChem*, page n/a, 2017. (p.60).

[198] Pierre Aubertin, Mohamed Ali Ben Aissa, Noureddine Raouafi, Suzanne Joiret, Alexa Courty, and Emmanuel Maisonhaute. Optical response and sers properties of individual large scale supracrystals made of small silver nanocrystals. *Nano Res.*, 8(5):1615–1626, 2015. (p.60).

[199] Amandine Andrieux-Ledier, Benoit Tremblay, and Alexa Courty. Synthesis of silver nanoparticles using different silver phosphine precursors: Formation mechanism and size control. *J. Phys. Chem. C*, 117(28):14850–14857, 2013. (p.64, 64, 64).

[200] Nanfeng Zheng, Jie Fan, and Galen D. Stucky. One-step one-phase synthesis of monodisperse noble-metallic nanoparticles and their colloidal crystals. *Journal of the American Chemical Society*, 128(20):6550–6551, 2006. (p.64, 64).

[201] A. Taleb, C. Petit, and M. P. Pileni. Synthesis of highly monodisperse silver nanoparticles from AOT reverse micelles: A way to 2D and 3D self-organization. *Chem. Mater.*, 9(4): 950–959, 1997. (pp.64, 64, 65).

[202] Pierre Aubertin. *Propriétés optiques, spectroscopiques et électrochimiques d' auto-organisation tridimensionnelles de nanoparticules*. Phd, Université Pierre et Marie Curie, UPMC, 2016. (p.64).

[203] Keir C. Neuman and Steven M. Block. Optical trapping. *Rev. Sci. Instrum.*, 75(9):2787–2809, 2004. (p.73).

[204] Onofrio M. Marago, Philip H. Jones, Pietro G. Gucciardi, Giovanni Volpe, and Andrea C. Ferrari. Optical trapping and manipulation of nanostructures. *Nature Nanotech.*, 8(11): 807–819, 2013. (p.73, 73).

[205] James P. Gordon. Radiation forces and momenta in dielectric media. *Phys. Rev. A*, 8: 14–21, Jul 1973. (p.73).

[206] R.B. Bird, W.E. Stewart, and E.N. Lightfoot. *Transport Phenomena*. A Wiley International edition. Wiley, 2007. (p.77).

[207] M. Giglio and A. Vendramini. Soret-type motion of macromolecules in solution. *Phys. Rev. Lett.*, 38:26–30, Jan 1977. (p.78).

[208] Berend-Jan de Gans, Rio Kita, Simone Wiegand, and Jutta Luettmer-Strathmann. Unusual thermal diffusion in polymer solutions. *Phys. Rev. Lett.*, 91:245501, Dec 2003. (p.78).

[209] Stefan Duhr and Dieter Braun. Thermophoretic depletion follows boltzmann distribution. *Phys. Rev. Lett.*, 96:168301, Apr 2006. (pp.78, 78, 79).

[210] Linhan Lin, Xiaolei Peng, and Yuebing Zheng. Reconfigurable opto-thermoelectric printing of colloidal particles. *Chem. Commun.*, 53:7357–7360, 2017. (p.78).

[211] Linhan Lin, Xiaolei Peng, Mingsong Wang, Leonardo Scarabelli, Zhangming Mao, Luis M. Liz-Marzan, Michael F. Becker, and Yuebing Zheng. Light-directed reversible assembly of plasmonic nanoparticles using plasmon-enhanced thermophoresis. *ACS Nano*, 10(10): 9659–9668, 2016. (p.78).

[212] Howard Brenner. Elementary kinematical model of thermal diffusion in liquids and gases. *Phys. Rev. E*, 74:036306, Sep 2006. (pp.78, 79).

[213] James R. Bielenberg and Howard Brenner. A hydrodynamic/brownian motion model of thermal diffusion in liquids. *Physica A*, 356(2):279 – 293, 2005. (p.78).

[214] Alois Würger. Temperature dependence of the soret motion in colloids. *Langmuir*, 25(12):

6696–6701, 2009. (pp.78, 79).

[215] Stefan Duhr and Dieter Braun. Why molecules move along a temperature gradient. *Proc. Natl. Acad. Sci. USA*, 103(52):19678–19682, 2006. (pp.78, 79).

[216] Alois Würger. Is soret equilibrium a non-equilibrium effect? *Comptes Rendus Mécanique*, 341(4):438 – 448, 2013. 10th International Meeting on Thermodiffusion. (p.79).

[217] Roberto Piazza. Thermophoresis: moving particles with thermal gradients. *Soft Matter*, 4:1740–1744, 2008. (p.79).

[218] R. Spill, W. Köhler, G. Lindenblatt, and W. Schaertl. Thermal diffusion and soret feedback of gold-doped polyorganosiloxane nanospheres in toluene. *Phys. Rev. E*, 62:8361–8368, Dec 2000. (p.79).

[219] Marco Braibanti, Daniele Vigolo, and Roberto Piazza. Does thermophoretic mobility depend on particle size? *Phys. Rev. Lett.*, 100:108303, Mar 2008. (p.79, 79).

[220] A. L. Sehnem, R. Aquino, A. F. C. Campos, F. A. Tourinho, J. Depeyrot, and A. M. Figueiredo Neto. Thermodiffusion in positively charged magnetic colloids: Influence of the particle diameter. *Phys. Rev. E*, 89:032308, Mar 2014. (p.79).

[221] Mingcheng Yang and Marisol Ripoll. Driving forces and polymer hydrodynamics in the Soret effect. *J. Phys. Condens. Matter*, 24(19):195101, 2012. (p.79).

[222] Andreas P. Bregulla and Frank Cichos. Size dependent efficiency of photophoretic swimmers. *Farad. Disc.*, 184:381–391, 2015. (p.79).

[223] Jérémie Palacci, Benjamin Abécassis, Cécile Cottin-Bizonne, Christophe Ybert, and Lydéric Bocquet. Colloidal motility and pattern formation under rectified diffusiophoresis. *Phys. Rev. Lett.*, 104:138302, Apr 2010. (p.82).

[224] Ralf Metzler, Jae-Hyung Jeon, Andrey G. Cherstvy, and Eli Barkai. Anomalous diffusion models and their properties: non-stationarity, non-ergodicity, and ageing at the centenary of single particle tracking. *Phys. Chem. Chem. Phys.*, 16:24128–24164, 2014. (p.87).

[225] Vitor Brasiliense, Jan Clausmeyer, Alice L. Dauphin, Jean-Marc Noël, Pascal Berto, Gilles Tessier, Wolfgang Schuhmann, and Fréderic Kanoufi. Opto-electrochemical in situ monitoring of the cathodic formation of single cobalt nanoparticles. *Angew. Chem. Int. Ed.*, 56 (35):10598–10601, 2017. (p.95).

[226] Vitor Brasiliense, Jan Clausmeyer, Alice L. Dauphin, Jean-Marc Noël, Pascal Berto, Gilles Tessier, Wolfgang Schuhmann, and Fréderic Kanoufi. Opto-electrochemical in situ monitoring of the cathodic formation of single cobalt nanoparticles. *Anal. Chem. (submitted)*, page n/a, 2017. (p.95).

[227] Gary Wulfsberg. *Chimie inorganique : Cours et exercices corrigés*. Sciences Sup, 2002. (p.96).

[228] Bryan M. Hunter, Harry B. Gray, and Astrid M. Müller. Earth-abundant heterogeneous water oxidation catalysts. *Chem. Rev.*, 116(22):14120–14136, 2016. (p.96, 96).

[229] Marcelo Carmo, David L. Fritz, and J⸱ A comprehensive review on PEM water electrolysis. *Int. J. Hydrog. Energy*, 38(12):4901 – 4934, 2013. (p.96).

[230] Xiumin Li, Xiaogang Hao, Abuliti Abudula, and Guoqing Guan. Nanostructured catalysts for electrochemical water splitting: current state and prospects. *J. Mater. Chem. A*, 4: 11973–12000, 2016. (p.96).

[231] Charles C. L. McCrory, Suho Jung, Jonas C. Peters, and Thomas F. Jaramillo. Benchmarking heterogeneous electrocatalysts for the oxygen evolution reaction. *J. Am. Chem. Soc.*, 135(45):16977–16987, 2013. (p.96, 96).

[232] N. Chouhan, R.S. Liu, and J. Zhang. *Photochemical Water Splitting: Materials and Applications.* Electrochemical Energy Storage and Conversion. CRC Press, 2017. (p.96).

[233] Matthew W. Kanan and Daniel G. Nocera. In situ formation of an oxygen-evolving catalyst in neutral water containing phosphate and co2+. *Science*, 321(5892):1072–1075, 2008. (pp.96, 101).

[234] Daniel A. Lutterman, Yogesh Surendranath, and Daniel G. Nocera. A self-healing oxygen-evolving catalyst. *J. Am. Chem. Soc.*, 131(11):3838–3839, 2009. (pp.96, 101).

[235] Yogesh Surendranath, Daniel A. Lutterman, Yi Liu, and Daniel G. Nocera. Nucleation, growth, and repair of a cobalt-based oxygen evolving catalyst. *J. Am. Chem. Soc.*, 134 (14):6326–6336, 2012. (pp.96, 115).

[236] Yogesh Surendranath, Mircea Dinca, and Daniel G. Nocera. Electrolyte-dependent electrosynthesis and activity of cobalt-based water oxidation catalysts. *J. Am. Chem. Soc.*, 131(7):2615–2620, 2009. (pp.96, 96, 101).

[237] Yi Liu and Daniel G. Nocera. Spectroscopic studies of nanoparticulate thin films of a cobalt-based oxygen evolution catalyst. *J. Phys. Chem. C*, 118(30):17060–17066, 2014. (p.96, 96).

[238] C Corolleur, F.G Gault, D Juttard, G Maire, and J.M Muller. Effect of the metal particle size in supported catalysts on the selectivity and the reaction mechanisms. *J. Catal.*, 27 (3):466 – 468, 1972. (p.96).

[239] Guoli Fan, Feng Li, David G. Evans, and Xue Duan. Catalytic applications of layered double hydroxides: recent advances and perspectives. *Chem. Soc. Rev.*, 43:7040–7066, 2014. (p.97).

[240] Paolo Actis, Sergiy Tokar, Jan Clausmeyer, Babak Babakinejad, Sofya Mikhaleva, Renaud Cornut, Yasufumi Takahashi, Ainara López Córdoba, Pavel Novak, Andrew I. Shevchuck, Jennifer A. Dougan, Sergei G. Kazarian, Petr V. Gorelkin, Alexander S. Erofeev, Igor V. Yaminsky, Patrick R. Unwin, Wolfgang Schuhmann, David Klenerman, Dmitri A. Rusakov, Elena V. Sviderskaya, and Yuri E. Korchev. Electrochemical nanoprobes for single-cell analysis. *ACS Nano*, 8(1):875–884, 2014. (pp.97, 98).

[241] Yasufumi Takahashi, Andrew I. Shevchuk, Pavel Novak, Yanjun Zhang, Neil Ebejer, Julie V. Macpherson, Patrick R. Unwin, Andrew J. Pollard, Debdulal Roy, Charles A. Clifford, Hitoshi Shiku, Tomokazu Matsue, David Klenerman, and Yuri E. Korchev. Multifunctional nanoprobes for nanoscale chemical imaging and localized chemical delivery at surfaces and interfaces. *Angew. Chem. Int. Ed.*, 50(41):9638–9642, 2011. (pp.97, 154).

[242] Patrick J. Rodgers, Shigeru Amemiya, Yixian Wang, and Michael V. Mirkin. Nanopipet voltammetry of common ions across the liquid-liquid interface. theory and limitations in kinetic analysis of nanoelectrode voltammograms. *Anal. Chem.*, 82(1):84–90, 2010. (p.97).

[243] A. C. Ferrari and J. Robertson. Interpretation of raman spectra of disordered and amorphous carbon. *Phys. Rev. B*, 61:14095–14107, May 2000. (p.97).

[244] Cyrille Costentin, Thomas R. Porter, and Jean-Michel Savéant. Conduction and reac-

tivity in heterogeneous-molecular catalysis: New insights in water oxidation catalysis by phosphate cobalt oxide films. *J. Am. Chem. Soc.*, 138(17):5615–5622, 2016. (p.101).

[245] Karthryn Podolske Ta and John Newman. Mass transfer and kinetic phenomena at the nickel hydroxide electrode. *J. Electrochem. Soc.*, 145(11):3860–3874, 1998. (p.109).

[246] E.M. Garcia, J.S. Santos, E.C. Pereira, and M.B.J.G. Freitas. Electrodeposition of cobalt from spent Li-ion battery cathodes by the electrochemistry quartz crystal microbalance technique. *J. Power Sources*, 185(1):549 – 553, 2008. (p.112).

[247] Anna L. Barker, Julie V. Macpherson, Christopher J. Slevin, and Patrick R. Unwin. Scanning electrochemical microscopy (SECM) as a probe of transfer processes in two-phase systems: Theory and experimental applications of SECM-induced transfer with arbitrary partition coefficients, diffusion coefficients, and interfacial kinetics. *J. Phys. Chem. B*, 102 (9):1586–1598, 1998. (p.114).

[248] Marcel Risch, Franziska Ringleb, Mike Kohlhoff, Peter Bogdanoff, Petko Chernev, Ivelina Zaharieva, and Holger Dau. Water oxidation by amorphous cobalt-based oxides: in situ tracking of redox transitions and mode of catalysis. *Energy Environ. Sci.*, 8:661–674, 2015. (pp.114, 116, 118).

[249] Cyrille Costentin, Thomas R. Porter, and Jean-Michel Savéant. Conduction and reactivity in heterogeneous-molecular catalysis: New insights in water oxidation catalysis by phosphate cobalt oxide films. *J. Am. Chem. Soc.*, 138(17):5615–5622, 2016. (pp.115, 115, 116, 118).

[250] Nicolas Kaeffer, Adina Morozan, Jennifer Fize, Eugenie Martinez, Laure Guetaz, and Vincent Artero. The dark side of molecular catalysis: Diimine–dioxime cobalt complexes are not the actual hydrogen evolution electrocatalyst in acidic aqueous solutions. *ACS Catalysis*, 6(6):3727–3737, 2016. (p.116).

[251] Hyun S. Ahn and Allen J. Bard. Surface interrogation of Co-Pi water oxidation catalyst by scanning electrochemical microscopy. *J. Am. Chem. Soc.*, 137(2):612–615, 2015. (p.118).

[252] J. Gregory McAlpin, Yogesh Surendranath, Mircea Dinca, Troy A. Stich, Sebastian A. Stoian, William H. Casey, Daniel G. Nocera, and R. David Britt. EPR evidence for Co(iv) species produced during water oxidation at neutral ph. *J. Am. Chem. Soc.*, 132(20):6882–6883, 2010. (p.118).

[253] S.F. Johnston. *Holographic Visions: A History of New Science.* Spencer, H.; Herbert Spencer lectures. OUP Oxford, 2006. (pp.129, 130, 131, 132, 134).

[254] Emmett N. Leith and Juris Upatnieks. Reconstructed wavefronts and communication theory. *J. Opt. Soc. Am.*, 52(10):1123–1130, Oct 1962. (pp.130, 132, 132).

[255] J.W. Goodman. *Introduction to Fourier Optics.* McGraw-Hill physical and quantum electronics series. W. H. Freeman, 2005. (pp.130, 132).

[256] Dennis Gabor. A new microscopic principle. *Nature*, 161:777– 778, 1965. (p.130).

[257] Emmett N. Leith and Juris Upatnieks. Wavefront reconstruction with continuous-tone objects. *J. Opt. Soc. Am.*, 53(12):1377–1381, Dec 1963. (p.132).

[258] Emmett N. Leith and Juris Upatnieks. Wavefront reconstruction with diffused illumination and three-dimensional objects. *J. Opt. Soc. Am.*, 54(11):1295–1301, Nov 1964. (pp.132, 134).

[259] R. F. Wuerker. Holography and holographic interferometry : Industrial applications. *Ann. N. Y. Acad. Sci.*, 168(3):492–505, 1969. (pp.133, 134).

[260] Jeff Hecht. Holography and the laser. *Opt. Photon. News*, 21(7):34–41, 2010. (pp.133, 134).

[261] Miyu Ozaki, Jun-ichi Kato, and Satoshi Kawata. Surface-plasmon holography with white-light illumination. *Science*, 332(6026):218–220, 2011. (pp.133, 134).

[262] J.W.C. Gates. Holography, industry and the rebirth of optics. *Review of Physics in Technology*, 2(3):173, 1971. (p.133).

[263] Staffan Schedin, Giancarlo Pedrini, Hans J. Tiziani, and Fernando Mendoza Santoyo. Simultaneous three-dimensional dynamic deformation measurements with pulsed digital holography. *Appl. Opt.*, 38(34):7056–7062, Dec 1999. (p.133, 133).

[264] J.N. Butters and J.A. Leendertz. Speckle pattern and holographic techniques in engineering metrology. *Opt. Laser Technol.*, 3(1):26 – 30, 1971. (p.133).

[265] A. Foust, V. Zampini, D. Tanese, E. Papagiakoumou, and V. Emiliani. Computer-generated holography enhances voltage dye fluorescence discrimination in adjacent neuronal structures. *Neurophotonics*, 2(2):021007, 4 2015. (p.133).

[266] G. Pedrini, Y.L. Zou, and H.J. Tiziani. Digital double-pulsed holographic interferometry for vibration analysis. *J. Mod. Opt.*, 42(2):367–374, 1995. (p.133).

[267] A. W. Lohmann and D. P. Paris. Binary fraunhofer holograms, generated by computer. *Appl. Opt.*, 6(10):1739–1748, Oct 1967. (p.133).

[268] B. R. Brown and A. W. Lohmann. Computer-generated binary holograms. *IBM Journal of Research and Development*, 13(2):160–168, 1969. (p.133).

[269] U. Schnars and W. Jüptner. Direct recording of holograms by a ccd target and numerical reconstruction. *Appl. Opt.*, 33(2):179–181, 1994. (p.133).

[270] Masahiro Yamaguchi. Light-field and holographic three-dimensional displays. *J. Opt. Soc. Am. A*, 33(12):2348–2364, Dec 2016. (p.133).

[271] Takashi Kakue, Takashi Nishitsuji, Tetsuya Kawashima, Keisuke Suzuki, Tomoyoshi Shimobaba, and Tomoyoshi Ito. Aerial projection of three-dimensional motion pictures by electro-holography and parabolic mirrors. *Sci. Rep.*, 5:11750, 2015. (p.133).

[272] Microsoft hololens website. `https://www.microsoft.com/en-us/hololens`. Accessed: 2017-08-17. (p.133).

[273] Emilio Sánchez-Ortiga, Ana Doblas, Genaro Saavedra, Manuel Martínez-Corral, and Jorge Garcia-Sucerquia. Off-axis digital holographic microscopy: practical design parameters for operating at diffraction limit. *Appl. Opt.*, 53(10):2058–2066, Apr 2014. (pp.138, 139).

[274] Nicolas Verrier and Michael Atlan. Off-axis digital hologram reconstruction: some practical considerations. *Appl. Opt.*, 50(34):H136–H146, Dec 2011. (p.139).

[275] Frédéric Verpillat. *Suivi 3D de nanoparticules d'or par holographie digitale*. PhD thesis, Université Pierre et Marie Curie - Paris VI, 2012. (p.141).

[276] Russell E. Thompson, Daniel R. Larson, and Watt W. Webb. Precise nanometer localization analysis for individual fluorescent probes. *Biophys. J.*, 82(5):2775 – 2783, 2002. (p.142).

[277] Tim Albrecht, Julie MacPherson, Olaf Magnussen, David Fermin, Richard Crooks, Justin

Gooding, Thom Hersbach, Frederic Kanoufi, Wolfgang Schuhmann, Cameron Bentley, Nongjian Tao, Sushanta Mitra, Katharina Krischer, Kristina Tschulik, Sanli Faez, Wojciech Nogala, Patrick Unwin, Yitao Long, Marc Koper, Zhongqun Tian, Mario A. Alpuche-Aviles, Henry White, Vitor Brasiliense, Christine Kranz, Wolfgang Schmickler, Keith Stevenson, Chao Jing, and Martin Edwards. Electrochemistry of single nanoparticles: general discussion. *Farad. Disc.*, 193:387–413, 2016. (p.143).

[278] H.C. van Hulst. *Light Scattering by Small Particles*. Dover, 1981. (p.143).

[279] Ralf Metzler, Jae-Hyung Jeon, Andrey G. Cherstvy, and Eli Barkai. Anomalous diffusion models and their properties: non-stationarity, non-ergodicity, and ageing at the centenary of single particle tracking. *Phys. Chem. Chem. Phys.*, 16:24128–24164, 2014. (p.146).

[280] H.C. Berg. *Random Walks in Biology*. Princeton paperbacks. Princeton University Press, 1993. (p.146).

[281] K. Svoboda and S. M. Block. Biological applications of optical forces. *Annu. Rev. Biophys.*, 23(1):247–285, 1994. (p.147).